Electron Correlations and Topology in Moiré Materials and Beyond



Ziwei Wang

Exeter College

University of Oxford

A thesis submitted for the degree of

Doctor of Philosophy in Theoretical Physics

Trinity 2026

Acknowledgements

To begin, I would like to express my deepest gratitude to my supervisor, Steve Simon, for his patient guidance and constant support throughout my DPhil. I have greatly enjoyed our many discussions, from which I learned an enormous amount. His ingenuity and clarity of thought have been a continual source of inspiration to me.

I am also very grateful to Sid Parameswaran for his mentorship and for many fruitful collaborations. I have always been deeply impressed by his physical intuition and remarkable quickness of thought, and I learned a great deal from both. Through his guidance and example, he has helped me become a better physicist.

I would especially like to thank Yves Kwan, with whom I had the pleasure of collaborating closely over many long hours. I have been continually impressed by his precision and care as a physicist, and I learned a great deal from working alongside him. I would also like to thank Glenn Wagner and Nick Bultinck for many enjoyable and insightful collaborations and discussions, and my experimental collaborators Mitali Banerjee and Zekang Zhou.

I would like to thank my colleagues and friends in the Beecroft building for the many stimulating discussions and exchanges of ideas over the years. I benefited greatly from the advice and guidance of many people in the community. I also have very fond memories of the many conversations in the corridors, around the coffee table, and at pub nights, all of which made my time here a particularly enjoyable experience. I would also like to give special thanks to fellow members of my cohort, Konstantinos Vasiliou and Chuqiao Lin, whose friendship and companionship meant a great deal to me during these years.

Finally, I would like to thank my friends and families for their companionship support throughout these years. I am especially grateful to my parents for their constant encouragement, patience, and unwavering belief in me.

Abstract

This thesis is primarily focused on the study of electron correlations and topology in moiré materials, though the contents of Chap. 5 and Chap. 6, while also relevant to moiré materials, constitute more general theoretical discussions.

Correlated insulators are commonly occurring phenomena in twisted bilayer graphene, and the incommensurate Kekulé spiral is one of the proposed candidate state and has recently been conclusively confirmed by experiments. In Chap. 3, we numerically explore the phase diagram of twisted symmetric trilayer graphene and observe that incommensurate Kekulé spirals and their commensurate counterparts can be stabilized in different regimes of the system. In a different direction, we explore the spin structure of incommensurate Kekulé spirals, discuss the microscopic mechanisms that determine it, and how this influences the neutral collective modes of the system.

Going beyond insulators, in Chap. 4, we examine the symmetry and Fermi surfaces of doped incommensurate Kekulé spiral states, and understand their roles as parent states in constraining the symmetry of potential superconducting orders. We then explore how the normal states phase diagrams can provide important clues for understanding double-dome superconductivity in twisted symmetric trilayer graphene.

In Chap. 5, we propose a new type of topological correlated insulator, namely the Chern texture insulator, which spontaneously breaks a U(1) symmetry in a system with underlying Chern bands. We demonstrate that this enforces non-trivial momentum space texture on the order parameter of this correlated insulator, and with the help of Hartree-Fock, we show that they could potentially be realized in a large number of moiré systems.

In the study of fractional quantum Hall effects and later fractional Chern insulators, one commonly discussed mathematical structure is the Girvin-MacDonald-Platzman algebra. In Chap. 6, we prove that, for *any* Chern band, if the band projected density algebra is closed, the algebra must *always* be the Girvin-MacDonald-Platzman algebra up to freedom to choose some form factors. We also discuss some related results on quantum geometry.

Abbreviations

1. BCS: Bardeen–Cooper–Schrieffer
2. BM: Bistritzer-MacDonald
3. BZ: Brillouin zone
4. CKS: commensurate Kekulé spiral
5. CTI: Chern texture insulator
6. FCI: fractional Chern insulator
7. FQAHE: fractional quantum anomalous Hall effect
8. FQHE: fractional quantum Hall effect
9. FS: Fermi surface
10. GMP: Girvin-MacDonald-Platzman
11. hBN: hexagonal boron nitride
12. HF: Hartree-Fock
13. IKS: incommensurate Kekulé spirals
14. IVC: intervalley coherence
15. K-IVC: Kramers-intervalley coherence
16. LL: Landau level
17. LLL: lowest Landau level
18. mBZ: moiré Brillouin zone
19. NGM: Nambu-Goldstone mode

20. ODA: optimal damping algorithm
21. RLV: reciprocal lattice vector
22. SOC: spin-orbit coupling
23. STM: scanning tunneling spectroscopy
24. TBG: twisted bilayer graphene
25. TBTG: twisted bilayer-trilayer graphene
26. TDBG: twisted double-bilayer graphene
27. TDHF: time-dependent Hartree-Fock
28. TEI: textured exciton insulator
29. TMBG: twisted mono-bilayer graphene
30. TMD: transitional metal dichalcogenide
31. TSTG: twisted symmetric trilayer graphene
32. TVP: tilted-valley-polarized
33. VP: valley-polarized

Publications

Publications marked with a dagger (†) are discussed in this thesis.
Asterisk (*) indicates equal contribution.

9. **Ziwei Wang**, Charlie Raca, Steven H. Simon, Symmetry and Quantum Geometry in Bloch Bands, arXiv:2607.21581 (2026)

8. Maosen Qin, **Ziwei Wang**, Gyeongmin Kim, Kenji Watanabe, Takashi Taniguchi, Steven H Simon, Siddharth A Parameswaran, Hryhoriy Polshyn, Engineering electrically-switchable quantum anomalous Hall states by spin-orbit coupling, arXiv:2606.13651 (2026)

7. † Yves H. Kwan, **Ziwei Wang**, Glenn Wagner, Nick Bultinck, Steven H. Simon, and Siddharth A. Parameswaran, Mean-field Modelling of Moiré Materials: A User's Guide with Selected Applications to Twisted Bilayer Graphene, Advances in Physics, 74:1-4, 11-96 (2025)

6. † **Ziwei Wang**, Glenn Wagner, Yves H. Kwan, Nick Bultinck, Steven H. Simon, and S.A. Parameswaran, Putting a new spin on the incommensurate Kekulé spiral: spin-valley locking, fermiology, collective modes, and implications for superconductivity, arXiv:2509.12320 (2025)

5. † Zekang Zhou, Jin Jiang, Paritosh Karnatak, **Ziwei Wang**, Glenn Wagner, Kenji Watanabe, Takashi Taniguchi, Christian Schönenberger, S. A. Parameswaran, Steven H. Simon, and Mitali Banerjee, Gate-tunable Double-dome Superconductivity in Twisted Trilayer Graphene, Nat. Phys. 21, 1773–1779 (2025)

4. † **Ziwei Wang***, Yves H. Kwan*, Glenn Wagner, Steven H. Simon, Nick Bultinck, and S. A. Parameswaran, Chern-textured exciton insulators with valley spiral order in moiré materials, Phys. Rev. B 112, 035130 (2025)

3. † Yves H. Kwan*, **Ziwei Wang***, Glenn Wagner, Steven H. Simon, S. A. Parameswaran, and Nick Bultinck, Textured exciton insulators, Phys. Rev. B 112, 035129 (2025)

2. † **Ziwei Wang** and Steven H. Simon, Closed Band-Projected Density Algebra Must Be Girvin-MacDonald-Platzman, Phys. Rev. Lett. 134, 136502 (2025)

1. † **Ziwei Wang**, Yves H. Kwan, Glenn Wagner, Nick Bultinck, Steven H. Simon, and S. A. Parameswaran, Kekulé spirals and charge transfer cascades in twisted symmetric trilayer graphene, Phys. Rev. B 109, L201119 (2024)

Contents

1 Introduction **1**

1.1 Overview of moiré materials 2

1.2 Theoretical approaches 5

1.3 Thesis outline 6

2 Background and methods **9**

2.1 Basics of twisted bilayer graphene 9

2.2 Continuum model of twisted bilayer graphene 11

2.2.1 Bistritzer-MacDonald continuum model with strain 11

2.2.2 Effects of heterostrain 13

2.2.3 Adding interactions 14

2.3 Hartree-Fock mean-field theory 18

2.3.1 Hartree-Fock basics 18

2.3.2 Solving the self-consistent mean-field equations 19

2.3.3 HF Implementation in moiré problems 21

2.3.4 Finite-size effects and Hartree-Fock interpolation 23

2.3.5 Time-dependent Hartree-Fock 24

2.3.6 Hartree-Fock and Hubbard model 26

3 Incommensurate Kekulé spirals **27**

3.1 What is the incommensurate Kekulé spiral? 27

3.1.1 IKS and Hartree-Fock 29

3.2 Kekulé spirals in twisted symmetric trilayer graphene 31

3.2.1 Modeling on twisted symmetric trilayer graphene 31

3.2.2 Phase diagram . . . 34
3.2.3 Commensurate Kekulé spirals. . . . 36
3.2.4 Charge-transfer cascades. . . . 37
3.3 Spin structure of incommensurate Kekulé spirals . . . 39
3.3.1 Methods . . . 40
3.3.2 Lifting spin-valley degeneracy in the IKS Manifold . . . 43
3.3.3 IKS ground states in the presence of applied fields . . . 52
3.4 Collective modes . . . 54
3.5 Remarks . . . 60

4 Doped IKS and superconductivity **63**
4.1 Twisted bilayer graphene . . . 64
4.1.1 Normal parent states in TBG . . . 64
4.1.2 Implications for superconductivity . . . 66
4.2 Twisted symmetric trilayer graphene . . . 69
4.2.1 Experimental observation . . . 70
4.2.2 Theoretical work . . . 70

5 Chern texture insulators **75**
5.1 Theory of Chern texture insulators . . . 76
5.1.1 Topology of Chern texture insulators . . . 79
5.1.2 LLL model and Chern texture insulators . . . 80
5.1.3 Phase diagram . . . 83
5.2 Chern texture insulators in moiré materials . . . 86
5.2.1 Continuum models . . . 86
5.2.2 Twisted double-bilayer graphene (ABAB) . . . 90
5.2.3 Twisted double-bilayer graphene (ABBA) . . . 93
5.2.4 Twisted monolayer-bilayer graphene . . . 96
5.2.5 Twisted bilayer-trilayer graphene . . . 98
5.2.6 Discussion . . . 99

6 Girvin-MacDonald-Platzman algebra **101**
6.1 Main result . . . 103

6.2 Proof . . . 103
6.2.1 Main proof . . . 103
6.2.2 Treatment of singularities . . . 106
6.2.3 Properties of form factors . . . 107
6.3 Further Results . . . 108
6.3.1 Constrain on multiplication algebras . . . 108
6.3.2 Condition of constant quantum geometry tensor . . . 108

7 Conclusions **111**

A Superconducting order parameter from IVC Fermi surfaces **113**
A.1 Spin polarized IKS . . . 113
A.2 Spin-valley locked IKS . . . 116
A.3 Spin singlet IKS . . . 117

B Additional experimental data **119**

C Delicate topology of Chern texture insulators **121**

D Gauge fixing and gauge-invariant velocity **123**
D.1 Gauge fixing for intervalley order parameter . . . 123
D.2 Gauge-invariant velocity on a grid . . . 124

Chapter 1

Introduction

When two periodic structures with slightly different periodicities are overlaid on top of one another, a longer wavelength interference pattern, called the moiré pattern, forms. As such, by stacking two or more layers of two-dimensional materials with angular offsets, different lattice constants, or both, one can construct new types of materials with moiré modulations i.e., moiré materials. In the recent decade, these materials have generated significant interest in the condensed matter physics community, starting with the experimental discovery [1] of enhanced density of states in a system where two layers of graphene are placed on top of one another with a small relative twist, i.e., "twisted bilayer graphene (TBG)", and subsequent theoretical prediction of vanishing Dirac velocities and flattened electronic bands at certain "magic angles" in TBG [2, 3] (see also Ref. [4]). Later on, the field received high level of interest due to the experimental discovery of correlated insulators and superconductivity in TBG [5, 6], which has prompted comparison with cuprates, which similarly see correlated insulators and superconductors in proximity. Nevertheless, as the field of moiré materials develops and matures, it has now gone far beyond an imitation of the study of conventional crystalline materials.

Moiré materials are now typically fabricated with the tear-and-stack method with sub-degree control over the twist angles [7]. Due to the inherently flexible nature of this method, since the discovery of TBG, a large variety of moiré materials have been both theoretically and experimentally studied, including various graphene based materials and those based on transitional metal dichalcogenides (TMD). This endless possible combination of materials is, in the opinion of the present author, one of the major attraction of moiré materials.

Another significant advantage of such moiré materials over conventional crystalline systems is that the moiré materials have large real space unit cells, allowing the filling factors to be tuned *in situ* with electric gates. This allows different electron densities to be studied within one device without involving chemical doping and the associated complications. On the theoretical side, moiré materials frequently carry a rich array of non-trivial topological properties, which will form part of the subject matter of this thesis.

This thesis presents the author's contribution to the study of electron correlation and topology in this broad class of two-dimensional materials. In Chap. 1.1, starting from TBG, we provide an overview of the field of moiré materials. The examples that we will discuss are naturally biased towards those that are more closely related to the author's own research and the rest of the thesis. In Chap. 1.2, we situate our theoretical approach in the broader landscape of theoretical studies of moiré materials. In Chap. 1.3, we provide a outline of this thesis.

1.1 Overview of moiré materials

One of the earliest and most significant discovery in the field of moiré materials is the prediction that when the twist angle is at a so-called "magic angle" of about 1.1° in TBG[1], due to the interference of the two layers, the renormalized Dirac velocity vanishes completely [2, 4]. Later on, it is found that under some idealized assumptions, not only does the Dirac velocity vanish at these angles, the entire central electronic bands become completely flat [3]. As the kinetic energy becomes small, interaction starts to dominate and correlated effects become prominent. This forms the basic theoretical background of magic-angle TBG.

The most significant early experimental discoveries about TBG, as already mentioned, is the observation of correlated insulators and superconductors in close proximity [5, 6]. One of the important questions raised is regarding the identity of the observed correlated insulators, and a large number of theoretical proposals have since been made. Among the many proposals, we would like to mention the incommensurate Kekulé spiral (IKS) state, which is proposed to be the zero-temperature ground states for all non-zero integer

[1]Strictly speaking, a series of magic angles were predicted and the largest one is about 1.1°. Most of the experimental and theoretical investigations so far are focused on the magic angle of 1.1°.

fillings from -3 to $+3$ [8] and a large range of non-integer fillings [9]. The key physical feature of IKS has been experimentally observed at a range of filling factors [10]. This state will be discussed in greater details in Chap. 3 and will form a recurring subject matter in this thesis. As for superconductivity, while its existence in TBG is robust and incontrovertible, many aspects of it remain debated in the literature. We will defer a discussion on this to Chap. 4. We also note that a range of other effects, such as pseudogap [10, 11], Pomeranchuk effects [12–14], and cascades [15, 16] have also been studied in TBG.

It was later realized that TBG is not the only class of materials that demonstrate the magic angle behavior. In Ref. [17, 18], the authors proposed a class of "alternating twisted multilayer graphene", that demonstrates very similar "magic angle" behavior. The simplest example is twisted symmetric trilayer graphene (TSTG), which consists of three sheets of monolayer graphene with the middle layer twisted relative to the top and bottom layers. This material shares many similarities with TBG, but affords greater tunability with externally applied electric field. Many phenomena observed in TBG, from IKS [19] to nodal superconducting gaps [20, 21] are also replicated in TSTG, where some phenomena, such as double-dome superconductivity, which will be discussed extensively in Chap. 4, are observed only in TSTG but not in TBG.

As the field of moiré materials develops and progresses, it becomes clear that the "magic angle" is not a necessary condition for non-trivial physics to appear. Indeed, as long as the interaction energy is comparable with the kinetic energy, interaction effects will play a significant role. This frees us from considering such fine-tuned constructions, and allows us to consider a much larger variety of possibilities.[2] Here, the main experimental limitation is that the constituent materials must be exfoliable. In this respect, some of the best experimentally studied materials are graphene, transitional metal dichalcogenides (TMD) and hexagonal boron nitride (hBN).

Graphene, including its monolayer and few layer variants, can be well-described as semimetal at charge neutrality. Besides TBG and alternating twisted multilayer graphene, one can also employ (untwisted) bilayer and multilayers as building components to construct moiré devices. TMD materials, on the other hand, are generally semiconductors. Unlike

[2]Realistic estimates of band-width of TBG at magic angles is about 10 meV [22, 23], which is similar to many other moiré materials without a "magic angle" description.

graphene-based systems, they have strong spin-orbit coupling such that the low-energy bands are spin-valley-locked [24]. Besides serving as the active component, TMD material can also be placed near graphene to induce spin-orbit-coupling [25, 26]. On the other end of the spectrum, hBN is an insulator, and is usually used as a substrate to encapsulate the active components such as graphene and TMD. Nevertheless, hBN also plays important roles in the physics of moiré materials, such as setting the dielectric screening of the device, inducing 2-fold rotation symmetry breaking when aligned with graphene [27], and generating a moiré pattern between graphene and hBN [28], as hBN has a different lattice constant than graphene [29].

At this point, we would like to point out that, besides strong interaction, non-trivial band topology is also an important feature for many of the moiré materials. Broadly speaking, non-trivial band topology includes, but is not limited to, strong topology and fragile topology. Strong topology is stable against addition of trivial bands, while fragile topology is unstable against addition of trivial bands [30]. In this context, strong topology is typified by Chern topology. A large class of moiré materials which do not have a certain 2-fold rotation symmetry is expected to host Chern bands. This includes graphene-based materials, such as twisted mono-bilayer graphene (TMBG) and TMD materials, such as such as $MoTe_2$ and WSe_2. In many of the materials, from twisted TMD [31] to graphene-based devices [32, 33], one observes spontaneously breaking of time-reversal symmetry and thereby quantized Hall conductance without external magnetic field, i.e., quantum anomalous Hall effects. Furthermore, theorists have long predicted the fractional version of this effect, i,e., fractional quantum anomalous Hall effect (FQAHE) or fractional Chern insulator (FCI) [34–36], and this has first been observed in twisted $MoTe_2$ [37–41] and rhombohedral graphene on hBN [42–44]. On the other hand, for materials like TBG (without aligned hBN), due to the combination of time-reversal symmetry and a two-fold rotation symmetry, the single-particle band structure does not contain Chern bands. Nevertheless, as the two Dirac points in the moiré Brillouin zone (mBZ) have the same windings, they cannot annihilate, and the central bands of TBG do not have a tight-binding description [30, 45, 46]. This is an example of fragile topology[3].

Finally, we note that, for the materials we have discussed so far, the moiré physics is

[3]If we promote the approximate particle-hole symmetry in TBG to an exact symmetry, it can be shown that the fragile topology becomes strong topology [47, 48].

derived from the band structure of the constituent materials near K-points, such as the Dirac points in graphene, as it is the K-points that are low-energy (i.e., close to the Fermi energy at charge neutrality) in these materials. In fact, there exist moiré materials where the relevant physics is centered at other high-symmetry points such as the Γ-point [49, 50] and M-points [51, 52], or less-symmetric momentum regions [53, 54]. Among them, M-point moiré materials have received significant attention recently, due to the predicted novel phenomena such as quasi-1D behaviours [51].

1.2 Theoretical approaches

A basic workflow in the theoretical study of moiré materials (and large parts of condensed matter physics in general) starts off by constructing a microscopic model of the system in question with inputs from *ab initio* simulations and experiments. Once we have obtained the microscopic model, we can approach it with a range of theoretical tools. In this thesis, our approach will rely heavily on numerical simulations, in particular, Hartree-Fock (HF) mean-field studies. In Chap. 2, we will thoroughly review the HF method and its application in moiré materials. Here, we would like to situate our approach in the broad range of theoretical tools available and understand its advantages and weaknesses.

At first glance, it may appear that HF, as a mean-field method, may be rather limited in its effectiveness. Indeed, many other beyond mean-field methods have been deployed in the studies of moiré materials, but they also have their own limitations. For example, determinantal quantum Monte Carlo [55–60] is a highly power method, but due to the well-known sign problem, it is only applicable to a subset of models at special densities. Exact diagonalization [61, 62], which is an essential tool to explore the physics of fractional Chern insulators (FCI) [63–66]), is clearly limited in system size and number of internal degrees of freedom that can be included. Similarly, density-matrix renormalization group and other tensor network methods [67–74] work best for problems with reduced degeneracy and for insulating states due to computational cost. This leaves mean-field approaches as some of the best available tools when tackling a generic problem.

On the other hand, mean-field approaches can be "surprisingly" reliable for the study of moiré systems. One justification comes from the study of twisted bilayer graphene,

where it can be shown that a Slater determinant state is the exact ground state at some idealized limit of the problem [75, 76], providing us a conceptual basis for our approach. More practically, HF has known to give predictions that are later verified by experiments, even away from this idealized limit. The incommensurate Kekulé spiral state, which we will introduce in Chap. 3, is one such example. It is for similar reasons that many groups have studied moiré materials using the HF method [8, 9, 71, 75–97]. Last but not least, it goes without saying that there are many problems that are intrinsically beyond the grasp of mean-field methods, and alternative methods will be necessary in those cases.

Besides ground states, one may also be interested in the excited states of the system. A crude method involves constructing particle-hole excitations "by hand" from the ground state Hartree-Fock bandstructure, but such a construction, besides other limitations, completely misses the collective excitations. In this thesis, we will study the excitations of the system using time-dependent Hartree-Fock, as elaborated in Chap. 2.3.5.

1.3 Thesis outline

In Chap. 2, we will introduce the interacting continuum model for TBG. As the continuum models for other graphene materials are basically adapted from that of TBG, the discussion underpins the theoretical framework of most of the contents of this thesis. In particular, we will explain how the single-particle model can be written down, with the effect of strain included, and how interaction is added to the Hamiltonian, with particular focus on band projection and the so-called "interaction scheme", which is used to avoid double-counting of interaction. Finally, we will discuss the basic formalism of Hartree-Fock (HF) and time-dependent Hartree-Fock (TDHF), and how they are applied to moiré materials.

The main body of the thesis is divided into 4 chapters. Chaps. 3 and 4 are focused on the physics of TBG and the closely related material TSTG. Chap. 5 is concerned with our proposal for some novel topological states, which will be applied to moiré materials, and Chap. 6 is concerned with certain general properties of Chern bands. While Chern topology is featured heavily in moiré materials, this Chapter may also be read as a stand alone result in mathematical physics.

Correlated insulators are one of the commonly reoccurring phenomena in TBG and

related systems. While many different candidate ground states have been predicted, incommensurate Kekulé spiral (IKS) [8] states certain count as one of the major successes, whose predicted signature, a graphene scale charge density wave with its phase rotating across moiré unit cells, has been detected experimentally [10]. Building on the prior success, in Chap. 3, we explore deeper into the IKS states. As already briefly mentioned, twisted symmetric trilayer graphene (TSTG) is a material that shares many similar properties with TBG, but with additional tunability with a perpendicular electric field. With numerical simulations, we confirm that IKS can also be stabilized in TSTG, in consistent with its experimental observation [98], and we further establish the existence of a commensurate version of the state at a regime not available in TBG. We also discuss the charge cascade phenomena in TSTG. Delving deeper into the properties of IKS states themselves, we explore the spin structure of IKS states, which has been glossed over in previous works. In doing so, we include corrections to the continuum model introduced in Chap. 2, and see how they play a central role in determining the true IKS ground state. We also discuss how the hierarchy of symmetry breaking determines the neutral collective modes of IKS ground states.

One of the major topics of interest in TBG and TSTG is superconductivity. While a comprehensive treatment of the topic is beyond the scope of this thesis, in the relatively short Chap. 4, we will examine the symmetry and Fermi surfaces of doped (non-superconducting) IKS states, and understand their roles as parent states in constraining the symmetry of the superconducting order parameters. We will also present our collaborative work with experimentalists on double-dome superconductivity in TSTG, and understand how the normal states' phase diagrams can provide important clues for understanding superconductivity in TSTG.

Topology features heavily in the discussion of moiré systems. While Chern insulators have now become a fairly frequent observations in moiré systems, and even fractional Chern insulators have been observed, in Chap. 5, we propose a different type of topological correlated insulators, namely the Chern texture insulators (CTI). The defining characteristic of a CTI is that it spontaneously breaks a U(1) symmetry in an underlying system with Chern bands. The underlying band topology enforces non-trivial momentum space texture on its order parameter, and we further show that the CTI possesses the so-called

"delicate topology". With the help of HF, we show that CTI could potentially be realized in a large number of moiré systems, with potential experimental implications.

Finally, we change course somewhat in Chap. 6, and present some results that apply to Chern bands in general. In the study of (fractional) quantum Hall effects and later fractional Chern insulators (which, as mentioned in the earlier parts of this Chapter, was first discovered in moiré materials), one commonly discussed mathematical structure is the Girvin-MacDonald-Platzman (GMP) algebra, which is essentially the commutation algebra obeyed by electron density operators projected into Landau levels. In the Chapter, we prove that, for *any* Chern band, if the band projected density algebra is closed, the algebra must *always* be the GMP algebra up to freedom to choose some form factors. We also discuss some related results on quantum geometry.

Chapter 2

Background and methods

2.1 Basics of twisted bilayer graphene

Imagine stacking two sheets of monolayer graphene on top of one another and rotating the top and bottom sheets by $+\theta/2$ and $-\theta/2$ respectively. Assuming that the twist angle is small, i.e., $\theta \ll 1$, these two sheets of graphene generate a moiré pattern between them, as illustrated in Fig. 2.1. The resulting structure is twisted bilayer graphene (TBG).

While the above description appears fairly straightforward, there are a few crucial details that require attention. First, for an arbitrary twist angle θ, the resulting pattern will not be periodic, except for a discrete set of commensurate angles [4]. For some of the theoretical calculations, where individual carbon atoms are directly modeled, one usually has to work at these commensurate angles. Nevertheless, in practice, as $\theta \ll 1$, the difference between commensurate and incommensurate angle is negligible and beyond experimental resolution. In the continuum model [2, 4] that we will introduce, the difference between commensurate and incommensurate angle is completely lost, allowing us to consider a continuous range of θ.

Second, while we have specified the angular offset of the two sheets of graphene, it is also conceivable to introduce a relative in-place displacement between the two sheets. It turns out that, within the $\theta \ll 1$ limit, this in-plane displacement can be neglected [2].

Third, in the above description, we have implicitly assumed that the graphene sheets are rotated as rigid bodies. This assumption does not hold in practice, and very early on, the rearrangement of atomic positions, called "lattice relaxation", has been known to play

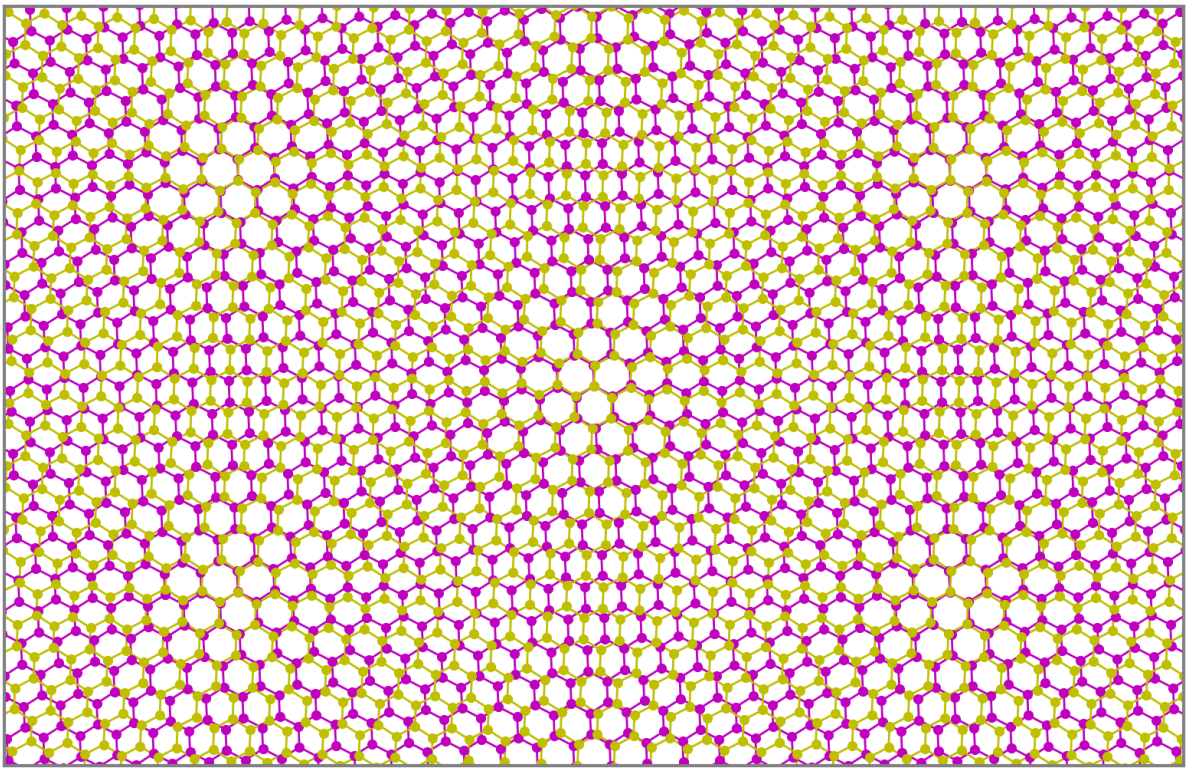


Figure 2.1: Illustration of moiré pattern in twisted bilayer graphene with 5° twist angle and assuming rigid rotations.

a significant role in determining the electronic structure of TBG [99, 100]. This point will be elaborated when we introduce the continuum model.

Finally, there are a few additional ways that an actual device differs from the idealized description. One aspect is that the twist angle may be non-uniform, i.e., twist-angle disorder [101], but the treatment of this issue is beyond the scope of this thesis. Another aspect is strain. While strain may also be disordered, even uniform strain is predicted to have a significant impact on the electronic structure and correlated physics [69, 102]. In this thesis, we will treat uniform strain systematically, while strain disorder is again beyond the scope of the present text.

2.2 Continuum model of twisted bilayer graphene

2.2.1 Bistritzer-MacDonald continuum model with strain

The now standard version of the continuum model was first written down by Bistritzer and MacDonald in Ref. [2], and therefore is also commonly called the Bistritzer-MacDonald (BM) model. The basic idea is that, since the moiré unit cell is much larger than the graphene unit cell, one can "coarse grain" over the graphene lattice and treat it as an effective continuum. Besides its application in TBG, the BM model can be adapted to a wide variety of moiré materials. By now, there has been many pedagogical derivations (see the appendix of Ref. [17] as an example) of this model available in the literature, so that in this thesis we merely present the model as it is. We will also include the effects of strain into the model, as it will be crucial for many of the phenomena to be discussed in this thesis. Our discussion on strain closely follows the conventions in Refs. [69, 102].

First, consider strain of magnitude ϵ and direction φ, measured counter-clockwise from the $\hat{x}$-axis, in a single layer. The symmetric strain tensor is given by

$$S(\epsilon,\varphi) = R^{-1}(\varphi)\begin{pmatrix} -\epsilon & 0 \\ 0 & \nu\epsilon \end{pmatrix} R(\varphi) = \begin{pmatrix} \epsilon_{xx} & \epsilon_{xy} \\ \epsilon_{xy} & \epsilon_{yy} \end{pmatrix} \tag{2.1}$$

where $R(\varphi)$ is a rotation matrix and $\nu = 0.16$ is the Poisson ratio. Including a twist angle θ, the transformation matrix, which acts via $\boldsymbol{r} \to M^T\boldsymbol{r}$, $\boldsymbol{g} \to M^{-1}\boldsymbol{g}$, is given for small ϵ, θ by $M \simeq 1 + \mathcal{E}^T$, where

$$\mathcal{E} \simeq \begin{pmatrix} \epsilon_{xx} & \epsilon_{xy} - \theta \\ \epsilon_{xy} + \theta & \epsilon_{yy} \end{pmatrix}. \tag{2.2}$$

For TBG, it is known that homostrain, where both layers experience the same strain, has negligible effect on the band structure [103], we focus on the case of heterostrain, i.e., the two layers experience opposite strain. To describe TBG (with $l = 1, 2$ labeling the top and bottom layers) under uniaxial heterostrain, we consider layer-dependent transformations parameterized by

$$\theta_1 = -\theta_2 = \frac{\theta}{2}, \quad \varphi_1 = \varphi_2 = \varphi, \quad \epsilon_1 = -\epsilon_2 = \frac{\epsilon}{2}. \tag{2.3}$$

Defining graphene reciprocal lattice vectors (RLVs)

$$\boldsymbol{G}_{G1} = \frac{4\pi}{3a}(\frac{\sqrt{3}}{2}, \frac{1}{2}), \quad \boldsymbol{G}_{G2} = \frac{4\pi}{3a}(\frac{\sqrt{3}}{2}, -\frac{1}{2}), \tag{2.4}$$

where $a = 0.142\,\text{nm}$ is the C-C bond length, we then find that the moiré RLVs are given by

$$\begin{aligned} \boldsymbol{G}_1 &= (M_1^{-1} - M_2^{-1})(\boldsymbol{G}_{G2} - \boldsymbol{G}_{G1}), \\ \boldsymbol{G}_2 &= (M_1^{-1} - M_2^{-1})\boldsymbol{G}_{G1}. \end{aligned} \tag{2.5}$$

The kinetic term in valley τ (where $\tau = \pm 1$ for K, K') is given by

$$\langle \boldsymbol{k}, l|\hat{H}_{\text{BM}}|\boldsymbol{k}', l'\rangle = \hbar v_F[M_l(\boldsymbol{k} - \tau\boldsymbol{A}_l) - \boldsymbol{K}_\tau] \cdot \begin{pmatrix} \tau\sigma_x \\ -\sigma_y \end{pmatrix} \delta_{\boldsymbol{k}\boldsymbol{k}'}\delta_{ll'} \tag{2.6}$$

where l is the layer,

$$\boldsymbol{A} = \frac{\beta}{2a}(\epsilon_{xx} - \epsilon_{yy}, -2\epsilon_{xy}), \tag{2.7}$$

and $\boldsymbol{K}_\tau = \frac{4\pi}{3\sqrt{3}a}(\tau, 0)$ is the original (i.e. in the absence of rotation and strain) Dirac momentum in valley τ. $\boldsymbol{k}$ is measured with respect to the global origin of momentum. We use the Dirac velocity $v_F = 8.8 \times 10^5\,\text{ms}^{-1}$.

The (local) interlayer hopping term from layer 2 to layer 1 in valley K is [2]

$$\langle \boldsymbol{k}, 1|\hat{H}_{\text{BM}}|\boldsymbol{k}', 2\rangle = T_1\delta_{\boldsymbol{k}-\boldsymbol{k}',\boldsymbol{0}} + T_2\delta_{\boldsymbol{k}-\boldsymbol{k}',\boldsymbol{G}_1+\boldsymbol{G}_2} + T_3\delta_{\boldsymbol{k}-\boldsymbol{k}',\boldsymbol{G}_2} \tag{2.8}$$

where the hopping matrices are given by

$$T_j = \begin{pmatrix} w_{\text{AA}} & w_{\text{AB}}e^{\frac{2\pi i(j-1)}{3}} \\ w_{\text{AB}}e^{-\frac{2\pi i(j-1)}{3}} & w_{\text{AA}} \end{pmatrix}. \tag{2.9}$$

The expressions for valley K' can be found by time-reversal. Here, a key dimensionless parameter is the ratio of intra-sublattice hopping to inter-sublattice hopping, called the chiral ratio, defined as $\kappa = w_{\text{AA}}/w_{\text{AB}}$. In the original work [2], the authors, assuming rigid rotations of graphene sheets, took the chiral ratio to be 1. Later on, Refs. [99, 100] found that lattice relaxation shrinks the AA-stacked region relative to the AB-stacked region.

This effect can be phenomenologically included by choosing $\kappa < 1$. While the precise value of κ is debatable, it is usually expected to fall in the range $0.5 < \kappa < 0.8$ [99, 100, 104, 105]. Taking the extreme limit $\kappa = 0$, Ref. [3] shows that, at the magic angle, not only the Fermi velocity drops to zero, but the bandwidths of the central bands also become strictly zero.

To numerically solve the above-written continuum model, it is necessary to impose an ultraviolet cutoff. One simple implementation is the circular cutoff, i.e., only retaining plane wave states with

$$|\boldsymbol{p} - \tau \boldsymbol{K}^1| < \Lambda \quad \text{for layer 1, and} \tag{2.10}$$

$$|\boldsymbol{p} - \tau \boldsymbol{K}^2| < \Lambda \quad \text{for layer 2,} \tag{2.11}$$

where the cutoff wavevector Λ satisfies $k_\theta \ll \Lambda < k_D$, and $\tau = \pm$ is the valley index.

2.2.2 Effects of heterostrain

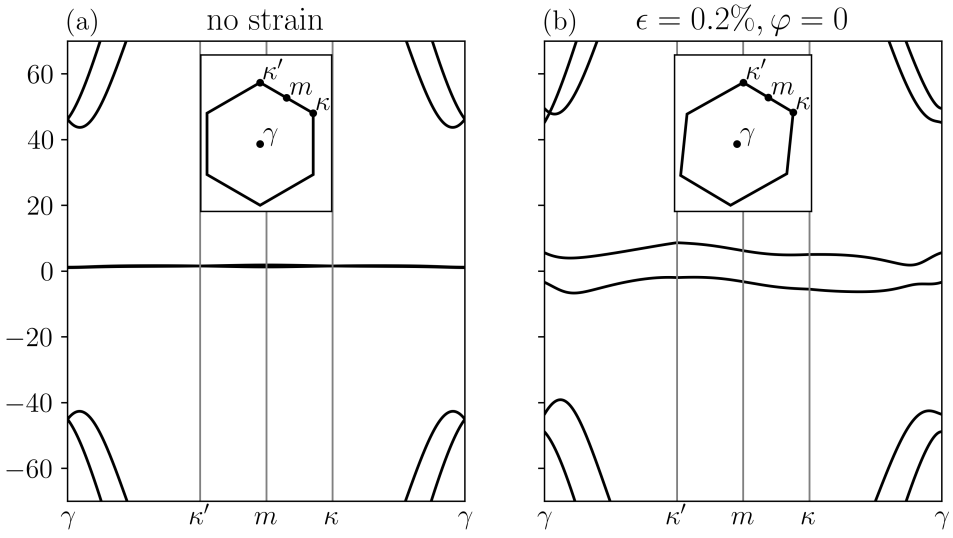


Figure 2.2: Comparing the bandstructure of TBG without (a) and with (b) heterostrain. For both plots, we have used twist angle $\theta = 1.1°$, $w_{\mathrm{AA}} = 75$ meV and $w_{\mathrm{AB}} = 110$ meV. The insets show the mBZ and the positions of the labeled points for the cases without and with heterostrain respectively.

The bandstructure of unstrained TBG at magic angle of 1.1° is shown in Fig. 2.2a. As we can observe, the bandwidths of the central bands are very small and of the order

of 1 meV. Including even a small amount of heterostrain drastically change the picture, as shown in Fig. 2.2b: the bandwidth increases significantly to the order of 10 meV. In Fig. 2.2b, the Dirac points are not visible. Nevertheless, the Dirac points remain present as they are protected by the $C_{2z}T$ symmetry, but as the three-fold rotation symmetry is broken by the heterostrain, they are are unpinned from κ and κ' points of the mBZ [102]. Experiments typically observe heterostrain of $0.1 - 0.7\%$ in the TBG devices [22, 106, 107]. As such, it is crucial to include strain in the modeling in order to account for experimental phenomenology correctly.

2.2.3 Adding interactions

Let the Bloch eigenstates of the single-particle BM Hamiltonian be denoted by $|\psi_{\tau a}(\boldsymbol{k})\rangle$, where $\tau = \pm 1$ indicates valley K or K', and a is a BM band label, with the associated creation operator denoted as $\hat{c}^\dagger_{\tau a}(\boldsymbol{k})$. For simplicity, we will choose the periodic gauge[1], i.e., $|\psi_{\tau a}(\boldsymbol{k}+\boldsymbol{G})\rangle = |\psi_{\tau a}(\boldsymbol{k})\rangle$ for any moiré RLV $\boldsymbol{G}$. The moiré cell-periodic functions, given by $|u_{\tau a}(\boldsymbol{k})\rangle = e^{-i\boldsymbol{k}\cdot\hat{\boldsymbol{r}}}\,|\psi_{\tau a}(\boldsymbol{k})\rangle$, are not periodic in its momentum argument. Instead, we have $|u_{\tau,a}(\boldsymbol{k}+\boldsymbol{G})\rangle = e^{-i\boldsymbol{G}\cdot\hat{\boldsymbol{r}}}\,|u_{\tau,a}(\boldsymbol{k})\rangle$.

The electron density operator for valley τ and spin s is given by

$$\hat{\rho}_{\tau s}(\boldsymbol{q}) = \sum_{\substack{\boldsymbol{k}\in\mathrm{mBZ}\\ ab}} \hat{c}^\dagger_{\tau as}(\boldsymbol{k})\lambda_{\tau,ab}(\boldsymbol{k},\boldsymbol{q})\hat{c}_{\tau bs}(\boldsymbol{k}+\boldsymbol{q}), \tag{2.12}$$

where the (spin-indepedent) form factor is given by

$$\lambda_{\tau,ab}(\boldsymbol{k},\boldsymbol{q}) = \langle u_{\tau,a}(\boldsymbol{k})|u_{\tau,b}(\boldsymbol{k}+\boldsymbol{q})\rangle = \sum_{\boldsymbol{G},l,\sigma} u^*_{\tau a;l\sigma}(\boldsymbol{k},\boldsymbol{G})u_{\tau b;l\sigma}(\boldsymbol{k}+\boldsymbol{q},\boldsymbol{G}) \tag{2.13}$$

$$= \lambda^*_{\tau,ba}(\boldsymbol{k}+\boldsymbol{q},-\boldsymbol{q}). \tag{2.14}$$

In terms of these form factors, the long-range density-density Coulomb Hamiltonian

[1]This can always be done provided we do not demand the gauge to be smooth.

can be written as

$$\begin{aligned}\hat{H}_{\text{int}} &= \frac{1}{2A}\sum_{\tau\tau' ss'}\sum_{\boldsymbol{q}\in\text{all}} V(\boldsymbol{q}) :\hat{\rho}_{\tau s}(\boldsymbol{q})\hat{\rho}^{\dagger}_{\tau' s'}(\boldsymbol{q}):_{\rho_0} \\ &= \frac{1}{2A}\sum_{\substack{ss'\tau\tau' \\ abcd}}\sum_{\boldsymbol{q}\in\text{all}}\sum_{\boldsymbol{k}^\alpha,\boldsymbol{k}^\beta\in\text{mBZ}} V(\boldsymbol{q})\lambda_{\tau,ab}(\boldsymbol{k}^\alpha,\boldsymbol{q})\lambda^{*}_{\tau',dc}(\boldsymbol{k}^\beta,\boldsymbol{q}) \\ &\qquad \times :\hat{c}^{\dagger}_{\tau a s}(\boldsymbol{k}^\alpha)\hat{c}^{\dagger}_{\tau' c s'}(\boldsymbol{k}^\beta+\boldsymbol{q})\hat{c}_{\tau' d s'}(\boldsymbol{k}^\beta)\hat{c}_{\tau b s}(\boldsymbol{k}^\alpha+\boldsymbol{q}):_{\rho^0},\end{aligned} \tag{2.15}$$

where A is the total area of the system. It should be noted that, in the above expression, $\boldsymbol{k}^\alpha$ and $\boldsymbol{k}^\beta$ are summed over the mBZ, whereas $\boldsymbol{q}$ is summed over *all* intravalley momentum transfers. The $:\ldots:_{\rho^0}$ notation specifies the *interaction scheme*, which is to be elaborated in the next subsection.

As the typical experimental set-up involves the TBG device being placed near electric gates, the interaction potential $V(q)$ is chosen either as the dual or single gate-screened form, depending on the experimental geometry, given by $\frac{e^2}{2\epsilon_0\epsilon_r q}\tanh qd_{\text{sc}}$ or $\frac{e^2\left(1-e^{-2qd_{\text{sc}}}\right)}{2\epsilon_0\epsilon_r q}$ respectively, with screening distance $d_{\text{sc}}\sim 5-40\,\text{nm}$ and relative permittivity $\epsilon_r\sim 4-30$ [75]. As the hBN subtrate is an anisotropic dielectric material, d_{sc} is not simply the physical gate distance d_g. Instead, they are related via $d_{\text{sc}}=d_g\sqrt{\epsilon_\parallel/\epsilon_\perp}$, where $\epsilon_\perp$ ($\epsilon_\parallel$) is the dielectric constant of hBN perpendicular (parallel) to the atomic plane [108]. The value of ϵ_r not only encompasses the contribution of the hBN dielectric, but also captures screening due to the remote bands [109].

Interaction schemes

In Eq. 2.15, the quartic term is accompanied by a 'normal-ordering' symbol $:\ldots:_{\rho^0}$. One may be tempted to pick the conventional normal-ordering so that all annihilation operators appear to the right of all creation operators. However, this leads to double-counting of interactions, as the parameters of the Hamiltonian are extracted from either experiments or *ab initio* calculations, which would have included some effects of interaction. As such, it is necessary to introduce an "interaction scheme" [2] to avoid such double-counting.

We define an interaction scheme by specifying a reference density matrix $\rho^0_{\tau s;ab}(\boldsymbol{k})=$

[2]Sometimes also called a "subtraction scheme" in the literature.

$\langle \hat{c}^\dagger_{\tau bs}(\boldsymbol{k}) \hat{c}_{\tau as}(\boldsymbol{k}) \rangle_0$. The interaction term Eq. 2.15 becomes

$$\hat{H}_{\text{int}} = \hat{H}_{\text{int, n.o.}} + \hat{H}_{\text{sub}}, \tag{2.16}$$

where

$$\begin{aligned} \hat{H}_{\text{int, n.o.}} = \frac{1}{2A} \sum_{\substack{ss'\tau\tau' \\ abcd}} \sum_{\boldsymbol{q}\in\text{all}} \sum_{\boldsymbol{k}^\alpha,\boldsymbol{k}^\beta\in\text{mBZ}} V(\boldsymbol{q}) \lambda_{\tau,ab}(\boldsymbol{k}^\alpha,\boldsymbol{q}) \lambda^*_{\tau',dc}(\boldsymbol{k}^\beta,\boldsymbol{q}) \\ \times \hat{c}^\dagger_{\tau as}(\boldsymbol{k}^\alpha) \hat{c}^\dagger_{\tau' cs'}(\boldsymbol{k}^\beta+\boldsymbol{q}) \hat{c}_{\tau' ds'}(\boldsymbol{k}^\beta) \hat{c}_{\tau bs}(\boldsymbol{k}^\alpha+\boldsymbol{q}), \end{aligned} \tag{2.17}$$

and

$$\begin{aligned} \hat{H}_{\text{sub}} = -\frac{1}{A} \sum_{\substack{\boldsymbol{k}^\alpha\in\text{mBZ} \\ s\tau ab}} \left[\sum_{\boldsymbol{G}} \sum_{\substack{\boldsymbol{k}^\beta\in\text{mBZ} \\ s'\tau' cd}} V(\boldsymbol{G}) \lambda^*_{\tau',dc}(\boldsymbol{k}^\beta,\boldsymbol{G}) \rho^0_{\tau s,dc}(\boldsymbol{k}^\beta) \right] \lambda_{\tau,ab}(\boldsymbol{k}^\alpha,\boldsymbol{q}) \hat{c}^\dagger_{\tau as}(\boldsymbol{k}^\alpha) \hat{c}_{\tau bs}(\boldsymbol{k}^\alpha) \\ + \frac{1}{A} \sum_{\substack{\boldsymbol{k}^\alpha\in\text{mBZ} \\ s\tau ab}} \sum_{\substack{\boldsymbol{q}\in\text{all} \\ cd}} V(\boldsymbol{q}) \lambda^*_{\tau,bc}(\boldsymbol{k}^\alpha,\boldsymbol{q}) \rho^0_{\tau s,dc}(\boldsymbol{k}^\alpha+\boldsymbol{q}) \lambda_{\tau,ad}(\boldsymbol{k}^\alpha,\boldsymbol{q}) \hat{c}^\dagger_{\tau as}(\boldsymbol{k}^\alpha) \hat{c}_{\tau bs}(\boldsymbol{k}^\alpha). \end{aligned} \tag{2.18}$$

We have split $\hat{H}_{\text{int}}$ into a piece $\hat{H}_{\text{int, n.o.}}$ corresponding to the interaction normal-ordered with respect to the Fock vacuum, and a one-body 'subtraction' correction $\hat{H}_{\text{sub}}$, which is given by the negative of the Hartree and Fock mean-field potentials (see the next section for an introduction to Hartree-Fock) of the state ρ^0 for the vacuum-normal-ordered interaction $\hat{H}_{\text{int, n.o.}}$.

Determining the correct interaction scheme is a non-trivial task. One possible approach is to determine the interaction scheme based on how interaction is included in the *ab initio* method that is used to determine the parameters in the Hamiltonian [110]. In practice, this tends not to be the most flexible approach, and a number of more heuristic approaches are frequently adopted instead. One commonly adopted scheme is the "central average scheme", commonly called the average scheme in literature, which corresponds to $\rho^0_{\tau s;ab} = \frac{1}{2}\delta_{ab}$ for the central bands and $\rho^0_{\tau s;ab} = \delta_{ab}$ for the remote valence bands. The remote conduction bands are unoccupied in the reference state. This is the most commonly adopted option, and is used throughout this thesis, unless otherwise specified. Another popular scheme is the "graphene scheme", where ρ^0 corresponds to occupying all valence

bands of decoupled graphene layers at charge neutrality. The consequences of different interaction schemes have been examined in several works [8, 9, 70, 71, 88, 90, 111–113].

Band Projection

For many-body numerical calculations, keeping all degrees of freedom is usually too computationally prohibitive, even for mean-field methods such as Hartree-Fock. On the other hands, most bands are sufficiently far from the Fermi energy that their contribution to the low-energy physical properties is expected to be very limited. As such, we perform band projection to reduce the effective degrees of freedom [70, 111]. While this may appear simple, it is slightly more non-trivial than simply discarding the remote degrees of freedom. This is because the occupied remote valence bands can still contribute a mean-field background potential. As such, one typically adopts the following approach:

We first identify a subset of *active* (act.) single-particle states, with the remaining *frozen* single-particle states being divided into frozen valence (f.v.) and frozen conduction (f.c.) ones. We restrict the many-body Hilbert space to those where all f.v. (f.c.) states are enforced to be occupied (unoccupied), while the active degree of freedom are left unconstrained. The effective Hamiltonian for the active degrees of freedom will experience additional one-body terms arising from the static Hartree and Fock potentials of the filled bands, which can be written as

$$\begin{aligned}\hat{H}_{\text{f.v.}} = \frac{1}{A} \sum_{\substack{\boldsymbol{k}^\alpha \in \text{mBZ} \\ s\tau, ab \in \text{act.}}} \left[\sum_{\boldsymbol{G}} \sum_{\substack{\boldsymbol{k}^\beta \in \text{mBZ} \\ s'\tau', v \in \text{f.v.}}} V(\boldsymbol{G}) \lambda^*_{\tau', vv}(\boldsymbol{k}^\beta, \boldsymbol{G}) \right] \lambda_{\tau, ab}(\boldsymbol{k}^\alpha, \boldsymbol{q}) \hat{c}^\dagger_{\tau as}(\boldsymbol{k}^\alpha) \hat{c}_{\tau bs}(\boldsymbol{k}^\alpha) \\ - \frac{1}{A} \sum_{\substack{\boldsymbol{k}^\alpha \in \text{mBZ} \\ s\tau, ab \in \text{act.}}} \sum_{\substack{\boldsymbol{q} \in \text{all} \\ v \in \text{f.v.}}} V(\boldsymbol{q}) \lambda^*_{\tau, bv}(\boldsymbol{k}^\alpha, \boldsymbol{q}) \lambda_{\tau, av}(\boldsymbol{k}^\alpha, \boldsymbol{q}) \hat{c}^\dagger_{\tau as}(\boldsymbol{k}^\alpha) \hat{c}_{\tau bs}(\boldsymbol{k}^\alpha).\end{aligned} \tag{2.19}$$

The band-projected Hamiltonian $\hat{H}_{\text{proj.}}$ can then be expressed as

$$\hat{H}_{\text{proj.}} = \hat{H}_{\text{BM}}\Big|_{\text{act.}} + \hat{H}_{\text{int, n.o.}}\Big|_{\text{act.}} + \hat{H}_{\text{sub}}\Big|_{\text{act.}} + \hat{H}_{\text{f.v.}}, \tag{2.20}$$

where $\hat{H}_{\text{BM}}$ in the previous section, $\hat{H}_{\text{int, n.o.}}$ is given in Eq. 2.17, and $\hat{H}_{\text{sub}}$ is given in Eq. 2.18. The notation $\hat{H}_{\text{int, n.o.}}\Big|_{\text{act.}}$ means that we simply restrict the creation/annihilation

operators in $\hat{H}_{\text{int, n.o.}}$ to those belonging to active bands only.

Note that when we write $\hat{H}_{\text{sub}}\Big|_{\text{act.}}$, we are removing the terms whose creation/annihilation operators fall outside the active bands, but we do not remove those bands from ρ_0 in the definition of the term (Eq. 2.18). For certain interaction schemes, there is a large cancellation between $\hat{H}_{\text{sub}}\Big|_{\text{act.}}$ and $\hat{H}_{\text{f.v.}}$, so that we effectively restrict ρ_0 to the active bands by including the $\hat{H}_{\text{f.v.}}$ term. For example, if we take the active bands to be the central bands, then the remote bands (which are all frozen) do not contribute at all to $\hat{H}_{\text{proj.}}$ for the central average scheme and the charge neutrality scheme. However, for schemes such as the "graphene scheme", such cancellation does not happen and one should construct $\hat{H}_{\text{sub}}\Big|_{\text{act.}}$ and $\hat{H}_{\text{f.v.}}$ separately.

2.3 Hartree-Fock mean-field theory

We now turn to a discussion of the Hartree-Fock (HF) mean-field approach. We first present a brief self-contained introduction to time-independent HF, before discussing the implementation of these techniques in TBG. We also discuss time-dependent Hartree-Fock (TDHF).

2.3.1 Hartree-Fock basics

Consider a Hamiltonian with kinetic energy $\hat{T}$ and two-particle interaction $\hat{V}$,

$$\hat{H} = \hat{T} + \hat{V} = \sum_{ab} T_{ab} \hat{c}_a^\dagger \hat{c}_b + \frac{1}{2} \sum_{abcd} V_{ab,cd} \hat{c}_a^\dagger \hat{c}_b^\dagger \hat{c}_d \hat{c}_c, \tag{2.21}$$

where $a, b, ...$ denote single-particle orbitals, and the two-electron interaction integrals are $V_{ab,cd} := \langle ab|\hat{V}|cd\rangle$. These interaction matrix elements satisfy $V_{ab,cd} = V_{ba,dc} = V^*_{cd,ab}$ but are not anti-symmetrized for fermion exchange. Hartree-Fock is a variational approximation that optimizes the ground state energy within the manifold of Slater determinants: states that can be written as $|\Psi\rangle = \prod_{1 \le i \le N_e} \hat{d}_i^\dagger |0\rangle$ for N_e particles and some electron creation operators $\hat{d}_i^\dagger$ that satisfy $\{\hat{d}_i, \hat{d}_j^\dagger\} = \delta_{ij}$.

A Slater determinant is fully specified by its one-body density matrix $P_{ab} = \langle \hat{c}_b^\dagger \hat{c}_a \rangle$, which is Hermitian ($P^\dagger = P$), idempotent ($P^2 = P$) and whose trace is equal to the

number of particles ($\mathrm{tr}(P) = N_e$). The energy expectation value of a Slater determinant can be evaluated using Wick's theorem

$$E[P] = \langle\Psi|\,\hat{H}\,|\Psi\rangle = \sum_{ab} T_{ab}P_{ba} + \frac{1}{2}\sum_{abcd}(V_{ac,bd} - V_{ac,db})P_{ba}P_{dc}. \tag{2.22}$$

We define the Hartree-Fock Hamiltonian

$$[H^{\mathrm{HF}}[P]]_{ab} = T_{ab} + \sum_{cd}(V_{ac,bd} - V_{ac,db})P_{dc}, \tag{2.23}$$

allowing us to rewrite the energy functional as

$$E[P] = \frac{1}{2}\,\mathrm{tr}\left(\left(T + H^{\mathrm{HF}}[P]\right)P\right). \tag{2.24}$$

It will be useful to also define the Hartree and Fock contributions to $H^{\mathrm{HF}}[P]$ separately

$$[H^{\mathrm{H}}[P]]_{ab} = \sum_{cd} V_{ac,bd}P_{dc} \tag{2.25}$$

$$[H^{\mathrm{F}}[P]]_{ab} = -\sum_{cd} V_{ac,db}P_{dc}. \tag{2.26}$$

In terms of these, the energy functional can be written as

$$E[P] = \mathrm{tr}(TP) + \frac{1}{2}\mathrm{tr}\left((H^{\mathrm{H}}[P] + H^{\mathrm{F}}[P])P\right). \tag{2.27}$$

It can be shown that, for P to correspond to a local *minimum* of $E[P]$ within the variational manifold of N_e-particle Slater determinants, a necessary condition is that P be given by occupying the N_e lowest-energy eigenstates of $H^{\mathrm{HF}}[P]$ (this is known as the "aufbau principle" analogous to atomic physics) [114]. This self-consistency condition is the basis for the iterative Hartree-Fock optimization procedure that we outline next.

2.3.2 Solving the self-consistent mean-field equations

In order to find a density matrix P that satisfies the self-consistency condition, one typically employs an iterative procedure. However, a naive implementation is known to sometimes oscillate between two or more states, and fail to converge. To tackle this, we

implement the optimal damping algorithm (ODA) [115], which provides a simple means to ensure (local) convergence of the HF self-consistency procedure. Below, we first outline the Hartree-Fock iteration procedure with ODA, and then justify the motivations behind the ODA algorithm.

In the **initialization step**, we choose some initial trial state P_0. The choice can be a random idempotent Hermitian matrix with an appropriate trace, or a more physically motivated trial wavefunction. Denoting the number of electrons as N_e and the number of orbitals as N, the k-th **iteration step** ($k \geq 0$) consists of the following sub-tasks:

1. Construct the mean-field Hamiltonian from the current state, i.e. $\tilde{H}_k \equiv H^{\mathrm{HF}}[\tilde{P}_k]$. For the first step, $\tilde{P}_0 \equiv P_0$ is the initial trial state just constructed.

2. Diagonalize $\tilde{H}_k$, i.e. find eigenvalues ϵ_i and eigenvectors $\psi_{i,a}$ that satisfy $\sum_b [\tilde{H}_k]_{ab}\psi_{i,b} = \epsilon_i \psi_{i,a}$ for $1 \leq i \leq N$, where we assume that the eigenvalues are ordered such that $\epsilon_i \leq \epsilon_{i+1}$.

3. Construct $[P_{k+1}]_{ab} = \sum_{1 \leq i \leq N_e} \psi_{i,a}\psi^*_{i,b}$.

4. If converged, terminate and return the final state $P_f := P_{k+1}$. Otherwise, proceed to the next step. To test convergence, we impose some convergence threshold $\epsilon \ll 1$, such that the procedure is deemed to have converged if

$$\left\| P_{k+1} - \tilde{P}_k \right\| < \epsilon, \tag{2.28}$$

   where $\|\cdot\|$ denotes the Frobenius norm of a matrix.

5. Compute $H_{k+1} = H^{\mathrm{HF}}[P_{k+1}]$

6. Compute

$$s = 2\,\mathrm{tr}\left(H_k(P_{k+1} - \tilde{P}_k)\right) \tag{2.29}$$

$$c = \mathrm{tr}\left((H_{k+1} - \tilde{H}_k)(P_{k+1} - \tilde{P}_k)\right) \tag{2.30}$$

7. If $c \leq -s/2$, let $\lambda = 1$. Otherwise, let $\lambda = -s/2c$. Set $\tilde{P}_{k+1} = (1-\lambda)\tilde{P}_k + \lambda P_{k+1}$ and go to the next iteration.

The key difference between ODA and a simple iterative algorithm lies in Steps 5 to 7 outlined above. In a simple algorithm, we would have used P_{k+1} as the input for the next round of iteration. The central idea behind the ODA is that, after constructing P_{k+1} in Step 3 of iteration k, instead of directly using it as the input for the next iteration, we first find the *optimal* (i.e. lowest energy) linear combination of P_{k+1} and P_k, and use this as the input for iteration $k+1$. We take

$$P_{\text{new}}(\lambda) = (1-\lambda)P_k + \lambda P_{k+1}, \tag{2.31}$$

where we treat $0 \leq \lambda \leq 1$ as a variational parameter and compute the energy

$$E[P_{\text{new}}(\lambda)] = E[P_k + \lambda(P_{k+1} - P_k)] = E[P_k] + \frac{s}{2}\lambda + \frac{1}{2}c\lambda^2, \tag{2.32}$$

where

$$s = 2\,\text{tr}\,(H_k(P_{k+1} - P_k)) \tag{2.33}$$

$$c = \text{tr}\,((H_{k+1} - H_k)(P_{k+1} - P_k))\,. \tag{2.34}$$

Since the HF energy is a quadratic function of the density matrix P, $E[P_{\text{new}}(\lambda)]$ is a quadratic function of λ. Minimizing the energy by setting $\partial E[P_{\text{new}}(\lambda)]/\partial\lambda = 0$ leads to $\lambda = -s/2c$. However, since we fix λ to be in the domain $0 \leq \lambda \leq 1$, if $c \leq -s/2$, we should set $\lambda = 1$. Since the optimization problem has a simple analytical solution, it can be performed efficiently.

2.3.3 HF Implementation in moiré problems

In this subsection, we discuss how the general framework of HF discussed in the preceding subsections can be applied to TBG.

Projected Hamiltonian with interaction scheme

With the appropriate implementation of the interaction scheme and band projection, we have arrived at the projected Hamiltonian in Eq. 2.20. In the general formulation of

Eq. 2.21, we assign the 'kinetic energy' $\hat{T}$ and 'two-particle interaction' $\hat{V}$ according to

$$\hat{T} = \hat{H}_{\mathrm{BM}}\Big|_{\mathrm{act.}} + \hat{H}_{\mathrm{sub}}\Big|_{\mathrm{act.}} + \hat{H}_{\mathrm{f.v.}} \tag{2.35}$$

$$\hat{V} = \hat{H}_{\mathrm{int,\ n.o.}}\Big|_{\mathrm{act.}} . \tag{2.36}$$

Mean-field equations: translationally-invariant Case

The specific HF equations that must be solved for TBG depend on which symmetries are enforced to be preserved, and which symmetries are allowed to be broken. This describes the 'restricted' HF variational manifold. Here, we impose the moiré translation-invariance, S_z conservation, but allow intervalley coherence (breaking of $\mathrm{U}(1)_V$ symmetry)[3]. In terms of the one-body density matrix, we have

$$P_{\tau' b s' \boldsymbol{k}^\beta, \tau a s \boldsymbol{k}^\alpha} \equiv \langle \hat{c}^\dagger_{\tau a s}(\boldsymbol{k}^\alpha) \hat{c}_{\tau' b s'}(\boldsymbol{k}^\beta) \rangle = 0 \ \text{ if } \ s \neq s' \text{ or } \boldsymbol{k}^\alpha \neq \boldsymbol{k}^\beta, \tag{2.37}$$

where $\tau = \pm 1$ for valley K and K' respectively. This block-diagonal structure allows us to parameterize the one-body density matrix as

$$P_{\tau' b, \tau a}(\boldsymbol{k}, s) \equiv \langle \hat{c}^\dagger_{\tau a s}(\boldsymbol{k}) \hat{c}_{\tau' b s}(\boldsymbol{k}) \rangle \, . \tag{2.38}$$

Due to the block-diagonal structure of one-particle density matrix and the symmetry of the Hamiltonian, the HF Hamiltonian is also diagonal in $\boldsymbol{k}$ and s, i.e.

$$H^{\mathrm{HF}}_{\tau a s \boldsymbol{k}^\alpha, \tau' b s' \boldsymbol{k}^\beta} = \delta_{s s'} \delta_{\boldsymbol{k}^\alpha \boldsymbol{k}^\beta} H^{\mathrm{HF}}_{\tau a, \tau' b}(\boldsymbol{k}^\alpha, s) \tag{2.39}$$

for some $H^{\mathrm{HF}}_{\tau a, \tau' s}(\boldsymbol{k}^\alpha, s)$. The interacting Hartree and Fock contributions can be expressed as

$$\begin{aligned} H^{\mathrm{H}}_{\tau a, \tau' b}(\boldsymbol{k}, s) &= \frac{\delta_{\tau\tau'}}{A} \sum_{s'\tau'' cd} \sum_{\boldsymbol{G}} \sum_{\boldsymbol{k}' \in \mathrm{mBZ}} V(\boldsymbol{G}) \lambda_{\tau, ab}(\boldsymbol{k}, \boldsymbol{G}) \lambda^*_{\tau'', dc}(\boldsymbol{k}', \boldsymbol{G}) P_{\tau'' d, \tau'' c}(\boldsymbol{k}', s') \\ H^{\mathrm{F}}_{\tau a, \tau' b}(\boldsymbol{k}, s) &= -\frac{1}{A} \sum_{cd} \sum_{\boldsymbol{q} \in \mathrm{all}} V(\boldsymbol{q}) \lambda_{\tau, ad}(\boldsymbol{k}, \boldsymbol{q}) \lambda^*_{\tau', bc}(\boldsymbol{k}, \boldsymbol{q}) P_{\tau d, \tau' c}(\boldsymbol{k} + \boldsymbol{q}, s). \end{aligned} \tag{2.40}$$

[3] In Chap. 3, we will discuss the necessary modification for a class of translation-symmetry breaking states.

The HF Hamiltonian is then

$$\hat{H}^{\mathrm{HF}} = \hat{T} + \hat{H}^{\mathrm{H}} + \hat{H}^{\mathrm{F}}. \tag{2.41}$$

Symmetry-preserving Diagonalization and the Aufbau Principle

Since the HF Hamiltonian can be decomposed into symmetry sectors labeled by $(\boldsymbol{k}, s)$, we can simply diagonalize the Hamiltonian of each sector, i.e. $\sum_\beta H^{\mathrm{HF}}_{\alpha,\beta}(\boldsymbol{k}, s)\psi_{i,\beta}(\boldsymbol{k}, s) = \epsilon_i(\boldsymbol{k}, s)\psi_{i,\alpha}(\boldsymbol{k}, s)$ for $1 \leq i \leq 4$ (assuming we are projecting only into the central bands), where α, β are composite indices for band and valley. This represents a significant speed-up in the computational time compared to the case where no symmetries are enforced. For a calculation that includes N_k momentum points, if one does not preserve any symmetry, the time complexity (per iteration) would be $O(N_k^3)$, from the matrix diagonalization. In contrast, the time complexity is $O(N_k^2)$ for the symmetry-preserving procedure, as the construction of $H^{\mathrm{HF}}[P]$ takes $O(N_k^2)$ time. After diagonalizing the HF Hamiltonian matrices, we occupy the N_e lowest-energy states out of *all* eigenstate.

2.3.4 Finite-size effects and Hartree-Fock interpolation

Besides the inherent limitation of being a mean-field method, any actual implementation of HF is also affected by the finite grid size of the momentum mesh, which can potentially modify the energetic competition of candidates for the ground state. A typical momentum mesh used in this thesis is 10×10 or larger, which is consistent with the typical sizes used for HF study of moiré materials in the literature. In particular, in Ref. [8], the authors studied the dependence of HF energy on a certain ordering vector (to be discussed in detail in Chap. 3) in TBG, and found that the dispersions for system sizes ranging from 11×11 to 20×20 neatly collapse into a single curve, suggesting our choice of 10×10 or larger for similar systems is reasonable. The reader is also referred to the discussion in Chap. 3.2.3 for a detailed comparison of energetics.

The self-consistency iterations are the most computationally expensive part of the HF calculations. For some settings, up to several thousand iterations may be required for convergence, thus limiting the system sizes that can be accessed. On the other hand, even when smaller size self-consistent HF identifies the correct ground state, obtaining high-resolution band structures and Fermi surfaces may still be crucial, e.g. to study

superconducting instabilities [116] of a doped correlated insulator. One solution is to use two different momentum meshes, a coarse mesh and a fine mesh, an approach termed *Hartree-Fock interpolation* [95]. The coarse mesh is used for the HF self-consistency procedure. After convergence, the Hartree and Fock terms in Eq. 2.40 are then re-evaluated on the fine mesh with the density matrix on the coarse mesh. More specifically, we construct

$$\begin{aligned} H^{\mathrm{H}}_{\tau a,\tau' b}(\boldsymbol{k},s) &= \frac{\delta_{\tau\tau'}}{A}\sum_{s'\tau''cd}\sum_{\boldsymbol{G}}\sum_{\boldsymbol{k}'\in\mathrm{c.m.}} V(\boldsymbol{G})\lambda_{\tau,ab}(\boldsymbol{k},\boldsymbol{G})\lambda^{*}_{\tau'',dc}(\boldsymbol{k}',\boldsymbol{G})P_{\tau''d,\tau''c}(\boldsymbol{k}',s') \\ H^{\mathrm{F}}_{\tau a,\tau' b}(\boldsymbol{k},s) &= -\frac{1}{A}\sum_{cd}\sum_{\boldsymbol{G}}\sum_{\boldsymbol{k}'\in\mathrm{c.m.}} V(\boldsymbol{k}'-\boldsymbol{k}+\boldsymbol{G})\lambda_{\tau,ad}(\boldsymbol{k},\boldsymbol{k}'-\boldsymbol{k}+\boldsymbol{G}) \\ &\quad\times\lambda^{*}_{\tau',bc}(\boldsymbol{k},\boldsymbol{k}'-\boldsymbol{k}+\boldsymbol{G})P_{\tau d,\tau' c}(\boldsymbol{k}',s). \end{aligned} \tag{2.42}$$

where c.m. denotes the coarse mesh in the mBZ, A is the area of the system of the coarse mesh, while $\boldsymbol{k}$ is allowed to take any value on the fine mesh. The HF Hamiltonian on the fine mesh is then diagonalized to obtain the mean-field band structure. Since this calculation only needs to be performed once after the final iteration, it does not add significantly to the computational cost.

2.3.5 Time-dependent Hartree-Fock

We summarize the time-dependent Hartree-Fock (TDHF) equations, which we will use to compute the neutral collective mode spectra in Chap. 3. The readers should refer to Refs. [117, 118] to understand where they come from.

Consider the interacting Hamiltonian expressed in a self-consistent Hartree-Fock (HF) basis

$$\hat{H} = \sum_{ab} T_{ab}c^{\dagger}_{a}c_{b} + \frac{1}{2}\sum_{abcd} V_{ab,cd}c^{\dagger}_{b}c^{\dagger}_{a}c_{c}c_{d}. \tag{2.43}$$

The HF eigenvalue of orbital a is E_a. Let $i,j,k,\ldots$ and $m,n,o,\ldots$ refer to occupied and unoccupied HF orbitals respectively. Define the A- and B-matrices as [119]

$$A_{mi,nj} = (E_m - E_i)\delta_{ij}\delta_{mn} + V_{mj,in} - V_{mj,ni} \tag{2.44}$$

$$B_{mi,nj} = V_{mn,ij} - V_{mn,ji}. \tag{2.45}$$

A is Hermitian and B is symmetric.

The Hermitian stability matrix $\mathcal{H}$ is

$$\mathcal{H} = \begin{pmatrix} A & B \\ B^* & A^* \end{pmatrix}. \tag{2.46}$$

If the HF state corresponds to a local variational minimum, then $\mathcal{H}$ is positive definite [120].

The $\mathcal{L}$-matrix is

$$\mathcal{L} = \sigma_Z \mathcal{H} = \begin{pmatrix} A & B \\ -B^* & -A^* \end{pmatrix} \tag{2.47}$$

with corresponding eigenvectors $w^\nu = (X^\nu, Y^\nu)$, symplectic norm $\Gamma^{\nu\nu'} = (X^\nu)^\dagger X^{\nu'} - (Y^\nu)^\dagger Y^{\nu'}$ and eigenvalues Ω^ν. Note the "particle-hole symmetry" $\mathcal{L} = -\sigma_X \mathcal{L}^* \sigma_X$, such that $(Y^{\nu *}, X^{\nu *})$ is also an eigenvector of $\mathcal{L}$ and has eigenvalue $-\Omega^{\nu *}$. If $\mathcal{H}$ is positive definite, then we can normalize such that $\Gamma^{\nu\nu'} = \mathrm{sgn}(\Omega^\nu)\delta_{\nu\nu'}$. In general, for a locally stable HF solution, the neutral collective mode spectrum refers to the non-negative half of the eigen-spectrum of $\mathcal{L}$.

For the application in TBG, due to the translation symmetry of the HF ground state, $\mathcal{L}$ block-decomposes into different momentum transfer sectors. More specifically, $A_{mi,nj}$ is only non-zero for $\boldsymbol{k}_m - \boldsymbol{k}_i = \boldsymbol{k}_n - \boldsymbol{k}_j$, and $B_{mi,nj}$ is only non-zero for $\boldsymbol{k}_m - \boldsymbol{k}_i = \boldsymbol{k}_j - \boldsymbol{k}_n$. As such, we write $A(\boldsymbol{q}) \equiv (A_{mi,nj})_{\boldsymbol{k}_n - \boldsymbol{k}_j = \boldsymbol{k}_m - \boldsymbol{k}_i = \boldsymbol{q}}$ and $B(\boldsymbol{q}) \equiv (B_{mi,nj})_{\boldsymbol{k}_n - \boldsymbol{k}_j = -\boldsymbol{k}_m + \boldsymbol{k}_i = \boldsymbol{q}}$ to denote such non-vanishing blocks of A- and B-matrices. For $\boldsymbol{q}$ being a time-reversal invariant momentum (TRIM), we define

$$\mathcal{L}_{\boldsymbol{q} \in \mathrm{TRIM}} = \begin{bmatrix} A(\boldsymbol{q}) & B(\boldsymbol{q}) \\ -B^*(\boldsymbol{q}) & -A^*(\boldsymbol{q}) \end{bmatrix}. \tag{2.48}$$

We can straightforwardly diagonalize the above to obtain collective mode energies $\omega(\boldsymbol{q}) = \mathrm{sgn}(X^\dagger X - Y^\dagger Y)\Omega(\boldsymbol{q})$ and their wavefunctions. Each pair of modes related by the aforementioned "particle-hole symmetry" is only included once.

On the other hand, for a non-TRIM momentum $\boldsymbol{q}$, we find the following structure

$$\mathcal{L}_{\boldsymbol{q}\notin\mathrm{TRIM}} = \begin{bmatrix} A(\boldsymbol{q}) & 0 & 0 & B(\boldsymbol{q}) \\ 0 & A(-\boldsymbol{q}) & B^T(\boldsymbol{q}) & 0 \\ 0 & -B^*(\boldsymbol{q}) & -A^*(\boldsymbol{q}) & 0 \\ -B^\dagger(\boldsymbol{q}) & 0 & 0 & -A^*(-\boldsymbol{q}) \end{bmatrix} \tag{2.49}$$

where the matrix index is ordered as $X(\boldsymbol{q}), X(-\boldsymbol{q}), Y(-\boldsymbol{q}), Y(\boldsymbol{q})$, and we have used the fact that the full A-matrix is Hermitian and the full B-matrix is symmetric. The advantage of writing $\mathcal{L}_{\boldsymbol{q}\notin\mathrm{TRIM}}$ this way is that we can study just the outer block, since it is related to the inner block simply as

$$\mathcal{L}_{\boldsymbol{q},\mathrm{outer}} = \begin{bmatrix} A(\boldsymbol{q}) & B(\boldsymbol{q}) \\ -B^\dagger(\boldsymbol{q}) & -A^*(-\boldsymbol{q}) \end{bmatrix} = -\sigma_X \mathcal{L}^*_{\boldsymbol{q},\mathrm{inner}} \sigma_X. \tag{2.50}$$

2.3.6 Hartree-Fock and Hubbard model

Before proceeding to study moiré systems with HF, we briefly review the success and limitations of the method when applied to the standard Hubbard model on a square lattice with nearest-neighbor hopping (with hopping t and interaction U). At half filling, the ground state exhibits antiferromagnetic long-range order and a finite charge gap for any $U > 0$ [121]. These features are qualitatively reproduced by HF. In particular, HF captures the weak-coupling antiferromagnetic instability ($U \ll t$), which is closely associated with the perfect nesting of the noninteracting Fermi surface. However, as HF assumes a static background, it fails to capture effects such as interaction-induced quasiparticle decay and the internal structure of the Hubbard bands. In the strong-coupling limit ($U \gg t$), the HF charge gap approaches U, with corrections only of order t^2/U, $\Delta_{\mathrm{HF}} = U - 8t^2/U + \cdots$ [122]. In the exact many-body problem, by contrast, the charge gap receives an $O(t)$ correction [123], an effect absent in HF.

Chapter 3

Incommensurate Kekulé spirals

3.1 What is the incommensurate Kekulé spiral?

One of the most prominent phenomena in TBG and many other moiré materials is that of correlated insulators across integer filling factors[1], and the nature of these correlated insulators has been the subject of extensive research and debate since their experimental discovery. The full review of this topic is beyond the scope of this thesis, so we will only briefly recall some of the key points of the discussion.

Without electron-electron interaction, TBG would be a band insulator at $\nu = \pm 4$, a semimetal at $\nu = 0$[2] and metals at all other filling factors. As such, interaction must be necessary for the observation of insulators at these integer fillings, and the most basic picture of correlated insulators in TBG is flavor polarization. Electrons in TBG have a 4-fold flavor degeneracy, arising from the 2 valley and 2 spin degrees of freedom. Here, "valley" refers to the low-energy regions in momentum space, and for TBG it arises from momenta close to the K and K' points in graphene. While the conservation of charge in each valley, i.e., $\mathrm{U}(1)_V$, is an emergent degree of freedom due to the separation of moiré scale and the atomic scale (governed by the small parameter θ), it holds to a very good degree of accuracy that it can be treated as an exact symmetry, as we have already done in introducing the continuum model in Chap. 2. The idea of flavor polarization

[1] Filling factor is measured in electron per moiré unit cell, with respect to some reference electron density. For TBG, the reference is charge neutrality.

[2] If heterostrain is present, in general the non-interacting ground state at $\nu = 0$ is also a metal, as the Dirac points are no longer equal in energy [102].

has been developed further in Ref. [75], whose authors established a strong-coupling framework where the correlated insulators can be understood as general ferromagnets under an approximate U(4) × U(4) symmetry by exploiting the hidden Chern symmetry in the central bands of TBG.

In this thesis, we will pay particular attention to correlated insulators that spontaneously break the valley $U(1)_V$ symmetry, whose order parameter can be schematically written as $\langle \hat{c}_+^\dagger \hat{c}_- \rangle$, where $\hat{c}_\pm^\dagger$ are some fermion creation operators in valleys K and K' respectively [3]. We will call states that break $U_v(1)$ symmetry as intervalley-coherent (IVC). If a valley polarized state can be thought of as an easy-axis ferromagnet, then an IVC state can be thought of as an easy-plane ferromagnet. In Ref. [75], the authors proposed a class of IVC states, called K-IVC[4], that is within the manifold of (approximate) U(4) × U(4) general ferromagnets, and they predicted it to be the insulating ground states at $\nu = -2, 0, +2$, based on HF simulations.

Despite being theoretically attractive, experimental observations contradicted some of the proposed properties of K-IVC. One of them, which is also important for the rest of our thesis, is the detection of the so-called Kekulé patterns. Kekulé patterns are a kind of charge density wave at the graphene scale that enlarges the graphene unit cell by $\sqrt{3} \times \sqrt{3}$. Its periodicity corresponds to the wavevector connecting the K and K' valleys of the graphene, and as such, it generally arises from IVC. Nevertheless, due to a special symmetry of K-IVC, Kekulé charge density patterns are proposed to vanish exactly in K-IVC [124, 125]. However, this Kekulé pattern has been experimentally observed in TBG with scanning tunneling experiments [10], ruling out the presence of K-IVC. One of the reasons why K-IVC does not appear as theoretically proposed is that, under realistic experimental set-ups, there is usually a small but non-negligible amount of strain in the device, which destabilizes K-IVC and stabilizes an alternative kind of order, namely the incommensurate Kekulé spiral (IKS) order, as we discuss below[5].

The IKS order was first proposed by Ref. [8]. It is also an IVC state, just like K-IVC. However, it differs from K-IVC in a few significant ways. First, it does not contain the

[3] Here we have not specified the momentum, spin and other structures of the order parameter.

[4] Here 'K' stands for 'Kramers'.

[5] For completeness, we would like to mention that even with close-to-zero strain, the experiment nevertheless contradicts the prediction of K-IVC [10]. This is sometimes attributed to the effect of phonons [126].

special symmetry in K-IVC so the Kekulé charge density pattern is not expected to vanish in IKS. Second, unlike the usual IVC states including K-IVC, the Kekulé pattern in IKS has a special moiré scale modulation, which arises from the momentum space structure of the order parameter in IKS. In a usual IVC state, the order parameter is expected to be of the from $\langle \hat{c}^\dagger(\boldsymbol{k})_+ \hat{c}(\boldsymbol{k})_- \rangle$[6], i.e., the coherence is between states with the same momenta, measured from the respective γ-point in the moiré Brillouin zone (mBZ), in the opposite valleys. In IKS, the order parameter is of the form $\langle \hat{c}^\dagger(\boldsymbol{k})_+ \hat{c}(\boldsymbol{k}+\boldsymbol{q}_{\mathrm{IVC}})_- \rangle$, for some non-zero ordering vector $\boldsymbol{q}_{\mathrm{IVC}}$. This $\boldsymbol{q}_{\mathrm{IVC}}$ is generally *incommensurate* (i.e., not a rational fraction of the moiré RLV), hence the name *incommensurate Kekulé spiral*[7]. This finite $\boldsymbol{q}_{\mathrm{IVC}}$ has been experimentally observed [10], giving strong experimental support for the existence of IKS. Finally, the spin structure of IKS is different from the K-IVC state. This was already realized when it was first proposed [8], though it was our work, as elaborated in Chap. 3.3, that fully elucidated its spin structure.

3.1.1 IKS and Hartree-Fock

We summarize how we can access the IKS state within the Hartree-Fock mean-field treatment. This method is established when IKS was first proposed [8]. As noted above, IKS order corresponds to the coherence between states with different moiré momenta. Therefore, it breaks moiré translation symmetry. However, it does so in a "spiral" fashion that does not lead to a moiré-scale modulation of the electron density. As such, rather than working with fully translational-breaking Hartree-Fock, we can instead work in a 'boosted' coordinate system where the Γ-points of valleys K and K' are shifted by an amount $\pm\boldsymbol{q}_{\mathrm{IVC}}/2$ with respect to each other, and treat $\boldsymbol{q}_{\mathrm{IVC}}$ as a variational parameter. In other words, we choose

$$P_{\tau' b s' \boldsymbol{k}^\beta, \tau a s \boldsymbol{k}^\alpha} \equiv \langle \hat{c}^\dagger_{\tau a s}(\boldsymbol{k}^\alpha) \hat{c}_{\tau' b s'}(\boldsymbol{k}^\beta) \rangle \sim \delta_{s s'} \delta_{\boldsymbol{k}^\alpha + \tau \boldsymbol{q}_{\mathrm{IVC}}/2, \boldsymbol{k}^\beta + \tau' \boldsymbol{q}_{\mathrm{IVC}}/2} \tag{3.1}$$

[6]Here, we are only focusing on the momentum and valley degrees of freedom, and suppressing the spin and BM band indices.

[7]It is called a "spiral" because $\langle \hat{c}^\dagger(\boldsymbol{k})_+ \hat{c}(\boldsymbol{k}+\boldsymbol{q}_{\mathrm{IVC}})_- \rangle$ and $\langle \hat{c}^\dagger(\boldsymbol{k})_+ \hat{c}(\boldsymbol{k}-\boldsymbol{q}_{\mathrm{IVC}})_- \rangle$ are not simultaneously non-zero, giving a definite sense of rotation of the IVC phase.

where $\tau = \pm 1$ for K and K' valley respectively, and the Kronecker deltas on the RHS enforce spin-collinearity[8], and the constraint that any IVC must occur with spiral wavevector $\boldsymbol{q}_{\mathrm{IVC}}$[9]. For convenience and to make contact with our previous notation, we now define a new set of operators $\hat{\tilde{c}}^\dagger_{\tau as}(\boldsymbol{k}) = \hat{c}^\dagger_{\tau as}(\boldsymbol{k} - \tau \boldsymbol{q}_{\mathrm{IVC}}/2)$, so that (throughout this subsection, we denote quantities with respect to this new set of momenta labels with a tilde)

$$\tilde{P}_{\tau' bs' \boldsymbol{k}^\beta, \tau a s \boldsymbol{k}^\alpha} \equiv \langle \hat{\tilde{c}}^\dagger_{\tau as}(\boldsymbol{k}^\alpha) \hat{\tilde{c}}_{\tau' bs'}(\boldsymbol{k}^\beta) \rangle \propto \delta_{ss'} \delta_{\boldsymbol{k}^\alpha, \boldsymbol{k}^\beta}. \tag{3.2}$$

This block-diagonal structure allows us to write the one-particle density matrix exactly as before, but with $\tilde{c}$-operators replacing c-operators:

$$\tilde{P}_{\tau' b, \tau a}(\boldsymbol{k}, s) \equiv \langle \hat{\tilde{c}}^\dagger_{\tau as}(\boldsymbol{k}) \hat{\tilde{c}}_{\tau' bs}(\boldsymbol{k}) \rangle \,. \tag{3.3}$$

In terms of the new set of operators, the normal-ordered Coulomb interaction is given by (compare with Eq. 2.17)

$$\begin{aligned} \hat{H}_{\mathrm{int,\,n.o.}} = \frac{1}{2A} \sum_{\substack{ss'\tau\tau' \\ abcd}} \sum_{\boldsymbol{q}} \sum_{\boldsymbol{k}^\alpha, \boldsymbol{k}^\beta} & V(\boldsymbol{q}) \tilde{\lambda}_{\tau,a,b}(\boldsymbol{k}^\alpha, \boldsymbol{q}) \tilde{\lambda}^*_{\tau',d,c}(\boldsymbol{k}^\beta, \boldsymbol{q}) \\ & \times \hat{\tilde{c}}^\dagger_{\tau as}(\boldsymbol{k}^\alpha) \hat{\tilde{c}}^\dagger_{\tau' cs'}(\boldsymbol{k}^\beta + \boldsymbol{q}) \hat{\tilde{c}}_{\tau' ds'}(\boldsymbol{k}^\beta) \hat{\tilde{c}}_{\tau bs}(\boldsymbol{k}^\alpha + \boldsymbol{q}), \end{aligned} \tag{3.4}$$

where $\tilde{\lambda}_{\tau,a,b}(\boldsymbol{k}, \boldsymbol{q}) = \lambda_{\tau,a,b}(\boldsymbol{k} - \tau \boldsymbol{q}_{\mathrm{IVC}}/2, \boldsymbol{q})$. It is then again easy to to show that the Hartree-Fock Hamiltonian in terms of the $\tilde{c}$ operators is again diagonal in $\boldsymbol{k}$ and s, i.e.

$$\tilde{H}^{\mathrm{HF}}_{\tau as \boldsymbol{k}^\alpha, \tau' bs' \boldsymbol{k}^\beta} = \delta_{ss'} \delta_{\boldsymbol{k}^\alpha, \boldsymbol{k}^\beta} \tilde{H}^{\mathrm{HF}}_{\tau a, \tau' s}(\boldsymbol{k}^\alpha, s) \tag{3.5}$$

for some $\tilde{H}^{\mathrm{HF}}_{\tau a, \tau' s}(\boldsymbol{k}^\alpha, s)$, and with Hartree and Fock contributions given by (compare with Eq. 2.40)

$$\begin{aligned} \tilde{H}^{\mathrm{H}}_{\tau a, \tau' b}(\boldsymbol{k}, s) &= \frac{\delta_{\tau\tau'}}{A} \sum_{s'\tau'' cd} \sum_{\boldsymbol{G}} \sum_{\boldsymbol{k}' \in \mathrm{mBZ}} V(\boldsymbol{G}) \tilde{\lambda}_{\tau,ab}(\boldsymbol{k}, \boldsymbol{G}) \tilde{\lambda}^*_{\tau'',dc}(\boldsymbol{k}', \boldsymbol{G}) \tilde{P}_{\tau'' d, \tau'' c}(\boldsymbol{k}', s') \\ \tilde{H}^{\mathrm{F}}_{\tau a, \tau' b}(\boldsymbol{k}, s) &= -\frac{1}{A} \sum_{cd} \sum_{\boldsymbol{q} \in \mathrm{all}} V(\boldsymbol{q}) \tilde{\lambda}_{\tau,ad}(\boldsymbol{k}, \boldsymbol{q}) \tilde{\lambda}^*_{\tau',bc}(\boldsymbol{k}, \boldsymbol{q}) \tilde{P}_{\tau d, \tau' c}(\boldsymbol{k} + \boldsymbol{q}, s). \end{aligned} \tag{3.6}$$

[8] The assumption of spin-collinearity will need to be relaxed in Chap. 3.3.

[9] The reader should be careful about the sign convention of $\boldsymbol{q}_{\mathrm{IVC}}$ when comparing with Ref. [8].

The mean-field Hamiltonian is obtained as the 'tilded' version of the standard translationally-invariant HF Hamiltonian presented in Eq. 2.41. Hence, the HF machinery introduced in Chap. 2.3.3 can be straightforwardly repurposed here, if we 'boost' the $\boldsymbol{k}$ argument of the form factors and the one-body terms (which can either come from the kinetic energy or the interaction scheme). In the periodic gauge that we use here, this operation is straightforward, and can be separately implemented before the HF self-consistent procedure.

3.2 Kekulé spirals in twisted symmetric trilayer graphene

Besides TBG, there are many other interesting moiré platforms that have been studied both experimentally and theoretically. One example is the twisted symmetric trilayer graphene (TSTG), which is made by stacking three sheets of graphene with the middle layer twisted by an angle θ relative to the top and bottom layers (Fig. 3.1(a)). It is important that the top and bottom layer have the same twist angles, as this ensure that the moiré patterns generated within the top and bottom pairs of layers are identical, preserving the overall moiré periodicity of the system. In the case that the top and bottom layers are not aligned, in general one will find supermoiré patterns [127].

In Ref. [98], Kekulé patterns with non-zero ordering vector $\boldsymbol{q}_{\mathrm{IVC}}$ has been observed with STM experiments on TSTG. This serves as the motivation for us to theoretically explore potential IKS order in TSTG.

3.2.1 Modeling on twisted symmetric trilayer graphene

Denoting the top, middle and bottom layers as $l = 1, 2, 3$ respectively, generalizing the continuum model for TBG to TSTG is straightforward: the kinetic terms (in each layer) are effectively the same as that in TBG (Eq. 2.6), i.e.,

$$\langle \boldsymbol{p}, l |\, H_{\mathrm{BM}} \,| \boldsymbol{p}', l \rangle = \hbar v_F \left[M_l(\boldsymbol{p} - \tau \boldsymbol{A}_l) - \boldsymbol{K}_\tau \right] \cdot \begin{pmatrix} \tau\sigma_x \\ -\sigma_y \end{pmatrix} \delta_{\boldsymbol{p},\boldsymbol{p}'} \tag{3.7}$$

for $l = 1, 2, 3$, where $\boldsymbol{A}_l$ is the strain-induced vector field, as defined in Eq. 2.7. Here, we have again included possible uniform strains in each layer. Just like the case for TBG,

we expect homostrain to play a similarly minor role in TSTG. Therefore, we restrict our attention to heterostrain, produced by unequal strain in the different layers. In principle, strain could break the mirror symmetry of the system and introduce incommensurate moiré patterns for the top and bottom pairs of layers, potentially leading to a supermoiré pattern. However, we focus here on the case where top and bottom layers experience identical strains, thus preserving the moiré periodicity of the system. This choice can be justified as STM experiments observe well defined moiré patterns in large regions of the TSTG samples [19, 20, 128]. As such, we will assume that the strains are along in the same directions in every layer, $\varphi_1 = \varphi_2 = \varphi_3 = \varphi$, and their magnitude satisfy $\epsilon_1 = -\epsilon_2 = \epsilon_3 = \epsilon/2$. Unless otherwise specified, we will simply take the strain to be along the x-axis, i.e., $\varphi = 0$. The hoppings between adjacent layers are given by the same moiré potential (Eq.2.8), i.e.,

$$\langle \boldsymbol{p}, 3 |\, H_{\mathrm{BM}} \,| \boldsymbol{p}', 2 \rangle = \langle \boldsymbol{p}, 1 |\, H_{\mathrm{BM}} \,| \boldsymbol{p}', 2 \rangle = T_1 \delta_{\boldsymbol{p}-\boldsymbol{p}',\boldsymbol{0}} + T_2 \delta_{\boldsymbol{p}-\boldsymbol{p}',\boldsymbol{b}_1+\boldsymbol{b}_2} + T_3 \delta_{\boldsymbol{p}-\boldsymbol{p}',\boldsymbol{b}_2}, \tag{3.8}$$

where T is defined in Eq. 2.9.

The single-particle Hamiltonian of TSTG can be decomposed [17] into a mirror-symmetry even sector, which is effectively a renormalized version of TBG, and a mirror-symmetry odd sector, which resembles monolayer graphene (Fig. 3.1(b)). The magic angles of TSTG and TBG (in the absence of strain) are related via $\theta_{\mathrm{TSTG}} = \sqrt{2}\theta_{\mathrm{TBG}} \approx 1.56°$.

In contrast to TBG, an electric displacement field normal to the layers has a significant effect: it produces an interlayer potential that breaks the mirror symmetry and mixes the odd and even sectors (Fig. 3.1(c)). This modifies the dispersion, expanding the parameter space for new phases. This effect can be included as an additional term in the Hamiltonian,

$$\langle \boldsymbol{p}, l |\, H_{\mathrm{V}} \,| \boldsymbol{p}', l' \rangle = \delta_{\boldsymbol{p},\boldsymbol{p}'} \delta_{l,l'} \frac{2-l}{2} \Delta V, \tag{3.9}$$

for layers $l = 1, 2, 3$. The full single-particle Hamiltonian we will consider is then given by

$$\hat{H} = \hat{H}_{\mathrm{BM}} + \hat{H}_{\mathrm{V}}. \tag{3.10}$$

The interaction is included in the same way as discussed in Chap. 2.

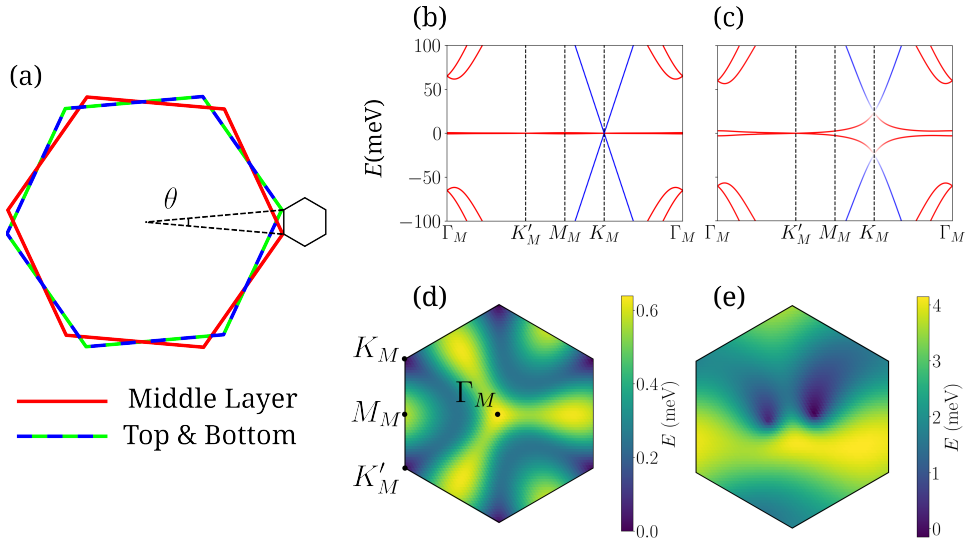


Figure 3.1: **Twisted symmetric trilayer graphene.** (a) The large hexagons denote graphene Brillouin zones of individual layers and the small hexagon denotes the moiré BZ for valley K. (b) Without interlayer potential, TSTG decomposes into a TBG sector (red) and a graphene sector (blue) with opposite mirror eigenvalues. (c) A finite interlayer potential (100 meV) breaks mirror symmetry and hybridizes the two sectors. The color represents the relative weight of the wavefunction on the zero-field TBG and graphene sectors. (d,e) TBG sector conduction band at zero interlayer potential without and with strain ($\epsilon = 0.1\%$) respectively. Strain breaks C_3-symmetry, unpinning the Dirac points, and increases the bandwidth. The corresponding band structures in valley K' can be found using time-reversal symmetry. Reproduced from Ref. [93].

3.2.2 Phase diagram

We perform band-projected self-consistent HF calculations on the model discussed above at the magic angle $\theta = 1.56°$. We use realistic hopping parameters $w_{AA} = 75\,\text{meV}$ and $w_{AB} = 110\,\text{meV}$, and include strain ϵ and interlayer potential ΔV as free parameters of the model. We model interactions via the dual-gate screened Coulomb potential $V(q) = (e^2/2\epsilon_0\epsilon_r q)\tanh qd$, with a screening length $d = 25$ nm and relative permittivity $\epsilon_r = 10$, leading to a typical interaction energy of the order of 10 meV. While this appears to be significantly smaller than the hopping amplitudes, it is actually similar, in order of magnitude, to the widths of the central bands under moderate strain and interlayer potential (see Fig. 3.1). To avoid double-counting interactions, we use the "central average scheme" as discussed in Chap. 2.2.3. Despite the lack of exact particle-hole symmetry, we find that the phase diagrams at ν and $-\nu$ are qualitatively similar. Hence we only present results for $|\nu| \geq 0$.

In order to capture the incommensurate Kekulé spirals (IKS) order or its commensurate counterparts, we adopt the procedure introduced in Chap. 3.1.1, with the generalization where we allow two spin sectors have *different* $\boldsymbol{q}_{\text{IVC}}$. As such, the one-particle density matrix takes the form

$$\langle \hat{c}^\dagger_{\boldsymbol{k}-\tau\boldsymbol{q}_s/2,\tau sa}\hat{c}_{\boldsymbol{k}-\tau'\boldsymbol{q}_s/2,\tau' sb}\rangle = P_{\tau a;\tau' b}(\boldsymbol{k}, s) \tag{3.11}$$

where s is spin index, a and b are single particle band indices, and $\boldsymbol{q}_s$ is the Kekulé spiral vector with possible spin-dependence. In the majority of cases, this spin-dependence is not relevant and we simply scan over $\boldsymbol{q}_\uparrow = \boldsymbol{q}_\downarrow \equiv \boldsymbol{q}_{\text{IVC}}$. Spin-dependence of Kekulé spiral vectors becomes relevant when both spin sectors have intervalley coherence and the two sectors are nonequivalent, as is the case for $\nu = 1$. As such, we have allowed $\boldsymbol{q}_\uparrow \neq \boldsymbol{q}_\downarrow$ when computing the phase diagram at $\nu = 1$. For the range of interlayer potentials considered in the main text, we found that allowing for more generic translation symmetry breaking beyond Eq. 3.11 does not lead to different results.

Fig. 3.2 shows the phase diagrams for $\nu = 0, 1, 2, 3$. Kekulé states involve non-zero Kekulé vector $\boldsymbol{q}_{\text{IVC}}$ and finite intervalley coherence. To diagnose the presence of these states and demonstrate their robustness, we show energy differences per unit cell between

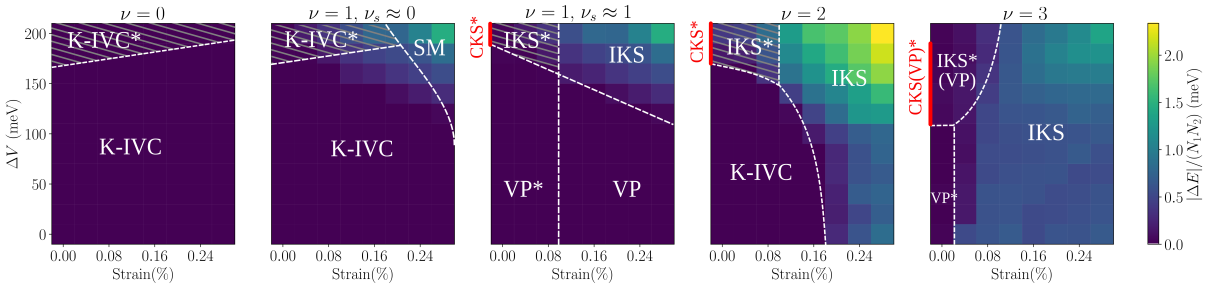


Figure 3.2: Phase diagrams as a function of strain (horizontal axis) and interlayer potential ΔV (vertical axis) at integer fillings ν. We have performed 10×10 self-consistent Hartree-Fock calculations, scanning over all possible Kekulé spiral vectors $\boldsymbol{q}$. ΔE is the energy difference per unit cell between the $\boldsymbol{q} = 0$ state with the overall energy minimum, and may be compared with temperature of a typical experiment in the field, which is of the order of 0.1 meV. The acronyms are: K-IVC for Kramers-intervalley coherence, VP for valley polarization, (C/I)KS for (commensurate/incommensurate) Kekulé spiral, SM for (compensated) semi-metal. Asterisk (*) denotes states that break C_2T-symmetry. The (C/I)KS*(VP) region in $\nu = 3$ consists of Kekulé spiral states with possible finite valley polarization. The red lines on the zero-strain axis indicate *commensurate* Kekulé spirals. The shaded regions have a finite charge gap. For $\nu = 1$, we have shown the phases and charge gaps of the two spin sectors separately, where ν_s denotes the filling of each spin sector. As ΔE cannot be separately defined for each spin sector, the data are simply duplicated in the two plots of $\nu = 1$. Reproduced from Ref. [93].

the lowest-energy $\boldsymbol{q}_{\text{IVC}} = 0$ solution and the energy achieved by minimizing over all $\boldsymbol{q}_{\text{IVC}}$: non-zero values indicate Kekulé spiral ground states.

At zero interlayer potential, the single-particle Hamiltonian decomposes into mirror-symmetry even (TBG) and odd (graphene) sectors. For all fillings and strains examined here, we observe no spontaneous breaking of this symmetry, and the two sectors are only coupled by Hartree terms. Compared to pure TBG, the inclusion of the graphene sector can lead to 'charge-transfer cascades' from the TBG sector, discussed below, but otherwise the phase diagram is consistent with the corresponding one for TBG [8]. We find that IKS order appears at $\nu = 2, 3$ at finite strain (Fig. 3.2). While for the range of strains shown in Fig. 3.2 we find Kramers intervalley-coherent (K-IVC) state at $\nu = 0, 1$, for larger strains the system transitions into IKS at $\nu = 1$ and a symmetric state at $\nu = 0$, again consistent with the situation in TBG.

A non-zero interlayer potential mixes the two symmetry sectors, and the simple picture of Hartree-coupled TBG and graphene sectors is no longer applicable. The mixing of relatively flat TBG bands with graphene bands leads to more dispersive central bands. This

favors the formation of IKS by reducing the minimal strain required for its stabilization, except at charge neutrality, where no Kekulé spiral is observed for either TBG or TSTG.

At high interlayer potential of about 200 meV, a common feature except at $\nu = 3$, is the breaking of C_2T symmetry and the opening of a charge gap. While strong C_2T-breaking has not been observed in monolayer graphene under ordinary conditions, as graphene orbitals are hybridized with TBG orbitals, the Dirac point becomes less dispersive and interaction-induced spontaneous symmetry breaking becomes possible. For $\nu = 3$, C_2T symmetry only spontaneously breaks in one of the two spin sectors, leaving the system gapless. We note that Ref. [129] finds a charge gap at $\nu = 2$, in qualitative agreement with our result.

The phase diagram is most complex at $\nu = 1$, where the two spin sectors have densities of approximately 0 and 1 electron per unit cell relative to their respective charge neutrality points (finite but small charge transfers between the two sectors could occur). The two sectors are only coupled with Hartree interaction, and otherwise exhibit their own physics. To capture the physics correctly, we allow for different Kekulé vectors for the two sectors [10]. In particular, we find ground states with K-IVC ($\boldsymbol{q}_\uparrow = 0$) in the spin sector at charge neutrality and IKS ($\boldsymbol{q}_\downarrow \neq 0$) in the other spin sector.

3.2.3 Commensurate Kekulé spirals.

A new phase that we identify in TSTG is the commensurate Kekulé spiral (CKS*) [11] at high interlayer potential and zero strain. In CKS*, the spiral wavevector relates the K_M-point of valley K where TBG and graphene hybridization is most prominent, to the Γ_M-point of valley K' (i.e. $\boldsymbol{q}_{\mathrm{IVC}} = \boldsymbol{k}_{\Gamma_M} - \boldsymbol{k}_{K_M}$) . The resulting spiral order is commensurate with moiré periodicity, as $3\boldsymbol{q}_{\mathrm{IVC}}$ is a moiré reciprocal lattice vector. We note that CKS* further differs from IKS in that it breaks C_2T symmetry. This is also true of other 'starred' states, including the (C/I)KS* at $\nu = 1, 2, 3$. At zero strain all Kekulé spiral states have commensurate $\boldsymbol{q}_{\mathrm{IVC}}$ (except $\nu = 3$ and large ΔV), but this commensurability is lost once any finite strain is introduced (though the graphene scale lock-in mechanism introduced

[10] For numerical efficiency we fix one spin sector to have $\boldsymbol{q} = 0$ as we observe no Kekulé spirals at $\nu = 0$. We have also performed HF allowing for most general symmetry breaking to confirm the adequacy of the method.

[11] The asterisk emphasises C_2T-symmetry breaking, though in TSTG we do not find C_2T-conserving commensurate Kekulé spiral states.

in Ref. [19] may stabilize commensuration at finite strain).

Finally, we note that, while CKS* is possible at all of $\nu = 1, 2, 3$, it is only robust (i.e. significant energy advantage over competing states) at $\nu = 2$, where it is the ground state up to about $\Delta V = 240$ meV. In particular, CKS* competes against states with $\boldsymbol{q}_{\mathrm{IVC}} = 0$. At $\Delta V = 220$ meV, $\nu = 2$ and no strain, the energy difference per moiré unit cell between the lowest-energy states with $\boldsymbol{q}_{\mathrm{IVC}} = 0$ and CKS* with 12×12 HF is found to be 0.586 meV, which is significantly higher than typical experimental temperature of about 0.1 meV. The finite-size effect is weak, as the same energy difference with 24×24 HF is found to be 0.597 meV, a discrepancy of less than 2%. As a side remark, we note that the energy competition discussed here does not include the competing states *within* the degenerate manifold from spontaneous symmetry breaking. This topic is discussed in Chap. 3.3.

3.2.4 Charge-transfer cascades.

At zero interlayer potential, the TBG and graphene sectors are coupled only by Hartree terms as the mirror symmetry is unbroken. While the total electron density is fixed, electronic charge could transfer non-trivially between the two sectors, as first noted in Ref. [95] at $\nu = 3$ and large chiral ratio. We now track this charge-transfer mechanism across general fillings, and with finite strain. We use a HF interpolation scheme [95] to mitigate finite-size effects on the dispersion and hence more accurately compute the charge transfer.

Fig. 3.3 shows the filling of the TBG sector ν_{TBG} as a function of total filling ν. We observe plateaus at integer values of ν_{TBG} near $\nu = 2$ and $\nu = 3$. This can be rationalized in terms of the formation of a correlated insulator with a finite charge gap in the TBG sector, such that injection of a small amount of additional charge only changes the filling in the graphene sector. The precise width of the plateau depends on the size of the TBG charge gap and the density of states of graphene at the chemical potential. We also find that the sum of unsigned Fermi volumes of all bands — a rough proxy for how 'metallic' the system is — can reach a local minimum at non-integer total fillings, meaning that the most insulator-like filling does not necessarily occur at integer ν due to the charge transfer.

In generating Fig. 3.3, we have determined the charge-transfer from self-consistent

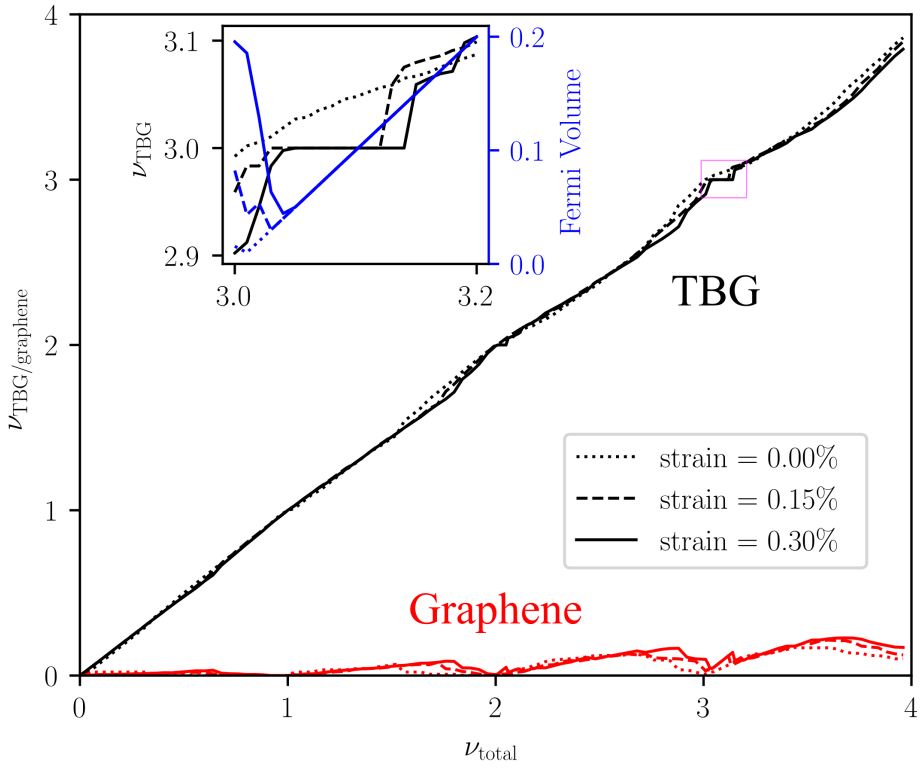


Figure 3.3: 'Charge transfer plateaus' in TSTG. We plot the fillings of TBG and graphene sectors from 10×10 self-consistent HF, interpolated to 60×60, as a function of total fillings. We notice plateaus at integer TBG fillings, which are due to a correlated charge gap in the TBG sector. In the inset, we additionally show the total unsigned Fermi volumes of all bands ('Fermi Volume') as a measure of the metallicity of the system. We notice that, due to non-trivial charge transfer between the two sectors, minima in 'Fermi Volume' need not occur exactly at total integer fillings. Reproduced from Ref. [93].

HF calculations of the full system. However, if we treat the Hartree interaction between the two sectors as a function of only the densities of the respective sectors (which can be justified by assuming the graphene sector charge density is approximately uniform), we can write[12]

$$\begin{aligned} E(n) = E_{\mathrm{TBG}}(n_{\mathrm{TBG}}) + E_{\mathrm{graphene}}(n - n_{\mathrm{TBG}}) \\ + U_0 n_{\mathrm{TBG}}(n - n_{\mathrm{TBG}}) \end{aligned} \tag{3.12}$$

where n denotes the total electron density and $U_0 = V(\boldsymbol{q} = 0)$. We can re-write this as

$$E(n) = \tilde{E}_{\mathrm{TBG}}(n_{\mathrm{TBG}}) + \tilde{E}_{\mathrm{graphene}}(n - n_{\mathrm{TBG}}) \tag{3.13}$$

[12]Here, the labels "TBG" and "graphene" refer to the TBG-like and graphene-like sectors of TSTG respectively.

where $\tilde{E}_{\mathrm{TBG}}(n_{\mathrm{TBG}}) = E_{\mathrm{TBG}}(n_{\mathrm{TBG}}) - U_0 n_{\mathrm{TBG}}^2/2$ is the energy of TBG sector with the electrostatic energy of uniform electron gas subtracted away, and similarly for $\tilde{E}_{\mathrm{graphene}}$. We have also dropped terms that depend only on total electron density. Minimization of the total energy corresponds to $dE/dn_{\mathrm{TBG}} = 0$, giving

$$\tilde{\mu}_{\mathrm{TBG}} = \tilde{\mu}_{\mathrm{graphene}}. \tag{3.14}$$

The graphene sector can be modeled as a non-interacting Dirac cone, so that we can estimate the charge transfer from the interacting physics of TBG sector alone.

3.3 Spin structure of incommensurate Kekulé spirals

In the above discussion of IKS states, we have been treating the spin structure in a simplified manner. In particular, we have mostly satisfied ourselves by assuming a spin-collinear configuration (i.e. conservation of s_z), so that we can speak of the properties of the states in each spin sector separately. In doing so, we have actually selected out some particular states from a larger manifold. This is because the Hamiltonian we have introduced in Chap. 2.2 has the symmetry of $\mathrm{SU}(2)_K \times \mathrm{SU}(2)_{K'}$ valley-dependent spin rotations. As such, the IKS states we have discussed are really manifolds of states related by these symmetries, and these symmetry-related states can carry different properties that are experimentally relevant. For example, as we will soon elaborate, states within the manifolds of $|\nu| = 2$ IKS states may show either charge density Kekulé patterns or spin density Kekulé patterns, which can be distinguished by STM experiments.

In reality, we do not expect states in the "degenerate" manifold to be equally relevant for experiments, as the large $\mathrm{SU}(2)_K \times \mathrm{SU}(2)_{K'}$ symmetry is actually broken in the real system. To determine the actual ground state, we incorporate the various modifications of the BM model and use the resulting augmented microscopic model to directly study the competition between various broken symmetry orders. We also use existing experimental results to inform our choice of parameters: for instance, as we will show below, the observability of the IKS in STM provides important clues to the spin structure, and thereby constrains the relative strength of a subset of the beyond-BM couplings.

Our main results may be summarized as follows. We explore the degenerate manifolds

of IKS ground states of the strained BM model at $|\nu| = 2, 3$, which are distinguished by their spin and valley structure. By incorporating perturbations that lift the degeneracy, we determine the specific states selected from this manifold. Notably, we find that a specific IKS state that preserves the physical time-reversal symmetry and exhibits maximal Kekulé charge density pattern — in accord with the STM experiments [10] — is the favored ground state at $|\nu| = 2$ due to electron-phonon coupling. We also discover a nontrivial Zeeman response of this $|\nu| = 2$ IKS state. For $|\nu| = 3$, we note that two distinct effects of the electron-phonon coupling — namely, inducing a valley anti-ferromagnetic Hund's coupling [130] and strengthening charge density Kekulé patterns [89] — have opposite effects. This may be understood as stemming separately from the the Fock and Hartree contributions of the effective electron-electron interaction induced upon integrating out phonons; we find that the anti-ferromagnetic tendency dominates.

In this section, for concreteness we will study IKS states in TBG. For TSTG, we expect similar results in relevant regimes.

3.3.1 Methods

Our starting point, as advertised, is the interacting BM Hamiltonian [2] with strain, to which we add various additional perturbations. Schematically, we have

$$\hat{H} = \hat{H}_{\text{BM}} + \hat{H}_{\text{int}} + \hat{H}', \tag{3.15}$$

where $\hat{H}_{\text{BM}}$ is the non-interacting BM Hamiltonian with strain, $\hat{H}_{\text{int}}$ is the dual-gate screened Coulomb interaction, and $\hat{H}'$ includes perturbations such as electron-phonon coupling ($\hat{H}_{\text{ph}}^{\text{inter}}$ for coupling to intervalley phonons), intervalley-Coulomb scattering ($\hat{H}_{\text{e-e}}^{\text{inter}}$), and possible external fields. The strained BM model with interaction, i.e., $\hat{H}_{\text{BM}} + \hat{H}_{\text{int}}$, has already been introduced in Chap. 2. Here, we focus on the perturbations that break the $\text{SU}(2)_K \times \text{SU}(2)_{K'}$ symmetry.

Electron-phonon coupling

In this thesis, we consider the effects of the in-plane transverse optical phonons with symmetry irreps A_1 and B_1 at the graphene zone corners [89, 130–134]. Note that we

do not consider the zone-center phonons or the low-energy moiré phonons or phasons, in the spirit of incorporating the minimal ingredients to capture the normal state phase structure; however, the latter may be important to include when exploring possible routes to superconductivity.

With these preliminaries, the phonon Hamiltonian is given by

$$\hat{H}_{\text{ph}} = \hbar\omega \sum_{l\alpha \boldsymbol{q}} \hat{a}^\dagger_{l\alpha}(\boldsymbol{q})\hat{a}_{l\alpha}(\boldsymbol{q}), \tag{3.16}$$

where l labels the layer, $\alpha = 1, 2$ labels the degenerate modes, and the phonon dispersion is approximated as constant, given by $\hbar\omega \simeq 160$ meV. The intervalley phonons couple to electrons as [132]

$$\hat{H}_{\text{EPC}} = \mathcal{F} \sum_{l\alpha} \int d\boldsymbol{r}\ \hat{\psi}^\dagger_l(\boldsymbol{r}) \left[\hat{u}_{l\alpha}(\boldsymbol{r})\Gamma_\alpha\right] \hat{\psi}_l(\boldsymbol{r}) \tag{3.17}$$

where $\hat{u}_{l\alpha}(\boldsymbol{r}) = \mathcal{D}\sum_{\boldsymbol{q}}[\hat{a}_{l\alpha}(\boldsymbol{q}) + \hat{a}^\dagger_{l\alpha}(-\boldsymbol{q})]$, $\hat{\psi}_l$ is a spinor in spin (s), valley (τ) and sublattice (σ) space, and $\mathcal{F}$ and $\mathcal{D}$ collect various phonon parameters. The coupling matrices are given by $\Gamma_1 = \tau_x\sigma_x$ and $\Gamma_2 = \tau_y\sigma_x$. The coupling strength is $g = A\frac{\mathcal{F}^2\mathcal{D}^2}{\hbar\omega}$, where A is the area of the system. We take the coupling strength to be around $g = 70\,\text{meVnm}^2$ [132], though estimates can vary widely in the literature [131].

Using a Schrieffer–Wolff transformation, we obtain an effective phonon-mediated electron-electron interaction given by [130]

$$\hat{H}^{\text{inter}}_{\text{ph}} = -\frac{2g}{A} \sum_{\boldsymbol{pkk'G}} \sum_{\substack{l\tau ss' \\ abcd}} f_{l,\tau ab}(\boldsymbol{k}, \boldsymbol{p}+\boldsymbol{G}) f^*_{l,\tau dc}(\boldsymbol{k'}, \boldsymbol{p}+\boldsymbol{G}) c^\dagger_{\boldsymbol{k},\tau sa} c^\dagger_{\boldsymbol{k'}+\boldsymbol{p},\bar{\tau}s'c} c_{\boldsymbol{k'},\tau s'd} c_{\boldsymbol{k}+\boldsymbol{p},\bar{\tau}sb}, \tag{3.18}$$

where the momenta $\boldsymbol{k}, \boldsymbol{k'}, \boldsymbol{p}$ are summed over the first moiré Brillouin zone (mBZ), and $\boldsymbol{G}$ is a moiré reciprocal lattice vectors. $c^\dagger_{\boldsymbol{k},\tau sa}$ is an electron creation operator for mBZ momentum $\boldsymbol{k}$, valley τ, spin s, and moiré band a. The matrix elements f are defined as

$$f_{l,\tau aa'}(\boldsymbol{k}, \boldsymbol{p}) = \langle u_{\tau a}(\boldsymbol{k}) | \sigma_x P_l | u_{\bar{\tau}a'}(\boldsymbol{k}+\boldsymbol{p}) \rangle\,, \tag{3.19}$$

where P_l is the projection operator to layer l, with $\bar{\tau}$ meaning the opposite valley from τ.

Intervalley Coulomb Scattering

In Chap. 2.2, we have ignored density operators $\rho_{\boldsymbol{q}}$ with momentum transfer $\boldsymbol{q}$ that scatter an electron to another valley, as illustrated in Fig. 3.4. To include the intervalley Coulomb scattering process, we can consider

$$\rho_{\boldsymbol{q}+\tau\Delta\boldsymbol{K}} = \sum_{\boldsymbol{k}\in\mathrm{BZ},ab\tau s} \langle u_{\boldsymbol{k}+\boldsymbol{q},\tau a}|u_{\boldsymbol{k},\bar{\tau}b}\rangle\, c^\dagger_{\boldsymbol{k}+\boldsymbol{q},\tau sa} c_{\boldsymbol{k},\bar{\tau}sb}, \tag{3.20}$$

where $\Delta\boldsymbol{K} = \boldsymbol{k}_{+\gamma} - \boldsymbol{k}_{-\gamma} \approx \boldsymbol{K}_+ - \boldsymbol{K}_-$ is the momentum difference between the two valleys (strictly speaking, it is measured from the γ-point of the moiré Brillouin zone in each valley, but one can approximate it as measured from the original graphene Dirac points), and $\boldsymbol{q}$ is now some small momentum on the moiré scale. We can then approximate $V(\boldsymbol{q}+\tau\Delta\boldsymbol{K}) \approx V(|\boldsymbol{K}_+ - \boldsymbol{K}_-|) \equiv V_{\mathrm{inter}}$, and the Hamiltonian is given by

$$\hat{H}^{\mathrm{inter}}_{\mathrm{e\text{-}e}} = \frac{V_{\mathrm{inter}}}{2A} \sum_{\boldsymbol{p}\boldsymbol{k}\boldsymbol{k}'\boldsymbol{G}} \sum_{\substack{\tau ss' \\ abcd}} f'_{\tau ab}(\boldsymbol{k}, \boldsymbol{p}+\boldsymbol{G}) f'^{*}_{\tau dc}(\boldsymbol{k}', \boldsymbol{p}+\boldsymbol{G}) c^\dagger_{\boldsymbol{k},\tau sa} c^\dagger_{\boldsymbol{k}'+\boldsymbol{p},\bar{\tau}s'c} c_{\boldsymbol{k}',\tau s'd} c_{\boldsymbol{k}+\boldsymbol{p},\bar{\tau}sb} \tag{3.21}$$

with matrix elements

$$f'_{\tau aa'}(\boldsymbol{k}, \boldsymbol{p}) = \langle u_{\tau a}(\boldsymbol{k})|u_{\bar{\tau}a'}(\boldsymbol{k}+\boldsymbol{p})\rangle\,. \tag{3.22}$$

Assuming the dual gate-screened Coulomb interaction is applicable at all momentum scales with the same dielectric constant $\epsilon_r = 10$, one finds $V_{\mathrm{inter}} \simeq 50$ meVnm^2. However, it may be more appropriate to use the dielectric constant of the substrate hBN of $\epsilon_r = 4.4$ [135] instead, as screening from remote bands is expected to be insignificant at the microscopic graphene scale [136]. This gives $V_{\mathrm{inter}} \simeq 120$ meVnm^2.

This simple treatment above involves some approximations, as we now summarize. First, we have ignored the actual form of wavefunctions on graphene scale, including the spatial offset of the two sublattices. This can be relevant in certain cases, e.g. when studying symmetry breaking in the valley-sublattice locked zeroth Landau level of monolayer graphene [136], but is not expected to be of qualitative significance in the present setting. Second, at the lattice scale the separation between the layers becomes non-negligible. Ref. [130] finds that the interlayer separation can sometimes *increase* the effective intervalley scattering, though this effect is dependent on the particular many-body wavefunction in

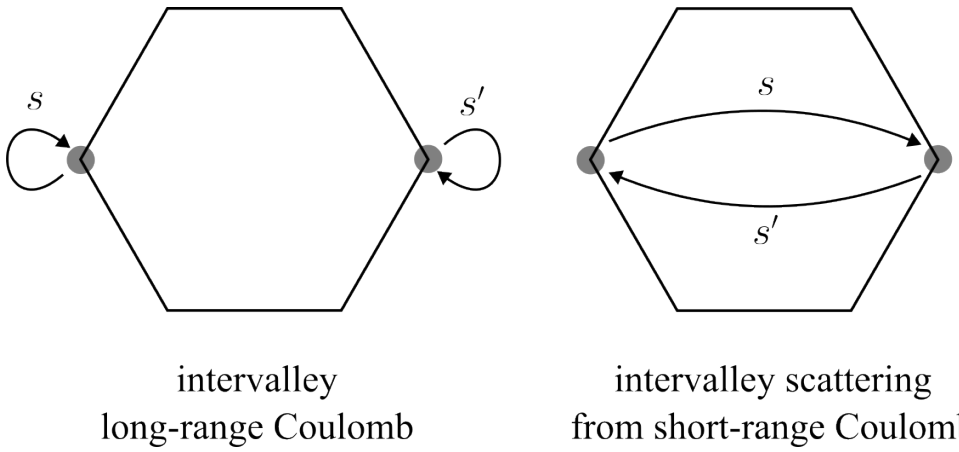


Figure 3.4: Long-range and short-range Coulomb interactions. The hexagons represent the Brillouin zone of graphene. While the long-range interaction also contains terms that couple the two valleys, each electron is scattered into the valley from which it originates. The short-range piece, on the other hand, exchanges electrons between the valleys, such that the net $\mathrm{U}(1)_V$ valley charge is unchanged but the interacting electrons have swapped their valley indices. Thus, while both terms are $\mathrm{U}(1)_V$-symmetric, the former enjoys an enhanced $[\mathrm{SU}(2)_K \times \mathrm{SU}(2)_{K'}]_s$ symmetry of independent spin rotations in each valley, whereas the latter only exhibits the physical $\mathrm{SU}(2)_s$ symmetry. Reproduced from Ref. [137].

consideration. Many of the results in this thesis only depend on the qualitative features of $\hat{H}^{\text{inter}}_{\text{e-e}}$, which are impervious to such modeling details. When the actual strength of intervalley Coulomb scattering is significant, we treat V_{inter} as a tunable parameter, whose true value is presumably not too far off from our rough estimate of $V_{\text{inter}} \simeq 120$ meVnm^2.

3.3.2 Lifting spin-valley degeneracy in the IKS Manifold

Using extended microscopic theory, we would like establish the spin structure of the IKS states. To motivate the problem, recall that Refs. [8, 9] performed HF calculations of TBG at integer and non-integer fillings with moderate strain, and found that IKS order is present at all nonzero integer fillings and a large range of non-integer fillings. While mapping out important features of the phase diagram in broad strokes, these previous works did not fully address the spin structure of these IKS states. This is because the interacting Hamiltonians considered there only included the dominant terms in the interaction, namely the long-range Coulomb interaction, leading to an enlarged $\mathrm{SU}(2)_K \times \mathrm{SU}(2)_{K'}$ symmetry, i.e. independent spin rotations within each valley. In a more realistic treatment, inter-valley processes such as intervalley Coulomb scattering and phonons are present, reducing the

$\mathrm{SU}(2)_K \times \mathrm{SU}(2)_{K'}$ symmetry to a global spin rotation symmetry, i.e. $\mathrm{SU}(2)_s$. While these terms are smaller than the dominant intra-valley Coulomb scattering, they are crucial in determining the spin structure of the IKS states.

In the following, we treat the cases of $|\nu| = 2$ and $|\nu| = 3$ separately. The $\mathrm{SU}(2)_K \times \mathrm{SU}(2)_{K'}$-symmetric degenerate manifold of $|\nu| = 3$ IKS states can be parametrized by the choice of spin polarization in each valley. Our main task is therefore to determine their relative orientation i.e. whether the spins in the different valleys are ferromagnetically or anti-ferromagnetically aligned. In contrast, $|\nu| = 2$ IKS consists of two copies of spinless IKS states and has no net spin polarization in each valley. Instead, the key physics is the relative $\mathrm{U}(1)_V$ phase between the two copies, which will be crucial in determining the microscopic Kekulé pattern.

$\nu = \pm 3$

The most primitive picture of the IKS state is as an intervalley coherent state of spinless electrons with a single occupied (or unoccupied) band. Introducing the physical spin, at $|\nu| = 3$ and for a Hamiltonian that preserves $\mathrm{SU}(2)_K \times \mathrm{SU}(2)_{K'}$-symmetry, the ground state manifold can be generated by the independent rotation of spins in the two valleys. Restricting to the central bands, the density matrix at $\nu = -3$ can be parameterized as

$$P(\boldsymbol{k}) = |\psi_{\boldsymbol{k}}\rangle \langle \psi_{\boldsymbol{k}}| \,, \tag{3.23}$$

where the single occupied HF band is

$$|\psi_{\boldsymbol{k}}\rangle = \alpha_{\boldsymbol{k}} |K, \boldsymbol{k}_+\rangle \otimes |\hat{\boldsymbol{n}}_+\rangle + \beta_{\boldsymbol{k}} e^{i\phi} |K', \boldsymbol{k}_-\rangle \otimes |\hat{\boldsymbol{n}}_-\rangle \,, \tag{3.24}$$

where $\boldsymbol{k}_\pm = \boldsymbol{k} \pm \frac{\boldsymbol{q}_{\mathrm{IKS}}}{2}$, for some IVC angle ϕ, spin direction vectors $|\hat{\boldsymbol{n}}_\pm\rangle$ and coefficients $|\alpha_{\boldsymbol{k}}|^2 + |\beta_{\boldsymbol{k}}|^2 = 1$. Here, $|K, \boldsymbol{k}\rangle$ ($|K', \boldsymbol{k}\rangle$) is some Bloch state in valley K (K') with moiré momentum $\boldsymbol{k}$. Physically, the state has a Kekulé charge density of $\langle \rho_{\boldsymbol{q} \sim \boldsymbol{K}_+ - \boldsymbol{K}_-} \rangle \propto \langle \hat{\boldsymbol{n}}_- | \hat{\boldsymbol{n}}_+ \rangle \propto \cos(\theta/2)$, where θ is the angle between $\hat{\boldsymbol{n}}_+$ and $\hat{\boldsymbol{n}}_-$, and a Kekulé spin density of $\langle \boldsymbol{S}_{\boldsymbol{q} \sim \boldsymbol{K}_+ - \boldsymbol{K}_-} \rangle \propto \langle \hat{\boldsymbol{n}}_- | \boldsymbol{s} | \hat{\boldsymbol{n}}_+ \rangle$. At $\nu = +3$, the state can be parameterized by $P(\boldsymbol{k}) = I - |\psi_{\boldsymbol{k}}\rangle \langle \psi_{\boldsymbol{k}}|$, where I is the identity matrix (corresponding to fully filled central bands) and $|\psi_{\boldsymbol{k}}\rangle$ is the wavefunction of the unoccupied HF band, which can also be put

into the form of Eq. 3.24.

Intervalley processes, such as the coupling of electrons to intervalley phonons and intervalley Coulomb scattering, lift the degeneracy of the ground state manifold and select out a particular relative orientation of $\hat{\boldsymbol{n}}_+$ and $\hat{\boldsymbol{n}}_-$ (of course, $\mathrm{SU}(2)_s$ symmetry precludes fixing the global spin axis.) The electron-phonon coupling (Eq. 3.18) can be schematically represented as (suppressing band and momentum indices)

$$H_{\mathrm{ph}}^{\mathrm{inter}} \sim -g c_{\tau s}^\dagger c_{\bar{\tau} s'}^\dagger c_{\tau s'} c_{\bar{\tau} s}. \tag{3.25}$$

Performing a mean-field decoupling, we find that the Fock term yields

$$E_{\mathrm{ph}}^F \sim +g \sum_{ss'\tau} \langle c_{\tau s}^\dagger c_{\tau s'} \rangle \langle c_{\bar{\tau} s'}^\dagger c_{\bar{\tau} s} \rangle \sim +g \hat{\boldsymbol{n}}_+ \cdot \hat{\boldsymbol{n}}_-, \tag{3.26}$$

which is the anti-ferromagnetic Hund's coupling usually referred to in the literature (we have dropped some constant terms). However, we note that as the state has finite intervalley coherence, we also obtain a non-zero contribution from the Hartree term of the decoupling, given by

$$E_{\mathrm{ph}}^H \sim -g \sum_{ss'\tau} \langle c_{\tau s}^\dagger c_{\bar{\tau} s} \rangle \langle c_{\bar{\tau} s'}^\dagger c_{\tau s'} \rangle \sim -g \hat{\boldsymbol{n}}_+ \cdot \hat{\boldsymbol{n}}_-, \tag{3.27}$$

which is ferromagnetic (again, we have dropped some constant terms). This is similar to the intuition that a Kekulé charge pattern lowers the ground state energy due to its coupling to physical lattice distortion, as discussed in Ref. [89]. Numerically, we find that the antiferromagnetic 'Fock' coupling dominates, thereby favouring $\hat{\boldsymbol{n}}_+ = -\hat{\boldsymbol{n}}_-$.

Intervalley Coulomb scattering (cf. Eq. 3.21) has a very similar form to that of the electron-phonon coupling, but with the opposite sign. It similarly exhibits competition between Hartree and Fock terms; numerically we find that it is effectively ferromagnetic, i.e. favoring $\hat{\boldsymbol{n}}_+ = \hat{\boldsymbol{n}}_-$. We note that Ref. [130] also found that electron-phonon coupling gives rise to an anti-ferromagnetic intervalley Hund's coupling, and intervalley Coulomb scattering gives rise to a ferromagnetic intervalley Hund's coupling. However, their work considered non-IVC states where the Hartree contribution, and hence its competition with the Fock term, is absent. The role of IVC is thus to effectively suppress the absolute

strength of the two couplings relative to the Fock-only value.

The antiferromagnetic ground state at $\nu = \pm 3$ is invariant under $\tau_z s_z$ (here, for definiteness, we have chosen $\langle \tau_z \boldsymbol{s} \rangle$ to point in the z-direction) so that the intervalley coherence occurs between opposite spin sectors. This induces a spin Kekulé pattern rather than a charge Kekulé pattern. However, $\tau_z s_z$ is not a true symmetry of the Hamiltonian, but rather a symmetry of the ground state due to the mean-field approximation inherent in HF. Beyond mean-field, we do not expect $\tau_z s_z$ to be preserved, so that the charge Kekulé pattern would be generally non-vanishing.

In realistic TBG, both phonons and intervalley Coulomb scattering are of course present. Since the two effects favor competing ground states, we observe a sharp phase transition as we tune the relative strength of the two perturbations. At typical values of g and V_{inter}, we find phonons to be dominant. This is consistent with electron spin resonance measurements which find the intervalley coupling to be antiferromagnetic [138].

$\nu = \pm 2$

The $|\nu| = 2$ IKS can be constructed from two copies of $|\nu| = 3$ IKS states, as we now show. For definiteness, we focus on the $\nu = -2$ case; $\nu = +2$ can be easily obtained by particle-hole conjugation.

Let us consider some $\nu = -3$ IKS given by (Eq. 3.24)

$$|\psi_{\boldsymbol{k}}\rangle = \alpha_{\boldsymbol{k}} |K, \boldsymbol{k}_+\rangle \otimes |\hat{\boldsymbol{n}}_+\rangle + \beta_{\boldsymbol{k}} e^{i\phi} |K', \boldsymbol{k}_-\rangle \otimes |\hat{\boldsymbol{n}}_-\rangle \,, \tag{3.28}$$

where as before we have $\boldsymbol{k}_\pm = \boldsymbol{k} \pm \frac{\boldsymbol{q}_{\text{IKS}}}{2}$. On physical grounds, we expect that $\alpha_{\boldsymbol{k}}$, $\beta_{\boldsymbol{k}}$ and $\boldsymbol{q}_{\text{IKS}}$ are fixed by the dominant energy scales such as single-particle dispersion under strain and long-range Coulomb interaction (we can choose some definite gauge and absorb the phase degree of freedom into the factor $e^{i\phi}$), so that $\hat{\boldsymbol{n}}_+$, $\hat{\boldsymbol{n}}_-$ and ϕ parameterize the degenerate manifold at $\mathrm{SU}(2)_K \times \mathrm{SU}(2)_{K'}$-level. The selection of preferred ground states from this degenerate manifold under $\mathrm{SU}(2)_K \times \mathrm{SU}(2)_{K'}$-breaking perturbation is the topic of the preceding section.

To construct $\nu = -2$ IKS, we introduce another copy of IKS (with the same modulation

vector $\boldsymbol{q}_{\text{IKS}}$), given by

$$|\psi'_{\boldsymbol{k}}\rangle = \alpha_{\boldsymbol{k}} |K, \boldsymbol{k}_+\rangle \otimes |\hat{\boldsymbol{n}}'_+\rangle + \beta_{\boldsymbol{k}} e^{i\phi'} |K', \boldsymbol{k}_-\rangle \otimes |\hat{\boldsymbol{n}}'_-\rangle \,, \tag{3.29}$$

and we demand that the two copies are orthogonal, i.e. $\langle\psi'_{\boldsymbol{k}}|\psi_{\boldsymbol{k}}\rangle = 0$ for every $\boldsymbol{k}$, such that the density matrix of $\nu = -2$ IKS state is given by

$$P(\boldsymbol{k}) = |\psi_{\boldsymbol{k}}\rangle \langle\psi_{\boldsymbol{k}}| + |\psi'_{\boldsymbol{k}}\rangle \langle\psi'_{\boldsymbol{k}}| \,. \tag{3.30}$$

Now, since

$$\langle\psi'_{\boldsymbol{k}}|\psi_{\boldsymbol{k}}\rangle = |\alpha_{\boldsymbol{k}}|^2 \langle\hat{\boldsymbol{n}}'_+|\hat{\boldsymbol{n}}_+\rangle + |\beta_{\boldsymbol{k}}|^2 e^{i(\phi-\phi')} \langle\hat{\boldsymbol{n}}'_-|\hat{\boldsymbol{n}}_-\rangle \,, \tag{3.31}$$

and $|\alpha_{\boldsymbol{k}}|^2$ and $|\beta_{\boldsymbol{k}}|^2$ are non-constant functions of $\boldsymbol{k}$ (since the valley polarization $|\alpha_{\boldsymbol{k}}|^2 - |\beta_{\boldsymbol{k}}|^2$ varies in the Brillouin zone [8] for topologically mandated reasons [139]), to ensure that $\langle\psi'_{\boldsymbol{k}}|\psi_{\boldsymbol{k}}\rangle$ vanishes at every $\boldsymbol{k}$ in the BZ, we must have $\hat{\boldsymbol{n}}'_\pm = -\hat{\boldsymbol{n}}_\pm$. This allows us to write

$$\begin{aligned} P(\boldsymbol{k}) = {} & |\alpha_{\boldsymbol{k}}|^2 |K, \boldsymbol{k}_+\rangle \langle K, \boldsymbol{k}_+| \otimes (|\hat{\boldsymbol{n}}_+\rangle \langle\hat{\boldsymbol{n}}_+| + |-\hat{\boldsymbol{n}}_+\rangle \langle-\hat{\boldsymbol{n}}_+|) \\ & + \alpha_{\boldsymbol{k}} \beta^*_{\boldsymbol{k}} |K, \boldsymbol{k}_+\rangle \langle K', \boldsymbol{k}_-| \otimes (e^{-i\phi} |\hat{\boldsymbol{n}}_+\rangle \langle\hat{\boldsymbol{n}}_-| + e^{-i\phi'} |-\hat{\boldsymbol{n}}_+\rangle \langle-\hat{\boldsymbol{n}}_-|) \\ & + \alpha^*_{\boldsymbol{k}} \beta_{\boldsymbol{k}} |K', \boldsymbol{k}_-\rangle \langle K, \boldsymbol{k}_+| \otimes (e^{i\phi} |\hat{\boldsymbol{n}}_-\rangle \langle\hat{\boldsymbol{n}}_+| + e^{i\phi'} |-\hat{\boldsymbol{n}}_-\rangle \langle-\hat{\boldsymbol{n}}_+|) \\ & + |\beta_{\boldsymbol{k}}|^2 |K', \boldsymbol{k}_-\rangle \langle K', \boldsymbol{k}_-| \otimes (|\hat{\boldsymbol{n}}_-\rangle \langle\hat{\boldsymbol{n}}_-| + |-\hat{\boldsymbol{n}}_-\rangle \langle-\hat{\boldsymbol{n}}_-|). \end{aligned} \tag{3.32}$$

Using $|\hat{\boldsymbol{n}}_+\rangle \langle\hat{\boldsymbol{n}}_+| + |-\hat{\boldsymbol{n}}_+\rangle \langle-\hat{\boldsymbol{n}}_+| = I_2$ (the 2-dimensional identity matrix), and defining $V \equiv e^{-i\phi} |\hat{\boldsymbol{n}}_+\rangle \langle\hat{\boldsymbol{n}}_-| + e^{-i\phi'} |-\hat{\boldsymbol{n}}_+\rangle \langle-\hat{\boldsymbol{n}}_-|$, we can write the density matrix more succinctly as

$$P(\boldsymbol{k}) = \begin{pmatrix} \tilde{P}_{++}(\boldsymbol{k}) \otimes I_2 & \tilde{P}_{+-}(\boldsymbol{k}) \otimes V \\ \tilde{P}_{-+}(\boldsymbol{k}) \otimes V^\dagger & \tilde{P}_{--}(\boldsymbol{k}) \otimes I_2 \end{pmatrix} \tag{3.33}$$

where we have defined $\tilde{P}_{++}(\boldsymbol{k}) = |\alpha_{\boldsymbol{k}}|^2 |K, \tilde{\boldsymbol{k}}\rangle \langle K, \tilde{\boldsymbol{k}}|$ and similarly for the other entries.

It is straightforward to show that $VV^\dagger = I_2$, i.e. $V \in \mathrm{U}(2)$. Importantly, this means that V can be parameterized by 4 real parameters, for example, through $V = e^{i\delta} e^{i\gamma(\hat{\boldsymbol{n}}\cdot\boldsymbol{s})}$, for some angles δ, γ and some unit vector $\hat{\boldsymbol{n}}$. In considering two copies of $\nu = -3$ IKS, we have introduced a total of 6 real parameters ($\hat{\boldsymbol{n}}_\pm$, ϕ and ϕ'). As such, this formulation is actually redundant (ultimately, this is because there is no unique way to split $P(\boldsymbol{k})$ into

$|\psi_{\boldsymbol{k}}\rangle\langle\psi_{\boldsymbol{k}}| + |\psi'_{\boldsymbol{k}}\rangle\langle\psi'_{\boldsymbol{k}}|$).

It is also straightforward to demonstrate that the manifold of states parameterized by unitary matrix V with fixed $\tilde{P}_{++}(\boldsymbol{k})$ *etc.* are indeed related by transformations in $\mathrm{SU}(2)_K \times \mathrm{SU}(2)_{K'}$. Choosing $V = I_2$, we have the spin singlet state, which preserves global spin rotations s_x, s_y and s_z symmetries (i.e. $\mathrm{SU}(2)_s$) but breaks symmetry of independent spin rotations in each valley generated by $\{\tau_z s_x, \tau_z s_y, \tau_z s_z\}$, and the valley U(1) symmetry generated by τ_z. This state can be written as

$$P_{\text{singlet}}(\boldsymbol{k}) = \tilde{P}(\boldsymbol{k}) \otimes I_2. \tag{3.34}$$

Consider the unitary transformation $U = e^{i\frac{\delta}{2}\tau_z} e^{i\frac{\gamma}{2}\tau_z(\hat{\boldsymbol{n}}\cdot\boldsymbol{s})}$, where $\hat{\boldsymbol{n}}$ is some unit vector in spin space. We have

$$UP_{\text{singlet}}(\boldsymbol{k})U^\dagger = \begin{pmatrix} \tilde{P}_{++}(\boldsymbol{k}) \otimes I & \tilde{P}_{+-}(\boldsymbol{k}) \otimes e^{i\delta} e^{i\gamma(\hat{\boldsymbol{n}}\cdot\boldsymbol{s})} \\ \tilde{P}_{-+}(\boldsymbol{k}) \otimes e^{-i\delta} e^{-i\gamma(\hat{\boldsymbol{n}}\cdot\boldsymbol{s})} & \tilde{P}_{--}(\boldsymbol{k}) \otimes I \end{pmatrix},$$

which is exactly the manifold of states defined by Eq. 3.33 with $V = e^{i\delta} e^{i\gamma(\hat{\boldsymbol{n}}\cdot\boldsymbol{s})}$. This shows that V is a parameterization of the manifold of degenerate $\nu = -2$ IKS states under $\mathrm{SU}(2)_K \times \mathrm{SU}(2)_{K'}$ symmetry, and we will sometimes write $P(\boldsymbol{k}; V)$ to make this explicit, where it is understood that $[\tilde{P}(\boldsymbol{k})]_{\tau\tau'}$ is fixed by the dominant $\mathrm{SU}(2)_K \times \mathrm{SU}(2)_{K'}$-preserving terms in Hamiltonian. We will also use the notations δ, γ and $\hat{\boldsymbol{n}}$ to refer to the particular parametrization of V given by $V = e^{i\delta} e^{i\gamma(\hat{\boldsymbol{n}}\cdot\boldsymbol{s})}$. Physically, the state consists of one copy of IKS in each sector with spin parallel or anti-parallel to $\hat{\boldsymbol{n}}$, with a relative $\mathrm{U}(1)_V$ phase difference of 2γ between the two spin sectors. This should be contrasted with the situation for $|\nu| = 3$, where we considered intervalley coherence between basis states with different spin directions (Eq. 3.24). This difference stems from the additional redundancy entailed in describing $|\nu| = 2$ IKS as two copies of $|\nu| = 3$ IKS states.

While the states $P(\boldsymbol{k}; V)$ are all energetically degenerate for a Hamiltonian that preserves $\mathrm{SU}(2)_K \times \mathrm{SU}(2)_{K'}$, they correspond to different spin and charge patterns on the graphene scale. To be precise, the Kekulé charge density $\langle \rho_{\boldsymbol{q}\sim\boldsymbol{K}_+-\boldsymbol{K}_-} \rangle \propto \mathrm{tr}(V) \propto \cos\gamma$, while the Kekulé spin density $\langle \boldsymbol{S}_{\boldsymbol{q}\sim\boldsymbol{K}_+-\boldsymbol{K}_-} \rangle \propto \mathrm{tr}(\boldsymbol{s}V) \propto \hat{\boldsymbol{n}} \sin\gamma$.

Coupling to intervalley phonons, as described in Chap. 3.3.1, breaks the symmetry of

independent spin rotations in each valley and (partially) lifts the ground state degeneracy. Since the valley diagonal part of $P(\boldsymbol{k})$ is actually fixed, the Fock term that arises from decoupling the electron-phonon coupling [cf. Eq. 3.18] expression is independent of V. As such, the only non-trivial energetic contribution comes from the Hartree piece, schematically given by

$$E_{\text{EPC}} \sim -\sum_{ss'\tau} \langle c^\dagger_{\tau s} c_{\bar{\tau} s} \rangle \langle c^\dagger_{\bar{\tau} s'} c_{\tau s'} \rangle \,, \tag{3.35}$$

which implies

$$E_{\text{EPC}} \sim -g|\text{tr}(V)|^2 \tag{3.36}$$

Since $\text{tr}(V) = 2e^{i\delta}\cos\gamma$, we conclude that the preferred ground state is a spin singlet state corresponding to $V = e^{i\delta}$ for $\delta \in [0, 2\pi)$ (and $\gamma = 0$). While there will be sub-leading modifications to $\tilde{P}(\boldsymbol{k})$ for finite electron-phonon coupling, the parameterization Eq. 3.33 remains valid, and we have numerically confirmed our results with self-consistent HF calculations. We also comment that the spin singlet IKS state preserves the physical (spinful) time-reversal symmetry $\mathcal{T}_s = s_y \tau_x \mathcal{K}$.

On the graphene scale, the spin singlet state corresponds to the Kekulé interference pattern from the two spin sectors being locked in phase, giving rise to maximal Kekulé charge density pattern. This is consistent with the notion that Kekulé charge pattern lowers the ground state energy due to its coupling to physical lattice distortion [89].

The intervalley Coulomb scattering takes a similar form to the phonon-induced interaction but with the opposite sign; in other words, we have

$$E^{\text{inter}}_{\text{e-e}} \sim +V_{\text{inter}}|\text{tr}(V)|^2, \tag{3.37}$$

which immediately implies that the energetically favored ground state in this case is given by $V = e^{i\delta}e^{i\frac{\pi}{2}(\hat{\boldsymbol{n}}\cdot\boldsymbol{s})}$ with $\text{tr}(V) = 0$, for some arbitrary angle δ and some arbitrary unit vector $\hat{\boldsymbol{n}}$. This again is verified in our HF calculations, and describes one copy of IKS state in each spin sector (parallel and anti-parallel to $\hat{\boldsymbol{n}}$) with π relative phase difference in the IVC angle. On the graphene scale, this corresponds to vanishing charge density Kekulé pattern but maximal spin Kekulé pattern. A minimal charge density Kekulé pattern is favored since it reduces the electrostatic Hartree penalty at wavevectors corresponding to the graphene Dirac momentum.

At this point, it is appropriate to refer back to the results at $|\nu| = 3$ and clarify the main differences. First, as already noted, while the IKS at $|\nu| = 3$ has intervalley coherence between states with different spins, we can always decompose a $|\nu| = 2$ IKS state as two copies of spin collinear IKS states, each of which exhibits intervalley coherence within a single spin sector. [Note that putting two copies of spin-valley-locked $\nu = -3$ IKS together results in a $\nu = -2$ IKS that admits a spin collinear decomposition along an appropriately chosen axis.] This also means that the picture of "ferromagnetic" and "antiferromagnetic" IKS relevant to $|\nu| = 3$ is no longer appropriate for $|\nu| = 2$, as the spin polarization in each valley always vanishes. Instead, the key parameter is 2γ, the difference in IVC phase in the two spin sectors. Second, for $|\nu| = 3$ and for the intervalley processes considered here, both the Hartree and Fock contributions are relevant, with the latter found to dominate numerically. For $|\nu| = 2$, the Fock contribution is constant, and therefore only the Hartree contribution is non-trivial. As such, the energetic considerations at $|\nu| = 2$ and $|\nu| = 3$ are very different.

As in the case of $|\nu| = 3$, we find electron-phonon coupling to dominate over intervalley Coulomb scattering in a realistic system at $|\nu| = 2$. This leads to a spin singlet state for $|\nu| = 2$ that maximizes the charge density Kekulé pattern, consistent with the observation of such patterns in STM [10, 19]. Alternatively, since estimates of g and V_{inter} vary, one can use the experimental observation of charge density Kekulé pattern at $|\nu| = 2$ as a means to bound the ratio g/V_{inter}, which can be then used to infer the ground states at other fillings such as $|\nu| = 3$.

Perturbation	Symmetries of Hamiltonian	Ground state manifold†	Broken generators	Nambu-Goldstone modes
Electron-Phonon Coupling	τ_z, s_x, s_y, s_z	$\hat{\boldsymbol{n}}_+ = -\hat{\boldsymbol{n}}_-$	$\tau_z, \boldsymbol{s}_\perp{}^\ddagger$	3 linear
Intervalley Coulomb Scattering	τ_z, s_x, s_y, s_z	$\hat{\boldsymbol{n}}_+ = \hat{\boldsymbol{n}}_-$	τ_z, $\boldsymbol{s}_\perp{}^\ddagger$	1 linear, 1 quadratic
Zeeman s_z	τ_z, s_z, $\tau_z s_z$	$\hat{\boldsymbol{n}}_+ = \hat{\boldsymbol{n}}_- = \hat{\boldsymbol{z}}$	τ_z	1 linear
Ising SOC $\tau_z s_z$	τ_z, s_z, $\tau_z s_z$	$\hat{\boldsymbol{n}}_+ = -\hat{\boldsymbol{n}}_- = \hat{\boldsymbol{z}}$	τ_z	1 linear

Table 3.1: Summary of effects of perturbations at $\nu = \pm 3$. Note that without any perturbations, the IKS would have 1 linear and 2 quadratic Nambu-Goldstone modes. †: $\hat{\boldsymbol{n}}_+, \hat{\boldsymbol{n}}_-$ indicate the direction of spin polarization in valleys K, K' respectively. The ground state manifold also includes an additional U(1) coordinate parameterizing the in-plane valley angle. ‡: $\boldsymbol{s}_\perp$ refers to the two spin operators perpendicular to $\hat{\boldsymbol{n}}_\pm$.

Perturbation	Symmetries of Hamiltonian	Ground state manifold†	Broken generators	Nambu-Goldstone modes
Electron-Phonon Coupling	τ_z, s_x, s_y, s_z	$e^{i\delta}$	τ_z	1 linear
Intervalley Coulomb Scattering	τ_z, s_x, s_y, s_z	$e^{i\delta} e^{i\frac{\pi}{2}(\hat{\boldsymbol{n}}\cdot\boldsymbol{s})}$	τ_z, $\boldsymbol{s}_\perp{}^\ddagger$	3 linear
Zeeman s_z	τ_z, s_z, $\tau_z s_z$	$e^{i\delta} e^{i\frac{\pi}{2}(\hat{\boldsymbol{n}}_{xy}\cdot\boldsymbol{s})}{}^{\ddagger\ddagger,\,\S}$	τ_z, s_z	2 linear
Ising SOC $\tau_z s_z$	τ_z, s_z, $\tau_z s_z$	$e^{i\delta} e^{i\gamma s_z}{}^\S$	τ_z, $\tau_z s_z$	2 linear

Table 3.2: Summary of effects of perturbations at $\nu = \pm 2$. Note that without any perturbations, the IKS would have 4 linear Nambu-Goldstone modes. †: The ground state is given by $P(\boldsymbol{k}; V)$ according to Eq. 3.33, where V is the entry listed in the table. §: The expressions only hold in the limit of infinitesimal perturbation. ‡: $\boldsymbol{s}_\perp$ refers to the two spin operators perpendicular to $\hat{\boldsymbol{n}}$. ‡‡: $\hat{\boldsymbol{n}}_{xy}$ refers to a unit vector in the xy-plane.

3.3.3 IKS ground states in the presence of applied fields

So far, we have considered how the intervalley processes from various interaction terms fix the spin structure of the IKS state. With this in hand, we can now consider the response of resulting state(s) to applied fields or other extrinsic single-particle terms that enter the Hamiltonian. Two such terms are of particular interest: a Zeeman splitting $\frac{1}{2}\Delta_{s_z}s_z$ (without spin-orbit coupling, the Zeeman axis is arbitrary; for definiteness we take it to be along s_z), and (b) an Ising-like spin orbit coupling (SOC) term $\frac{1}{2}\Delta_{\tau_z s_z}\tau_z s_z$. Zeeman splitting can be generated by applying a magnetic field. However, as we are not considering the orbital effects of magnetic field here, the discussion is most relevant to the case of in-plane magnetic field in twisted symmetric trilayer graphene (TSTG); although closely related to TBG, unlike TBG [140] for symmetry reasons this material only has a negligible orbital coupling to in-plane magnetic fields [141, 142]. SOC, on the other hand, can be induced by proximity-coupling to a transition-metal dichalcogenide, where $\Delta_{\tau_z s_z}$ typically reaches a few meV [143].

For $|\nu| = 3$, the effects of both types of applied field are straightforward to understand: the Zeeman splitting aligns the spins in both valleys along the field, whereas the Ising SOC anti-aligns them. As discussed in Chap. 3.3.2, in the absence of applied fields we expect the ground state of realistic systems to be a valley anti-ferromagnet due to electron-phonon coupling, which dominates over the intervalley Coulomb scattering. Upon applying a Zeeman field, the magnetization axes of the spins will progressively cant towards the external field axis until they are parallel to it, at which point the magnetization saturates (Fig. 3.6d). On the other hand, both Ising SOC and electron-phonon coupling favor valley anti-ferromagnet, so the addition of Ising SOC to a realistic system only serves to select out a particular direction for the valley anti-ferromagnetic order. These effects are listed in Table 3.1.

More careful analysis is required to understand the effects of of applied fields on the IKS ground state at $|\nu| = 2$. Consider for the moment switching off the $\mathrm{SU}(2)_K \times \mathrm{SU}(2)_{K'}$-breaking interaction terms. From the perspective of the simplest $|\nu| = 2$ spin singlet IKS, the expectation is that a Zeeman term $\propto s_z$ will just shrink the gap and leave the density matrix unchanged. However, we find that the actual ground state exhibits a spontaneous

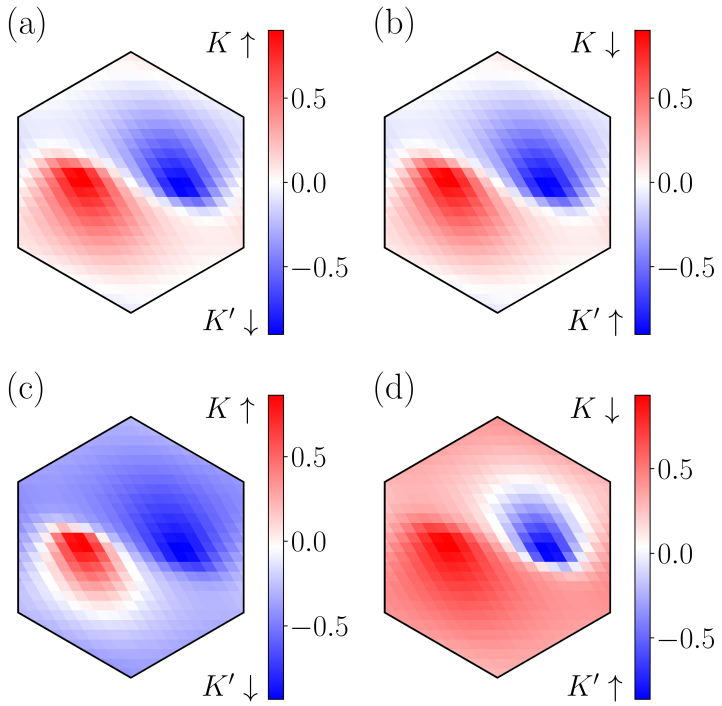


Figure 3.5: (a),(b) Valley/spin polarization of unoccupied bands of the IKS state at $\nu = 2$ without Zeeman splitting, showing $s_z\tau_z = \pm 1$ sectors respectively. We have chosen the state that would be selected out by infinitesimal Zeeman splitting from the degenerate manifold. (c),(d) Same as (a),(b) except with Zeeman splitting $\Delta_{s_z} = 0.8\,\text{meV}$. The system develops a net spin polarization but no net valley polarization. Results are computed using 20×20 HF with $\epsilon = 0.3\%$, $w_{\text{AA}} = 80$ meV, $\theta = 1.05°$, including 2 bands per spin and valley sector. The IKS vector is given by $\boldsymbol{q}_{\text{IKS}} = 0.5\boldsymbol{G}_1$. Reproduced from Ref. [137].

breaking of τ_z (since it has IVC) and s_z, but the combined symmetry $\tau_z s_z$ is preserved, i.e. separate charge conservation in the $\tau_z s_z = +1$ ($K\uparrow$ and $K'\downarrow$) and $\tau_z s_z = -1$ ($K\downarrow$ and $K'\uparrow$) sectors. Application of Δ_{s_z} smoothly deforms the bands in each sector, as shown in Fig. 3.5, leading to a net spin polarization $\langle s_z \rangle$ that grows linearly with applied field. This is favorable compared to a state that preserves s_z symmetry, which can only develop spin polarization by moving electrons across the charge gap. The paramagnetic response can be traced back to the existence of gapless spin-valley Goldstone modes at $\Delta_{s_z} = 0$, as discussed below in Chap. 3.4. In the zero field limit, the preferred ground state can be written as $P(\boldsymbol{k}; V)$ where $V = e^{i\delta} e^{i\frac{\pi}{2}(\hat{\boldsymbol{n}}_{xy}\cdot\boldsymbol{s})}$ for some unit vector $\hat{\boldsymbol{n}}_{xy}$ in the xy-plane. However, we emphasize that all such P have vanishing spin polarization, so the ground state at finite Δ_{s_z} does not admit such a parameterization. For the case of applied Ising SOC, τ_z and $\tau_z s_z$ are spontaneously broken while s_z is preserved, such that $\langle \tau_z s_z \rangle$ increases linearly with applied $\Delta_{\tau_z s_z}$. The results are summarized in Table. 3.2.

Now we consider a more realistic system with electron-phonon coupling and under Zeeman splitting (intervalley Coulomb scattering is left out as its effects are assumed to be dominated by electron-phonon coupling). Referring to Table 3.2, we note that electron-phonon coupling favors ground states that preserve all global spin rotation symmetries, but Zeeman splitting favors states that spontaneously break s_z symmetry. With a finite electron-phonon coupling strength, we find that s_z symmetry remains unbroken up to a finite Δ_{s_z} (Fig. 3.6a). As noted previously, if s_z is preserved, no magnetization is expected to develop unless the Zeeman splitting is large enough to overcome the charge gap of the order of 10 meV. In reality, beyond some finite threshold well below the charge gap, the Zeeman perturbation leads to the spontaneous breaking of s_z symmetry and development of spin polarization (Fig. 3.6b).

The non-trivial dependence of spin polarization on Zeeman field also leads to non-trivial behavior of other properties, such as the charge gap, as shown in Fig. 3.6c. For finite electron-phonon coupling, the charge gap first decreases linearly with externally applied field, corresponding to the intrinsic g_s-factor of electronic spins. The spontaneous breaking of s_z symmetry and development of spin polarization beyond some finite threshold leads to a significant distortion of the band structure and rapid decrease of the charge gap. Similar 'kinks' in the charge gap as a function of external field have been experimentally observed [144, 145]. However, one should be cautious in interpreting this similarity, since for both out-of-plane direction as in the experiments and in-plane direction, magnetic field also couples to orbital degrees of freedom in TBG [140].

3.4 Collective modes

The $\mathrm{SU}(2)_K \times \mathrm{SU}(2)_{K'}$ breaking perturbations described in Chap. 3.3.2 select out states from the degenerate manifold, which impacts the ground state charge and spin density patterns on the graphene scale. In this section, we discuss how the lifting of degeneracies affects the collective modes about these states, with a particular focus on the Nambu-Goldstone modes (NGM) arising from spontaneously broken continuous symmetries.

To calculate the number of NGMs, we use the method discussed in Ref. [146], outlined below. For a set of linearly independent spontaneously broken generators $\hat{Q}_i$ for $i =$

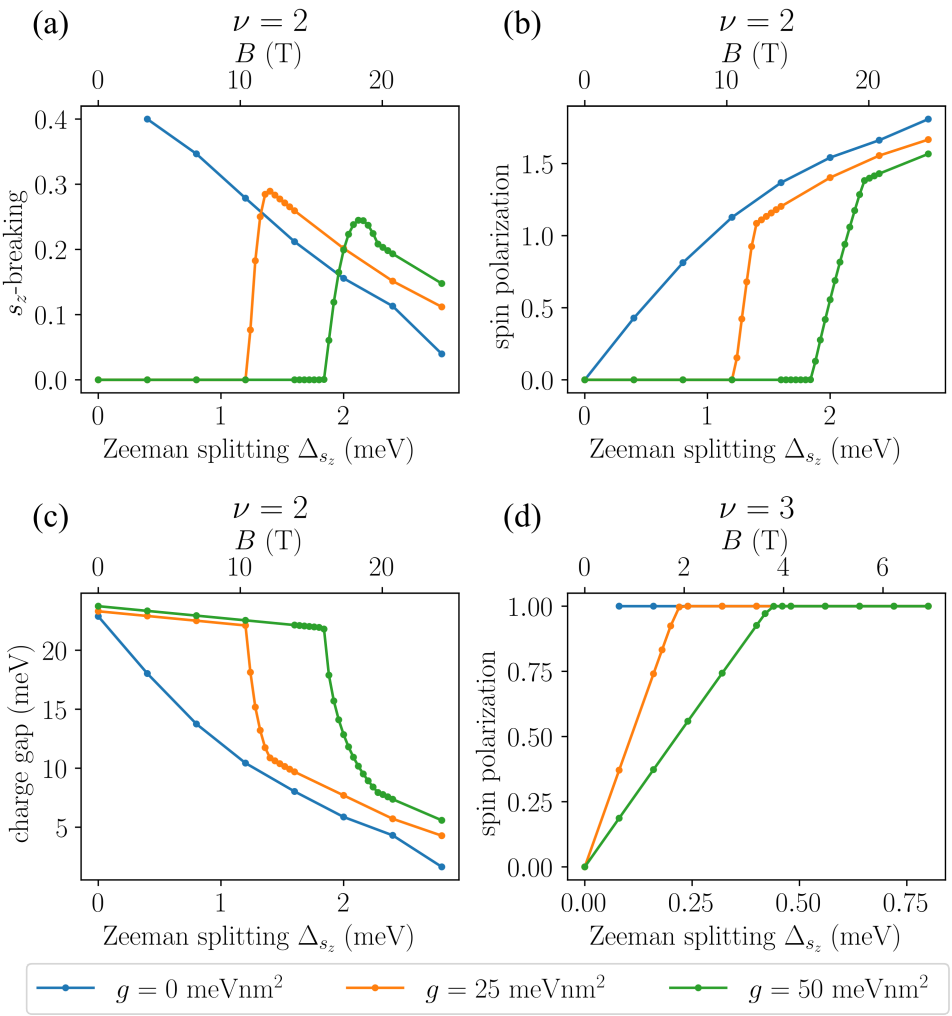


Figure 3.6: (a) Degree of breaking of the U(1) symmetry generated by s_z, defined as $\|P_{\uparrow\downarrow}\|^2 / (N_1 N_2)$ for a $N_1 \times N_2$ system (the vertical bars denote Frobenius norm), (b) spin polarization, and (c) charge gap as a function of Zeeman splitting for different electron-phonon coupling strengths at $\nu = 2$. (d) Spin polarization as a function of Zeeman splitting at $\nu = 3$. Results are computed using 10×10 HF with $\epsilon = 0.3\%$, $w_{\mathrm{AA}} = 80$ meV, and $\theta = 1.05°$. The IKS vector $\boldsymbol{q}_{\mathrm{IKS}} = 0.5\boldsymbol{G}_1$ for all of the states shown. Reproduced from Ref. [137].

$1, ..., n_{\mathrm{BG}}$, one defines a real antisymmetric matrix ρ such that

$$\rho_{ij} \propto -i \langle [\hat{Q}_i, \hat{Q}_j] \rangle \,, \tag{3.38}$$

where the expectation value is taken with respect to the symmetry-broken ground state. The number of NGBs is given by

$$n_{\mathrm{NGM}} = n_{\mathrm{BG}} - \frac{1}{2}\mathrm{rank}\rho. \tag{3.39}$$

The NGMs can be further divided into Type-A and Type-B, whose counting satisfies

$$n_A + 2n_B = n_{\mathrm{BG}}. \tag{3.40}$$

Barring systems with fine-tuned parameters, Type-A NGMs have linear dispersion and Type-B NGMs have quadratic dispersion.

Before including the perturbations, we first consider the NGMs of IKS states in the Hamiltonian with full $\mathrm{SU}(2)_K \times \mathrm{SU}(2)_{K'}$ symmetry. While the broken symmetry generators depend on which broken symmetry state from the degenerate manifold is considered, they yield equivalent excitation spectra. As such, we may analyze the most convenient choice.

At $|\nu| = 2$, we pick the spin singlet ground state which spontaneously breaks τ_z, as well as $\tau_z s_i$ for $i = x, y, z$. It can be straightforwardly shown that the matrix ρ in Eq. 3.38 is identically zero. Therefore, there are four linear NGMs, equal to the number of broken generators. When electron-phonon coupling is taken into account, the spin singlet ground state is selected. $\tau_z s_i$ are now explicitly broken and therefore are no longer broken generators. The only remaining broken generator is τ_z, and this leads to one linear NGM, with small gaps for the other three former NGMs. The effects of various other perturbations and their effects on the number of NGMs are summarized in Table 3.2.

At $|\nu| = 3$, in the absence of perturbations, we pick the fully ferromagnetic IKS corresponding to $\hat{\boldsymbol{n}}_\pm = \hat{z}$ in Eq. 3.24, which breaks the independent generators $\tau_z, \tau_z s_x, \tau_z s_y, s_x, s_y$. Since the state has non-zero $\langle s_z \rangle$, it can be shown that there are 1 linear and 2 quadratic NGMs. Table 3.1 summarizes the effects of the perturbations on the NGM counting for $|\nu| = 3$.

We further numerically compute the neutral excitation spectra of these states using time-dependent Hartree-Fock (TDHF) theory, as explained in the Chap. 2. The results of the calculations for $\nu = 2, 3$ with or without electron-phonon coupling and intervalley scattering are shown in Fig. 3.7. The total numbers of gapless modes agree with predictions.

Besides the NGMs, we observe an additional set of gapped collective modes at about $E \approx 15$ meV for both $\nu = 2$ and $\nu = 3$, below the particle-hole continuum. There are 8 such modes at $\nu = 2$, and 4 such modes at $\nu = 3$. Including the NGMs (and their gapped versions under perturbations), there are in total 12 collective modes at $\nu = 2$ and 7 collective modes at $\nu = 3$. This is consistent with the counting of $16 - \nu^2$ soft modes from the broken U(8) symmetry of the 8 central TBG bands [147]. We note that, even without the perturbations discussed in this section, the BM Hamiltonian already explicitly breaks the U(8) symmetry. For 0.3% strain, the Brillouin-zone averaged energy difference of the central bands is about 15 meV, very close to the energy of this additional set of collective excitations. As a side note, according to Ref. [147], besides the kinetic energy, the difference between inter-Chern and intra-Chern coupling also breaks the U(8) symmetry. As such, to restore the U(8) symmetry and promote the gapped collective modes to NGMs, one not only needs to work in the limit of zero strain and the chiral limit to ensure perfectly flat bands, but also needs to (nonphysically) modify the distribution of the Berry curvature of the underlying Chern basis of the central bands such that the Berry curvature is concentrated at a single point, so as to remove the difference between inter-Chern and intra-Chern coupling. Finally, we remark that, due to the presence of remote bands and beyond mean-field effects, the actual charge gap is likely to be much smaller than the ∼20 meV shown in Fig. 3.7. As such, this additional set of collective modes may overlap with the particle-hole continuum in a real system.

Fig. 3.8a shows the neutral excitation spectrum at $\nu = 2.16$ in the $\mathrm{SU}(2)_K \times \mathrm{SU}(2)_{K'}$ limit. The ground state is a doped version of the $\nu = 2$ IKS with the same set of broken symmetries. This leads to a low-energy collective mode spectrum that is essentially the same as that at $\nu = 2$. However, in contrast with the case of integer fillings, here the particle-hole excitations are not gapped, though the finite grid size in momentum space leads to an apparent 'gap' for the particle-hole excitations. To better study these particle-hole excitations, we compute the particle-hole excitation spectrum from an interpolated

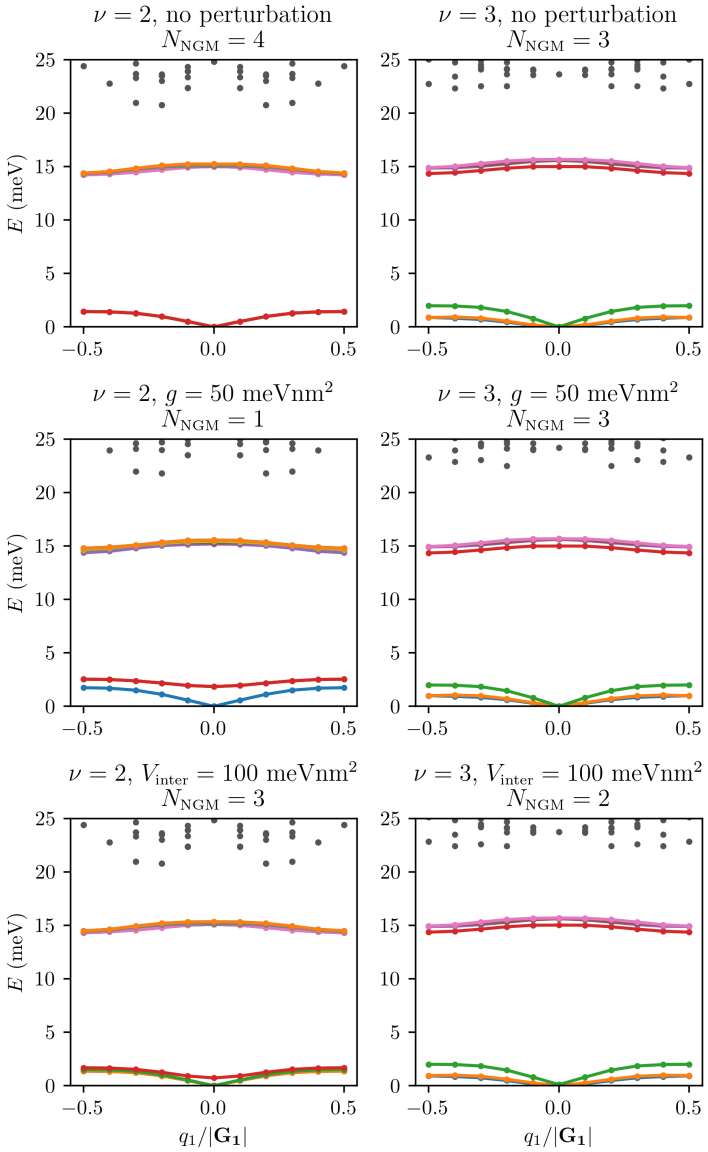


Figure 3.7: Neutral excitation spectra at $\nu = 2$ and $\nu = 3$ for IKS states with no perturbation (top row), with finite electron-phonon coupling (middle row), or with finite intervalley Coulomb scattering (bottom row). Collective excitations are shown with solid lines and particle-hole excitations are shown with gray dots. The plots show the spectra along the $\boldsymbol{G}_1$ direction in the mBZ with $q_2 = 0$. The results are obtained from 10×10 TDHF with 0.3% strain, including 2 bands per spin/valley, and not including the effects of non-local tunneling. The ground state IKS has IVC at $\boldsymbol{q}_{\mathrm{IVC}} = 0.5\boldsymbol{G}_1$. The numbers of gapless modes agree with theoretical expectations. Reproduced from Ref. [137].

HF band structure and map out the boundaries of particle-hole continuum, as shown in Fig. 3.8b. While the small-momentum part of the low-energy collective modes overlaps with the particle-hole continuum, they may remain relatively undamped since the latter are intra-band excitations that do not carry significant flavor character and hence couple weakly to NGMs. The U(1) valley mode has been invoked to explain anomalously long relaxation times in optical pump probe experiments in the vicinity of $|\nu| = 2$ [148].

An in-plane magnetic field in TBG appears to quench the isospin ordering, as quantified by the reduction of electronic entropy [12, 14], in a broad range of fillings, related to the so-called "isospin Pomeranchuk effect". As discussed in previous sections, IKS states at and around $\nu = 3$ have finite spin polarizations in each of the two valleys, which are placed into a spin-valley locked configuration since the electron-phonon coupling favours an anti-ferromagnetic alignment. This is also true near $\nu = 1$ (see in Fig. 4.1 in the next Chapter). An in-plane magnetic field aligns the spin moments along the field, thereby quenching isospin fluctuations and potentially explaining the experimental findings near $\nu = 1$. For fillings near $\nu = 2$, a more careful analysis is required, as we now sketch. In the $\mathrm{SU}(2)_K \times \mathrm{SU}(2)_{K'}$ limit, the IKS state at $|\nu| = 2$ has 4 NGMs (see Tab. 3.2). With electron-phonon coupling, the NGM arising from valley U(1) symmetry-breaking remains gapless, while the 3 NGMs due to valley-spin fluctuations develop a small gap. However, since the experimental temperature (about 10 K in Ref. [14]) is similar to the electron-phonon coupling strength, we expect that these fluctuations remain active and contribute to the entropy of the system. With applied Zeeman field, two of these spin-valley fluctuations are further quenched[13], leading to a reduction in entropy. Note that strictly speaking, there are no Goldstone modes at $T > 0$ due to the absence of continuous symmetry breaking at finite temperature. However, the Goldstone mode count should still quantify the number of soft fluctuations expected to contribute electronic entropy. The arguments above apply equally to non-integer fillings around $|\nu| = 2$ up to the transition at ν_c, since for these fillings the doped IKS retains the same symmetries as at $|\nu| = 2$.

[13]The neutral modes related to the τ_z and $\tau_z s_z$ generators are unaffected by the Zeeman field.

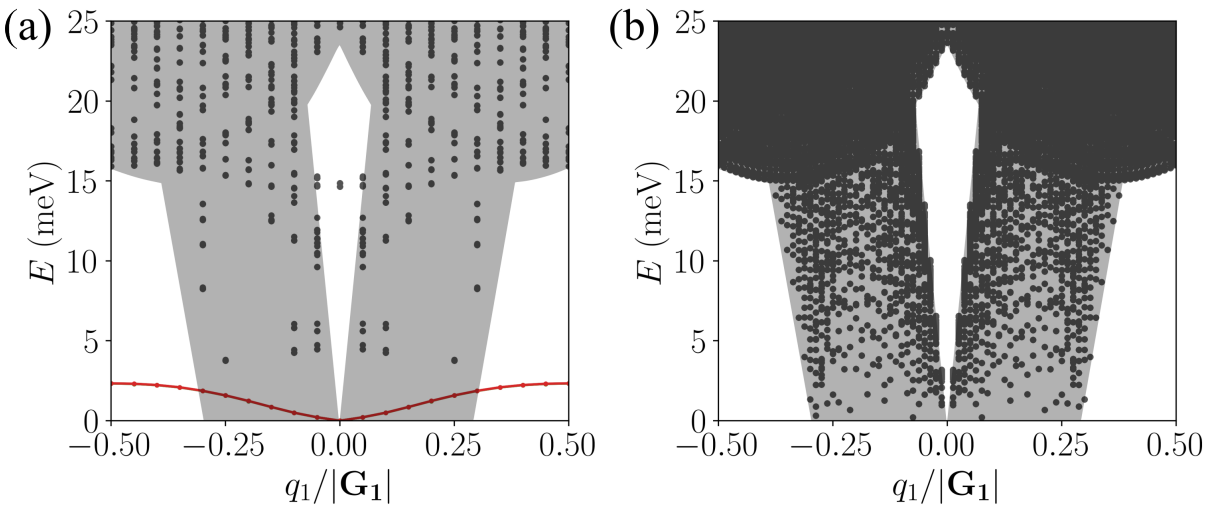


Figure 3.8: (a) Neutral excitation spectra at $\nu = 2.16$ along the $\boldsymbol{G}_1$ direction in the mBZ with $q_2 = 0$. The results are obtained from 20×20 TDHF, with 0.3% strain, 2 bands per spin/valley and without including non-local tunneling or electron-phonon coupling. The solid lines denote low-energy collective excitations, and gray dots denote other excitations. The shaded region is the particle-hole continuum, as extracted from (b). We observe Nambu-Goldstone modes that are qualitatively the same as those for $\nu = 2$. (b) The particle-hole excitation spectrum extracted from the 80×80 interpolated Hartree-Fock band structure at the same parameters. The shaded region represents the particle-hole continuum extracted from the data. Reproduced from Ref. [137].

3.5 Remarks

In this Chapter, we have systematically studied its ground state phase diagram of TSTG under strain and interlayer potential. At zero interlayer potential, since the system decomposes into TBG and graphene sectors, the physics is similar to that of TBG, including the emergence of IKS order at finite strain. At finite interlayer potential, we find new effects such as the breaking of C_2T symmetry and the formation of a commensurate Kekulé spiral state. Our prediction that the Kekulé spiral state at $\nu = 2$ breaks C_2T symmetry and opens up a charge gap is in agreement with experimental results [129]. While the high interlayer potential required to stabilize the phase in TSTG necessitates a dual-gate device, precluding the direct detection of its Kekulé pattern using STM, the mechanism behind the formation of CKS order is more general. Later, in Chapter 5, we will see that many moiré materials can potentially also manifest the CKS order, though they generally involve explicitly broken C_2 symmetry. We have further investigated the normal (non-superconducting) state of TSTG at non-integer fillings. We establish a

charge-transfer cascade mechanism between the TBG and graphene sectors in the absence of interlayer potential, and show that this is consistent with a picture where the two sectors are coupled by Hartree interactions and the TBG sector density of states tracks that of standalone TBG. Notably, we find that integer fillings of the TBG sector and 'maximally insulating' densities need not coincide with overall integer filling, which has implications for experimentally mapping the phase diagram of TSTG.

Delving deeper into the properties of IKS, we have demonstrated that the inclusion of additional perturbations is central to establishing the *spin structure* of the IKS state in strained samples, and furthermore, that a careful analysis of the resulting charge Kekulé patterns provides important clues about the relative strength of various perturbations. Specifically, we incorporate coupling to intervalley phonons, intervalley Coulomb scattering, and possibly external fields. The importance of these perturbations is highlighted by the fact that they break the $\mathrm{SU}(2)_K \times \mathrm{SU}(2)_{K'}$ symmetry (i.e. independent rotations of spin in the two valleys) enjoyed by the strained, interacting BM model (which conventionally includes only the long-range piece of the Coulomb interaction). This motivates a picture of an energy scale hierarchy wherein the dominant terms — strain and long-range interactions — select out a manifold of degenerate IKS states related by $\mathrm{SU}(2)_K \times \mathrm{SU}(2)_{K'}$, whose degeneracy is (partially) lifted by the smaller residual terms.

The degeneracy-lifting leads to a range of competing IKS states distinguished most clearly by their spin structures, but with direct implication on the types of graphene-scale density-wave patterns. Notably, we find that electron-phonon coupling and intervalley Coulomb scattering have the opposite effects. At $|\nu| = 2$, phonons favor a spin-singlet ground state, which is consistent with the STM observation of charge density Kekulé pattern (the dominance of phonons is also consistent with estimates of the coupling strengths). Within this regime, we find that the IKS state at $|\nu| = 3$ is spin-valley locked.

Besides ground state properties, we also study the collective excitation spectra of the IKS states under various perturbations. We confirm that the numbers and types of Nambu-Goldstone modes computed numerically from TDHF agree with theoretical expectations based on symmetry analysis. In addition, as the Zeeman splitting gaps out some collective modes, we expect electronic entropy to be quenched by in-plane magnetic field even when there is no net spin polarization nor spin-valley locking at zero field, as it

is around $|\nu| = 2$. This is consistent with experimental observations [12, 14].

Chapter 4

Doped IKS and superconductivity

Superconductivity is one of the most heavily studied phenomena in twisted bilayer graphene and related systems. While it is beyond the scope of the present text to provide a comprehensive review of the topic, we would like to highly some key experimental results that demonstrate why this topic is of interest and situate our own discussion.

The earliest experiment to observe superconductivity in TBG is Ref. [5]. We would like to highlight two key features observed in the experiment: first, the superconducting temperature is of the order of a few Kelvins. While in absolute terms this does not appear impressive, due to the low Fermi temperature of TBG, such a superconducting temperature firmly places TBG among the "high-temperature" superconductors [5]. Second, close proximity between superconductivity and correlated insulators is observed, similar to cuprates. This immediately raises the question of the role of electron interaction in the formation of superconductivity in TBG.

Due to the aforementioned features, there is a strong reason to suspect that superconductivity in TBG is unconventional. Experimental evidence supporting the unconventional nature of the superconductivity[1] includes, but is not limited to, tunneling spectra that support a nodal SC order parameter [11, 20, 21], gap ratios far exceed expectations from Bardeen–Cooper–Schrieffer (BCS) theory [11], Pauli-limit violation under in-plane magnetic field [5, 149], and power-law superfluid stiffness with temperature [150]. Nevertheless, we caution that the interpretation of experimental results can be subject to debate (for example, a recent tunneling experiment [21] casts doubts on whether the gaps observed

[1]Here, we also include experiments with the closely related material platform TSTG.

in some of the previous experiments were truly superconducting gaps), and a consensus regarding the nature of the superconducting order parameter in TBG has not yet been reached.

One of the main debate in the field of SC in TBG and related materials is the relation between SC and the correlated parent states. Here, we would like to single out a recent experiment, Ref. [21]. In the tunneling experiment, the authors observed the emergence and coexistence of a double-gap regime in TSTG at low temperature, with the outer gap attributed to order of the correlated parent state (specifically, IVC order) and the inner gap attributed to superconductivity. This allows us to consider a schematic picture where the correlation in the parent state significantly renormalizes the properties of the bandstructure, and SC forms from the renormalized bandstructure without destroying the underlying correlation in the parent state. Following this general picture, in this Chapter, we would like to explore the correlated parent (i.e. non-superconducting) metallic phases of TBG and related materials, and understand how they may impact the formation of SC.

4.1 Twisted bilayer graphene

4.1.1 Normal parent states in TBG

In Chap. 3, we have studied the IKS states at integer fillings $\nu = \pm 2$ and $\nu = \pm 3$ in details, and we find that coupling to K-phonons plays a crucial role in determining the spin structure of these IKS states. Here, we study the effects at non-integer fillings, focusing on how the IVC strength is influenced by the electron-phonon coupling g. In Fig. 4.1a, we show the IVC strength, defined as $2\left\|P_{+-}\right\|^2/(N_1N_2)$ for an $N_1 \times N_2$ system ($\|\cdot\|$ denotes the Frobenius norm), in the filling interval $0 < \nu < 4$ (the results for negative ν are similar as the model has approximate particle-hole symmetry). Regardless of electron-phonon coupling, we observe peaks in IVC at integer fillings $\nu = 2, 3$ and around $\nu = 1$, with the peak at $\nu = 2$ about twice as high as those at or around $\nu = 1, 3$. This is consistent with the notation that $|\nu| = 2$ IKS states consist of two copies of $|\nu| = 3$ IKS states, as elaborated in Chap. 3.3.2. We note that the ground state at $\nu = 1$ does not have a finite charge gap [8].

In order to capture the effect of phonons, we introduce an indicator of the strength

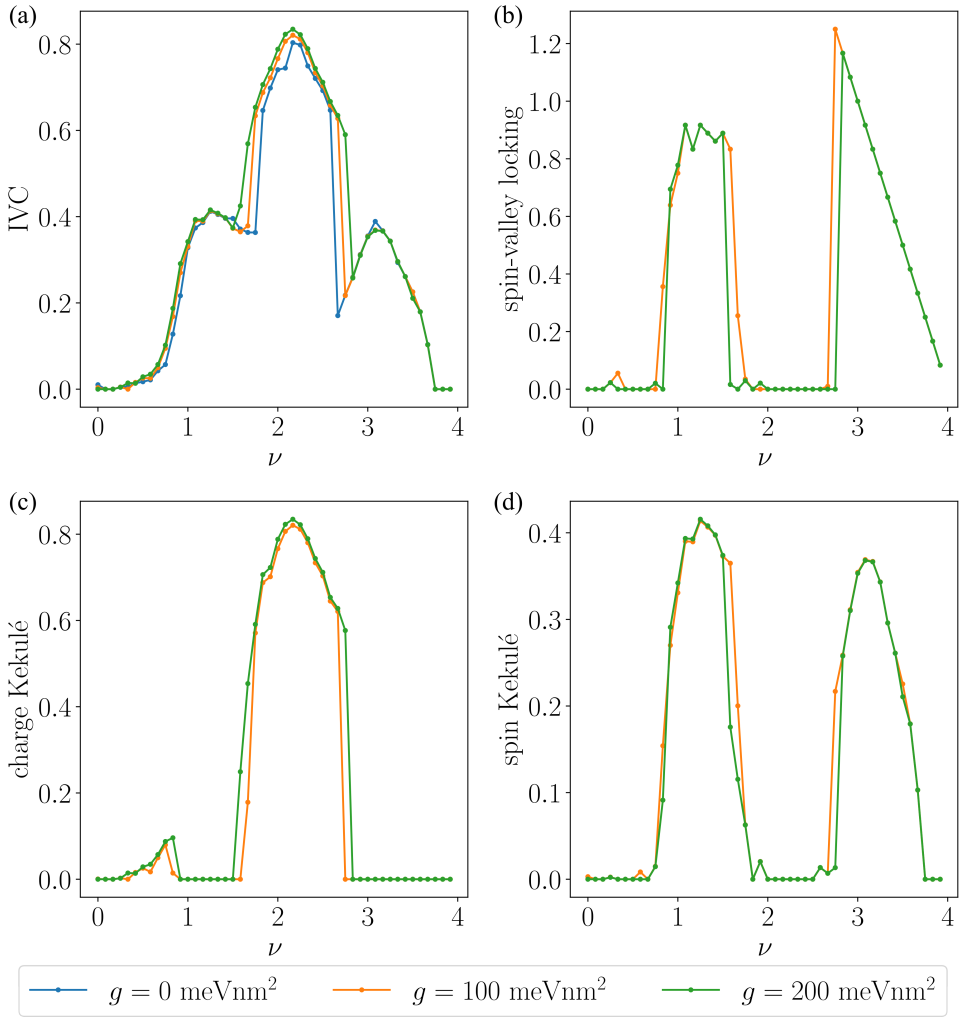


Figure 4.1: (a) IVC order parameter, (b) spin-valley locking, strength of (c) charge, and (d) spin Kekulé patterns (see the text for the definitions used) of the Hartree-Fock ground states for different values of the electron-phonon coupling constant g. The system size used is 12×12 and the magnitude of strain is 0.5%. We have omitted $g = 0$ for (b,c,d), since $\mathrm{SU}(2)_K \times \mathrm{SU}(2)_{K'}$ symmetry implies that there are no definite values for the plotted quantities. Reproduced from Ref. [137].

of the charge Kekulé pattern given by $\|\mathrm{tr}_s P_{+-}\|^2/(N_1N_2)$ (tr_s is the trace over the spin indices), and that of spin Kekulé pattern, given by $\sum_i \|\mathrm{tr}_s(s_i P_{+-})\|^2/(N_1N_2)$. With the inclusion of electron-phonon coupling, the IVC around $\nu = 2$ is strengthened. This is expected, as coupling to zone-corner phonons favors a Kekulé charge density of the IKS [89], as discussed for $|\nu| = 2$ in Chap. 3.3.2, and this extends to non-integer fillings around $\nu = 2$, as shown in Fig. 4.1c[2]. As discussed in Chap. 3.3.2, due to the antiferromagnetic nature of electron-phonon coupling, we found the IKS state at $|\nu| = 3$ to be spin-valley locked, leading to no charge density Kekulé pattern. Instead, we find non-vanishing spin Kekulé pattern. As shown in Fig. 4.1b,d, non-integer fillings near $\nu = 3$ also have significant spin-valley locking (defined as $|\mathrm{tr}(\boldsymbol{s}\tau_z P)|/(N_1N_2)$ for an $N_1 \times N_2$ system) and exhibit a spin Kekulé pattern. As shown in Fig. 4.1b, spin-valley locking is also present around $\nu = 1$. Since electron-phonon coupling does not directly couple to the spin-valley locked IVC, we do not observe a similarly marked increase of the IVC strength near $\nu = 1, 3$. We note a first order transition at about $\nu_c \approx 2.6$ (the value shifts closer to 3 with larger electron-phonon coupling) that separates non-integer filling states with same symmetry as $\nu = 2$ and states with the same symmetry as $\nu = 3$. This is a relevant threshold that will feature in later discussions. A similar threshold with $\nu_c \approx -2.6$ exists on the hole-doped side.

4.1.2 Implications for superconductivity

We now turn to an assessment of (doped) IKS states as possible parent states for superconductivity in TBG in the filling range $-3 < \nu < -2$. As discussed earlier, mean field calculations show a first order transition signaled by an abrupt jump in the intervalley coherence and spin-valley locking order parameter,[3] at a critical density ν_c as shown in Fig. 4.1. Our numerical calculations find $\nu_c \approx -2.6$ in the limit of vanishing electron-phonon coupling (although it can depend on the magnitude of strain and values of other parameters used), and it evolves towards -3 with increasing electron-phonon coupling. The critical density ν_c separates two distinct behaviors. For $\nu_c < \nu < -2$, the state is a

[2]Strictly speaking, the measure we have introduced does not distinguish between charge density and charge current order. Nevertheless, since the states at and near $\nu = 2$ preserves the physical time-reversal symmetry, the Kekulé pattern must be of charge density character.

[3]The Hamiltonian used in this calculation is approximately particle-hole symmetric.

doped version of IKS at $\nu = -2$, with unbroken global spin rotation symmetry $\mathrm{SU}(2)_s$ (assuming non-zero electron-phonon coupling). At $-3 < \nu < \nu_c$, the state is a doped version of IKS at $\nu = -3$, with finite spin-valley locking. The symmetry properties of the ground states are also reflected in the symmetries of the Fermi surfaces. In Fig. 4.2, we show typical Fermi surfaces for both regimes. For $-3 < \nu < \nu_c$, there is a single spin-valley locked Fermi surface, while for $\nu_c < \nu < -2$, there are two identical Fermi surfaces in the two spin sectors. As we will see in the next section on a related experiment in TSTG, the superconductivity on the $-3 < \nu < \nu_c$ side appears to be weaker than the $\nu_c < \nu < -2$ side. Nevertheless, the superconductivity does not completely vanish on the weaker side, and here, we would like to consider the two regimes separately and attempt to understand what the properties of correlated parent state inform us about the potential superconducting order.

The authors of Ref. [151] argued for superconductivity originating from a (non-IVC) spin-valley locked parent state in the filling range $-3 < \nu < -2$. The IKS at $-3 < \nu < \nu_c$ similarly has a finite spin-valley locking, though the Fermi surface is contained in a single IKS band with intervalley coherence between opposite spin sectors, as shown in Fig. 4.2a, whereas the spin-valley locked state considered in Ref. [151] has two bands at the Fermi level related by a simultaneous flip of spin and valley index. Nevertheless, as detailed in the Appendix A, we find that the pairing symmetry of a superconductor evolving out of such an IKS parent state shows a mixture of spin singlet and spin triplet characteristics, similar to that considered in Ref. [151], and much of their discussion applies here as well. In particular, such a state remains consistent with the experimentally observed Pauli limit violation [20, 149, 152], enhancement of superconductivity by spin-orbit coupling (SOC) [25], and quenching of isospin ordering by in-plane magnetic field [12, 14].

Nevertheless, we caution that the experimental observations mentioned above cannot fully rule out superconductivity from an $\mathrm{SU}(2)_s$-symmetric parent state. Violation of the Pauli limit is possible with spin-triplet pairing or strong electron correlations, and the enhancement of superconductivity with SOC does not rule out the co-existence of a different superconducting mechanism in a system without externally applied SOC. Furthermore, as we have argued in Chap. 3.4, the quenching of isospin order by in-plane magnetic field is also consistent with the doped IKS state at $\nu_c < \nu < -2$, which is $\mathrm{SU}(2)_s$ symmetric.

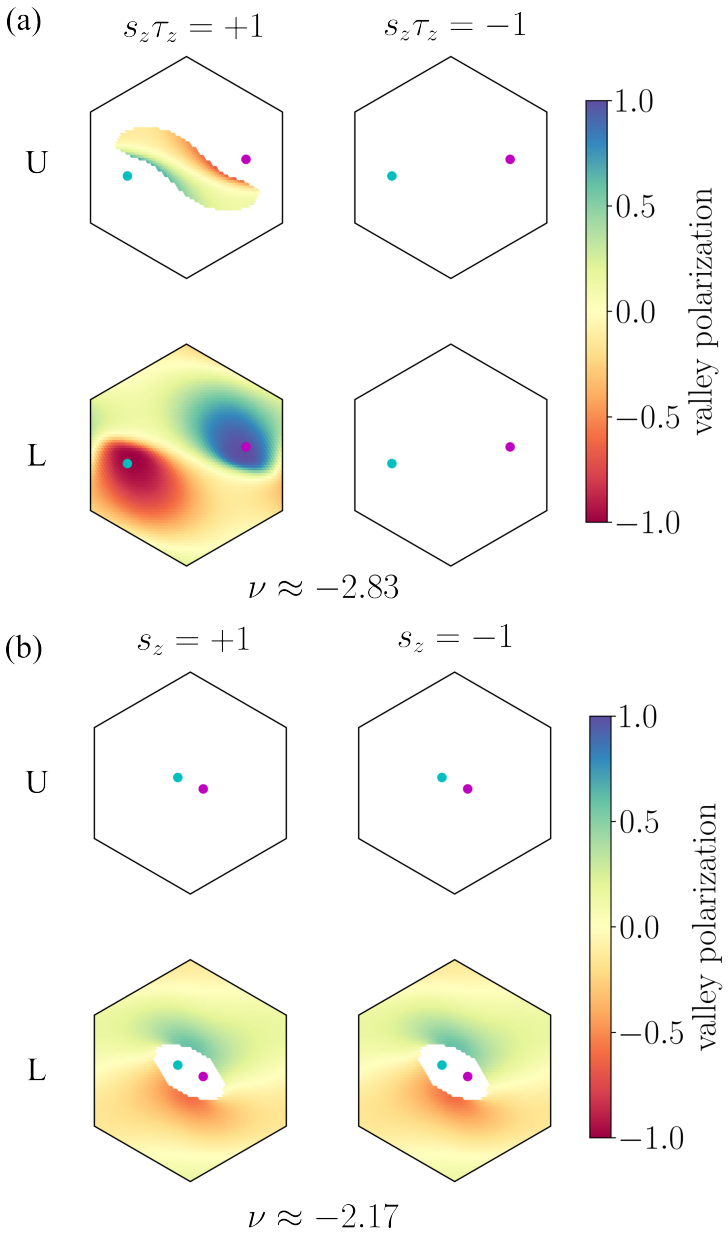


Figure 4.2: Fermi surfaces of the doped IKS states for (a) $\nu < \nu_c$ and (b) $\nu > \nu_c$. For (a), the state is spin-valley locked and we show the electron occupation for each $s_z\tau_z$ sector (for definiteness we have assumed $\langle \boldsymbol{s}\tau_z \rangle$ is along the z-direction). For (b), the state is spin singlet and we show the electron occupation for the two identical spin sectors. We label the lowest band in each charge sector as L and the second lowest band as U. The color plots show valley polarization of occupied orbitals, whereas white spaces indicate unoccupied orbitals. Cyan and magenta dots indicate the γ-points of valley K and K' respectively (due to finite $\boldsymbol{q}_{\text{IKS}}$, the two γ-points do not align). We performed 12×12 Hartree-Fock with 0.3% strain, $g = 70$ meVnm^2 and $V_{\text{inter}} = 100$ meVnm^2. The data are then interpolated to 60×60 with HF interpolation scheme. Reproduced from Ref. [137].

While the pairing symmetry in the $-3 < \nu < \nu_c$ doping range would contain a specific mixture of spin singlet and spin triplet characteristics due to the broken SU(2)$_s$-

symmetry, in the $\nu_c < \nu < -2$ doping regime, the pairing could either be spin singlet or triplet as $\mathrm{SU}(2)_s$ is preserved in the parent state (see App. A for more discussion). For $-2.5 < \nu < -2.2$, Ref. [20] observed evidence for a gapped superconductor in TSTG. This may naturally suggest a spin singlet s-wave pairing symmetry, though the authors proposed that a superconductor with a nodal order parameter can remain gapped in the strong-coupling regime. On the other hand, Ref. [11] reported signatures of nodal superconductivity in the entire filling range $-3 < \nu < -2$ in TBG. We also note the Pauli-limit violation observed in Ref. [149] for TSTG, suggesting a spin-triplet pairing mechanism instead. However, as we have already remarked, the Pauli limit is only valid for the weakly coupled regime, which may not be appropriate near $\nu = -2$.

As shown in Chap. 3, electron-phonon coupling selects out the spin-singlet normal ground state and enforces the time-reversal symmetry for $\nu_c < \nu < -2$. As such, s-wave superconductors that form from such a parent state would satisfy Anderson's theorem and hence be robust against quenched disorder that preserves time reversal symmetry.

In the above discussion, ν_c divides the filling range $-3 < \nu < -2$ into two regimes with the same isospin symmetries as the correlated insulators at $\nu = -3$ and $\nu = -2$ respectively. Experimentally, the correlated insulators on the hole-doped side are less robust than those on the electron side, and the above discussion is expected to be most applicable to samples that exhibit insulating behaviors at both $\nu = -2$ and $\nu = -3$ [5, 12, 153–155]. In an ongoing work, we investigate systems that do not form insulators at $\nu = -3$ or $\nu = -2$ by properly modeling the particle-hole asymmetry in TBG.

4.2 Twisted symmetric trilayer graphene

In Chap. 3, we introduced the basic properties and the normal state phase diagrams of twisted symmetric trilayer graphene (TSTG). We have seen that it shares many similar properties with TBG at low interlayer potential, but can manifest distinct phenomena at larger interlayer potential. In this section, we discuss our work in collaboration with the experimental group exploring superconductivity in TSTG.

4.2.1 Experimental observation

The experiment involves a magic angle TSTG device with $\theta = 1.55°$ doubly encapsulated in hBN. The device is shaped into a Hall-bar geometry with contacts attached so as to allow its longitudinal and transverse conductivity to be measured. Below, we selectively present some of the experimental results, which are most relevant to our later theoretical contribution. Within experimental discussions, it is typical to represent the interlayer potential with the "displacement field" D, such that the potential difference between top and bottom layers ΔV is related to the displacement field D by $\Delta V = \frac{2dD}{\epsilon_{g,\perp}}$, where $\epsilon_{g,\perp}$ is the out-of-plane dielectric constant of graphene.

Fig. 4.3a shows the longitudinal resistivity, R_{xx}, as a function of displacement field D and filling factor ν without applied magnetic field. The dark blue region corresponds to superconductivity. We can divide the phase space into three regions. In Region I, there is only one superconducting dome, shown in Fig. 4.3c. Critical current and critical magnetic field decrease rapidly as filling factor decreases from $\nu = -2.35$. Region II is at intermediate displacement fields. In this region, superconductivity exhibits a double-dome feature in both DC current (I_{dc}) and magnetic field dependence. The filling factor in-between the two domes is denoted as ν^*. Region III occurs at higher displacement fields, and the system once again exhibits a single superconducting dome, as shown in Fig. 4.3e, which shrinks and eventually disappears at very high displacement field. Fig. 4.3b shows the R_{xx} in the $\nu - D$ plane with a out-of-plane magnetic field $B = 0.1$ T. We observe a characteristic wedge-shaped region, denoted by red dotted lines, where superconductivity is suppressed by the magnetic field. This corresponds to the regions between the two domes in Region II.

4.2.2 Theoretical work

To gain insight into the observation of double-dome superconductivity, we turn to Hartree-Fock calculations on TSTG. As reproduced in Fig. B.2 in Appendix B, the temperature dependence of R_{xx} at fillings $\nu = -2.2$ and $\nu = -2.8$ shows clear differences far above T_c, suggesting that the normal state undergoes changes across ν^*. This can be captured by computing the Hartree-Fock ground state, and hence the Fermi surface from which the

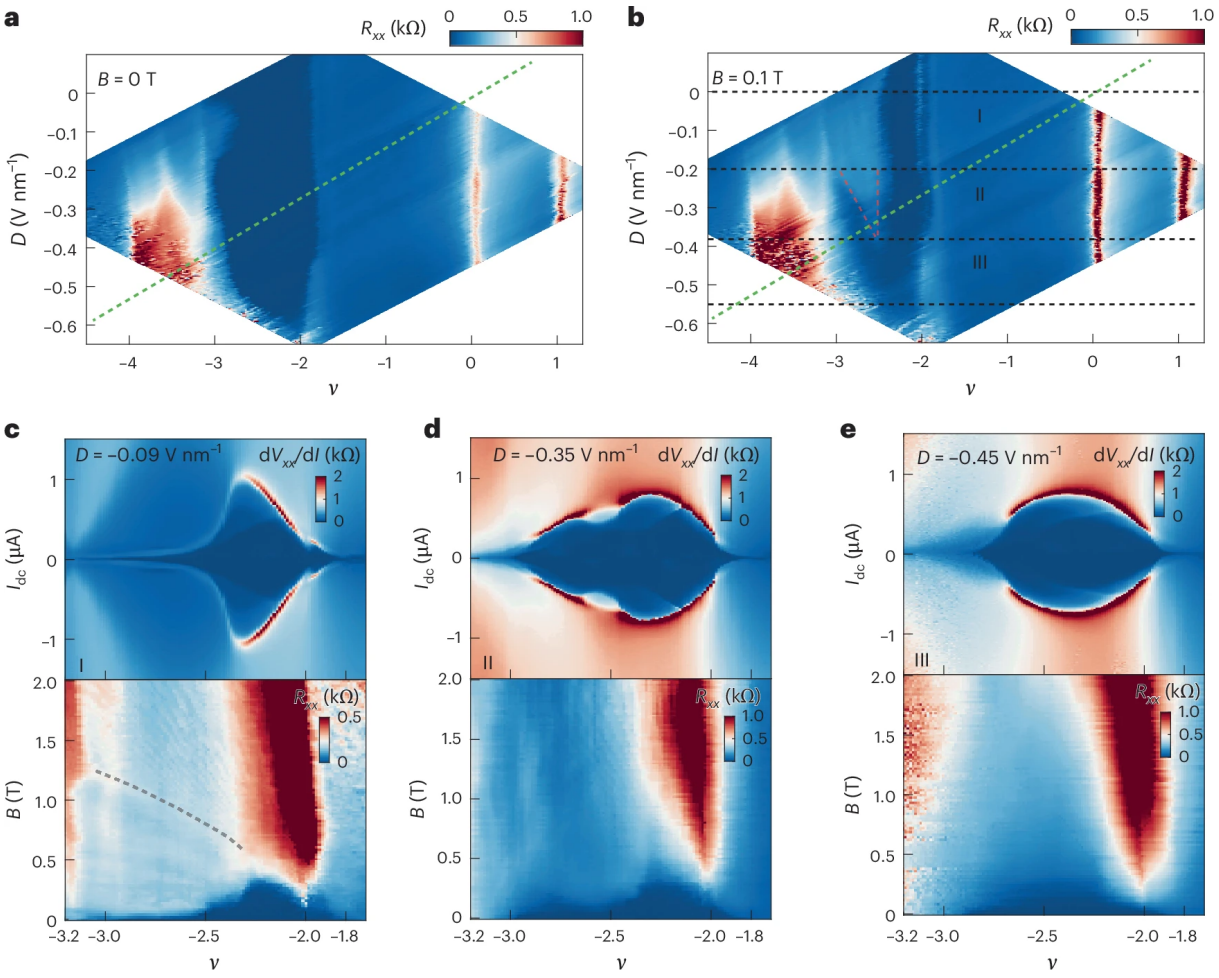


Figure 4.3: **a,b**, $\nu - D$ mapping at $B = 0$T (**a**) and $B = 0.1$T (**b**). The green dashed lines in **a,b** show the relationship between the displacement field and filling factor under single gate tuning. **c,d,e**, Differential resistance (top panel) versus ν and I_{dc} at different displacement field $D = -0.09V/\text{nm}$ (**a**), $D = -0.35V/\text{nm}$ (**b**), $D = -0.45V/\text{nm}$ (**c**) and corresponding Landau fan (bottom panel). In a low-displacement field region (**c**), the Dirac band, isolated alongside a flat band, generates Dirac Landau levels, complementing Landau levels stemming from the flat band. Charge transfer between the two sets of Landau levels gives rise to the curved feature in the lower left portion of the $\nu - B$ plane (marked with a dashed line as a guide to the eye). In this region, a single superconducting dome exists, and the critical current of the superconducting state sharply decreases with increasing doping. The Dirac band is already hybridized with flat bands in the high displacement field regime (**e**). Landau levels solely originate from this hybridized band. In addition, only one superconducting dome exists, and the superconducting region shrinks as the displacement field increases until the superconducting dome vanishes entirely. The Dirac band is hybridizing with a flat band in the intermediate displacement field region (**d**), and the double dome superconductivity appears. Reproduced from Ref. [156].

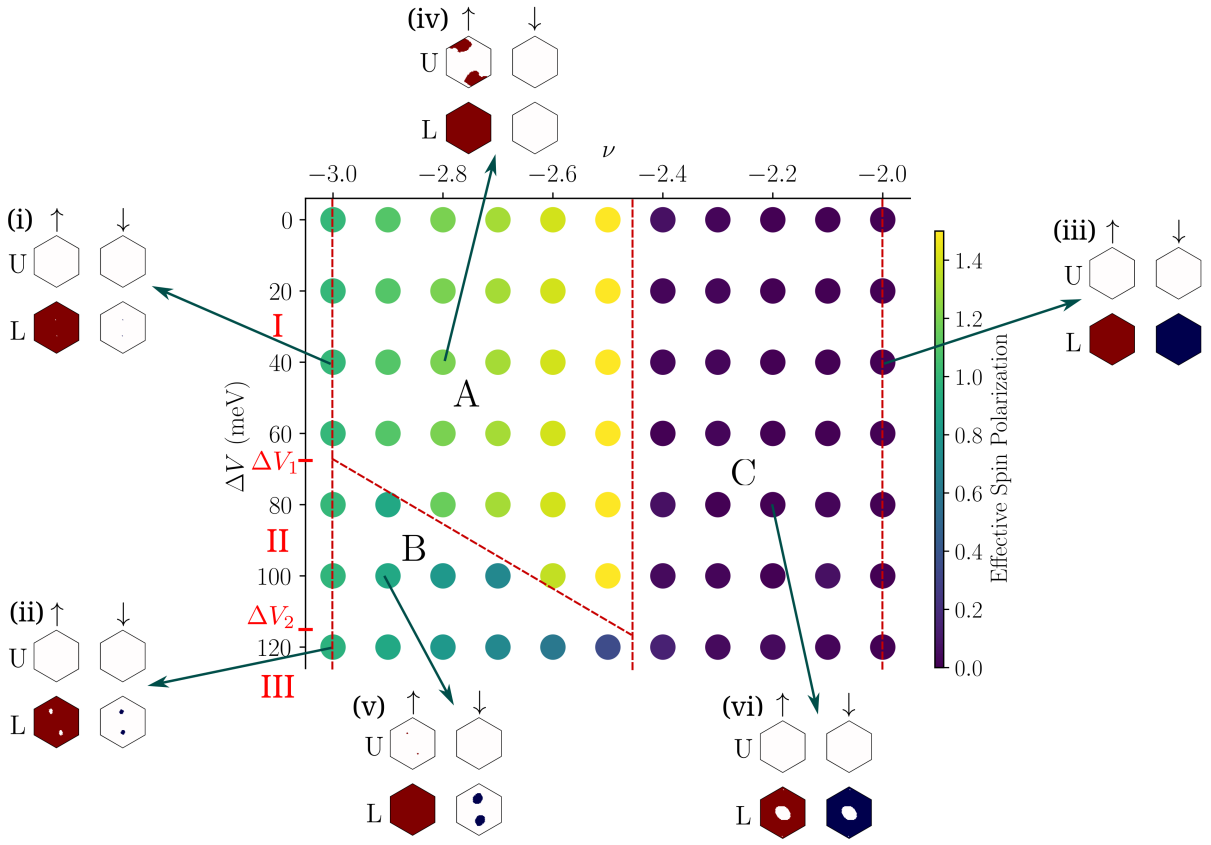


Figure 4.4: The main figure shows the effective spin polarization of the Hartree-Fock ground state as a function of the filling ν and interlayer potential ΔV. The latter serves as a proxy for the displacement field D; regimes of ΔV consistent with regions I-III of Fig. 4.3 are indicated. The detailed parameters used are discussed in the Methods section. The phase diagram shows a wedge (labeled A) where the effective spin polarization is peaked, which coincides with the region of suppressed superconductivity in Fig. 4.3b. Regions B and C correspond to the left and right domes, respectively. Insets (i)-(vi) show representative examples of the normal state Fermi surfaces (FSs) in the upper (U) and lower (L) IKS bands labeled by their effective spin ($\uparrow$ / $\downarrow$). Upon electron doping $\nu = -3$, for small ΔV (region A), the small bandwidth means it is energetically favourable to populate the upper IKS band, while for large ΔV (region B), the larger bandwidth favours populating the lower IKS band of the opposite effective spin. For $\nu > \nu^*$ (region C), the lower IKS bands in both effective spin sectors are equally occupied. Adapted from Ref. [156].

superconductor emerges.

We use the same Hamiltonian as introduced in Chap. 2 and 3. We fix the gate distance $d = 25$ nm, dielectric constant $\epsilon_r = 20$, and twist angle $\theta = 1.56°$. In addition, we include uniaxial heterostrain of strength $\epsilon = 0.15\%$ along the x-axis direction (the coordinate system is chosen such that x-axis is perpendicular to some of the carbon-carbon bonds). This is consistent with typical values detected in many moiré graphene samples using scanning tunneling microscopy (STM) [15, 23, 107, 157]. In addition, the two-fold Landau fan degeneracy at filling $\nu = -2$, as seen in Fig. B.1, strongly suggests that our sample has strain, as the feature is not reproduced in realistic theoretical models of the flat bands unless strain is included [9]. Our Hartree-Fock calculations are performed on a 10×10 momentum mesh, and are Hartree-Fock-interpolated, using the scheme discussed in Chap. 2, to a 50×50 mesh to construct the Fermi surfaces.

Fig. 4.4 (main figure) shows the effective spin polarization of the Hartree-Fock ground state, the IKS state, in the range of fillings $\nu = -3$ to $\nu = -2$ for varying interlayer potential ΔV, which serves as a proxy for the displacement field D. This calculation does not include the effects that break the symmetry of valley-dependent spin rotations, discussed in Chap. 3.3, so the effective spin corresponds to either the physical spin or the valley-filtered spin (i.e., spin-valley locking). Nevertheless, based on the discussion in Chap. 3.3, we expect the effective spin polarization discussed here to correspond to valley-filtered spin. As shown in Fig. 4.4 (insets), the Hartree-Fock band structure below charge neutrality consists of an upper and lower IKS band in each effective spin sector. At $\nu = -3$ and small ΔV, there is a single filled lower IKS band in the "up" effective spin sector (Fig. 4.4i). At larger ΔV there is some charge transfer between the two lower IKS bands, leading to a small Fermi surface at $\nu = -3$ (Fig. 5ii) consistent with experimental observation of 'reset' behaviour at $\nu = -3$ only at small displacement fields [158, 159]. Upon doping from $\nu = -3$ towards neutrality, there are two possibilities: For small ΔV (region A of Fig. 4.4), the upper IKS band of effective spin $\uparrow$ starts filling (Fig. 4.4iv). For large ΔV (region B), the lower IKS band of effective spin $\downarrow$ starts filling (Fig. 4.4v). For $\nu > \nu^*$ (region C), the lower IKS bands in both effective spin sectors are equally occupied (Fig. 4.4vi).

The Hartree-Fock state in regions A and B only has a single effective spin flavor,

implying odd parity superconductivity. The state in region C has two effective spin flavors, which allows both even and odd parity superconductivity. The measurements in Fig. B.2a show a higher T_c in the right dome compared to the left dome. This is consistent with our theory: The pairing symmetries for the left dome (region B) are a subset of those in the right dome (region C). The higher T_c for the right dome, as well as the distinct STM signatures of the two domes [20], suggest that inter-effective spin pairing is realized in the right dome and is more robust than intra-effective spin pairing. In both these cases, the superconductivity involves the lower IKS bands. The region of suppressed superconductivity coincides with the wedge in which we find the Fermi surface to lie in an upper IKS band (region A), suggesting that this is antagonistic to the formation of strong superconductivity. Understanding the susceptibility of the upper and lower IKS band to superconductivity may shed light on the superconducting mechanism. We note that the distinction between region A and C closely parallel the first-order transition in TBG discussed in the previous section.

We conjecture that TSTG hosts two types of pairing, a relatively robust nodeless even-parity pairing and a weaker nodal odd-parity pairing that are associated respectively with the right and left domes. The even-parity pairing obeys Anderson's theorem, making it stable to moiré scale disorder, potentially explaining its robustness. Assuming an antiferromagnetic intervalley Hund's coupling (supported by Ref. [138] and our calculation in Chap. 3.3), the effective spin polarization in our analysis corresponds to opposite spin polarization in the two valleys. A future experiment with substrate-induced spin-orbit coupling, controlled by the direction of displacement field, can serve as a way to test the theory. Spin-orbit coupling should favor region A and disfavor region C, leading to a shrinking of the right dome.

Chapter 5

Chern texture insulators

In the preceding Chapters, we have been mostly concerned with correlated states that demonstrate intricate patterns of spontaneous symmetry breaking in moiré materials. In this Chapter, we would like to add in the element of topology. In particular, we consider systems where the underlying bands have non-trivial topological invariants and a correlated state that spontaneous breaks a global U(1) symmetry within these bands. We will find that, even though the original non-trivial topological invariants may not survive, the order parameter describing the symmetry-breaking will form a topologically non-trivial texture across the Brillouin zone. As the U(1) order parameter has the same symmetry as an excitonic order parameter, we call this kind of correlated insulators, "textured exciton insulators" (TEI)[1]. In this thesis, we will focus on a particular type of TEI, namely the "Chern texture insulator" (CTI), which arises from an obstruction due to underlying Chern bands. We will find that, even though such texturing is typically energetically unfavorable at strong coupling, they can be a generic non-fractionalized and translation symmetry-preserving insulating state when kinetic energy is comparable with the interaction energy. Finally, with extensive Hartree-Fock (HF) calculations, we identify several moiré materials as candidates for realizing CTIs. We further discuss possible experimental signatures of our proposals.

[1]It is called "exciton insulators" because the U(1) order parameter is equivalent to an exciton order parameter.

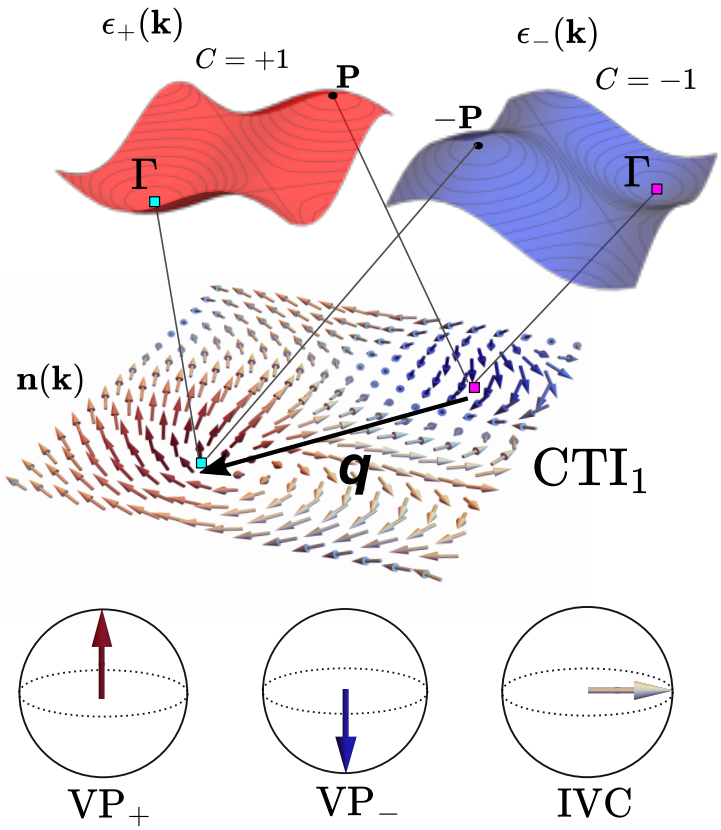


Figure 5.1: **Schematic representation of a Chern texture insulator from $C = \pm 1$ bands.** Top plots show the non-interacting band structures $\epsilon_\tau(\boldsymbol{k})$ in valley $\tau = \pm$ with Chern numbers $C_\tau = \pm 1$ and corresponding creation operators $c^\dagger_{\boldsymbol{k},\tau}$. The Γ-point, where the dispersion has its minimum, is indicated with a cyan (magenta) square in $\tau = +\ (-)$. The maximum of the dispersion is at $\tau\mathbf{P}$. Middle plot shows the momentum-dependent valley pseudospin order $\boldsymbol{n}(\boldsymbol{k})$ in the CTI_1 state at half-filling in a smooth gauge. The pseudospin order is defined by its components $n_i(\boldsymbol{k}) = \sum_{\tau,\tau'} \langle \tilde{c}^\dagger_{\boldsymbol{k},\tau} \sigma^i_{\tau,\tau'} \tilde{c}_{\boldsymbol{k},\tau'} \rangle$, where σ^i is a Pauli matrix with $i = x, y, z$, $\tilde{c}^\dagger_{\boldsymbol{k},+} = c^\dagger_{\boldsymbol{k},+}$, and $\tilde{c}^\dagger_{\boldsymbol{k},-} = c^\dagger_{\boldsymbol{k}+\boldsymbol{q},-}$. Intervalley coherence hybridizes $\boldsymbol{k}$ in $\tau = +$ with $\boldsymbol{k} + \boldsymbol{q}$ in $\tau = -$. The spiral wavevector $\boldsymbol{q}$ is influenced by kinetic energy considerations, e.g. aligning the band maximum at $\boldsymbol{P}$ in $\tau = +$ with the band minimum at Γ in $\tau = -$. Color shows the τ_z component, which is also related to the Berry curvature. $\boldsymbol{n}(\boldsymbol{k})$ is defined using a smooth gauge, which implies that the order parameter winds by 4π around the Brillouin zone due to topological considerations. Bottom plots illustrate Bloch spheres with the pseudospin $\boldsymbol{n}(\boldsymbol{k})$ corresponding to valley polarization along $\tau = +$, valley polarization along $\tau = -$, and intervalley coherence respectively. Reproduced from Ref. [139].

5.1 Theory of Chern texture insulators

We start off our discussion by introducing the simplest setting in which a textured excitonic insulator can arise, consisting of a pair of degenerate Chern bands with $C_\tau = \tau C$, distinguished by a 'valley' index $\tau = \pm 1$. Charge is separately conserved in each of the

valley ($\mathrm{U}(1)_V$), and time-reversal symmetry maps between the two valleys. As we have seen in the earlier parts of this thesis, such a valley degree of freedom is very commonly seen in moiré materials. Working at an electron density sufficient to fill one of the two bands, we would like to ask: how do interactions open a gap in this system?

Without the formation of fractional order, a gap can only be opened with the spontaneous breaking of some symmetry. Provided there is no breaking of the generalized translation symmetry[2] nor that of the total conservation of charge (i.e., superconducting order), opening up a gap requires the breaking of at least one of the two symmetries: time-reversal symmetry or $\mathrm{U}(1)_V$ [160–162]. The former can be formed by a fully valley-polarized (VP) phase, which is a Chern insulator. If $\mathrm{U}(1)_V$ is broken instead, there must be a non-zero order parameter of the form $\Delta_{\boldsymbol{k}\boldsymbol{k}'} = \langle c^\dagger_{\tau,\boldsymbol{k}} c_{-\tau,\boldsymbol{k}'} \rangle$. Assuming that the translation symmetry is not broken[3], the order parameter must be diagonal in $\boldsymbol{k}$-space, such that we may write $\Delta_{\boldsymbol{k}} = \langle c^\dagger_{\tau,\boldsymbol{k}} c_{-\tau,\boldsymbol{k}} \rangle$. It was realized that such an order parameter must have non-trivial winding in the Brillouin zone and hence must vanish at some points [163]. More precisely, define the angle of the order parameter as $\theta_{\boldsymbol{k}} = \mathrm{angle}(\Delta_{\boldsymbol{k}})$, one can show that

$$\oint_{\partial \mathrm{BZ}} \nabla_{\boldsymbol{k}} \theta_{\boldsymbol{k}} \cdot d\boldsymbol{k} = 4\pi C. \tag{5.1}$$

That is to say, the phase angle $\theta_{\boldsymbol{k}}$ must wind $4\pi C$ around the Brillouin zone. To avoid singularity, $\Delta_{\boldsymbol{k}}$ must vanish somewhere within the BZ. As such an order parameter cannot be constant in the BZ, it is argued to be energetically unfavorable in the flat-band, strong coupling limit [163–165].

As we shall see shortly, by introducing a finite bandwidth that moves the system from strong-coupling to intermediate coupling regime, a new type of $\mathrm{U}(1)_V$-breaking insulator, which we call "Chern texture insulator" (CTI) emerges under generic conditions. We can understand the state as following: the system contains two single-particle states at each point in $\boldsymbol{k}$-space. For such a two-state system, using the Bloch sphere analogy, we can define the pseudospin vector as $n_i(\boldsymbol{k}) = \sum_{\tau,\tau'} \langle c^\dagger_{\boldsymbol{k},\tau} \sigma^i_{\tau,\tau'} c_{\boldsymbol{k},\tau'} \rangle$, where σ^i is a Pauli matrix with $i = x, y, z$. As discussed, the intervalley coherent (IVC) order parameter

[2]Generalized translation symmetry is generated by the valley-dependent operator $\hat{T}_{\boldsymbol{R}} e^{i\boldsymbol{q}\cdot\boldsymbol{R}\tau/2}$.

[3]Earlier, we have only assumed that the *generalized* translation symmetry is not broken. This will be re-visited at a later discussion but is unimportant for now.

$\Delta_{\boldsymbol{k}} = \langle c^\dagger_{\tau,\boldsymbol{k}} c_{-\tau,\boldsymbol{k}} \rangle$ must vanish at some points within the BZ, which we call "nodes". At these nodes, the pseudospin vector has no component in the xy-plane, and must point along the positive or negative z-axis instead, corresponding to polarization into the + or − valleys respectively. For a typical scenario where there are two such nodes, and since we have assumed that time-reversal symmetry remains unbroken, the two nodes must be related by time-reversal. As time-reversal swaps the two valleys, the valley polarization must have the opposite signs at these two nodes. Such is the structure of the CTI, and is illustrated in Fig. 5.1. Alternatively, we may consider the case where the nodes have the same valley polarization, in which case the time-reversal symmetry must be broken and generally leads to a state with $|C| \neq 0$. We call such a state "tilted valley-polarized" (TVP) state. We can understand the stabilization of the CTI at intermediate coupling regime from the fact that finite bandwidth generally favors equal occupation of the two valleys, and interaction favors smoothly varying pseudospin vectors. This leads to a state with regions (in the BZ) of IVC forming between valley polarized regions, which is exactly what we have described as CTI.

Finally, we address the possibility to break the translation symmetry but preserves the generalized translation symmetry, which may be written as $\hat{T}_{\boldsymbol{R}} e^{i\boldsymbol{q}\cdot\boldsymbol{R}\tau/2}$ for any lattice vector $\boldsymbol{R}$ and some wavevector $\boldsymbol{q}$. Clearly, if the $\mathrm{U}(1)_V$-symmetry were not broken, preserving the translation symmetry is equivalent to preserving generalized translation symmetry with any $\boldsymbol{q}$. In our case, we are interested in states that spontaneously break the $\mathrm{U}(1)_V$-symmetry. In such a case, preserving the generalized translation symmetry $\hat{T}_{\boldsymbol{R}} e^{i\boldsymbol{q}\cdot\boldsymbol{R}\tau/2}$ implies that IVC entangles electrons at $\boldsymbol{k} - \tau\boldsymbol{q}/2$ in valley τ. This is the same idea as the finite order vector in the IKS state. In general, one can understand the optimal (i.e., ground state) $\boldsymbol{q}$ as governed by the heuristic "lobe principle" that aligns the energetic minimum in one valley with the energetic maximum in the other valley [8], as illustrated in Fig. 5.1. Indeed, the flexibility of $\boldsymbol{q}$ gives significant variational freedom for the CTI state to minimize its energy, explaining why it generally emerges as a competitive ground state in the intermediate coupling regime.

5.1.1 Topology of Chern texture insulators

In order to understand the topology of CTI, it is useful to understand the different types of topology that one encounters in band topology. The most well-established one is strong topology, whose topological invariant is stable against the inclusion of additional topologically trivial bands, and in general, they presents obstruction to symmetric Wannier orbitals. The most well known example of strong topology is that of a Chern band. A weaker form of topology is the fragile topology [30], which also demonstrates obstruction to symmetric Wannier orbitals, but is unstable against adding filled topologically trivial bands. More recently, the idea of delicate topology has been introduced [166, 167]. Unlike fragile topology, delicate topology does not present an obstruction to constructing exponentially localized Wannier orbitals, and is unstable against the inclusion of filled or unfilled bands. However, delicate topology is non-trivial in that each Wannier function cannot be completely localized to a single primitive unit cell. Which of these notions applies to the Chern texture insulator?

In Appendix C, we demonstrate that CTI state is not stable against the inclusion of additional bands, either filled or unfilled (there, we explicitly consider the example of a remote unfilled bands, but a parallel discussion can be made for the addition of remote filled bands), and it does not pose an obstruction towards forming exponentially localized Wannier orbitals as $C = 0$[4]. This rules out the possibility of it being strong or fragile topology. Nevertheless, we can demonstrate that a CTI presents an obstruction to fully localized moments, in the sense that certain correlators cannot be fully onsite for a CTI. For definiteness, consider a tight-binding formulation with lattice-site index σ and valley index τ. We label the single-particle bands with band index n and valley index τ, and we assume that, without loss of generality, that $n = 0$ corresponds to a pair of Chern bands with Chern number $C_{0,\tau} = \tau C$ for some non-zero C. We now project into this pair of bands, and consider an intervalley coherent state that is formed from these two bands, and we want to show that correlators like $\langle c^\dagger_{+\sigma}(\boldsymbol{r}) c_{-\sigma'}(\boldsymbol{r}')\rangle$ cannot be purely onsite.

[4]One may wonder if we consider the symmetries involved, whether CTI may present an obstruction to such *symmetric* Wannier orbitals. However, in our discussion, the only symmetry that is central is the $\mathrm{U}(1)_V$ symmetry (time-reversal symmetry is helpful in formulating the problem, but one can breaks it without removing the IVC nodes so it is not essential to our concept), but it has been spontaneously broken.

We can expand these real-space fermion creation operators in terms of the creation operations in the band basis, i.e.,

$$c^\dagger_{\tau\sigma}(\boldsymbol{r}) = \sum_{\boldsymbol{k}} e^{-i\boldsymbol{k}\cdot\boldsymbol{r}} u_{\tau\sigma 0} c^\dagger_{\boldsymbol{k}\tau 0} + \ldots, \tag{5.2}$$

for some $u_{\tau\sigma 0}$. Here, 0 labels the band we have projected into, and the ellipsis denotes terms that involve bands we have projected out. Now, we assume, without loss of generality, that the intervalley ordering vector $\boldsymbol{q} = 0$, and we immediately have

$$\langle c^\dagger_{+\sigma}(\boldsymbol{r}) c_{-\sigma'}(\boldsymbol{r}')\rangle = u_{+\sigma 0} u^*_{-\sigma' 0} \sum_{\boldsymbol{k}} e^{-i\boldsymbol{k}\cdot(\boldsymbol{r}-\boldsymbol{r}')} \langle c^\dagger_{\boldsymbol{k}+0} c_{\boldsymbol{k}-0}\rangle . \tag{5.3}$$

Due to the aforementioned topological obstruction, $\langle c^\dagger_{\boldsymbol{k}+0} c_{\boldsymbol{k}-0}\rangle$ must vanish at some points in the BZ and therefore cannot be constant. As such, its Fourier transform cannot be strictly local, i.e., $\langle c^\dagger_{+\sigma}(\boldsymbol{r}) c_{-\sigma'}(\boldsymbol{r}')\rangle$ cannot be purely onsite, as claimed.

In short, CTI can be understood as an obstruction to fully localized moments. Such an obstruction is similar to the notion of 'multicellularity' introduced in the context of delicate topological phases [166]. While it can be removed by mixing in remote bands (as shown in Appendix C), this is typically penalized energetically in many settings, making the delicate topological limit a good starting approximation.

5.1.2 LLL model and Chern texture insulators

We now construct an interacting model that realize CTI and its competing states. The calculations in this section were originally done by the present author's collaborator, Yves H. Kwan, in Ref. [139].

Since the basic ingredients involve a pair of Chern bands with opposite Chern numbers, we consider two flavors of electrons experiencing opposite magnetic fields, and we project out all other Landau levels to leave behind the lowest Landau levels (LLL), one for each flavor sector, which we identify with the two "valleys". More precisely, for valley $\tau = \pm$, the magnetic field is given by $\boldsymbol{B} = -\tau B\hat{z}$. We will set the magnetic length ℓ_B to 1, and choose Landau gauge $\boldsymbol{A} = -\tau Bx\hat{y}$. We note that related setups of opposite-field Landau levels have previously been considered in Refs. [163, 168–178].

We choose the (magnetic) unit cell to be squares with lattice constant $a = \sqrt{2\pi}$, corresponding to one flux per unit cell[5]. We define the magnitude of the reciprocal lattice vector (RLV) $Q = \frac{2\pi}{a} = a$, and we consider the set up on a $N_x a \times N_y a$ torus geometry. The first magnetic BZ contains momenta $\boldsymbol{k}$ such that $k_x \in [0, Q), k_y \in [0, Q)$, for both valleys. The magnetic Bloch functions, with associated creation operators $d^\dagger_{\boldsymbol{k},\tau}$,

$$\phi_{\boldsymbol{k}\tau}(\boldsymbol{r}) = \frac{1}{\sqrt{N_x}} \sum_n e^{i\tau k_x (k_y + nQ)} u_{k_y + nQ, \tau}(\boldsymbol{r}), \tag{5.4}$$

with

$$\begin{aligned} u_{k\tau}(\boldsymbol{r}) &= \frac{1}{\sqrt{\pi^{\frac{1}{2}} L_y}} e^{iky} e^{-\frac{(x - \tau k)^2}{2}} \\ k_x &= \frac{2\pi n}{N_x a}, \quad n = 0, \ldots, N_x - 1 \\ k_y &= \frac{2\pi n}{N_y a}, \quad n = 0, \ldots, N_y - 1, \end{aligned} \tag{5.5}$$

are eigenfunctions of the magnetic translation operators

$$\begin{aligned} \tilde{T}_{\tau,x} = e^{-i\tau Q y} T_x, \quad \tilde{T}_{\tau,y} = T_y \\ \phi_{\boldsymbol{k},\tau}(\boldsymbol{r} + a\hat{x}) = e^{i\tau Q y} e^{i k_x a} \phi_{\boldsymbol{k},\tau}(\boldsymbol{r}) \\ \phi_{\boldsymbol{k},\tau}(\boldsymbol{r} + a\hat{y}) = e^{i k_y a} \phi_{\boldsymbol{k},\tau}(\boldsymbol{r}) \end{aligned} \tag{5.6}$$

where T_x, T_y are ordinary translation operators (i.e. $T_x = e^{iap_x}$). The magnetic Bloch functions are defined with a *smooth* gauge that is quasi-periodic in the momentum argument $\boldsymbol{k}$,

$$\phi_{\boldsymbol{k}+Q\hat{x},\tau}(\boldsymbol{r}) = e^{i\tau k_y Q} \phi_{\boldsymbol{k},\tau}(\boldsymbol{r}), \quad \phi_{\boldsymbol{k}+Q\hat{y},\tau}(\boldsymbol{r}) = \phi_{\boldsymbol{k},\tau}(\boldsymbol{r}). \tag{5.7}$$

The anti-unitary time-reversal symmetry $\hat{\mathcal{T}}$ acts as

$$\hat{\mathcal{T}} d^\dagger_{\boldsymbol{k},\tau} \hat{\mathcal{T}}^{-1} = d^\dagger_{-\boldsymbol{k},-\tau}. \tag{5.8}$$

[5]While the shape of magnetic unit cell is arbitrary, we will soon introduce an actual potential that matches the periodicity.

Single-particle dispersion

To include a single-particle dispersion, we consider a periodic potential

$$\hat{H}_\tau^{\mathrm{SP}} = \int d\boldsymbol{r}\, V_{\mathrm{SP}}(\boldsymbol{r})\psi_\tau^\dagger(\boldsymbol{r})\psi_\tau(\boldsymbol{r}), \tag{5.9}$$

where $\psi_\tau^\dagger(\boldsymbol{r})$ is the fermion creation operator, and project the potential onto the LLLs. For a lowest-harmonic square cosine potential

$$V_{\mathrm{SP}}(\boldsymbol{r}) = -w\left(\cos\frac{2\pi x}{a} + \cos\frac{2\pi y}{a}\right), \tag{5.10}$$

the dispersion after projecting onto LLL is given by

$$\epsilon_\tau(\boldsymbol{k}) = -\frac{W}{4}(\cos k_x a + \cos k_y a), \quad W = 4we^{-\frac{\pi}{2}}, \tag{5.11}$$

which will be used in this section unless otherwise stated.

Interactions

We consider the $\mathrm{U}(1)_V$-symmetric density-density interaction

$$\hat{H}_{\mathrm{int}} = \frac{1}{2A}\sum_{\boldsymbol{q}\in\mathrm{all},\tau,\tau'} \tilde{U}_{\tau\tau'}(\boldsymbol{q}) :\rho_\tau(\boldsymbol{q})\rho_{\tau'}(-\boldsymbol{q}): \tag{5.12}$$

where $A = N_x N_y a^2$ is the system area, and $\rho_\tau(\boldsymbol{q})$ is the density operator $e^{i\boldsymbol{q}\cdot\hat{\boldsymbol{r}}}$ projected into the LLL of the relevant valley.

The interaction in the valley space is given by

$$\tilde{U}_{\tau\tau'}(\boldsymbol{q}) = \begin{pmatrix} u_0(\boldsymbol{q}) + u_1(\boldsymbol{q}) & u_0(\boldsymbol{q}) - u_1(\boldsymbol{q}) \\ u_0(\boldsymbol{q}) - u_1(\boldsymbol{q}) & u_0(\boldsymbol{q}) + u_1(\boldsymbol{q}) \end{pmatrix}_{\tau\tau'}. \tag{5.13}$$

For the isotropic component $u_0(\boldsymbol{q})$, we choose the dual gate screened interaction $u_0(\boldsymbol{q}) = 2\pi U\frac{\tanh qd_{\mathrm{sc}}}{q}$, mirroring realistic set-ups in two-dimensional materials. We also introduce a valley-anisotropic component $u_1(\boldsymbol{q})$. For simplicity, we consider an overall scaling

$$u_1(\boldsymbol{q}) = \alpha_{\mathrm{v}} u_0(\boldsymbol{q}). \tag{5.14}$$

Unless otherwise stated, we set $U = 1$.

Hartree-Fock

We will solve the model with Hartree-Fock calculations. As already discussed, the ground state may have a non-zero intervalley ordering vector $\boldsymbol{q}$. To capture it, we use the same method as discussed in Chap. 3, first developed for the IKS state. We write the order parameter as

$$\Delta_{\boldsymbol{q}}(\boldsymbol{k}) \equiv \langle d^{\dagger}_{\boldsymbol{k},+} d_{\boldsymbol{k}+\boldsymbol{q},-} \rangle. \tag{5.15}$$

5.1.3 Phase diagram

We explore the phase diagram of the LLL model with the interaction anisotropy α_{v} and the bandwidth W as parameters, as shown Fig. 5.2. All the states shown in the diagram have finite charge gaps. The broad features of the phase diagram is as following: at the lower left corner where ($\alpha_{\mathrm{v}} = W = 0$), the (fully) valley-polarized (VP) state is the ground state. As either the bandwidth W is increased, or the interaction anisotropy α_{v} is increased, the ground state transitions into the CTI state, with a sliver of TVP state in between. As Landau levels have Chern numbers ± 1, we denote the CTI state as CTI_1. Both CTI and TVP are IVC states, and we find the optimal ordering vector to be $\boldsymbol{q} = (Q/2, Q/2)$, except along the $W = 0$ axis, where all the ordering vectors are degenerate.

Let us focus on the α_{v}-axis first. At the isotropic limit, the ground state is the valley-polarized (VP) state, which is also a Chern insulator with $|C| = 1$. Increasing α_{v} corresponds to increasing the intra-valley interaction relative to the inter-valley interaction, favoring IVC over VP. This is similar to increasing the interlayer distance in quantum hall bilayer problem. However, in the typical quantum Hall bilayer problem, where the two layers experience magnetic fields in the same direction, any non-zero interlayer distance d immediate drives the state to an interlayer coherent state to minimize the charging energy [179, 180]. However, as the intervalley coherent state faces an energy penalty due to the winding of order parameter [163], there is a finite threshold for α_{v} to destabilize the VP state.

At $\alpha_{\mathrm{v}} \simeq 0.013$, the $\mathrm{U}(1)_V$ becomes spontaneously broken, leading to the TVP phase, which remains a Chern insulator with $|C| = 1$. As shown in Fig. 5.3b, IVC is developed

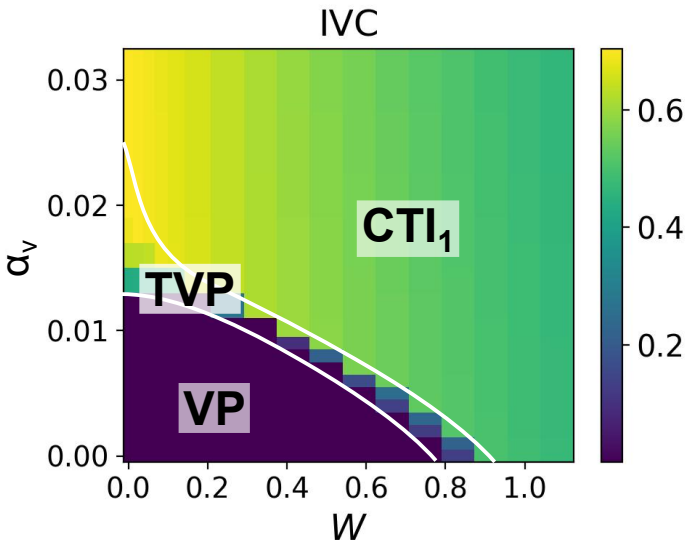


Figure 5.2: **HF phase diagram of the LLL model at half-filling.** α_v is the valley interaction anisotropy, and W is the kinetic bandwidth arising from a square cosine potential. The gate distance $d_{sc} = 6a$, and the interaction scale $U = 1$ (see Chap. 5.1.2). Color indicates the magnitude of intervalley coherence (IVC). White lines indicate approximate phase boundaries. System size is 24×24, and the valley boost is fixed to either $\boldsymbol{q} = (0, 0)$ or $(Q/2, Q/2)$. VP: valley-polarized; TVP: tilted valley-polarized; CTI_1: Chern texture insulator. Reproduced from Ref. [139].

in the entire BZ except two points, i.e. vortex cores. We see that the IVC angle winds around each vortex core by 2π, summing up to a total of 4π winding, as expected. For the TVP phase, we see that the two vortex cores are polarized into the same valley. At a larger $\alpha_v \simeq 0.025$, the valley polarization of one of the vortex cores flips direction(Fig. 5.3c), resulting in our proposed CTI_1 state.

Along the W-axis, the same series of transitions play out. Different from the case on the α_v-axis, as a real potential is introduced, different ordering vectors $\boldsymbol{q}$ are no longer equivalent. For the square cosine potential used here, the dispersion $\epsilon(\boldsymbol{k})$ has a minimum at $(0, 0)$ and a maximum at $(Q/2, Q/2)$. As the optimal ordering vector is one that aligns the maximum of one valley with the minimum with the other valley [8], ground states that break $\text{U}(1)_V$, i.e., CTI and TVP, have ordering vector $\boldsymbol{q} = (Q/2, Q/2)$. As we will see in the next section, moiré materials are potential candidates that can realize CTIs. Since the band widths are in general finite in moiré materials, while the intra-valley and inter-valley interaction naturally have the same strengths as the two valleys are not spatially separated (i.e., there is no "intervalley distance"), the W-axis is a closer proxy to actual materials.

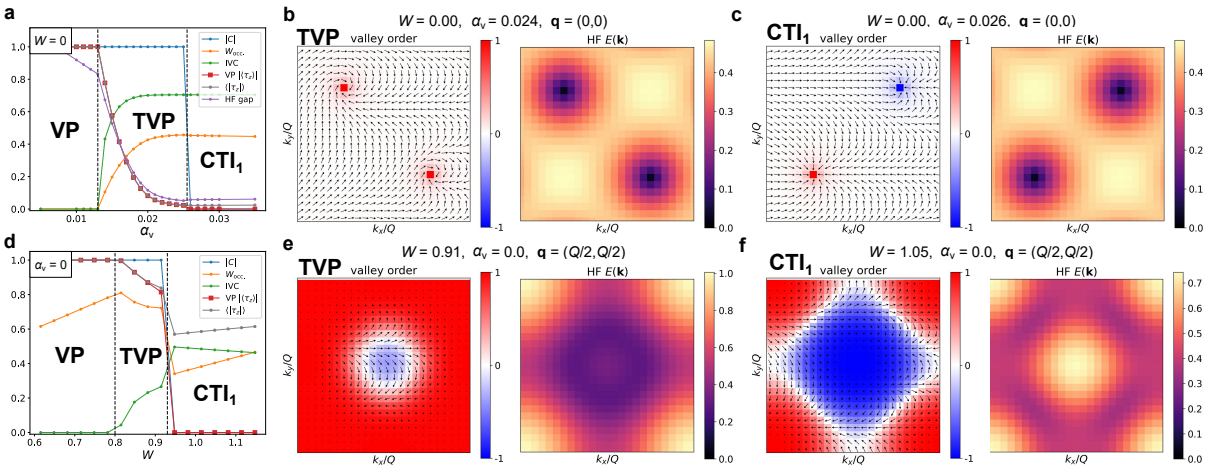


Figure 5.3: **HF phase diagram of the LLL model at half-filling along the $\alpha_{\mathbf{v}}$ and W axes.** The gate distance $d_{\mathrm{sc}} = 6a$, and the interaction scale $U = 1$. a) Phase diagram as a function of anistropy α_{v} for zero dispersion ($W = 0$). C is the Chern number, $W_{\mathrm{occ.}}$ is the bandwidth of the occupied HF valence band, IVC is intervalley coherence, and VP is valley polarization. Boost is fixed at $\boldsymbol{q} = (0, 0)$. b) Properties of a representative TVP state. Left: momentum-dependent valley order parameter. Color indicates $\langle \tau_z \rangle$, while arrows indicate in-plane order. Right: HF conduction band dispersion. The valence band has $-E(\boldsymbol{k})$ due to particle-hole symmetry. c,e,f) Same as b) except for different parameters and states. d) Same as a) except as a function of dispersion W for zero anistropy ($\alpha_{\mathrm{v}} = 0$). Boost is fixed at $\boldsymbol{q} = (Q/2, Q/2)$. System size for all plots is 24×24. Reproduced from Ref. [139].

Furthermore, we note that, while the TVP and CTI phases along the α_{v}-axis and W-axis are continuously connected, as shown in Fig. 5.2, their wavefunctions have significant quantitative differences, as shown in Fig. 5.3, due to different energetic considerations.

5.2 Chern texture insulators in moiré materials

The prototypical moiré material is the twisted bilayer graphene (TBG). However, the two-fold rotation symmetry $\hat{\mathcal{C}}_{2z}$ in TBG, together with the time reversal symmetry, forces Berry curvature to vanish in the single-particle band structure, while to realize CTI, a necessary ingredient is Chern bands. As such, we consider a number of moiré materials without $\hat{\mathcal{C}}_{2z}$ symmetry instead, and, using microscopically faithful self-consistent Hartree-Fock (HF) calculations, we demonstrate that CTIs are energetically competitive ground states in many of these materials. En route, we address the various further complications of realistic materials absent in simplified models, such as various competing orders, the interaction-induced hybridization of single-particle bands within each valley, etc. Even after incorporating these features, we find robust CTI order survives within a reasonable parameter regime across a large class of materials, as summarized in Tab. 5.1. In each of these cases, the order is linked to a moiré-scale modulation of intervalley coherence, that in several cases can potentially be directly detected through scanning probe measurements similar to those used to identify IKS order [10, 98]. Our work thus provides yet another illustration of how the combinatorial versatility of moiré systems provides fertile ground for seeking new and complex correlated states of matter with cutting-edge probes.

5.2.1 Continuum models

We perform self-consistent HF calculations on several moiré materials. To do so, we adopt modified versions of the continuum model introduced in Chap. 2. For a more compact notation, we will adopt a matrix notation to capture the layer and sublattice degrees of freedom. In the discussion of this Chapter, we will not include strain in our models.

System	$\hat{\mathcal{C}}_{2z}$-breaking	CTI$_n$ index	Phase Diag.
TDBG (ABAB)	explicit	2	Fig. 5.5
TDBG (ABBA)	explicit	$0, 1, -1$	Figs. 5.7,5.8
TMBG	explicit	0, 2	Fig. 5.10
TBTG	explicit	2	Fig. 5.11b

Table 5.1: **Chern-textured exciton insulators (CTIs) in moiré materials studied in this thesis.** The IVC order parameter winding is $4\pi n$ in the CTI$_n$ phase. For $n = 0$, the state is considered a 'trivial IVC' phase. [tMoTe$_2$: twisted bilayer MoTe$_2$; TDBG: twisted double-bilayer graphene; TMBG: twisted mono-bilayer graphene; HTG: helical trilayer graphene; TBTG: twisted double-trilayer graphene (with AB-ABA stacking order); TSTG: twisted symmetric trilayer graphene; TBG: twisted bilayer graphene].

Twisted double-bilayer graphene (ABAB)

Twisted double-bilayer graphene (TDBG) [152, 181–191] is a heterostructure consisting of two Bernal (i.e. crystallographic AB or BA stacked) graphene bilayers placed on top of each other with a twist angle θ. Owing to the presence of Bernal bilayer stacks, the system does not possess $\hat{\mathcal{C}}_{2z}$ symmetry. The ABAB and ABBA stacking configurations are inequivalent; we first consider the former stacking order. In this case, the single-particle Hamiltonian for valley K is given by $H_K = H_{K,0} + H_V$, where the Hamiltonian in the absence of external displacement fields is [165, 192–195]

$$H_{K,0} = \begin{pmatrix} H_0^A(\boldsymbol{k}_1) & g(\boldsymbol{k}_1) & & \\ g^\dagger(\boldsymbol{k}_1) & H_0^B(\boldsymbol{k}_1) & U & \\ & U^\dagger & H_0^A(\boldsymbol{k}_2) & g(\boldsymbol{k}_2) \\ & & g^\dagger(\boldsymbol{k}_2) & H_0^B(\boldsymbol{k}_2) \end{pmatrix}, \tag{5.16}$$

and we approximate the effect of an external displacement field with a linear interlayer potential[6]

$$H_V = \mathrm{diag}\left(-\frac{1}{2}I_2, -\frac{1}{6}I_2, \frac{1}{6}I_2, \frac{1}{2}I_2\right)\Delta V, \tag{5.17}$$

where I_2 is the 2×2 identity matrix in sublattice space. In Eq. 5.16, $\boldsymbol{k}_l = \boldsymbol{k} - \boldsymbol{K}_l$ is the momentum measured from the (rotated) Dirac point of layer $l = 1, 2$. With $k_\theta = \frac{8\pi}{3\sqrt{3}a_{\mathrm{CC}}}\sin(\theta/2)$ where $a_{\mathrm{CC}} = 1.42 \times 10^{-10}\,\mathrm{m}$ is the length of C-C bond, we define the

[6]For all materials considered, we model the displacement field by a linearly varying potential that differs by ΔV between the outermost layers.

primitive vectors of the moiré reciprocal lattice as $\boldsymbol{G}_1 = k_\theta(\sqrt{3}, 0)$ and $\boldsymbol{G}_2 = k_\theta(-\frac{\sqrt{3}}{2}, \frac{3}{2})$. The Dirac points of the two layers are related by $\boldsymbol{K}_1 - \boldsymbol{K}_2 = \frac{1}{3}\boldsymbol{G}_1 + \frac{2}{3}\boldsymbol{G}_2$. In Eq. 5.16, we also define

$$H_0 = v\boldsymbol{k} \cdot \boldsymbol{\sigma} \tag{5.18}$$

$$H_0^A(\boldsymbol{k}) = H_0(\boldsymbol{k}) + \frac{1}{2}(I_2 - \sigma^z)\Delta' \tag{5.19}$$

$$H_0^B(\boldsymbol{k}) = H_0(\boldsymbol{k}) + \frac{1}{2}(I_2 + \sigma^z)\Delta' \tag{5.20}$$

$$g(\boldsymbol{k}) = \begin{pmatrix} -\hbar v_4 k_- & -\hbar v_3 k_+ \\ \gamma_1 & -\hbar v_4 k_- \end{pmatrix}, \tag{5.21}$$

where $\boldsymbol{\sigma} = (\sigma^x, \sigma^y)$ are the Pauli matrices in sublattice space, v is the graphene Fermi velocity, and $k_\pm = k_x \pm ik_y$. H_0^A and H_0^B capture the physics within each layer of graphene, and g represents hopping between the two layers within each Bernal bilayer stack. The parameters are given by $\gamma_0 = 2.610$ eV, $\gamma_1 = 0.361$ eV, $\gamma_3 = 0.283$ eV, $\gamma_4 = 0.138$ eV and $\Delta' = 0.015\,\text{eV}$ [196]. The v_i's are related to the γ_i's by $v_i = \frac{3a}{2\hbar}\gamma_i$ and $v \equiv v_0$. The interlayer moiré coupling is the same as that in TBG, i.e.,

$$U = T_1 + T_2 e^{i(\boldsymbol{G}_1 + \boldsymbol{G}_2)\cdot\boldsymbol{r}} + T_3 e^{i\boldsymbol{G}_2\cdot\boldsymbol{r}}, \tag{5.22}$$

where the T_i matrices are defined in Eq. 2.9. We take $w_{AB} = 0.11$ eV, $w_{AA} = 0.08$ eV, and consider a twist angle $\theta = 1.2°$ unless otherwise specified.

The continuum Hamiltonian in valley K' is determined by $H_{K'}(\boldsymbol{k}) = H_K^*(-\boldsymbol{k})$ due to TRS. Unless otherwise stated, we assume $SU(2)_\text{s}$ spin-rotation symmetry for graphene-based materials due to the negligible spin-orbit coupling.

Twisted double-bilayer graphene (ABBA)

TDBG can also be fabricated in an alternative ABBA stacking arrangement [152, 183, 191]. Using the conventions established in the preceding subsection, the single-particle

Hamiltonian in valley K is $H_K = H_{K,0} + H_V$, where $H_{K,0}$ is given by [192, 193]

$$H_{K,0} = \begin{pmatrix} H_0^A(\boldsymbol{k}_1) & g(\boldsymbol{k}_1) & & \\ g^\dagger(\boldsymbol{k}_1) & H_0^B(\boldsymbol{k}_1) & U & \\ & U^\dagger & H_0^B(\boldsymbol{k}_2) & g^\dagger(\boldsymbol{k}_2) \\ & & g(\boldsymbol{k}_2) & H_0^A(\boldsymbol{k}_2) \end{pmatrix}, \tag{5.23}$$

and H_V is defined in Eq. 5.17. All single-particle parameters are identical to those used in the previous subsection.

Twisted monolayer-bilayer graphene

Twisted monolayer-bilayer graphene (TMBG) [197–203] is $\hat{\mathcal{C}}_{2z}$-breaking heterostructure that consists of one graphene monolayer and one Bernal graphene bilayer stacked together with a twist. Using the conventions established in Chap. 5.2.1, the single-particle Hamiltonian for TMBG in valley K is given by [193, 204]

$$H_K = \begin{pmatrix} H_0(\boldsymbol{k}_1) - \frac{1}{2}\Delta V & U & \\ U^\dagger & H_0^A(\boldsymbol{k}_2) & g(\boldsymbol{k}_2) \\ & g^\dagger(\boldsymbol{k}_2) & H_0^B(\boldsymbol{k}_2) + \frac{1}{2}\Delta V \end{pmatrix}. \tag{5.24}$$

All single-particle parameters are identical to those in Chap. 5.2.1.

Twisted bilayer-trilayer graphene

Twisted bilayer-trilayer graphene (TBTG) [205] is a $\hat{\mathcal{C}}_{2z}$-breaking heterostructure consisting of a Bernal-stacked graphene bilayer placed on top of a Bernal-stacked graphene trilayer with a twist angle θ. In this thesis, we only consider the AB-ABA stacking configuration. The single-particle Hamiltonian for valley K is given by $H_K = H_{K,0} + H_V$, where the

Hamiltonian in the absence of external displacement fields is [193, 204]

$$H_{K,0} = \begin{pmatrix} H_0^A(\boldsymbol{k}_1) & g(\boldsymbol{k}_1) & & & \\ g^\dagger(\boldsymbol{k}_1) & H_0^B(\boldsymbol{k}_1) & U & & \\ & U^\dagger & H_0^A(\boldsymbol{k}_2) & g(\boldsymbol{k}_2) & \\ & & g^\dagger(\boldsymbol{k}_2) & H_0^B(\boldsymbol{k}_2) & g^\dagger(\boldsymbol{k}_2) \\ & & & g(\boldsymbol{k}_2) & H_0^A(\boldsymbol{k}_2) \end{pmatrix}, \tag{5.25}$$

and the interlayer potential is given by

$$H_V = \mathrm{diag}\left(-\frac{1}{2}I_2, -\frac{1}{4}I_2, 0, \frac{1}{4}I_2, \frac{1}{2}I_2\right)\Delta V. \tag{5.26}$$

All single-particle parameters are identical to those in Chap. 5.2.1.

5.2.2 Twisted double-bilayer graphene (ABAB)

As shown in Fig. 5.4a, the single particle band structure of TDBG with ABAB stacking order at $\theta = 1.2°$ has well-isolated Chern bands with $|C| = 2$ under moderate interlayer potential ΔV [164, 192, 193]. Within this window of ΔV, self-consistent HF calculations at $\nu = 1, 2, 3$ find flavor-polarized strong-coupling insulators at strong interaction strengths (i.e. small relative permittivity ϵ_r), as shown in Fig. 5.5. For weaker interactions, we find a greater tendency towards gapless metallic phases. However for all the fillings investigated here, we obtain insulating CTIs for a window of finite interlayer potentials.

We now focus on $\nu = 2$, where the CTI is observed over a large region of parameter space. The behaviour of the CTI at $\nu = 2$ is identical in both spin sectors, so we only show results for one spin sector. With electron doping and well-separated conduction and valence bands, we expect the non-trivial physics to occur within the non-interacting conduction bands. As such, we define the IVC order parameter $\Delta_{\boldsymbol{q}}(\boldsymbol{k})$ as

$$\Delta_{\boldsymbol{q}}(\boldsymbol{k}) \equiv \langle c^\dagger_{\boldsymbol{k},+} c_{\boldsymbol{k}+\boldsymbol{q},-} \rangle \tag{5.27}$$

where $c^\dagger_{\boldsymbol{k}\tau}$ is the spin-up electron creation operator in the conduction band of valley τ. The order parameter, shown in Fig. 5.4d, shows vortices with 8π-winding around the

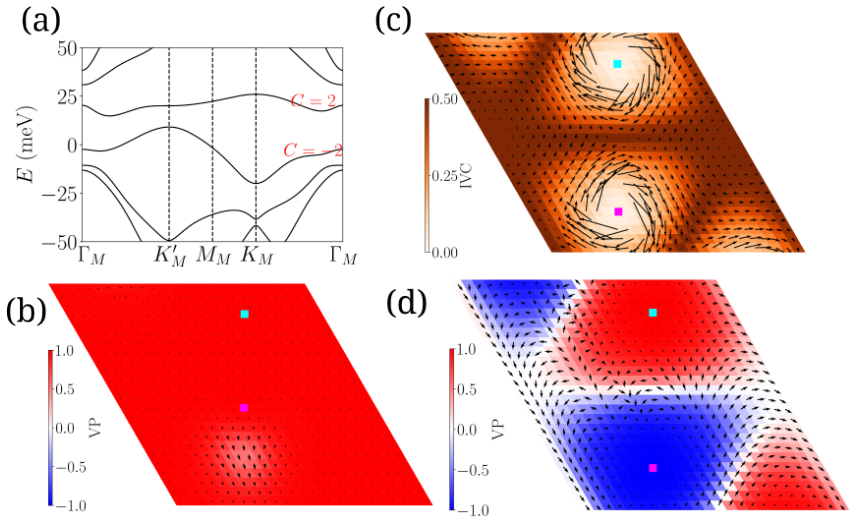


Figure 5.4: **ABAB-stacked twisted double-bilayer graphene (TDBG) at $\theta = 1.2°$.** a) Single-particle band structure at $\Delta V = 40$ meV in valley K ($\tau = +$). b) Momentum-dependent valley polarization (VP), shown as color, and intervalley coherence (IVC), shown with arrows, of the $\nu = +2$ tilted valley polarized (TVP) state at $\Delta V = 40$ meV and $\epsilon_r = 17$, from 24×24 HF. Cyan (magenta) square denotes Γ_M point of valley K (K'). We also note that TVP has incommensurate $\boldsymbol{q}$, as the minimum of the non-interacting conduction band is not at a high-symmetry momentum. c) The IVC intensity, shown as color, and gauge-invariant velocity (Eq. 5.28), shown with arrows, of the $\nu = +2$ CTI_2 at $\Delta V = 40$ meV and $\epsilon_r = 20$, from 24×24 HF. Diverging velocities very close to vortex cores are not shown. d) Same as b) except for the CTI_2 shown in c). We observe that the intervalley order winds by 8π around the mBZ, which is consistent with the Chern number difference of 4 between the conduction band in the K and K' valleys. For b,c,d), we only show the quantities in one spin sector. Reproduced from Ref. [92].

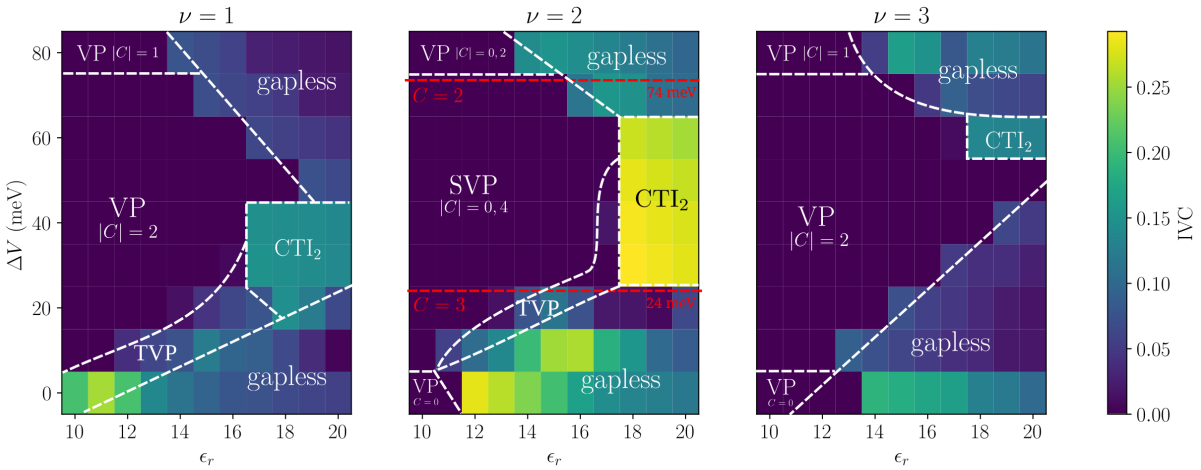


Figure 5.5: **Phase diagram of ABAB-stacked twisted double-bilayer graphene (TDBG) at $\theta = 1.2°$.** The results are obtained using 12×12 HF at $\nu = 1, 2, 3$. VP denotes valley-polarized states, which also carry a non-zero spin polarization. SVP denotes spin- or valley-polarized states, which are degenerate in HF. TVP denotes tilted valley-polarized states. Topological transitions in the non-interacting band structure are marked in red, with the Chern number labels that of the central conduction band. Reproduced from Ref. [92].

moiré Brillouin zone (mBZ), which is topologically required due to the Chern numbers $C = \pm 2$ of the constituent conduction bands. This leads us to identify the phase as a CTI$_2$. We note that the vorticity is carried by two vortices with winding number 2. While the order parameter is dependent on the gauge choice[7], we also define the gauge-independent velocity as

$$\boldsymbol{j}_{\boldsymbol{k}} = \boldsymbol{\nabla}\theta_{\boldsymbol{k}} + \boldsymbol{A}_{\boldsymbol{k},+} - \boldsymbol{A}_{\boldsymbol{k}+\boldsymbol{q},-} \tag{5.28}$$

where $\theta_{\boldsymbol{k}} = \arg(\Delta_{\boldsymbol{q}}(\boldsymbol{k}))$ is the angle of the IVC order parameter and $\boldsymbol{A}_{\boldsymbol{k}\tau} = i \langle u_{\boldsymbol{k}\tau} | \partial_{\boldsymbol{k}} u_{\boldsymbol{k}\tau} \rangle$ is the Berry-connection. As shown in Fig. 5.4c, the velocity diverges near the vortices, which is compensated by the vanishing IVC order parameter. In addition to the CTI$_2$, we have also found a sliver of the tilted valley-polarized (TVP) phase (Fig. 5.4b), which was introduced in Ref. [206].

The physics of CTI in $\nu = 1, 3$ is essentially identical to that in $\nu = 2$, except that for these odd integer fillings, IVC is only present in one of the two spin sectors (namely, the spin sector with filling factor 1 relative to its charge neutrality). We note that the interaction-induced band normalization depends on the total filling, leading to the CTI

[7] Appendix D.1 details how we implement a smooth but non-periodic gauge-fixing.

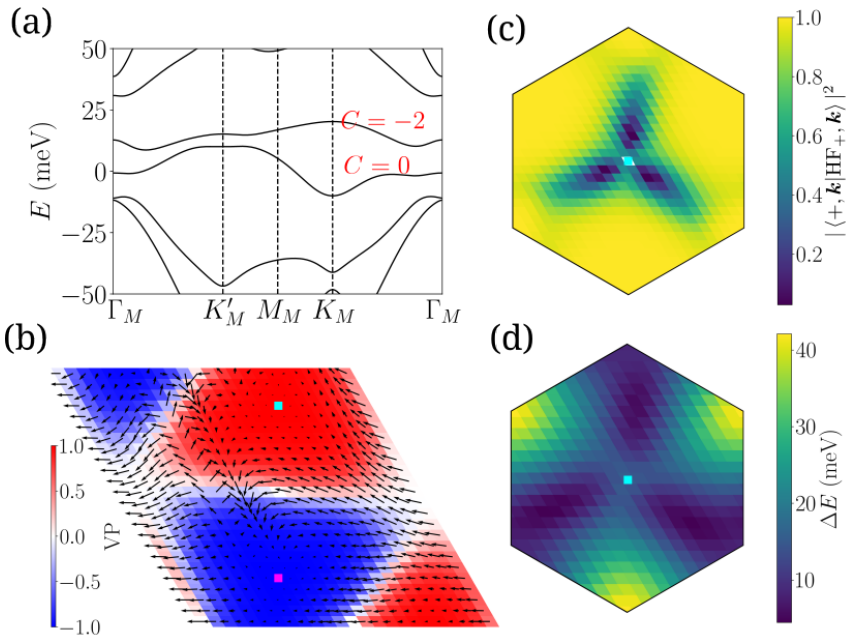


Figure 5.6: **ABBA-stacked twisted double-bilayer graphene (TDBG) at $\theta = 1.2°$.** a) Single-particle band structure at $\Delta V = 20$ meV in valley K ($\tau = +$). The two central bands are separated by a direct gap, making the Chern number well-defined for each band, but they have a negative indirect gap. b) Valley polarization (VP), shown as color, and intervalley coherence (IVC) in the valley-filtered basis, shown with arrows, of the $\nu = +2$ CTI_1 state at $\Delta V = 20$ meV and $\epsilon_r = 16$ from 24×24 HF. Cyan (magenta) square denotes the Γ_M point of valley K (K') in b,c,d). c) The momentum-resolved overlap in valley K of the valley-filtered basis in b) and the single-particle conduction basis. We observe that in some regions, the overlap vanishes due to mixing with the single-particle valence band, allowing the Chern number of the valley-filtered bands to differ from the single-particle conduction bands. d) The direct band gap between the HF valence and conduction bands in valley K for a symmetry-preserving 16×16 HF calculation at $\nu = +2$. Comparing with c), we observe that band hybridization occurs where the energy difference is small. For b,c,d), we only show the quantities in one spin sector. Reproduced from Ref. [92].

being found at different regions of parameter space for different fillings.

5.2.3 Twisted double-bilayer graphene (ABBA)

Similar to ABAB-stacked TDBG, we observe the presence of CTIs at all of $\nu = 1, 2, 3$ for ABBA-stacked TDBG (Fig. 5.7). We again focus on $\nu = +2$, which contains the largest region of gapped IVC insulators. However, we observe some complications not present in the simplest setting with just one band per valley. As discussed in the previous subsection, in the the regime where the CTI is observed in $\nu = +2$ ABAB-stacked TDBG, the conduction band is sufficiently separated from the valence band and other remote bands

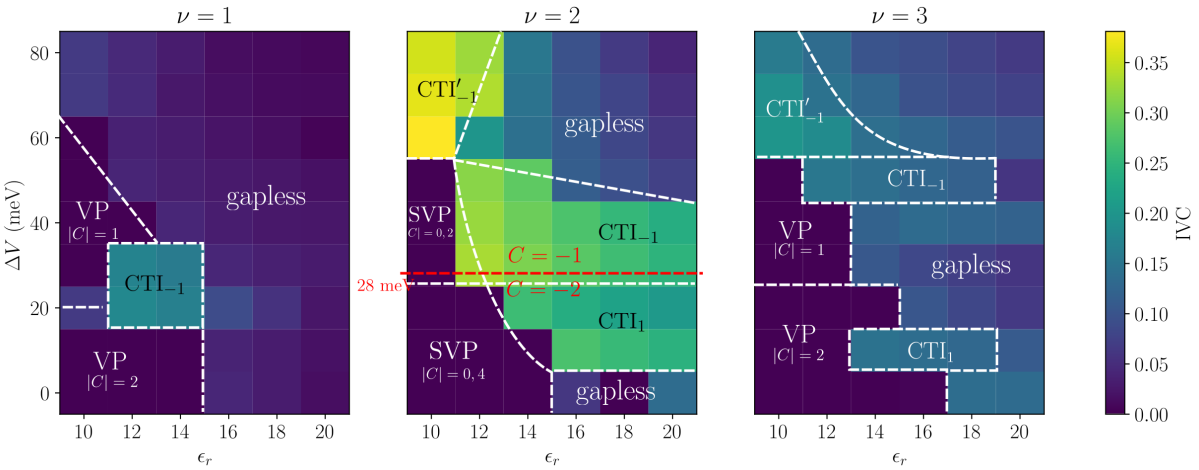


Figure 5.7: **Phase diagram of ABBA-stacked twisted double-bilayer graphene (TDBG) at $\theta = 1.2°$.** The results are obtained using 12×12 HF at $\nu = 1, 2, 3$. VP denotes valley-polarized states, which also carry a non-zero spin polarization. SVP denotes spin- or valley-polarized states, which are degenerate in HF. TVP denotes tilted-valley-polarized states. Topological transitions in the non-interacting band structure are marked in red, with the Chern number refers to that of the central conduction band. CTI′ has a different intervalley spiral wavevector $\boldsymbol{q}$ from the unprimed CTI states. Reproduced from Ref. [92].

to prevent them from participating non-trivally in the IVC. In ABBA-stacked TDBG, at a small interlayer potential of $\Delta V = 20$ meV, the central conduction bands are also topological with $|C| = 2$ [192, 193], but they can significantly mix with the central valence bands owing to the lack of clear energetic separation (Fig. 5.6a).

To understand the nature of intervalley coherent phases obtained in HF calculations in such cases, we consider the following valley-filtered basis. If the HF spectrum contains an isolated IVC band above or below E_F (within a spin sector), we can unfold this HF band $|\mathrm{HF}, \boldsymbol{k}\rangle$ into two normalized valley-diagonal bands $|\mathrm{HF}_+, \boldsymbol{k}\rangle$ and $|\mathrm{HF}_-, \boldsymbol{k}\rangle$:

$$|\mathrm{HF}, \boldsymbol{k}\rangle = \alpha(\boldsymbol{k}) \, |\mathrm{HF}_+, \boldsymbol{k}\rangle + \beta(\boldsymbol{k}) \, |\mathrm{HF}_-, \boldsymbol{k}\rangle \, . \tag{5.29}$$

For the IVC states in ABBA-stacked TDBG at $\nu = 2$, we define the valley-filtered basis using the unfilled HF band immediately above E_F in each spin sector, since it is isolated from the filled bands and higher remote conduction bands by charge gaps (the latter do not mix with the central bands in any significant way). We note that the valley-filtered basis for a CTI defined using Eq. 5.29 is ambiguous at discrete points in each valley where $|\mathrm{HF}, \boldsymbol{k}\rangle$ is fully polarized into the other valley, but this can be resolved by assuming that

the valley-filtered basis is continuous in $\boldsymbol{k}$-space. We also comment that even though we extract the valley-filtered basis from an unfilled HF band, we continue to define the order parameter as $\Delta_{\boldsymbol{q}}(\boldsymbol{k}) \equiv \langle c^\dagger_{\boldsymbol{k},+} c_{\boldsymbol{k}+\boldsymbol{q},-} \rangle$, where $c^\dagger_{\boldsymbol{k}\tau}$ are *electron* creation operators for the valley-filtered basis[8].

At $\Delta V = 20$ meV, the single-particle conduction band has Chern number $C = -2$ $(+2)$ in valley K (K'), while the valence bands are trivial. For strong interactions, HF calculations at $\nu = +2$ find flavor-polarized insulators (Fig. 5.7). For weaker interactions, we find a $\hat{\mathcal{T}}$ and $SU(2)_{\mathrm{s}}$-symmetric IVC insulator[9]. However, the corresponding valley-filtered basis is found to have $C = +1$ (-1) in valley K (K'), which differs from that of the single-particle conduction bands, and the IVC order parameter winds by 4π instead of -8π around the mBZ (Fig. 5.6b). This means that we obtain a CTI_1, instead of a CTI_{-2} that would be naïvely expected by considering the non-interacting band topology. In Fig. 5.6c, we plot the overlap of the valley-filtered band with the single-particle conduction band, which vanishes at three $\hat{\mathcal{C}}_{3z}$-related points in the mBZ. This allows the valley Chern number of the valley-filtered basis to differ from that of the single-particle conduction basis.

We note that the absolute value of the valley-filtered basis Chern number is lowered from 2 to 1. This is consistent with the notion that there is a tendency to reduce the winding (i.e. 'unfrustrate' the topological obstruction) of the order parameter, since this allows for more favorable exchange energetics. The system achieves this by substantially hybridizing with the single-particle valence band. Due to the kinetic energy penalty, such hybridization preferentially occurs at regions with small direct gap. We can roughly estimate the hybridization positions by performing symmetry-preserving HF at this filling, which partially accounts for interaction-induced renormalization effects (Fig. 5.6d). In this specific example, the hybridization occurs away from high symmetry points. This restricts the valley-filtered basis Chern number to change by multiples of 3 [207], which does not permit a full lifting of the topological frustration. For larger ΔV, we observe additional CTI_n phases, including two CTI_{-1} regions with distinct $\boldsymbol{q}$, highlighting the complex interplay between the kinetic energy and interaction effects.

[8]The hole order parameter would differ by a minus sign.

[9]Within spin-collinear HF calculations, states with different IVC angles in the two spin sectors are degenerate with $SU(2)_{\mathrm{s}}$-symmetric IVC states.

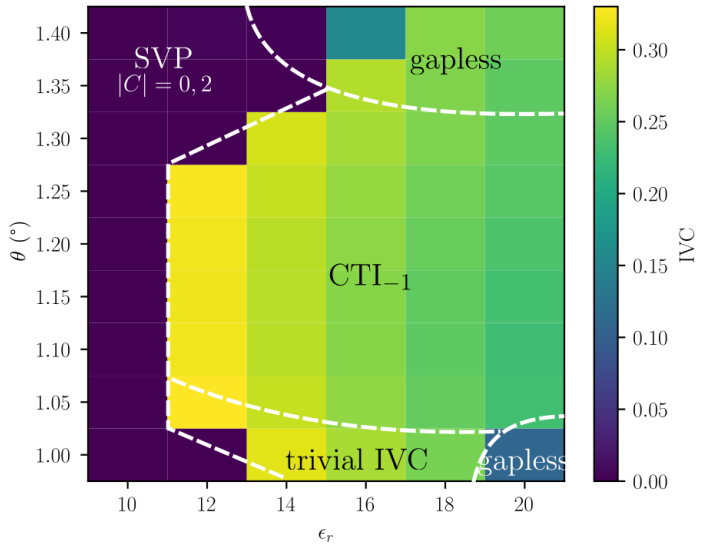


Figure 5.8: **Phase diagram of ABBA-stacked twisted double-bilayer graphene (TDBG) with variable twist angle.** The results are obtained using 12×12 HF at $\nu = 2$ and $\Delta V = 40$ meV. SVP denotes spin- or valley-polarized states, which are degenerate in HF. We observe that the CTI is stable under a range of twist angles. Reproduced from Ref. [92].

We have also performed HF calculations at $\nu = 2$ for different twist angles θ to confirm that the CTI in ABBA-stacked TDBG is stable under a range of twist angles (Fig. 5.8).

5.2.4 Twisted monolayer-bilayer graphene

Twisted monolayer-bilayer graphene (TMBG) is similar to ABAB-stacked TDBG in that it realizes an isolated conduction band with valley Chern number 2 at finite interlayer potential [193, 204] (Fig. 5.9). Its phase diagram is shown in Fig. 5.10. We find regions of CTI_2 at moderately high interlayer potential ΔV for $\nu = 1, 2$. At lower interlayer potentials, we also find a trivial IVC insulator with TRS at $\nu = 2$, where 'trivial' means that the valley-filtered bands have vanishing Chern number (Fig. 5.9c). This allows the IVC to be non-vanishing across the mBZ. For such small ΔV, the non-interacting conduction and valence bands are not isolated (Fig. 5.9a), leading to strong inter-band hybridization which alleviates the IVC obstructions.

We stress that the IVC vortices discussed so far are momentum-space vortices, which are distinct from possible vortices in the real-space IVC order parameter. We define the latter as $\Delta_f(\boldsymbol{r}) = \langle \psi^\dagger_{+,f}(\boldsymbol{r}) \psi_{-,f}(\boldsymbol{r}) \rangle$, where $+, -$ are valley labels and f indexes other

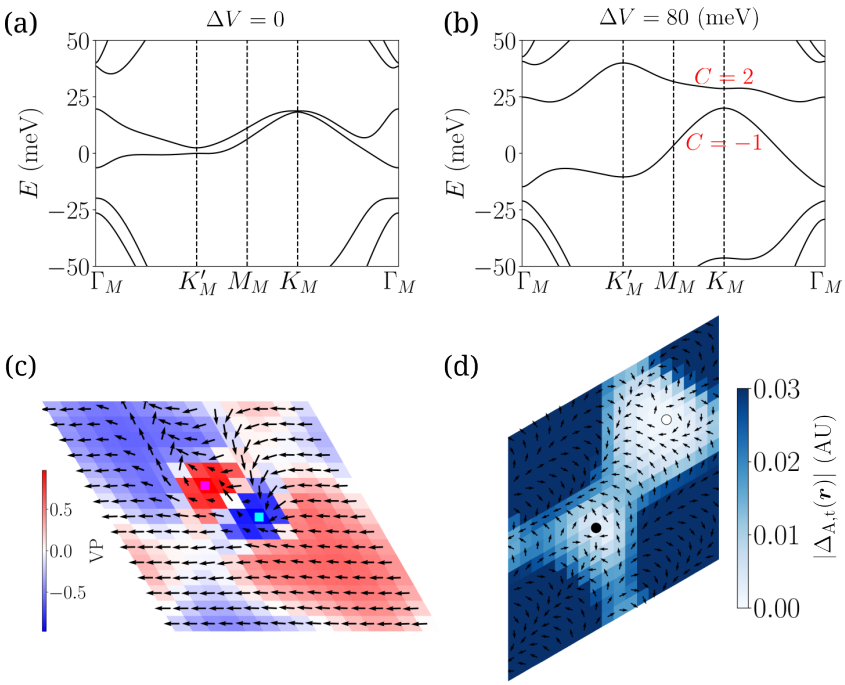


Figure 5.9: **Twisted monolayer-bilayer graphene (TMBG) at $\theta = 1.2°$.** a) Single-particle band structure at zero interlayer potential. The direct gap between the two central bands is nearly vanishing. b) At finite interlayer potential of $\Delta V = 80$ (meV), the conduction and valence bands are well-isolated with Chern numbers 2 and -1 respectively. c) The *momentum-space* valley polarization (VP), shown as color, and intervalley coherence (IVC) in the valley-filtered basis, shown with arrows, of the $\nu = +2$ trivial IVC state at $\Delta V = 0$ and $\epsilon_r = 12$ in 15×15 HF. Cyan (magenta) square denotes the Γ_M point of valley K (K'). d) The same state as in c), but showing the *real-space* IVC order parameter *within* a moiré unit cell for sublattice A on the top layer. The color shows the IVC magnitude and the arrows show the IVC phase angle, where we have subtracted off the spiral modulation due to finite $\boldsymbol{q}$. There is a vortex-antivortex pair, labelled with black and white circles. Note that the upper limit of the color scale has been clamped to show the regions near vortices more clearly. Reproduced from Ref. [92].

degrees of freedom such as sublattice or layer. For the trivial IVC state in TMBG, we consider the real-space order parameter on sublattice A of the top layer, and observe a vortex and anti-vortex within the moiré unit cell (Fig. 5.9d). Hence, we conclude that the presence or absence of real-space IVC vortices cannot be directly used to discriminate between a CTI and a trivial IVC state. However, detailed scanning of the intra-moiré cell IVC pattern is still invaluable in providing evidence for the existence of specific IVC states, as was done for the IKS in TBG in Ref. [10].

In Ref. [198], insulating states with vanishing Chern number $C = 0$ were experimentally observed in TMBG at $\nu = 1$ with finite displacement field in multiple devices with twist

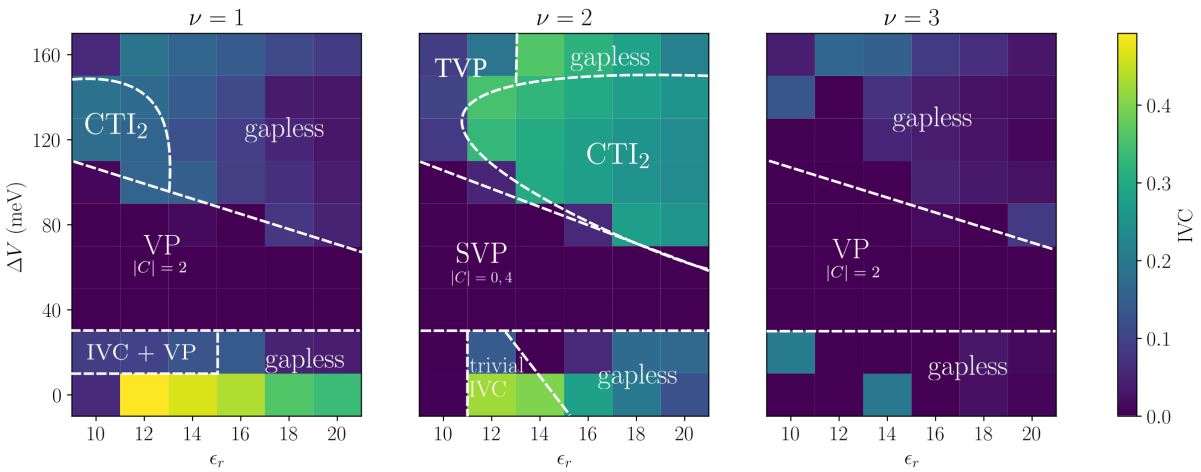


Figure 5.10: **Phase diagram of twisted monolayer-bilayer graphene (TMBG) at $\theta = 1.2°$.** The results are obtained using 12×12 HF at $\nu = 1, 2, 3$. VP denotes valley-polarized states, which also carry a non-zero spin polarization. SVP denotes spin- or valley-polarized states, which are degenerate in HF. TVP denotes tilted-valley-polarized states. IVC + VP denotes a state that is IVC in one spin sector and VP in the other spin sector. Reproduced from Ref. [92].

angles $\theta \simeq 1.1° - 1.2°$. Since a fully flavor polarized state is expected to have a non-zero Chern number due to the single-particle band structure, while the CTI states have zero Chern number, this indirectly supports a CTI state. The theoretically calculated valley magnon instability with finite momentum transfer in Ref. [198] is also consistent with the finite-$\boldsymbol{q}$ nature our proposed CTI state. Further, the experimental signature of time-reversal symmetry-breaking upon hole doping away from $\nu = 1$ [198] is consistent with our Hartree-Fock analysis [208], and does not contradict the time-reversal-symmetric nature of the state at the integer filling.

5.2.5 Twisted bilayer-trilayer graphene

In Ref. [205], the authors experimentally found insulating states with Chern number 0 at $\nu = 1$ in twisted bilayer-trilayer graphene (TBTG) with stacking order AB-ABA at $\nu = 1$ in the presence of a displacement field and a small perpendicular magnetic field. As shown in Fig. 5.11a, with applied interlayer potential, the conduction band in valley K has a Chern number of 2, suggesting that the observed Chern number 0 state cannot be a valley polarized state. On the other hand, the CTI, being time-reversal invariant, is consistent with the measurement. To investigate this, we performed HF calculations of

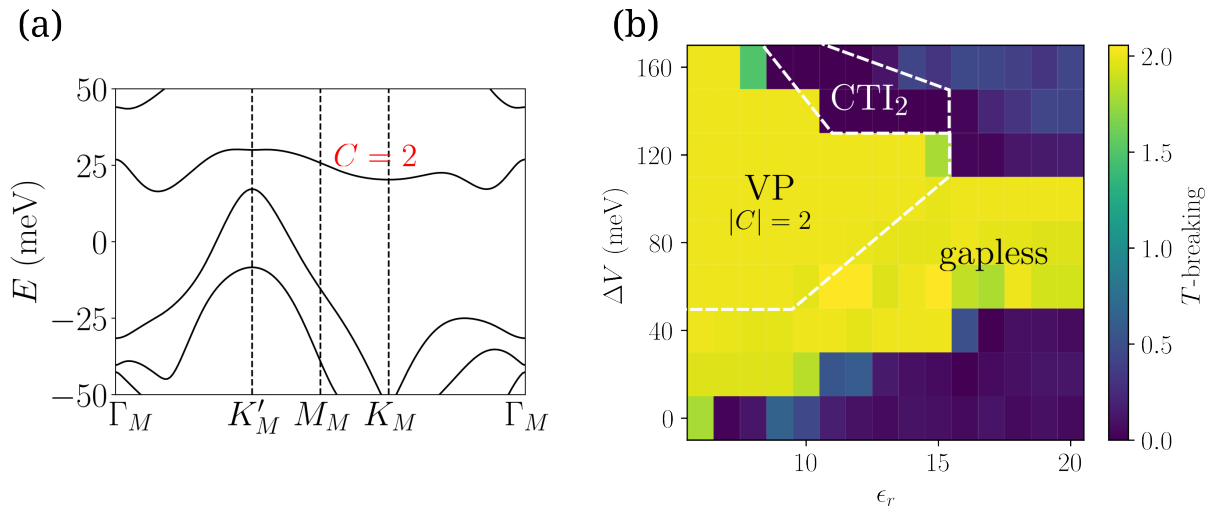


Figure 5.11: **Twisted bilayer-trilayer graphene (TBTG) at $\theta = 1.5°$.** a) Single-particle band structure at $\Delta V = 120$ meV in valley K. The valence band highly dispersive while the conduction band is moderately flat with a Chern number 2. b) Phase diagram from 12×12 HF at $\nu = 1$. VP denotes valley-polarized states, which also carry a non-zero spin polarization. Reproduced from Ref. [92].

TBTG at $\nu = 1$ without a magnetic field. We found a CTI phase with a high interlayer potential and relatively strong interaction, as shown in Fig. 5.11b, while large regions of the phase diagram shows gapless ground states. We speculate that the application of a perpendicular magnetic field, through Zeeman splitting and orbital reconstruction, is responsible for further favoring gapped CTI states over gapless states.

5.2.6 Discussion

While we have found that several moiré materials favor the formation of CTIs in realistic parameter regimes, uncertainty in the modelling of the materials, in particular the effective interaction strength parameterized by ϵ_r, precludes more detailed predictions in the absence of specific experimental details. Other single-particle effects not treated here, such as strain, would also impact the phase boundaries. We also note that our calculations assume generalized translation symmetry on the moiré scale and hence ignores possible charge density wave (CDW) orders on this scale. Future work is required to establish the energetic competition of the CTI versus various moiré-scale density wave states.

CTIs are time-reversal invariant, meaning that, unlike Chern insulators, they do not produce a quantized charge Hall response, which makes their experimental detection more

challenging. In Ref. [198], the authors detected a $C = 0$ insulating state at $\nu = 1$ in TMBG at finite interlayer potential. Since valley polarized states are expected to carry non-zero Chern numbers due to the non-interacting band topology, this provides an indirect piece of evidence for the existence of the CTI here. We note that the authors found non-vanishing anomalous Hall response at finite doping away from $\nu = 1$. An important direction therefore is to theoretically investigate whether time-reversal symmetry is broken when CTIs are doped away from integer fillings (as was studied in Ref. [9] for the IKS in TBG). In cases where time-reversal continues to be preserved, then the CTI may be a potential correlated insulating parent state that can be doped to yield superconductivity, although this seems to occur very rarely in $\hat{C}_{2z}$-breaking moiré platforms.

Due to their finite intervalley coherence, CTIs in moiré systems are expected to produce translation symmetry-breaking patterns on the *atomic* scale, such as $\sqrt{3}\times\sqrt{3}$ Kekulé charge patterns observed with scanning tunnelling microscopy in twisted graphene materials [10, 98, 124, 125]. Detection of such patterns provides supporting evidence for the existence of IVC which is necessary for CTIs. Furthermore, the spiral wavevector $\boldsymbol{q}$ can be extracted from detailed analysis of the *moiré*-scale modulation of the IVC [10, 98], which can be compared with theoretical predictions. We emphasize that, unlike the real-space IVC vortices detected in Ref. [10] *within* a moiré unit cell, the valley pseudospin texturing we have discussed for CTIs occurs in momentum space. As we have illustrated with an explicit example from TMBG, it is possible for a state without momentum space vortices (a 'trivial IVC' insulator by our criteria) to still carry vortices in the real-space IVC order parameter. Nevertheless, detailed real-space maps of the IVC texturing within a moiré cell can be fruitfully compared between experiment and theory to reinforce the interpretation of specific correlated states [10].

Chapter 6

Girvin-MacDonald-Platzman algebra

Topology features heavily in the study of moiré materials. As discussed in the introductory chapter, one of the most sought-after phenomena, the fractional quantum anomalous Hall effect (FQAHE), also known as fractional Chern insulators (FCI)[1], was first experimentally realized in moiré systems. In this Chapter, we go beyond the particular focus of moiré materials, and study the the physics of Chern bands and FCI in generality.

In the study of the fractional quantum Hall effect (FQHE), the authors of Refs. [209, 210] found that projected density operators in the lowest Landau level (LLL) satisfy a specific closed algebra, which would later be known as the Girvin-MacDonald-Platzman (GMP) algebra. It was also realized that higher Landau levels (LLs) satisfy a similar algebra with different so-called form factors, and it is such algebra with generic form factors that we call the GMP algebra here. (We present this algebra explicitly in Eqs. 6.1, 6.2 below). With kinetic energy being suppressed in Landau levels and the interaction given by density-density terms, it is understood that the GMP algebra should capture Landau level physics completely. Later on, in search of fractional Chern insulators (FCIs) [34–36], i.e. systems that host FQHE without the application of an external magnetic field, much effort was directed towards designing bands that resemble the Landau levels. Since LL physics is captured by the GMP algebra, it is deemed desirable to reproduce the GMP algebra in a Chern band, at least in some limits. In Ref. [211], the authors

[1]The two terms emphasize different aspects of the effects. FQAHE emphasizes the lack of magnetic field, while FCI emphasizes the presence of periodic potential. Some authors also consider fractional quantum Hall effects with finite magnetic field as FCI, as long as periodic potential plays a physical role. In this thesis, we treat FCI and FQAHE as identical terms.

demonstrated that to reproduce the long wavelength limit of the GMP algebra, the Berry curvature should be constant in the Brillouin zone. In Ref. [212], the author found that the necessary and sufficient condition for a band to satisfy the GMP algebra *with LLL-like form factors* involves, besides Berry curvature, an additional condition on the quantum metric of the band, which would later be known as the ideal flatband condition. (The ideal flatband condition does not apply to GMP algebra with more general form factors.)

Admittedly, there have been no experimental systems, other than Landau levels, that realize the GMP algebra exactly, and according to Ref. [213], the GMP algebra is impossible in a tight-binding model (i.e. finite number of degrees of freedom per unit cell). Nevertheless, how closely the Chern band reproduces the GMP algebra, based on Berry curvature and quantum geometry, is thought of as crucial to evaluating FCI candidates, with much theoretical efforts devoted in this direction [211, 212, 214–226]. In Ref. [227], experimental evidence supported the correlation between Berry-flatness and robustness of FCI (see also counter-arguments given in Refs. [213, 228, 229]). Furthermore, in Ref. [230], a mapping was developed between systems that satisfy the ideal flatband condition, which counts twisted bilayer graphene and other moiré materials (exactly so in the chiral limit, approximately so with more realistic parameters) as examples [204, 225, 231–235], to Landau levels, which satisfy the GMP algebra. In Ref. [236], the authors further argued that such ideal flatbands satisfy a density commutation relation that can be built up from the GMP algebra. As such, we believe systems with GMP algebra, as an idealized set-up that can be compared with and mapped to other less ideal systems, remain a highly relevant topic in the field of FCI research and beyond.

The GMP algebra was first derived for electrons in a strong magnetic field, and this is one possible closed algebra that projected density operators can obey. Though no other closed density operator algebra is known, one may nevertheless wonder if any other closed algebra exists, which may deserve equal research interest. In this Chapter, we show that *the GMP algebra in two and three dimensions, up to form factors, are the only possible closed algebra that projected density operators may satisfy*, demonstrating the unique place the GMP algebra occupies in the study of Chern bands.

6.1 Main result

For any Bloch band structure, one can define the band-projected density operator $\bar{\rho}(\boldsymbol{q}) = \mathcal{P}e^{i\boldsymbol{q}\cdot\boldsymbol{r}}\mathcal{P}$, where $\mathcal{P}$ projects to a single band. Suppose the algebra of these operators close

$$[\bar{\rho}(\boldsymbol{q}_1), \bar{\rho}(\boldsymbol{q}_2)] = f(\boldsymbol{q}_1, \boldsymbol{q}_2)\ \bar{\rho}(\boldsymbol{q}_1 + \boldsymbol{q}_2) \tag{6.1}$$

thus defining a Lie algebra. We show that in two and three dimensions, f can only have the form

$$f(\boldsymbol{q}_1, \boldsymbol{q}_2) = 2i\frac{F(\boldsymbol{q}_1)F(\boldsymbol{q}_2)}{F(\boldsymbol{q}_1 + \boldsymbol{q}_2)} \sin\left(\frac{1}{2}\boldsymbol{\Omega}\cdot(\boldsymbol{q}_1 \times \boldsymbol{q}_2)\right) \tag{6.2}$$

for some function F that satisfies $F(-\boldsymbol{q}) = F^*(\boldsymbol{q})$ and a fixed real vector $\boldsymbol{\Omega}$. Eqs. 6.1, 6.2 are known as the GMP algebra, F is known as the form factor, and $\boldsymbol{\Omega}$ will turn out to be the Berry curvature (a vector in three dimensions, and a vector normal to the plane in two dimensions).

6.2 Proof

6.2.1 Main proof

From the definition $\bar{\rho}_{\boldsymbol{q}} = \mathcal{P}e^{i\boldsymbol{q}\cdot\boldsymbol{r}}\mathcal{P}$, we can write the projected density operator in Bloch basis as

$$\bar{\rho}_{\boldsymbol{q}} = \int_{\mathrm{BZ}} d^2\boldsymbol{k}\, \langle u_{\boldsymbol{k}+\boldsymbol{q}}|u_{\boldsymbol{k}}\rangle\, |\boldsymbol{k}+\boldsymbol{q}\rangle\, \langle \boldsymbol{k}| \tag{6.3}$$

where $|\boldsymbol{k}\rangle$ denotes the Bloch state with momentum $\boldsymbol{k}$ and $|u_{\boldsymbol{k}}\rangle = e^{-i\boldsymbol{k}\cdot\boldsymbol{r}}\,|\boldsymbol{k}\rangle$ is the periodic part of the Bloch state, and the integration is over the Brillouin zone (BZ). Since we will only consider a single Bloch band, the band index has been suppressed. We will choose the gauge such that the Bloch states $|\boldsymbol{k}\rangle$ vary smoothly with $\boldsymbol{k}$, but in general they do not have Brillouin zone periodicity.

Using the orthonormality of Bloch states, we have

$$\bar{\rho}_{\boldsymbol{q}_1}\bar{\rho}_{\boldsymbol{q}_2} = \int_{\mathrm{BZ}} d^2\boldsymbol{k}\, \langle u_{\boldsymbol{k}+\boldsymbol{q}_1+\boldsymbol{q}_2}|u_{\boldsymbol{k}+\boldsymbol{q}_2}\rangle\, \langle u_{\boldsymbol{k}+\boldsymbol{q}_2}|u_{\boldsymbol{k}}\rangle\, |\boldsymbol{k}+\boldsymbol{q}_1+\boldsymbol{q}_2\rangle\, \langle \boldsymbol{k}|\,. \tag{6.4}$$

We then define

$$\tilde{f}(\boldsymbol{q}_1, \boldsymbol{q}_2; \boldsymbol{k}) = \frac{\langle u_{\boldsymbol{k}+\boldsymbol{q}_1+\boldsymbol{q}_2} | u_{\boldsymbol{k}+\boldsymbol{q}_2} \rangle \langle u_{\boldsymbol{k}+\boldsymbol{q}_2} | u_{\boldsymbol{k}} \rangle}{\langle u_{\boldsymbol{k}+\boldsymbol{q}_1+\boldsymbol{q}_2} | u_{\boldsymbol{k}} \rangle} \tag{6.5}$$

and

$$f(\boldsymbol{q}_1, \boldsymbol{q}_2)_{\boldsymbol{k}} = \tilde{f}(\boldsymbol{q}_1, \boldsymbol{q}_2; \boldsymbol{k}) - \tilde{f}(\boldsymbol{q}_2, \boldsymbol{q}_1; \boldsymbol{k}) \quad . \tag{6.6}$$

Plugging Eqs. 6.4 and 6.3 into Eq. 6.1 it is easy to establish that in order for the $\bar{\rho}_{\boldsymbol{q}}$ operators to be closed under commutation it must be the case that $f(\boldsymbol{q}_1, \boldsymbol{q}_2)_{\boldsymbol{k}}$ is $\boldsymbol{k}$-independent, so that

$$f(\boldsymbol{q}_1, \boldsymbol{q}_2)_{\boldsymbol{k}} = f(\boldsymbol{q}_1, \boldsymbol{q}_2) \quad .$$

The aim of this work is to show that if the function $f(\boldsymbol{q}_1, \boldsymbol{q}_2)_{\boldsymbol{k}}$, as defined in Eq.6.5 and 6.6, is independent of $\boldsymbol{k}$, it must take the form of Eq. 6.2.

We first consider the expression $f(\boldsymbol{q} - \boldsymbol{\epsilon}, \boldsymbol{\epsilon})_{\boldsymbol{k}}$ for small $\boldsymbol{\epsilon}$. Note that it is zero for $\boldsymbol{\epsilon} = 0$. Using the definitions Eqs. 6.5 and 6.6, we expand to first order in $\boldsymbol{\epsilon}$, and we find

$$f(\boldsymbol{q} - \boldsymbol{\epsilon}, \boldsymbol{\epsilon})_{\boldsymbol{k}} = \boldsymbol{\epsilon} \cdot \boldsymbol{G}(\boldsymbol{q})_{\boldsymbol{k}}$$

with

$$\boldsymbol{G}(\boldsymbol{q})_{\boldsymbol{k}} = i\boldsymbol{\mathcal{A}}(\boldsymbol{k} + \boldsymbol{q}) - i\boldsymbol{\mathcal{A}}(\boldsymbol{k}) + \boldsymbol{\nabla}_{\boldsymbol{k}} \log \langle u_{\boldsymbol{k}+\boldsymbol{q}} | u_{\boldsymbol{k}} \rangle \tag{6.7}$$

where we have defined the Berry connection as

$$\boldsymbol{\mathcal{A}}(\boldsymbol{k}) = -i \langle u_{\boldsymbol{k}} | \boldsymbol{\nabla}_{\boldsymbol{k}} | u_{\boldsymbol{k}} \rangle \quad .$$

For the moment, we have assumed that $\langle u_{\boldsymbol{k}+\boldsymbol{q}} | u_{\boldsymbol{k}} \rangle \neq 0$ so that its logarithm is well-defined. We will revisit the issue of possibly singularities later on.

In Ref. [211], the authors found that, in 2-dimensions,

$$[\bar{\rho}_{\boldsymbol{q}_1}, \bar{\rho}_{\boldsymbol{q}_2}] | \boldsymbol{k} \rangle \approx i\Omega(\boldsymbol{k}) \hat{z} \cdot (\boldsymbol{q}_1 \times \boldsymbol{q}_2) \bar{\rho}_{\boldsymbol{q}_1+\boldsymbol{q}_2} | \boldsymbol{k} \rangle$$

where $\Omega(\boldsymbol{k})$ is the Berry curvature at $\boldsymbol{k}$, in the limits where $\boldsymbol{q}_1$ and $\boldsymbol{q}_2$ are small. This immediately implies that for the projected density operator to be closed, Berry curvature must be constant in the Brillouin zone. The result also obviously generalizes to 3-

dimensions,

$$[\bar{\rho}_{\boldsymbol{q}_1}, \bar{\rho}_{\boldsymbol{q}_2}]|\boldsymbol{k}\rangle \approx i\boldsymbol{\Omega}(\boldsymbol{k}) \cdot (\boldsymbol{q}_1 \times \boldsymbol{q}_2)\bar{\rho}_{\boldsymbol{q}_1+\boldsymbol{q}_2}|\boldsymbol{k}\rangle \tag{6.8}$$

where $\boldsymbol{\Omega}(\boldsymbol{k}) = \boldsymbol{\nabla}_{\boldsymbol{k}} \times \boldsymbol{\mathcal{A}}(\boldsymbol{k})$ is the Berry curvature vector. For constant Berry curvature, we can write

$$\boldsymbol{\mathcal{A}}(\boldsymbol{k}) = \frac{1}{2}\boldsymbol{\Omega} \times \boldsymbol{k} + \boldsymbol{\nabla}_{\boldsymbol{k}}\phi(\boldsymbol{k})$$

for some unknown real function ϕ.

Given this form, we have

$$\boldsymbol{G}(\boldsymbol{q})_{\boldsymbol{k}} - \frac{i}{2}\boldsymbol{\Omega} \times \boldsymbol{q} = \boldsymbol{\nabla}_{\boldsymbol{k}} \left[i\phi(\boldsymbol{k}+\boldsymbol{q}) - i\phi(\boldsymbol{k}) + \log\langle u_{\boldsymbol{k}+\boldsymbol{q}}|u_{\boldsymbol{k}}\rangle\right] \tag{6.9}$$

In order for our algebra to close, $f(\boldsymbol{q}_1, \boldsymbol{q}_2)_{\boldsymbol{k}}$ must be independent of $\boldsymbol{k}$, which means the left-hand-side of Eq. 6.9 is independent of $\boldsymbol{k}$. This implies

$$i\phi(\boldsymbol{k}+\boldsymbol{q}) - i\phi(\boldsymbol{k}) + \log\langle u_{\boldsymbol{k}+\boldsymbol{q}}|u_{\boldsymbol{k}}\rangle = \boldsymbol{k} \cdot \boldsymbol{W}(\boldsymbol{q}) + Y(\boldsymbol{q}) \tag{6.10}$$

for some unknown vector function $\boldsymbol{W}$ and scalar function Y. Thus we have

$$\langle u_{\boldsymbol{k}+\boldsymbol{q}}|u_{\boldsymbol{k}}\rangle = e^{-i\phi(\boldsymbol{k}+\boldsymbol{q})+i\phi(\boldsymbol{k})+\boldsymbol{k}\cdot\boldsymbol{W}(\boldsymbol{q})+Y(\boldsymbol{q})} \quad . \tag{6.11}$$

We then substitute this result back into the definition of $\tilde{f}$ (Eq. 6.5) and note that all the factors of ϕ immediately cancel. We then have

$$\tilde{f}(\boldsymbol{q}_1, \boldsymbol{q}_2; \boldsymbol{k}) = e^{(\boldsymbol{k}+\boldsymbol{q}_2)\cdot\boldsymbol{W}(\boldsymbol{q}_1)+\boldsymbol{k}\cdot\boldsymbol{W}(\boldsymbol{q}_2)-\boldsymbol{k}\cdot\boldsymbol{W}(\boldsymbol{q}_1+\boldsymbol{q}_2)+Y(\boldsymbol{q}_1)+Y(\boldsymbol{q}_2)-Y(\boldsymbol{q}_1+\boldsymbol{q}_2)}$$

Here we recognize e^Y as being (part of) the form factor F. Now we demand $f(\boldsymbol{q}_1, \boldsymbol{q}_2)_{\boldsymbol{k}}$ in Eq. 6.6 be $\boldsymbol{k}$ independent. This then requires that

$$\boldsymbol{W}(\boldsymbol{q}_1) + \boldsymbol{W}(\boldsymbol{q}_2) - \boldsymbol{W}(\boldsymbol{q}_1 + \boldsymbol{q}_2) = 0 \tag{6.12}$$

which is Cauchy's functional equation. Given continuity of the function $\boldsymbol{W}$, the only solution is [237]

$$\boldsymbol{W}(\boldsymbol{q}) = \underline{M}\boldsymbol{q} \tag{6.13}$$

where $\underline{M}$ is some fixed matrix acting on $\boldsymbol{q}$. We then obtain

$$f(\boldsymbol{q}_1, \boldsymbol{q}_2) = \frac{\tilde{F}(\boldsymbol{q}_1)\tilde{F}(\boldsymbol{q}_2)}{\tilde{F}(\boldsymbol{q}_1 + \boldsymbol{q}_2)} \left[e^{\boldsymbol{q}_2 \cdot \underline{M} \boldsymbol{q}_1} - e^{\boldsymbol{q}_1 \cdot \underline{M} \boldsymbol{q}_2} \right]$$

with $\tilde{F} = e^Y$. The symmetric part of $\underline{M}$ can be absorbed into the form factors F by defining

$$F(\boldsymbol{q}) = \tilde{F}(\boldsymbol{q}) e^{-\frac{1}{2}\boldsymbol{q} \cdot \underline{M} \boldsymbol{q}} \tag{6.14}$$

we then have

$$f(\boldsymbol{q}_1, \boldsymbol{q}_2) = 2\frac{F(\boldsymbol{q}_1)F(\boldsymbol{q}_2)}{F(\boldsymbol{q}_1 + \boldsymbol{q}_2)} \sinh[\frac{1}{2}(\boldsymbol{q}_2 \cdot \underline{M}\boldsymbol{q}_1 - \boldsymbol{q}_1 \cdot \underline{M}\boldsymbol{q}_2)]$$

which could also be written in the form of Eq. 6.2 for some unknown constant vector $\boldsymbol{\Omega}$.

Given the form of Eq. 6.11, as $\boldsymbol{q} \to \boldsymbol{0}$, we have $Y(\boldsymbol{0}) \to 0$. Thus for small $\boldsymbol{q}_1, \boldsymbol{q}_2$, the prefactor $\frac{F(\boldsymbol{q}_1)F(\boldsymbol{q}_2)}{F(\boldsymbol{q}_1+\boldsymbol{q}_2)}$ becomes unity. Now, matching the small $\boldsymbol{q}$ limit in Eq. 6.8, we identify the unknown constant vector $\boldsymbol{\Omega}$ as the Berry curvature vector (in 2-dimension, it simply reduces to $\boldsymbol{\Omega} = \Omega\hat{z}$, where Ω is the scalar Berry curvature). That $F(\boldsymbol{q}) = F^*(-\boldsymbol{q})$ can be easily established from its construction, as elaborated in Chap. 6.2.3, and we have reached the desired result.

6.2.2 Treatment of singularities

Now we revisit the issue of possible singular behaviour in Eq. 6.7 due to vanishing $\langle u_{\boldsymbol{k}+\boldsymbol{q}} | u_{\boldsymbol{k}} \rangle$, which also leads to divergences in f. Since overlaps are smooth, we assume $\langle u_{\boldsymbol{k}+\boldsymbol{q}} | u_{\boldsymbol{k}} \rangle$ only vanishes on lower dimensional sub-manifolds. One might worry that in the space of $\boldsymbol{k}, \boldsymbol{q}$, the sub-manifold where $\langle u_{\boldsymbol{k}+\boldsymbol{q}} | u_{\boldsymbol{k}} \rangle$ vanishes could separate the space into disconnected regions. If this is true, Eq. 6.10 could have different solutions in the different regions.

Consider a region free of singularity. From Eq. 6.11, we obtain

$$\langle u_{\boldsymbol{k}} | u_{\boldsymbol{k}+\boldsymbol{q}} \rangle = e^{-i\phi(\boldsymbol{k}) + i\phi(\boldsymbol{k}+\boldsymbol{q}) + (\boldsymbol{k}+\boldsymbol{q}) \cdot \boldsymbol{W}(-\boldsymbol{q}) + Y(-\boldsymbol{q})} \quad . \tag{6.15}$$

But $\langle u_{\boldsymbol{k}}|u_{\boldsymbol{k}+\boldsymbol{q}}\rangle = \langle u_{\boldsymbol{k}+\boldsymbol{q}}|u_{\boldsymbol{k}}\rangle^*$, so comparing Eqs. 6.11 and 6.15 we have

$$e^{(\boldsymbol{k}+\boldsymbol{q})\cdot\boldsymbol{W}(-\boldsymbol{q})+Y(-\boldsymbol{q})} = e^{\boldsymbol{k}\cdot\boldsymbol{W}^*(\boldsymbol{q})+Y^*(\boldsymbol{q})} \tag{6.16}$$

Comparing the $\boldsymbol{k}$ dependence, we have $\boldsymbol{W}(-\boldsymbol{q}) = \boldsymbol{W}^*(\boldsymbol{q})$. Knowing that $\boldsymbol{W}(\boldsymbol{q}) = \underline{M}\boldsymbol{q}$ we find $\underline{M}^* = -\underline{M}$, i.e. $\boldsymbol{W}$ is purely imaginary. Thus

$$|\langle u_{\boldsymbol{k}+\boldsymbol{q}}|u_{\boldsymbol{k}}\rangle| = |e^{Y(\boldsymbol{q})}|$$

is independent of $\boldsymbol{k}$.

This means, for a fixed $\boldsymbol{q}$, in each region where $\langle u_{\boldsymbol{k}+\boldsymbol{q}}|u_{\boldsymbol{k}}\rangle$ does not vanish, $|\langle u_{\boldsymbol{k}+\boldsymbol{q}}|u_{\boldsymbol{k}}\rangle|$ must be constant. Given $\langle u_{\boldsymbol{k}+\boldsymbol{q}}|u_{\boldsymbol{k}}\rangle$ is continuous, we conclude that for a fixed $\boldsymbol{q}$, if $\langle u_{\boldsymbol{k}+\boldsymbol{q}}|u_{\boldsymbol{k}}\rangle$ is non-zero at any $\boldsymbol{k}$, it is non-zero for all $\boldsymbol{k}$. That is, the only possible singular behaviour in Eq. 6.10 is where the logarithm diverges for a sub-manifold of $\boldsymbol{q}$ and all $\boldsymbol{k}$

In the main proof above we invoked the solution to Cauchy's functional equation. The same solution (Eq. 6.13) must hold even if one allows for discontinuities or singularities in $\boldsymbol{W}(\boldsymbol{q})$ on a set of measure zero [238]. Thus, the main proof presented above holds even with singularities.

6.2.3 Properties of form factors

Starting with Eq. 6.16 and comparing the $\boldsymbol{k}$-independent component on both sides, we find that $Y(-\boldsymbol{q}) = Y^*(\boldsymbol{q}) - \boldsymbol{q}\cdot\boldsymbol{W}(-\boldsymbol{q}) = Y^*(\boldsymbol{q}) + \boldsymbol{q}\cdot\underline{M}\boldsymbol{q}$. From Eq. 6.14 we have

$$F(\boldsymbol{q}) = e^{Y(\boldsymbol{q})-\frac{1}{2}\boldsymbol{q}\cdot\underline{M}\boldsymbol{q}}$$

This means

$$\begin{aligned} F(-\boldsymbol{q}) &= e^{Y(-\boldsymbol{q})-\frac{1}{2}\boldsymbol{q}\cdot\underline{M}\boldsymbol{q}} = e^{Y^*(\boldsymbol{q})+\frac{1}{2}\boldsymbol{q}\cdot\underline{M}\boldsymbol{q}} \\ &= e^{Y^*(\boldsymbol{q})-\frac{1}{2}\boldsymbol{q}\cdot\underline{M}^*\boldsymbol{q}} = F^*(\boldsymbol{q}) \end{aligned}$$

where we have used $\underline{M}^* = -\underline{M}$. As such, we have established $F(-\boldsymbol{q}) = F^*(\boldsymbol{q})$.

6.3 Further Results

6.3.1 Constrain on multiplication algebras

We can also consider closed multiplication algebras

$$\bar{\rho}_{\boldsymbol{q}_1}\bar{\rho}_{\boldsymbol{q}_2} = \tilde{f}(\boldsymbol{q}_1, \boldsymbol{q}_2)\bar{\rho}_{\boldsymbol{q}_1+\boldsymbol{q}_2} \quad .$$

Obviously this implies a closed commutator algebra.

Landau levels do indeed satisfy such a closed multiplication algebra as well as the closed commutation algebra. This is not a coincidence. From the form of Eq. 6.12 we also obtain the most general form of $\tilde{f}$, independent of $\boldsymbol{k}$. That is, projected density operators that are closed under commutation are also closed under multiplication.

6.3.2 Condition of constant quantum geometry tensor

The quantum geometry tensor is defined as

$$Q^{ab}(\boldsymbol{k}) = \langle \partial_{k_a} u_{\boldsymbol{k}} | Q_{\boldsymbol{k}} | \partial_{k_b} u_{\boldsymbol{k}} \rangle \tag{6.17}$$

where $Q_{\boldsymbol{k}} = 1 - |u_{\boldsymbol{k}}\rangle \langle u_{\boldsymbol{k}}|$. Its symmetric part is the quantum metric tensor while its anti-symmetric part is the Berry curvature. Assuming a GMP algebra, it is easy to use Eq. 6.11 to establish that the $Q_{ab}(\boldsymbol{k})$ must also be independent of $\boldsymbol{k}$. (This result was known for GMP algebra with LLL-like form factors previously [212] but, to our knowledge, not more generally.) We emphasize that the converse is not true: a band with both constant Berry curvature and constant quantum metric tensor is not necessarily GMP. An example of this is explicitly constructed below:

Consider Landau levels on a torus or infinite plane. We choose unit cell dimensions a_x, a_y such that $a_x a_y$ encloses one magnetic flux quantum. Define $\boldsymbol{a}_1 = (a_x, 0)$ and $\boldsymbol{a}_2 = (0, a_y)$, and the magnetic translation by $\boldsymbol{R}$ is denoted by $t_{\boldsymbol{R}}$ with $t_{-\boldsymbol{R}} = t_{\boldsymbol{R}}^\dagger$. The usual Landau level Hamiltonian is denoted $H_0 = \hbar\omega_c(a^\dagger a + \frac{1}{2})$, where $a^\dagger$ is the Landau level raising operator and ω_c is the cyclotron frequency. We use units where the magnetic length $l_B \equiv 1$ and $\hbar \equiv 1$.

We consider a system with a three-state pseudo-spin degree of freedom. Denoting $t \equiv t_{2\boldsymbol{a}_1}$ for simplicity, we consider the following Hamiltonian

$$\begin{pmatrix} H_0 + \frac{1}{2}(t+t^\dagger)\epsilon_0 & \frac{i}{\sqrt{2}}(t-t^\dagger)a\epsilon_0 & \left(-1+\frac{1}{2}(t+t^\dagger)\right)\frac{1}{\sqrt{2}}a^2\epsilon_0 \\ \frac{i}{\sqrt{2}}(t-t^\dagger)a^\dagger\epsilon_0 & H_0 - \omega_c - (1+t+t^\dagger)\epsilon_0 & \frac{i}{2}(t-t^\dagger)a\epsilon_0 \\ \left(-1+\frac{1}{2}(t+t^\dagger)\right)\frac{1}{\sqrt{2}}(a^\dagger)^2\epsilon_0 & \frac{i}{2}(t-t^\dagger)a^\dagger\epsilon_0 & H_0 - 2\omega_c + \frac{1}{2}(t+t^\dagger)\epsilon_0 \end{pmatrix}$$

This Hamiltonian has a flat band at $E = \frac{1}{2}\omega_c - 3\epsilon_0$, with the periodic parts of its wavefunctions given by (assuming ω_c and ϵ_0 are chosen to avoid accidental degeneracy)

$$u_{\boldsymbol{k}}(\boldsymbol{r}) = \begin{pmatrix} \sin(k_x a_x) u_{0\boldsymbol{k}}(\boldsymbol{r})/\sqrt{2} \\ \cos(k_x a_x) u_{1\boldsymbol{k}}(\boldsymbol{r}) \\ \sin(k_x a_x) u_{2\boldsymbol{k}}(\boldsymbol{r})/\sqrt{2} \end{pmatrix}$$

where $u_{n,\boldsymbol{k}}$ is the periodic part of the usual n-th Landau level wavefunction. (In the context of Landau levels, we understand "periodic" as invariant under *magnetic* translation operators.) We can show that (using the same convention as Ref. [222])

$$\langle u_{\boldsymbol{k}+\boldsymbol{q}} | u_{\boldsymbol{k}} \rangle = e^{-\boldsymbol{q}^2/4} e^{iq_x(k_y+q_y/2)} \left[\cos(q_x a_x) \left(1 - \frac{\boldsymbol{q}^2}{2}\right) + \frac{1}{16} \sin\left((k_x+q_x)a_x\right) \sin(k_x a_x) \boldsymbol{q}^4 \right]$$

where we have used the fact that $\langle u_{n,\boldsymbol{k}+\boldsymbol{q}} | u_{n,\boldsymbol{k}} \rangle = e^{-\boldsymbol{q}^2/4} e^{iq_x(k_y+q_y/2)} L_n(q^2/2)$ with L_n being the Laguerre polynomial.

It can be verified straightforwardly that the quantum geometry tensor (Eq. 6.17) is $\boldsymbol{k}$-independent for the band constructed above, given by

$$\underline{Q} = \begin{pmatrix} 5/2 & i/2 \\ -i/2 & 3/2 \end{pmatrix}$$

This means that both the Berry curvature and the quantum metric tensor are flat. However, due to the non-trivial $\boldsymbol{k}$-dependence in the $\boldsymbol{q}^4$ term in Eq. 6.18, $f(\boldsymbol{q}_1, \boldsymbol{q}_2)_{\boldsymbol{k}}$ is not $\boldsymbol{k}$-independent, and the density algebra is not closed. This example shows that flat quantum geometry tensor is not a sufficient condition for closed density algebra, and it reflects that quantum geometry is a long wavelength behaviour which does not fix the

behaviour of the system at all momentum scales. (Unless the quantum metric tensor satisfies a more restrictive condition on its determinant, which leads to GMP algebra with LLL-like form factors at all momentum scales [212]. This special case does not apply to GMP algebra with general form factors.)

Suppose we consider the following Hamiltonian instead

$$\begin{pmatrix} H_0 + (t+t^\dagger)\epsilon_0 & i(t-t^\dagger)\epsilon_0 \\ i(t-t^\dagger)\epsilon_0 & H_0 - (t+t^\dagger)\epsilon_0 \end{pmatrix}$$

It has a flat band at $E = \frac{3}{2}\omega_c - 2\epsilon_0$, with the periodic parts of its wavefunctions given by (assuming $4\epsilon \neq n\omega_c$ for any integer n to avoid accidental degeneracy)

$$\tilde{u}_{\boldsymbol{k}}(\boldsymbol{r}) = \begin{pmatrix} \sin(k_x a_x) u_{1\boldsymbol{k}}(\boldsymbol{r}) \\ \cos(k_x a_x) u_{1\boldsymbol{k}}(\boldsymbol{r}) \end{pmatrix}$$

The overlaps are given by

$$\langle \tilde{u}_{\boldsymbol{k}+\boldsymbol{q}} | \tilde{u}_{\boldsymbol{k}} \rangle = e^{-\boldsymbol{q}^2/4} e^{iq_x(k_y+q_y/2)} \cos(q_x a_x) \left(1 - \frac{\boldsymbol{q}^2}{2}\right)$$

which is the same as Eq. 6.18 but without the $\boldsymbol{q}^4$ term. The quantum geometry tensor is identical with the previous example, but the generalized GMP algebra will be obeyed. This shows that knowledge about quantum geometry tensor is generally insufficient for diagnosing in general whether the GMP algebra holds.

Chapter 7

Conclusions

Spontaneous symmetry breaking is an extensively studied topic in condensed matter physics. Due to the large number of flavor degrees of freedom, a wide variety of competing orders are usually possible in moiré materials, and it requires careful numerical computations to determine the correct ground states. One example is the incommensurate Kekulé spiral (IKS) state in twisted bilayer graphene and related materials, which breaks the valley U(1) symmetry and the translation symmetry, but preserves a set of combined symmetries of translation and U(1) rotation. In Chapter 3, using self-consistent Hartree-Fock, we investigate the relevance of this phase of matter in twisted symmetric trilayer graphene (TSTG), which shares similarities with TBG, but has more tunability and more complicated band structure. In our work, besides finding IKS states in TSTG in some regime, we also find a commensurate counterpart of the IKS state that also breaks an additional discrete symmetry. Delving deeper into the properties of IKS states, we determine their actual spin structure in TBG by including symmetry breaking perturbations such as coupling to intervalley phonons that are relevant in actual materials but are usually neglected in previous works, with implication for the collective modes spectra.

Focusing on the properties of metallic states, in Chapter 4, we investigate symmetry and Fermi surfaces of doped IKS in TBG, with a particular emphasis on the filling range $-3 < \nu < -2$. We uncover a first order transition that divides this range of filling into two regimes, with different implications for the symmetries of superconducting order that could potentially descend from these normal states. We proceed to consider the case of TSTG, where the enlarged parameter space allows for the experimental discovery of double-dome

superconductivity. By examining the normal ground states of TSTG, we find that isospin transitions between different IKS states have a strong impact on the fermi surfaces in TSTG and can help explain the observed double-dome superconductivity.

In Chapter 5, we propose and study a new type of insulating states termed Chern texture insulators (CTI), which are correlated insulators that break some U(1) symmetry in a system with underlying Chern bands. We find CTI to show non-trivial structure, such as non-zero winding and node formation, of the relevant order parameter in the momentum space. We further find that the resulting topology has the subtle property of being "delicate", in that it is unstable upon the inclusion of additional bands. Nevertheless, we demonstrate that such insulators have non-trivial properties such as obstruction to the trivial atomic limit. While the above discussion can be formulated generally without reference to any specific material, the most natural place where the set-up can be realized is in moiré materials. Various moiré materials have the non-trivial topological invariants required, and with extensive Hartree-Fock calculations, we find plenty of them can potentially host CTI.

In the theoretical study of fractional quantum Hall effect (FQHE) and fractional Chern insulators (FCI), one frequently discussed concept is the Girvin-MacDonald-Platzman (GMP) algebra, which is a set of commutation relations satisfied by density operator projected into Landau levels. They govern the properties of partially filled Landau levels under density-to-density interaction (which give rise to FQHE), and several proposed quantum-geometric criteria on the stability of FCI are closely related to this set of algebra. In Chapter 6, we prove that the GMP algebra, up to form factors, is the only closed algebra that projected density operators can satisfy in two and three dimensions, highlighting the central place it occupies in the study of Chern bands in general. We also find that, while closed algebra implies uniform quantum geometry, the converse is not true, which we demonstrate with an explicit counter-example.

Appendix A

Superconducting order parameter from IVC Fermi surfaces

In this section, we discuss the symmetry of the superconducting order parameters that can form from IKS parent states. For convenience, we absorb $\boldsymbol{q}_{\text{IKS}}$ into the definition of momentum.

A.1 Spin polarized IKS

The following discussion is relevant to IKS at $-3 < \nu < \nu_c$ but with ferromagnetic intervalley Hund's coupling. Consider a spin polarized IVC system. Within the non-trivial spin sector (we suppress the spin index for brevity), we have a Fermi surface where the corresponding band (which we call band 1) is described by the creation operator

$$c_1^\dagger(\boldsymbol{k}) = \frac{1}{\sqrt{2}}(e^{-i\varphi_{\boldsymbol{k}}/2}c_K^\dagger(\boldsymbol{k}) + e^{i\varphi_{\boldsymbol{k}}/2}c_{K'}^\dagger(\boldsymbol{k})) \tag{A.1}$$

where $\varphi_{\boldsymbol{k}}$ is some function of $\boldsymbol{k}$. Suppose the system has some spinless time-reversal symmetry that acts as

$$\mathcal{T}c_\tau^\dagger(\boldsymbol{k})\mathcal{T}^{-1} = c_{\bar{\tau}}^\dagger(-\boldsymbol{k}). \tag{A.2}$$

We also assume that the IVC state does not spontaneously break this time-reversal symmetry, such that

$$\mathcal{T}c_1^\dagger(\boldsymbol{k})\mathcal{T}^{-1} = c_1^\dagger(-\boldsymbol{k}). \tag{A.3}$$

This immediately implies

$$\varphi_{-\boldsymbol{k}} = \varphi_{\boldsymbol{k}}. \tag{A.4}$$

We can also define the orthogonal IVC band to be

$$c_2^\dagger(\boldsymbol{k}) = \frac{1}{\sqrt{2}}(e^{-i\varphi_{\boldsymbol{k}}/2}c_K^\dagger(\boldsymbol{k}) - e^{i\varphi_{\boldsymbol{k}}/2}c_{K'}^\dagger(\boldsymbol{k})). \tag{A.5}$$

We can invert the relation to find

$$\begin{pmatrix} c_K^\dagger(\boldsymbol{k}) \\ c_{K'}^\dagger(\boldsymbol{k}) \end{pmatrix} = \frac{1}{\sqrt{2}} \begin{pmatrix} e^{i\varphi_{\boldsymbol{k}}/2} & e^{i\varphi_{\boldsymbol{k}}/2} \\ e^{-i\varphi_{\boldsymbol{k}}/2} & -e^{-i\varphi_{\boldsymbol{k}}/2} \end{pmatrix} \begin{pmatrix} c_1^\dagger(\boldsymbol{k}) \\ c_2^\dagger(\boldsymbol{k}) \end{pmatrix}. \tag{A.6}$$

Suppose IVC band 1 undergoes superconducting pairing with

$$\Delta_1(\boldsymbol{k}) = \langle c_1^\dagger(\boldsymbol{k})c_1^\dagger(-\boldsymbol{k})\rangle = -\Delta_1(-\boldsymbol{k}). \tag{A.7}$$

In the valley basis, we define the SC order parameter as

$$[\Delta_{\boldsymbol{k}}]_{\tau\tau'} = \langle c_\tau^\dagger(\boldsymbol{k})c_{\tau'}^\dagger(-\boldsymbol{k})\rangle\,. \tag{A.8}$$

We find

$$\Delta_{\boldsymbol{k}} = \frac{1}{2} \begin{pmatrix} e^{i\varphi_{\boldsymbol{k}}} & 1 \\ 1 & e^{-i\varphi_{\boldsymbol{k}}} \end{pmatrix} \Delta_1(\boldsymbol{k}) \tag{A.9}$$

where we have used $\varphi_{-\boldsymbol{k}} = \varphi_{\boldsymbol{k}}$ to simplify the expression. Note that $\Delta_{\boldsymbol{k}} = -\Delta_{-\boldsymbol{k}}^T$, as expected from fermionic statistics.

Borrowing standard notation for triplet superconductivity and treating the valley index as a pseudo-spin index, we can write

$$\Delta_{\boldsymbol{k}} = i(\boldsymbol{d}_v(\boldsymbol{k}) \cdot \boldsymbol{\tau})\tau_y \tag{A.10}$$

(where the subscript v is meant to emphasize that the vector is in valley space instead of

physical spin space) with

$$\boldsymbol{d}_v(\boldsymbol{k}) = \frac{1}{2}\Delta_1(\boldsymbol{k}) \begin{pmatrix} -i\sin\varphi_{\boldsymbol{k}} \\ -i\cos\varphi_{\boldsymbol{k}} \\ 1 \end{pmatrix} \tag{A.11}$$

satisfying $\boldsymbol{d}_v(\boldsymbol{k}) = -\boldsymbol{d}_v(-\boldsymbol{k})$.

We note that this is "non-unitary", in the sense that

$$\boldsymbol{q}_v \equiv i\boldsymbol{d}_v \times \boldsymbol{d}_v^* = \frac{1}{2}|\Delta_1(\boldsymbol{k})|^2 \begin{pmatrix} \cos\varphi_{\boldsymbol{k}} \\ -\sin\varphi_{\boldsymbol{k}} \\ 0 \end{pmatrix} \tag{A.12}$$

is non-zero. Being non-unitary indicates a preferred direction in the valley space. This is expected, since the parent state breaks the valley U(1) symmetry.

If we were to express the order parameter in the full basis $(c^\dagger_{K,\uparrow}, c^\dagger_{K,\downarrow}, c^\dagger_{K',\uparrow}, c^\dagger_{K',\downarrow})$, we have

$$\Delta_{\boldsymbol{k}} = \frac{1}{2} \begin{pmatrix} e^{i\varphi_{\boldsymbol{k}}} & 0 & 1 & 0 \\ 0 & 0 & 0 & 0 \\ 1 & 0 & e^{-i\varphi_{\boldsymbol{k}}} & 0 \\ 0 & 0 & 0 & 0 \end{pmatrix} \Delta_1(\boldsymbol{k}). \tag{A.13}$$

or, in $\boldsymbol{d}$-vector formalism,

$$\Delta_{\boldsymbol{k}} = \left(\frac{1+s_z}{2}\right) i(\boldsymbol{d}_v(\boldsymbol{k})\cdot\boldsymbol{\tau})\tau_y \tag{A.14}$$

In this discussion, we find the pairing is purely "triplet" in valley index. This is a result of assuming maximum IVC (i.e. no valley polarization at any $\boldsymbol{k}$-point). Consider a more general parameterization

$$c_1^\dagger(\boldsymbol{k}) = \alpha_{\boldsymbol{k}} c_K^\dagger(\boldsymbol{k}) + \beta_{\boldsymbol{k}} c_{K'}^\dagger(\boldsymbol{k}) \tag{A.15}$$

with $|\alpha_{\boldsymbol{k}}|^2 + |\beta_{\boldsymbol{k}}|^2 = 1$. Time-reversal symmetry now demands

$$\alpha_{-\boldsymbol{k}} = \beta_{\boldsymbol{k}}^*, \quad \beta_{-\boldsymbol{k}} = \alpha_{\boldsymbol{k}}^* \tag{A.16}$$

and we find, in the basis of $(c^\dagger_{K\uparrow}, c^\dagger_{K'\downarrow})$,

$$\Delta_{\boldsymbol{k}} = \begin{pmatrix} \alpha^*_{\boldsymbol{k}}\beta_{\boldsymbol{k}} & |\alpha_{\boldsymbol{k}}|^2 \\ |\beta_{\boldsymbol{k}}|^2 & \alpha_{\boldsymbol{k}}\beta^*_{\boldsymbol{k}} \end{pmatrix} \Delta_1(\boldsymbol{k}). \tag{A.17}$$

In general, if $|\alpha_{\boldsymbol{k}}|^2 \neq |\beta_{\boldsymbol{k}}|^2$, the order parameter has a mixture of "singlet" and "triplet" characters.

A.2 Spin-valley locked IKS

The following discussion is relevant to IKS at $-3 < \nu < \nu_c$ with the expected anti-ferromagnetic intervalley Hund's coupling. Consider a spin-valley locked IVC system, which we can assume to be non-trivial only in the $s_z\tau_z = +1$ sector. We have an IVC band described by

$$c^\dagger_1(\boldsymbol{k}) = \frac{1}{\sqrt{2}}(e^{-i\varphi_{\boldsymbol{k}}/2}c^\dagger_{K\uparrow}(\boldsymbol{k}) + e^{i\varphi_{\boldsymbol{k}}/2}c^\dagger_{K'\downarrow}(\boldsymbol{k})). \tag{A.18}$$

We will consider a time-reversal-symmetry-like operator that acts as

$$\mathcal{T}' c^\dagger_{K\uparrow}(\boldsymbol{k})\mathcal{T}'^{-1} = c^\dagger_{K'\downarrow}(-\boldsymbol{k}) \tag{A.19}$$

$$\mathcal{T}' c^\dagger_{K'\downarrow}(\boldsymbol{k})\mathcal{T}'^{-1} = c^\dagger_{K\uparrow}(-\boldsymbol{k}). \tag{A.20}$$

We note that this operator is not the physical spinful time-reversal operator, as $\mathcal{T}'^2 = +1$, but this is the relevant operator for the case of anti-ferromagnetic IKS.

The discussion in the preceding section follows similarly, by simply replacing $c^\dagger_{K'\uparrow}$ with $c^\dagger_{K'\downarrow}$. In the basis $(c^\dagger_{K,\uparrow}, c^\dagger_{K,\downarrow}, c^\dagger_{K',\uparrow}, c^\dagger_{K',\downarrow})$, the superconducting order parameter is given by

$$\Delta_{\boldsymbol{k}} = \frac{1}{2}\begin{pmatrix} e^{i\varphi_{\boldsymbol{k}}} & 0 & 0 & 1 \\ 0 & 0 & 0 & 0 \\ 0 & 0 & 0 & 0 \\ 1 & 0 & 0 & e^{-i\varphi_{\boldsymbol{k}}} \end{pmatrix} \Delta_1(\boldsymbol{k}) \tag{A.21}$$

where $\Delta_1(\boldsymbol{k}) = \langle c^\dagger_1(\boldsymbol{k})c^\dagger_1(-\boldsymbol{k})\rangle$. We can write this as in the $\boldsymbol{d}$-formalism *for the physical*

spin as

$$\Delta_{\boldsymbol{k}} = \frac{1}{4}\Delta_1(\boldsymbol{k})\{[(-i\sin\varphi_{\boldsymbol{k}}\tau_0 - \cos\varphi_{\boldsymbol{k}}\tau_z)s_x + (-i\cos\varphi_{\boldsymbol{k}}\tau_0 + \sin\varphi_{\boldsymbol{k}}\tau_z)s_y + \tau_x s_z](is_y) - \tau_y s_y\}. \tag{A.22}$$

That is,

$$\Delta_{\boldsymbol{k}} = i(\tilde{\boldsymbol{d}}(\boldsymbol{k})\cdot\boldsymbol{s} + \tilde{d}_0 s_0)s_y \tag{A.23}$$

with

$$\tilde{\boldsymbol{d}}(\boldsymbol{k}) = \frac{1}{4}\Delta_1(\boldsymbol{k})\begin{pmatrix} -i\sin\varphi_{\boldsymbol{k}}\tau_0 - \cos\varphi_{\boldsymbol{k}}\tau_z \\ -i\cos\varphi_{\boldsymbol{k}}\tau_0 + \sin\varphi_{\boldsymbol{k}}\tau_z \\ \tau_x \end{pmatrix} \tag{A.24}$$

and

$$\tilde{d}_0 = \frac{i}{4}\Delta_1(\boldsymbol{k})\tau_y. \tag{A.25}$$

In general, the pairing is a mixture of spin singlet and spin triplet.

A.3 Spin singlet IKS

For IKS at $\nu_c < \nu < -2$, we have two intervalley-coherent bands. Here we focus on the case where we have a spin singlet IKS parent state that corresponds to the preferred ground state at finite electron-phonon coupling. The relevant IVC bands where the Fermi surfaces reside in are

$$c^\dagger_{1\uparrow}(\boldsymbol{k}) = \frac{1}{\sqrt{2}}(e^{-i\varphi_{\boldsymbol{k}}/2}c^\dagger_{K\uparrow}(\boldsymbol{k}) + e^{i\varphi_{\boldsymbol{k}}/2}c^\dagger_{K'\uparrow}(\boldsymbol{k})) \tag{A.26}$$

$$c^\dagger_{1\downarrow}(\boldsymbol{k}) = \frac{1}{\sqrt{2}}(e^{-i\varphi_{\boldsymbol{k}}/2}c^\dagger_{K\downarrow}(\boldsymbol{k}) + e^{i\varphi_{\boldsymbol{k}}/2}c^\dagger_{K'\downarrow}(\boldsymbol{k})). \tag{A.27}$$

Different from the single-band case, in this case the parent state does not break $\mathrm{SU}(2)_s$ symmetry. We write the superconducting order parameter as $[\Delta_1(\boldsymbol{k})]_{ss'} = \langle c^\dagger_{1s}(\boldsymbol{k})c^\dagger_{1s'}(-\boldsymbol{k})\rangle$, and due to fermionic statistics, we must have $\Delta_1(\boldsymbol{k}) = -\Delta_1^T(-\boldsymbol{k})$. The order parameter could be either a spin singlet or a spin triplet, and the forms follow the usual discussion of

superconducting pairing symmetry. That is, for spin singlet, we have

$$\Delta_1(\boldsymbol{k}) = \begin{pmatrix} 0 & \psi(\boldsymbol{k}) \\ -\psi(\boldsymbol{k}) & 0 \end{pmatrix} = is_y\psi(\boldsymbol{k}) \tag{A.28}$$

with $\psi(-\boldsymbol{k}) = \psi(\boldsymbol{k})$. For spin triplet, we have

$$\Delta_1(\boldsymbol{k}) = \begin{pmatrix} -d_x(\boldsymbol{k}) + id_y(\boldsymbol{k}) & d_z(\boldsymbol{k}) \\ d_z(\boldsymbol{k}) & d_x(\boldsymbol{k}) + id_y(\boldsymbol{k}) \end{pmatrix} = i(\boldsymbol{d}\cdot\boldsymbol{s})s_y \tag{A.29}$$

for some $\boldsymbol{d}(\boldsymbol{k}) = -\boldsymbol{d}(-\boldsymbol{k})$. Note that, different from the use of $\boldsymbol{d}$ notation in previous subsections, due to the unbroken $\mathrm{SU}(2)_s$ symmetry of the parent state, the $\boldsymbol{d}$ vector is *a priori* an arbitrary odd function.

We can use the procedures in the previous subsections to convert from the IVC band basis $(c^\dagger_{1\uparrow}, c^\dagger_{1\downarrow})$ back into the single-particle valley-diagonal basis $(c^\dagger_{K,\uparrow}, c^\dagger_{K,\downarrow}, c^\dagger_{K',\uparrow}, c^\dagger_{K',\downarrow})$. For brevity, this is omitted here. Furthermore, the discussion of the spin structure is clearly unaffected if we assume a more general form of IVC given by

$$c^\dagger_{1s}(\boldsymbol{k}) = \alpha_{\boldsymbol{k}} c^\dagger_{Ks}(\boldsymbol{k}) + \beta_{\boldsymbol{k}} c^\dagger_{K's}(\boldsymbol{k})$$

for $s = \uparrow, \downarrow$, since $\alpha_{\boldsymbol{k}}, \beta_{\boldsymbol{k}}$ are independent of the spin index due to $\mathrm{SU}(2)_s$ symmetry.

Appendix B

Additional experimental data

Below, we reproduce some additional data for the experiment discussed in Chap. 4.

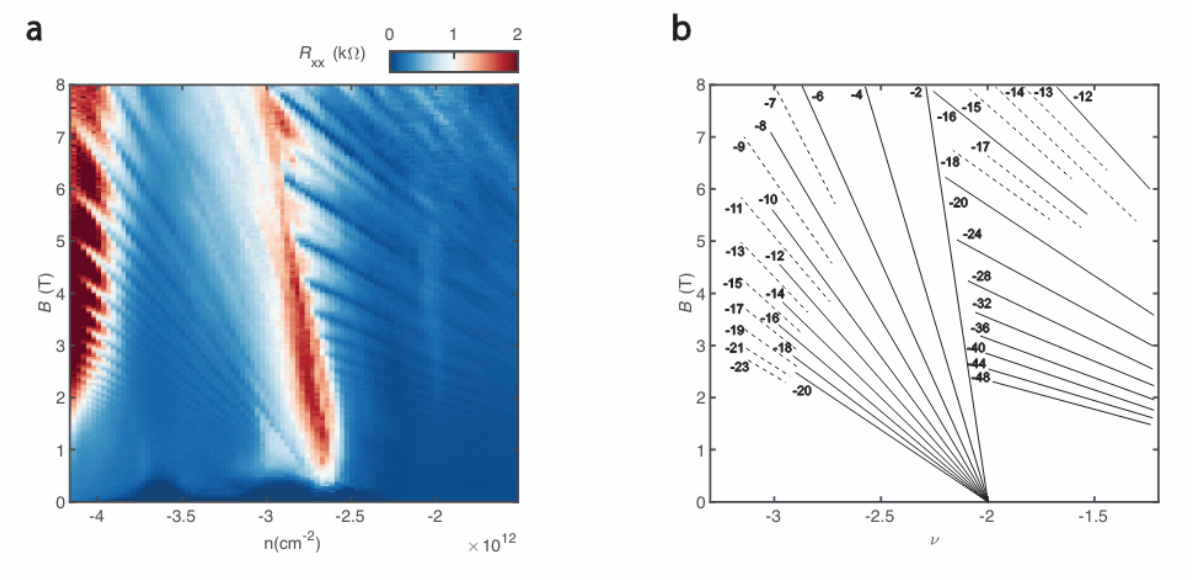


Figure B.1: Shubnikov-de Haas oscillations at $\nu = -2$. The Landau fan diagram shows that the Landau levels stemming from $\nu = -2$ have a sequence of $-2, -4, -6$ with a twofold degeneracy. Reproduced from Ref. [156].

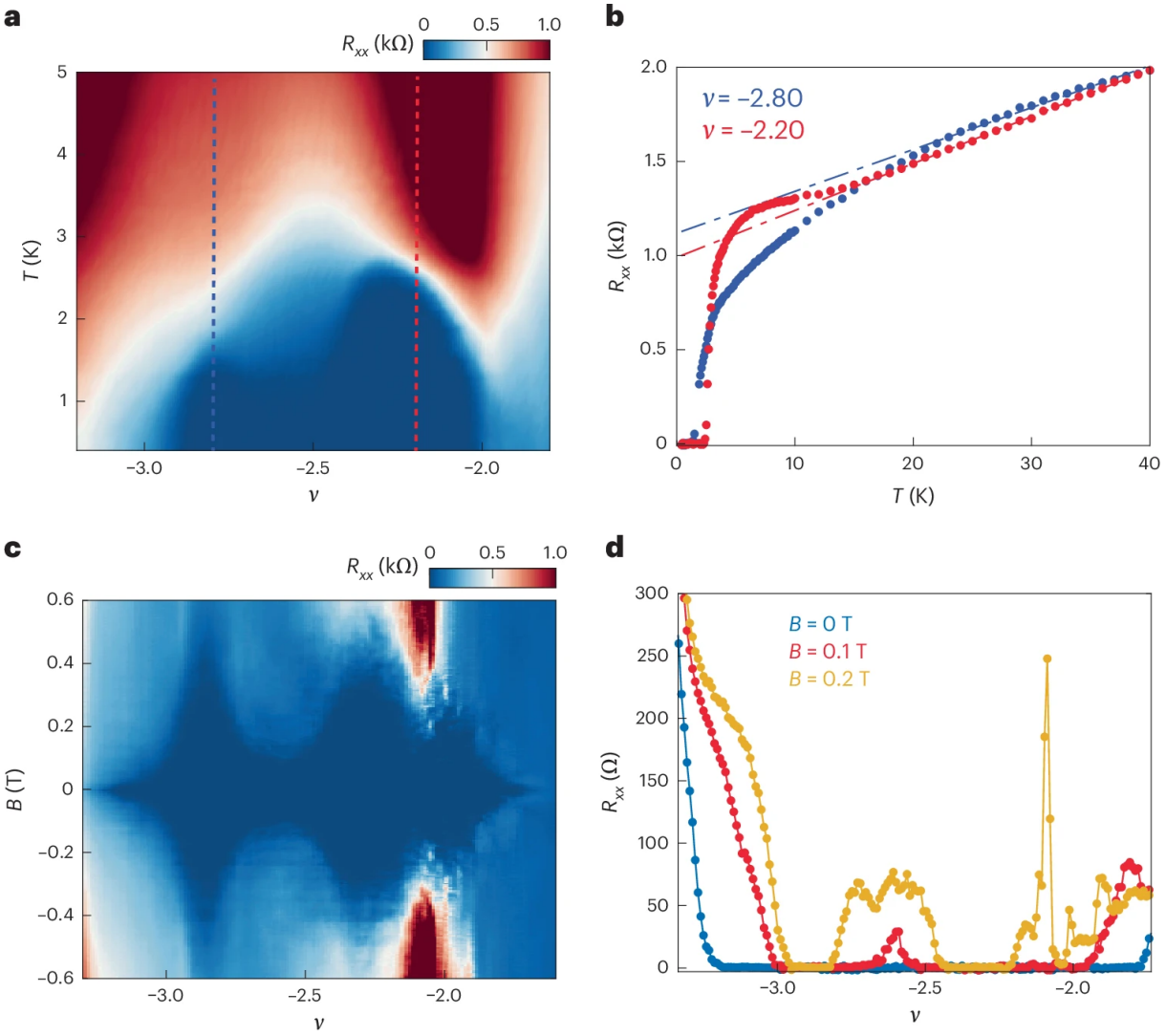


Figure B.2: **a**, Temperature dependence of R_{xx} in the hole side superconducting regime. The superconducting phase is strongly suppressed near $\nu^* = -2.6$. **b**, line cuts of R_{xx} in **a** when $\nu = -2.2$ and $\nu = -2.8$. Dashed lines are the linear fit of R_{xx} versus T in the high-temperature region. **c**, The magnetic field dependence of R_{xx} also shows a clear feature of double dome superconductivity. The left and right dome's superconductivity are very robust, with a maximum critical magnetic field larger than 300 mT. Near $\nu^* = -2.6$, superconductivity is sufficiently weakened. **d**, Line-cuts from **c** at three different magnetic fields. At zero magnetic field, the superconducting region extends below $\nu = -3$ and above $\nu = -2$. When $B = 0.1$T, the superconducting regime shrinks from both sides, and a small resistance peak appears near $\nu^* = -2.6$. When $B = 0.2$T, the resistance peak near $\nu^* = -2.6$ becomes enhanced, and the $\nu = -2$ correlated state appears. Reproduced from Ref. [156].

Appendix C

Delicate topology of Chern texture insulators

In this section, we illustrate that a CTI can be deformed infinitesimally to a trivial IVC state without closing the charge gap by introducing additional degrees of freedom. Here, a trivial IVC state, unlike CTI, has its IVC to be non-vanishing in the entire BZ. For simplicity, we will consider bands CTI_1, i.e., CTI formed from a pair of Chern bands with $C = \pm 1$.

As the CTI is formed as a coherent state between the two valleys, we can, denoting the (cell-periodic part of the) wavefunctions of each valley as $|u_\tau(\boldsymbol{k})\rangle$[1], write the general form of the filled band of the CTI as

$$|u_{\mathrm{CTI}}(\boldsymbol{k})\rangle = \sum_\tau c_\tau(\boldsymbol{k})\, |u_\tau(\boldsymbol{k})\rangle\,. \tag{C.1}$$

We assume that the CTI is fully-polarized towards $\tau = -$ at $\boldsymbol{k}_0$. This means that $c_-(\boldsymbol{k}) \sim 1$ near $\boldsymbol{k}_0$, and we must have a vortex in $c_+(\boldsymbol{k})$. With appropriate choice of the gauge, we can choose $c_+(\boldsymbol{k}) \sim (k_x - k_{0x}) + i(k_y - k_{0y})$. Hence the CTI wavefunction near $\boldsymbol{k}_0$ can be parameterized as

$$|u_{\mathrm{CTI}}(\boldsymbol{k})\rangle = ((k_x - k_{0x}) + i(k_y - k_{0y}))\, |u_+(\boldsymbol{k})\rangle + \sqrt{1 - |\boldsymbol{k} - \boldsymbol{k}_0|^2}\, |u_-(\boldsymbol{k})\rangle\,. \tag{C.2}$$

[1]These valley wavefunctions are assumed to be smooth, such that $\partial_{k_a} |u_\tau(\boldsymbol{k})\rangle$ is finite. In general, they will not be periodic.

We now introduce a remote band $|u_{+,\mathrm{rem}}(\boldsymbol{k})\rangle$ in valley + [2]. Again, we will assume that $|u_{+,\mathrm{rem}}(\boldsymbol{k})\rangle$ is fixed with a smooth gauge. The basic strategy is to mix in the remote band $|u_{+,\mathrm{rem}}(\boldsymbol{k})\rangle$ near $\boldsymbol{k}_0$ to manufacture some finite IVC at $\boldsymbol{k}_0$, thereby trivialize the CTI state. Since we only need to do this in the momentum space near $\boldsymbol{k}_0$, we consider an arbitrarily small and smooth function $\delta(\boldsymbol{k})$ that decays rapidly away from $\boldsymbol{k}_0$[3]. We can then construct the following state, which, near $\boldsymbol{k}_0$, can be written as

$$\begin{aligned} |u_{\mathrm{trivial}}(\boldsymbol{k})\rangle = &((k_x - k_{0x}) + i(k_y - k_{0y}))\,|u_+(\boldsymbol{k})\rangle \\ &+ \delta(\boldsymbol{k})\,|u_{+,\mathrm{rem}}(\boldsymbol{k})\rangle \\ &+ \sqrt{1 - |\boldsymbol{k} - \boldsymbol{k}_0|^2 - \delta(\boldsymbol{k})^2}\,|u_-(\boldsymbol{k})\rangle\,. \end{aligned} \tag{C.3}$$

There is an analogous deformation using $|u_{-,\mathrm{rem}}(\boldsymbol{k})\rangle$ at $-\boldsymbol{k}_0$, where the CTI is fully polarized towards + valley.

$|u_{\mathrm{trivial}}(\boldsymbol{k})\rangle$ lies arbitrarily close to $|u_{\mathrm{CTI}}(\boldsymbol{k})\rangle$, but $|u_{\mathrm{trivial}}(\boldsymbol{k})\rangle$ is trivial as the IVC never vanishes[4]. In the process, $|u_{\mathrm{trivial}}\rangle$ remains a smooth function of $\boldsymbol{k}$, as both the original $|u_{\mathrm{CTI}}(\boldsymbol{k})\rangle$ and $|u_{+,\mathrm{rem}}(\boldsymbol{k})\rangle$ are wavefunctions that vary smoothly with $\boldsymbol{k}$, and $\delta(\boldsymbol{k})$ has also been chosen to be smooth. This implies that the gap has not been closed in the process. Furthermore, as we have made use of $|u_{\pm,\mathrm{rem}}(\boldsymbol{k})\rangle$ near $\pm\boldsymbol{k}_0$ respectively, the global topology of these remote bands clearly do not matter, and they can be chosen to be trivial. As such, we have shown that the CTI band is unstable against the inclusion of trivial bands.

We now show that the initial CTI can be further deformed to a trivial atomic limit using the remote states. To be do, we now specify that the remote bands are constructed from a single atomic site per unit cell for each valley, $|\boldsymbol{R}, \tau\rangle$. If we further smoothly deform the IVC band by consistently removing the weights of the original $|u_\tau(\boldsymbol{k})\rangle$, we reach the following state,

$$|u_{\mathrm{atomic}}(\boldsymbol{k})\rangle = \frac{1}{\sqrt{2}}(|u_{+,\mathrm{rem}}(\boldsymbol{k})\rangle + |u_{-,\mathrm{rem}}(\boldsymbol{k})\rangle). \tag{C.4}$$

This state clearly has Wannier orbitals that live within single unit cells, given by $\frac{1}{\sqrt{2}}(|\boldsymbol{R}, +\rangle + |\boldsymbol{R}, -\rangle)$.

[2] As we will see, it is not even necessary to introduce the entire band, but only a finite patch of it.

[3] Indeed, we may even impose that $\delta(\boldsymbol{k})$ has compact support

[4] The nodes of IVC at $\pm\boldsymbol{k}_0$ have been removed, and since our operation can be done on a neighborhood arbitrarily close to $\pm\boldsymbol{k}_0$, we do note introduce new IVC nodes.

Appendix D

Gauge fixing and gauge-invariant velocity

D.1 Gauge fixing for intervalley order parameter

The intervalley order parameter $\Delta_{\boldsymbol{q}}(\boldsymbol{k}) \equiv \langle d^\dagger_{\boldsymbol{k},+} d_{\boldsymbol{k}+\boldsymbol{q},-} \rangle$ is dependent on the choice of gauge for the $d^\dagger_{\boldsymbol{k}\tau}$ operators. While many choices are possible, we require that the gauge is smooth within the BZ. That is, we require $|\langle u(\boldsymbol{k}+\delta\boldsymbol{k})|u(\boldsymbol{k})\rangle - 1| \to 0$ when $|\delta\boldsymbol{k}| \to 0$ for all $\boldsymbol{k}$, provided no BZ boundary is crossed, where $|u(\boldsymbol{k})\rangle$ is the periodic part of the Bloch wavefunction. Numerically, we carry out the procedure described below.

Consider an $N_1 \times N_2$ system. Denote $\boldsymbol{g}_i = \boldsymbol{G}_i/N_i$ for $i = 1, 2$, where $\boldsymbol{G}_i$ is the i-th basis reciprocal lattice vector. Consider first the $\tau = +$ valley. Denote the crystal momentum $\tilde{\boldsymbol{k}} = \boldsymbol{k} - \tilde{\boldsymbol{\gamma}} = m_1\boldsymbol{g_1} + m_2\boldsymbol{g}_2$ as (m_1, m_2), where the chosen reference point $\tilde{\boldsymbol{\gamma}}$ needs not be Γ_M, and $0 \leq m_i \leq N_i - 1$. Starting from $(0, 0)$, we specify the gauge at $(m, 0)$ by demanding

$$\arg(\langle u(m_1+1, 0)|u(m_1, 0)\rangle) = 0 \tag{D.1}$$

for $m_1 = 0, ..., N_1 - 2$. We then fix the gauge at all other points by demanding

$$\arg(\langle u(m_1, m_2+1)|u(m_1, m_2)\rangle) = 0 \tag{D.2}$$

for $m_1 = 0, ..., N_1 - 1$ and $m_2 = 0, ..., N_2 - 2$. This gauge is akin to the 'Landau gauge' for an arbitrary Chern band. For the $\tau = -$ valley, we perform the same procedure, except

we define $\tilde{\boldsymbol{k}} = \boldsymbol{k} + \boldsymbol{q} - \tilde{\boldsymbol{\gamma}} = m_1\boldsymbol{g_1} + m_2\boldsymbol{g_2}$ to ensure the alignment of the BZ boundaries in both valleys.

D.2 Gauge-invariant velocity on a grid

The gauge invariant velocity on a continuous $\boldsymbol{k}$-space is defined in Eq. 5.28. For numerical calculation on a finite grid, we adopt the following definition

$$\boldsymbol{j}(\boldsymbol{k}) \cdot \delta\boldsymbol{k} = \arg\left(\frac{\Delta_{\boldsymbol{q}}(\boldsymbol{k}+\delta\boldsymbol{k})}{\Delta_{\boldsymbol{q}}(\boldsymbol{k})} \frac{\langle u_{\boldsymbol{k}+\delta\boldsymbol{k},+}|u_{\boldsymbol{k}+}\rangle}{\langle u_{\boldsymbol{k}+\boldsymbol{q}+\delta\boldsymbol{k},-}|u_{\boldsymbol{k}+\boldsymbol{q},-}\rangle}\right) \tag{D.3}$$

where the principal range is $\arg(x) \in [-\pi, \pi)$, as we expect $|\boldsymbol{j}(\boldsymbol{k}) \cdot \delta\boldsymbol{k}| \ll 1$ for a sufficiently fine momentum grid and not too close to the vortex core, where the velocity diverges. This definition reduces to the correct continuum limit by setting $|\delta\boldsymbol{k}| \to 0$ and has the advantage of being numerically reliable for arbitrarily non-smooth gauge choice.

Bibliography

[1] Guohong Li et al. "Observation of Van Hove singularities in twisted graphene layers". In: *Nature Physics* 6.2 (Nov. 2009), pp. 109–113. DOI: 10.1038/nphys1463.

[2] Rafi Bistritzer and Allan H. MacDonald. "Moiré bands in twisted double-layer graphene". In: *Proceedings of the National Academy of Sciences* 108.30 (July 2011), pp. 12233–12237. ISSN: 0027-8424. DOI: 10.1073/pnas.1108174108. eprint: https://www.pnas.org/content/108/30/12233.full.pdf.

[3] Grigory Tarnopolsky, Alex Jura Kruchkov, and Ashvin Vishwanath. "Origin of Magic Angles in Twisted Bilayer Graphene". In: *Physical Review Letters* 122.10 (10 Mar. 2019). Publisher: American Physical Society, p. 106405. DOI: 10.1103/physrevlett.122.106405.

[4] J. M. B. Lopes dos Santos, N. M. R. Peres, and A. H. Castro Neto. "Graphene Bilayer with a Twist: Electronic Structure". In: *Physical Review Letters* 99.25 (25 Dec. 2007), p. 256802. DOI: 10.1103/physrevlett.99.256802.

[5] Yuan Cao et al. "Unconventional superconductivity in magic-angle graphene superlattices". In: *Nature* 556.7699 (Mar. 2018), pp. 43–50. ISSN: 1476-4687. DOI: 10.1038/nature26160.

[6] Yuan Cao et al. "Correlated insulator behaviour at half-filling in magic-angle graphene superlattices". In: *Nature* 556.7699 (Mar. 2018), pp. 80–84. ISSN: 1476-4687. DOI: 10.1038/nature26154.

[7] Kyounghwan Kim et al. "Van Der Waals Heterostructures with High Accuracy Rotational Alignment". In: *Nano Letters* 16.3 (Mar. 2016), pp. 1989–1995. ISSN: 1530-6984. DOI: 10.1021/acs.nanolett.5b05263.

[8] Y. H. Kwan et al. "Kekulé Spiral Order at All Nonzero Integer Fillings in Twisted Bilayer Graphene". In: *Physical Review X* 11.4 (4 Dec. 2021), p. 041063. DOI: 10.1103/physrevx.11.041063.

[9] Glenn Wagner et al. "Global Phase Diagram of the Normal State of Twisted Bilayer Graphene". In: *Physical Review Letters* 128.15 (15 Apr. 2022), p. 156401. DOI: 10.1103/physrevlett.128.156401.

[10] Kevin P. Nuckolls et al. "Quantum textures of the many-body wavefunctions in magic-angle graphene". In: *Nature* 620.7974 (Aug. 2023), pp. 525–532. ISSN: 1476-4687. DOI: 10.1038/s41586-023-06226-x.

[11] Myungchul Oh et al. "Evidence for unconventional superconductivity in twisted bilayer graphene". In: *Nature* 600.7888 (Oct. 2021), pp. 240–245. ISSN: 1476-4687. DOI: 10.1038/s41586-021-04121-x.

[12] Yu Saito et al. "Isospin Pomeranchuk effect in twisted bilayer graphene". In: *Nature* 592.7853 (Apr. 2021), pp. 220–224. DOI: 10.1038/s41586-021-03409-2.

[13] Shuang Wu et al. “Chern insulators, van Hove singularities and topological flat bands in magic-angle twisted bilayer graphene”. In: *Nature Materials* 20.4 (Feb. 2021), pp. 488–494. ISSN: 1476-4660. DOI: 10.1038/s41563-020-00911-2.

[14] Asaf Rozen et al. “Entropic evidence for a Pomeranchuk effect in magic-angle graphene”. In: *Nature* 592.7853 (Apr. 2021), pp. 214–219. DOI: 10.1038/s41586-021-03319-3.

[15] Dillon Wong et al. “Cascade of electronic transitions in magic-angle twisted bilayer graphene”. In: *Nature* 582.7811 (June 2020), pp. 198–202. ISSN: 1476-4687. DOI: 10.1038/s41586-020-2339-0.

[16] U. Zondiner et al. “Cascade of phase transitions and Dirac revivals in magic-angle graphene”. In: *Nature* 582.7811 (June 2020), pp. 203–208. ISSN: 1476-4687. DOI: 10.1038/s41586-020-2373-y.

[17] Eslam Khalaf et al. “Magic angle hierarchy in twisted graphene multilayers”. In: *Physical Review B* 100.8 (Aug. 2019), p. 085109. DOI: 10.1103/physrevb.100.085109.

[18] Bo Xie et al. “Alternating Twisted Multilayer Graphene: Generic Partition Rules, Double Flat Bands, and Orbital Magnetoelectric Effect”. In: *npj Computational Materials* 8.1 (May 2022), pp. 1–8. ISSN: 2057-3960. DOI: 10.1038/s41524-022-00789-5.

[19] Hyunjin Kim et al. “Imaging inter-valley coherent order in magic-angle twisted trilayer graphene”. In: *Nature* 623.7989 (Nov. 2023). Number: 7989 Publisher: Nature Publishing Group, pp. 942–948. ISSN: 1476-4687. DOI: 10.1038/s41586-023-06663-8.

[20] Hyunjin Kim et al. “Evidence for Unconventional Superconductivity in Twisted Trilayer Graphene”. In: *Nature* 606.7914 (June 2022), pp. 494–500. ISSN: 1476-4687. DOI: 10.1038/s41586-022-04715-z.

[21] Hyunjin Kim et al. “Resolving Intervalley Gaps and Many-Body Resonances in Moiré Superconductors”. In: *Nature* 650.8102 (Feb. 2026), pp. 592–598. ISSN: 1476-4687. DOI: 10.1038/s41586-025-10067-1.

[22] Youngjoon Choi et al. “Electronic correlations in twisted bilayer graphene near the magic angle”. In: *Nature Physics* 15.11 (Aug. 2019), pp. 1174–1180. DOI: 10.1038/s41567-019-0606-5.

[23] Alexander Kerelsky et al. “Maximized electron interactions at the magic angle in twisted bilayer graphene”. In: *Nature* 572 (2019), p. 95.

[24] Fengcheng Wu et al. “Topological Insulators in Twisted Transition Metal Dichalcogenide Homobilayers”. In: *Phys. Rev. Lett.* 122 (8 Feb. 2019), p. 086402. DOI: 10.1103/PhysRevLett.122.086402.

[25] Harpreet Singh Arora et al. “Superconductivity in metallic twisted bilayer graphene stabilized by WSe2”. In: *Nature* 583.7816 (July 2020), pp. 379–384. ISSN: 1476-4687. DOI: 10.1038/s41586-020-2473-8.

[26] Ruiheng Su et al. “Superconductivity in Twisted Double Bilayer Graphene Stabilized by WSe2”. In: *Nature Materials* 22.11 (Nov. 2023), pp. 1332–1337. ISSN: 1476-4660. DOI: 10.1038/s41563-023-01653-7.

[27] Gianluca Giovannetti et al. “Substrate-Induced Band Gap in Graphene on Hexagonal Boron Nitride: Ab Initio Density Functional Calculations”. In: *Physical Review B* 76.7 (Aug. 2007), p. 073103. DOI: 10.1103/PhysRevB.76.073103.

[28] Matthew Yankowitz et al. “Emergence of Superlattice Dirac Points in Graphene on Hexagonal Boron Nitride”. In: *Nature Physics* 8.5 (May 2012), pp. 382–386. ISSN: 1745-2481. DOI: 10.1038/nphys2272.

[29] W. Paszkowicz et al. “Lattice Parameters and Anisotropic Thermal Expansion of Hexagonal Boron Nitride in the 10–297.5 K Temperature Range”. In: *Applied Physics A* 75.3 (Sept. 2002), pp. 431–435. ISSN: 1432-0630. DOI: 10.1007/s003390100999.

[30] Hoi Chun Po, Haruki Watanabe, and Ashvin Vishwanath. “Fragile Topology and Wannier Obstructions”. In: *Phys. Rev. Lett.* 121 (12 Sept. 2018), p. 126402. DOI: 10.1103/PhysRevLett.121.126402.

[31] Tingxin Li et al. “Quantum anomalous Hall effect from intertwined moiré bands”. In: *Nature* 600.7890 (2021), pp. 641–646.

[32] M. Serlin et al. “Intrinsic quantized anomalous Hall effect in a moiré heterostructure”. In: *Science* 367.6480 (Feb. 2020), pp. 900–903. ISSN: 0036-8075. DOI: 10.1126/science.aay5533.

[33] Guorui Chen et al. “Tunable correlated Chern insulator and ferromagnetism in a moiré superlattice”. In: *Nature* 579.7797 (Mar. 2020), pp. 56–61. DOI: 10.1038/s41586-020-2049-7.

[34] Emil J. Bergholtz and Zhao Liu. “Topological flat band models and fractional Chern insulators”. In: *International Journal of Modern Physics B* 27.24 (2013), p. 1330017. DOI: 10.1142/S021797921330017X.

[35] Siddharth A. Parameswaran, Rahul Roy, and Shivaji L. Sondhi. “Fractional quantum Hall physics in topological flat bands”. In: *Comptes Rendus. Physique* 14.9-10 (2013), pp. 816–839. DOI: 10.1016/j.crhy.2013.04.003.

[36] Zhao Liu and Emil J. Bergholtz. “Recent developments in fractional Chern insulators”. In: *Encyclopedia of Condensed Matter Physics (2ed)*. Ed. by Tapash Chakraborty. Oxford: Academic Press, 2024, pp. 515–538. ISBN: 978-0-323-91408-6. DOI: https://doi.org/10.1016/B978-0-323-90800-9.00136-0.

[37] Jiaqi Cai et al. “Signatures of Fractional Quantum Anomalous Hall States in Twisted MoTe2”. In: *Nature* 622.7981 (June 2023), pp. 63–68. ISSN: 1476-4687. DOI: 10.1038/s41586-023-06289-w.

[38] Yihang Zeng et al. “Thermodynamic evidence of fractional Chern insulator in moiré MoTe2”. In: *Nature* 622.7981 (July 2023), pp. 69–73. ISSN: 1476-4687. DOI: 10.1038/s41586-023-06452-3.

[39] Fan Xu et al. “Observation of Integer and Fractional Quantum Anomalous Hall Effects in Twisted Bilayer $MoTe_2$”. In: *Phys. Rev. X* 13 (3 Sept. 2023), p. 031037. DOI: 10.1103/PhysRevX.13.031037.

[40] Heonjoon Park et al. “Observation of fractionally quantized anomalous Hall effect”. In: *Nature* 622.7981 (2023), pp. 74–79. DOI: 10.1038/s41586-023-06536-0.

[41] Kaifei Kang et al. “Observation of the fractional quantum spin Hall effect in moir\’e MoTe2”. In: *arXiv preprint arXiv:2402.03294* (2024).

[42] Zhengguang Lu et al. “Fractional Quantum Anomalous Hall Effect in Multilayer Graphene”. In: *Nature* 626.8000 (Feb. 2024), pp. 759–764. ISSN: 1476-4687. DOI: 10.1038/s41586-023-07010-7.

[43] Zhengguang Lu et al. “Extended Quantum Anomalous Hall States in Graphene/hBN Moiré Superlattices”. In: *Nature* 637.8048 (Jan. 2025), pp. 1090–1095. ISSN: 1476-4687. DOI: 10.1038/s41586-024-08470-1.

[44] Jian Xie et al. “Tunable Fractional Chern Insulators in Rhombohedral Graphene Superlattices”. In: *Nature Materials* 24.7 (July 2025), pp. 1042–1048. ISSN: 1476-4660. DOI: 10.1038/s41563-025-02225-7.

[45] Hoi Chun Po et al. “Origin of Mott Insulating Behavior and Superconductivity in Twisted Bilayer Graphene”. In: *Physical Review X* 8.3 (Sept. 2018), p. 031089. ISSN: 2160-3308. DOI: 10.1103/PhysRevX.8.031089.

[46] Liujun Zou et al. “Band Structure of Twisted Bilayer Graphene: Emergent Symmetries, Commensurate Approximants, and Wannier Obstructions”. In: *Physical Review B* 98.8 (Aug. 2018), p. 085435. DOI: 10.1103/PhysRevB.98.085435.

[47] Zhida Song et al. “All Magic Angles in Twisted Bilayer Graphene are Topological”. In: *Physical Review Letters* 123.3 (3 July 2019), p. 036401. DOI: 10.1103/physrevlett.123.036401.

[48] Zhi-Da Song et al. “Twisted bilayer graphene. II. Stable symmetry anomaly”. In: *Phys. Rev. B* 103 (20 May 2021), p. 205412. DOI: 10.1103/PhysRevB.103.205412.

[49] Mattia Angeli and Allan H. MacDonald. “Gamma valley transition metal dichalcogenide moiré bands”. In: *Proceedings of the National Academy of Sciences* 118.10 (2021), e2021826118. DOI: 10.1073/pnas.2021826118. eprint: https://www.pnas.org/doi/pdf/10.1073/pnas.2021826118.

[50] Martin Claassen et al. “Ultra-strong spin–orbit coupling and topological moiréengineering in twisted ZrS2 bilayers”. In: *Nature Communications* 13.1 (2022), p. 4915. DOI: 10.1038/s41467-022-31604-w.

[51] Dumitru Călugăru et al. “Moirématerials based on M-point twisting”. In: *Nature* 643.8071 (2025), pp. 376–381. DOI: 10.1038/s41586-025-09187-5.

[52] Julian Ingham, Mathias S. Scheurer, and Harley D. Scammell. *Moiré M-valley bilayers: quasi-one-dimensional physics, unconventional spin textures and twisted van Hove singularities*. 2025. arXiv: 2503.11754 [cond-mat.str-el].

[53] Yi-Ming Wu, Chaitanya Murthy, and Steven A. Kivelson. “Possible Sliding Regimes in Twisted Bilayer WTe_2”. In: *Phys. Rev. Lett.* 133 (24 Dec. 2024), p. 246501. DOI: 10.1103/PhysRevLett.133.246501.

[54] Pengjie Wang et al. “One-dimensional Luttinger liquids in a two-dimensional moiré lattice”. In: *Nature* 605.7908 (2022), pp. 57–62.

[55] Johannes S. Hofmann et al. “Fermionic Monte Carlo Study of a Realistic Model of Twisted Bilayer Graphene”. In: *Physical Review X* 12.1 (1 Mar. 2022), p. 011061. DOI: 10.1103/physrevx.12.011061.

[56] Xu Zhang et al. “Momentum Space Quantum Monte Carlo on Twisted Bilayer Graphene”. In: *Chinese Physics Letters* 38.7 (July 2021), p. 077305. DOI: 10.1088/0256-307x/38/7/077305.

[57] Xu Zhang et al. “Polynomial sign problem and topological Mott insulator in twisted bilayer graphene”. In: *Phys. Rev. B* 107 (24 June 2023), p. L241105. DOI: 10.1103/PhysRevB.107.L241105.

[58] Cheng Huang et al. “Evolution from quantum anomalous Hall insulator to heavy-fermion semimetal in magic-angle twisted bilayer graphene”. In: *Phys. Rev. B* 109 (12 Mar. 2024), p. 125404. DOI: 10.1103/PhysRevB.109.125404.

[59] Yuan Da Liao et al. “Correlation-Induced Insulating Topological Phases at Charge Neutrality in Twisted Bilayer Graphene”. In: *Phys. Rev. X* 11 (1 Jan. 2021), p. 011014. DOI: 10.1103/PhysRevX.11.011014.

[60] Yuan-Da Liao et al. “Correlated insulating phases in the twisted bilayer graphene*”. In: *Chinese Physics B* 30.1 (Jan. 2021), p. 017305. DOI: 10.1088/1674-1056/abcfa3.

[61] Fang Xie et al. “Twisted bilayer graphene. VI. An exact diagonalization study at nonzero integer filling”. In: *Physical Review B* 103.20 (20 May 2021), p. 205416. DOI: 10.1103/physrevb.103.205416.

[62] Pawel Potasz, Ming Xie, and A. H. MacDonald. “Exact Diagonalization for Magic-Angle Twisted Bilayer Graphene”. In: *Physical Review Letters* 127.14 (Sept. 2021). DOI: 10.1103/physrevlett.127.147203.

[63] Ahmed Abouelkomsan, Zhao Liu, and Emil J. Bergholtz. “Particle-Hole Duality, Emergent Fermi Liquids, and Fractional Chern Insulators in Moiré Flatbands”. In: *Phys. Rev. Lett.* 124 (10 Mar. 2020), p. 106803. DOI: 10.1103/PhysRevLett.124.106803.

[64] Cécile Repellin and T. Senthil. “Chern bands of twisted bilayer graphene: Fractional Chern insulators and spin phase transition”. In: *Phys. Rev. Res.* 2 (2 May 2020), p. 023238. DOI: 10.1103/PhysRevResearch.2.023238.

[65] Patrick Wilhelm, Thomas C. Lang, and Andreas M. Läuchli. “Interplay of fractional Chern insulator and charge density wave phases in twisted bilayer graphene”. In: *Phys. Rev. B* 103 (12 Mar. 2021), p. 125406. DOI: 10.1103/PhysRevB.103.125406.

[66] Heqiu Li et al. “Contrasting twisted bilayer graphene and transition metal dichalcogenides for fractional Chern insulators: An emergent gauge picture”. In: *Phys. Rev. B* 109 (24 June 2024), p. 245131. DOI: 10.1103/PhysRevB.109.245131.

[67] Tomohiro Soejima et al. “Efficient simulation of moiré materials using the density matrix renormalization group”. In: *Physical Review B* 102.20 (20 Nov. 2020), p. 205111. DOI: 10.1103/physrevb.102.205111.

[68] Jian Kang and Oskar Vafek. “Non-Abelian Dirac node braiding and near-degeneracy of correlated phases at odd integer filling in magic-angle twisted bilayer graphene”. In: *Physical Review B* 102.3 (3 July 2020), p. 035161. DOI: 10.1103/physrevb.102.035161.

[69] Daniel E. Parker et al. “Strain-Induced Quantum Phase Transitions in Magic-Angle Graphene”. In: *Physical Review Letters* 127.2 (2 July 2021), p. 027601. DOI: 10.1103/physrevlett.127.027601.

[70] Daniel Parker et al. *Field-tuned and zero-field fractional Chern insulators in magic angle graphene*. 2021. arXiv: 2112.13837 [cond-mat.str-el].

[71] Fabian M. Faulstich et al. “Interacting models for twisted bilayer graphene: A quantum chemistry approach”. In: *Phys. Rev. B* 107 (23 June 2023), p. 235123. DOI: 10.1103/PhysRevB.107.235123.

[72] Tianle Wang et al. “Ground-state order in magic-angle graphene at filling $\nu = -3$: A full-scale density matrix renormalization group study”. In: *Phys. Rev. B* 108 (23 Dec. 2023), p. 235128. DOI: 10.1103/PhysRevB.108.235128.

[73] Bin-Bin Chen et al. “Realization of topological Mott insulator in a twisted bilayer graphene lattice model”. In: *Nature Communications* 12.1 (Sept. 2021). DOI: 10.1038/s41467-021-25438-1.

[74] Xiyue Lin et al. “Exciton Proliferation and Fate of the Topological Mott Insulator in a Twisted Bilayer Graphene Lattice Model”. In: *Phys. Rev. Lett.* 128 (15 Apr. 2022), p. 157201. DOI: 10.1103/PhysRevLett.128.157201.

[75] Nick Bultinck et al. “Ground State and Hidden Symmetry of Magic-Angle Graphene at Even Integer Filling”. In: *Physical Review X* 10.3 (3 Aug. 2020). Publisher: American Physical Society, p. 031034. DOI: 10.1103/physrevx.10.031034.

[76] Biao Lian et al. “Twisted bilayer graphene. IV. Exact insulator ground states and phase diagram”. In: *Physical Review B* 103.20 (20 May 2021), p. 205414. DOI: 10.1103/physrevb.103.205414.

[77] Jian Kang, B. Andrei Bernevig, and Oskar Vafek. “Cascades between Light and Heavy Fermions in the Normal State of Magic-Angle Twisted Bilayer Graphene”. In: *Physical Review Letters* 127.26 (26 Dec. 2021), p. 266402. DOI: 10.1103/physrevlett.127.266402.

[78] Yi Zhang et al. “Correlated insulating phases of twisted bilayer graphene at commensurate filling fractions: A Hartree-Fock study”. In: *Physical Review B* 102.3 (3 July 2020), p. 035136. DOI: 10.1103/physrevb.102.035136.

[79] Shang Liu et al. “Nematic topological semimetal and insulator in magic-angle bilayer graphene at charge neutrality”. In: *Physical Review Research* 3.1 (1 Jan. 2021), p. 013033. DOI: 10.1103/physrevresearch.3.013033.

[80] Ming Xie and A. H. MacDonald. “Nature of the Correlated Insulator States in Twisted Bilayer Graphene”. In: *Physical Review Letters* 124.9 (9 Mar. 2020), p. 097601. DOI: 10.1103/physrevlett.124.097601.

[81] Ming Xie and A. H. MacDonald. “Weak-Field Hall Resistivity and Spin-Valley Flavor Symmetry Breaking in Magic-Angle Twisted Bilayer Graphene”. In: *Physical Review Letters* 127.19 (19 Nov. 2021), p. 196401. DOI: 10.1103/physrevlett.127.196401.

[82] Tommaso Cea and Francisco Guinea. “Band structure and insulating states driven by Coulomb interaction in twisted bilayer graphene”. In: *Physical Review B* 102.4 (4 July 2020), p. 045107. DOI: 10.1103/physrevb.102.045107.

[83] Shihao Zhang, Xin Lu, and Jianpeng Liu. “Correlated Insulators, Density Wave States, and Their Nonlinear Optical Response in Magic-Angle Twisted Bilayer Graphene”. In: *Phys. Rev. Lett.* 128.24 (24 June 2022), p. 247402. DOI: 10.1103/PhysRevLett.128.247402.

[84] Jianpeng Liu and Xi Dai. “Theories for the correlated insulating states and quantum anomalous Hall effect phenomena in twisted bilayer graphene”. In: *Physical Review B* 103.3 (3 Jan. 2021), p. 035427. DOI: 10.1103/physrevb.103.035427.

[85] Tommaso Cea, Niels R. Walet, and Francisco Guinea. “Electronic band structure and pinning of Fermi energy to Van Hove singularities in twisted bilayer graphene: A self-consistent approach”. In: *Physical Review B* 100.20 (20 Nov. 2019), p. 205113. DOI: 10.1103/physrevb.100.205113.

[86] Francisco Guinea and Niels R. Walet. “Electrostatic effects, band distortions, and superconductivity in twisted graphene bilayers”. In: *Proceedings of the National Academy of Sciences* 115.52 (Dec. 2018), pp. 13174–13179. ISSN: 0027-8424. DOI: 10.1073/pnas.1810947115.

[87] Fang Xie et al. “Phase diagram of twisted bilayer graphene at filling factor $\nu = \pm 3$”. In: *Phys. Rev. B* 107.7 (7 Feb. 2023), p. 075156. DOI: 10.1103/PhysRevB.107.075156.

[88] Kasra Hejazi, Xiao Chen, and Leon Balents. “Hybrid Wannier Chern bands in magic angle twisted bilayer graphene and the quantized anomalous Hall effect”. In: *Physical Review Research* 3.1 (1 Mar. 2021), p. 013242. DOI: 10.1103/physrevresearch.3.013242.

[89] Yves H. Kwan et al. “Electron-phonon coupling and competing Kekulé orders in twisted bilayer graphene”. In: *Phys. Rev. B* 110 (8 Aug. 2024), p. 085160. DOI: 10.1103/PhysRevB.110.085160.

[90] Yves H. Kwan et al. *Skyrmions in twisted bilayer graphene: stability, pairing, and crystallization*. 2021. DOI: 10.48550/ARXIV.2112.06936.

[91] Yves H. Kwan et al. “Domain wall competition in the Chern insulating regime of twisted bilayer graphene”. In: *Physical Review B* 104.11 (11 Sept. 2021), p. 115404. DOI: 10.1103/physrevb.104.115404.

[92] Ziwei Wang et al. “Chern-textured exciton insulators with valley spiral order in moiré materials”. In: *Phys. Rev. B* 112 (3 July 2025), p. 035130. DOI: 10.1103/chsd-123t.

[93] Ziwei Wang et al. “Kekulé spirals and charge transfer cascades in twisted symmetric trilayer graphene”. In: *Phys. Rev. B* 109.20 (20 May 2024), p. L201119. DOI: 10.1103/PhysRevB.109.L201119.

[94] Jonah Herzog-Arbeitman et al. “Kekulé spiral order from strained topological heavy fermions”. In: *Phys. Rev. B* 112 (12 Sept. 2025), p. 125129. DOI: 10.1103/rr5g-3js8.

[95] Fang Xie et al. “Twisted symmetric trilayer graphene. II. Projected Hartree-Fock study”. In: *Phys. Rev. B* 104.11 (11 Sept. 2021), p. 115167. DOI: 10.1103/PhysRevB.104.115167.

[96] Maine Christos, Subir Sachdev, and Mathias S. Scheurer. “Correlated Insulators, Semimetals, and Superconductivity in Twisted Trilayer Graphene”. In: *Physical Review X* 12.2 (Apr. 2022), p. 021018. DOI: 10.1103/physrevx.12.021018.

[97] Clara N. Breiø and Brian M. Andersen. “Chern insulator phases and spontaneous spin and valley order in a moiré lattice model for magic-angle twisted bilayer graphene”. In: *Phys. Rev. B* 107 (16 Apr. 2023), p. 165114. DOI: 10.1103/PhysRevB.107.165114.

[98] Hyunjin Kim et al. “Imaging inter-valley coherent order in magic-angle twisted trilayer graphene”. In: *Nature* 623.7989 (2023), pp. 942–948.

[99] Nguyen N. T. Nam and Mikito Koshino. “Lattice relaxation and energy band modulation in twisted bilayer graphene”. In: *Physical Review B* 96.7 (Aug. 2017), p. 075311. DOI: 10.1103/physrevb.96.075311.

[100] Stephen Carr et al. “Exact continuum model for low-energy electronic states of twisted bilayer graphene”. In: *Physical Review Research* 1.1 (1 Aug. 2019), p. 013001. DOI: 10.1103/physrevresearch.1.013001.

[101] Aviram Uri et al. “Mapping the twist-angle disorder and Landau levels in magic-angle graphene”. In: *Nature* 581.7806 (2020), pp. 47–52.

[102] Zhen Bi, Noah F. Q. Yuan, and Liang Fu. “Designing flat bands by strain”. In: *Physical Review B* 100.3 (3 July 2019), p. 035448. DOI: 10.1103/physrevb.100.035448.

[103] Loïc Huder et al. “Electronic Spectrum of Twisted Graphene Layers under Heterostrain”. In: *Phys. Rev. Lett.* 120.15 (15 Apr. 2018), p. 156405. DOI: 10.1103/PhysRevLett.120.156405.

[104] Mikito Koshino et al. “Maximally Localized Wannier Orbitals and the Extended Hubbard Model for Twisted Bilayer Graphene”. In: *Physical Review X* 8.3 (3 Sept. 2018), p. 031087. DOI: 10.1103/physrevx.8.031087.

[105] Patrick J. Ledwith et al. *TB or Not TB? Contrasting Properties of Twisted Bilayer Graphene and the Alternating Twist n-Layer Structures ($n=3, 4, 5, \dots$)*. Nov. 2021. DOI: 10.48550/ARXIV.2111.11060. arXiv: 2111.11060 [cond-mat].

[106] Alexander Kerelsky et al. "Maximized electron interactions at the magic angle in twisted bilayer graphene". In: *Nature* 572.7767 (July 2019), pp. 95–100. DOI: 10.1038/s41586-019-1431-9.

[107] Yonglong Xie et al. "Spectroscopic signatures of many-body correlations in magic-angle twisted bilayer graphene". In: *Nature* 572.7767 (July 2019), pp. 101–105. DOI: 10.1038/s41586-019-1422-x.

[108] Agnes Valenti et al. *Critical Gate Distance for Wigner Crystallization in the Two-Dimensional Electron Gas*. https://arxiv.org/abs/2501.16430v1. Jan. 2025. DOI: 10.1103/2qgp-v27h.

[109] E. H. Hwang and S. Das Sarma. "Dielectric Function, Screening, and Plasmons in Two-Dimensional Graphene". In: *Physical Review B* 75.20 (May 2007), p. 205418. DOI: 10.1103/PhysRevB.75.205418.

[110] Raehyun Kim et al. *Ab Initio Quantum Embedding Description of Magic Angle Twisted Bilayer Graphene at Even-Integer Fillings*. Mar. 2026. DOI: 10.48550/arXiv.2603.10433. arXiv: 2603.10433 [cond-mat].

[111] Yves H. Kwan et al. "Moiré fractional Chern insulators. III. Hartree-Fock phase diagram, magic angle regime for Chern insulator states, role of moiré potential, and Goldstone gaps in rhombohedral graphene superlattices". In: *Phys. Rev. B* 112.7 (7 Aug. 2025), p. 075109. DOI: 10.1103/PhysRevB.112.075109.

[112] Jiabin Yu et al. "Moiré fractional Chern insulators. IV. Fluctuation-driven collapse in multiband exact diagonalization calculations on rhombohedral graphene". In: *Phys. Rev. B* 112 (7 Aug. 2025), p. 075110. DOI: 10.1103/PhysRevB.112.075110.

[113] Jiabin Yu et al. "Fractional Chern insulators versus nonmagnetic states in twisted bilayer $MoTe_2$". In: *Phys. Rev. B* 109 (4 Jan. 2024), p. 045147. DOI: 10.1103/PhysRevB.109.045147.

[114] P.-L. Lions. "Solutions of Hartree-Fock Equations for Coulomb Systems". In: *Communications in Mathematical Physics* 109.1 (Jan. 1987), pp. 33–97. ISSN: 0010-3616, 1432-0916.

[115] Eric Cancès and Claude Le Bris. "Can We Outperform the DIIS Approach for Electronic Structure Calculations?" In: *International Journal of Quantum Chemistry* 79.2 (2000), pp. 82–90. ISSN: 1097-461X. DOI: 10.1002/1097-461X(2000)79:2<82::AID-QUA3>3.0.CO;2-I.

[116] Glenn Wagner et al. "Coulomb-driven band unflattening suppresses K-phonon pairing in moiré graphene". In: *Phys. Rev. B* 109 (10 Mar. 2024), p. 104504. DOI: 10.1103/PhysRevB.109.104504.

[117] A. D. McLACHLAN and M. A. BALL. "Time-Dependent Hartree—Fock Theory for Molecules". In: *Reviews of Modern Physics* 36.3 (July 1964), pp. 844–855. DOI: 10.1103/RevModPhys.36.844.

[118] J. Schirmer. "Review of the Foundations of Time-Dependent Density-Functional Theory (TDDFT)". In: *Physical Chemistry Chemical Physics* 27.10 (2025), pp. 4992–5005. DOI: 10.1039/D4CP04551C.

[119] Peter Ring and Peter Schuck. *The nuclear many-body problem*. Springer Science & Business Media, Mar. 2004. ISBN: 978-3-540-21206-5.

[120] David J Thouless. “Stability conditions and nuclear rotations in the Hartree-Fock theory”. In: *Nuclear Physics* 21 (1960), pp. 225–232.

[121] J. E. Hirsch. “Two-dimensional Hubbard model: Numerical simulation study”. In: *Physical Review B* 31.7 (1985), pp. 4403–4419. DOI: 10.1103/PhysRevB.31.4403.

[122] E. Langmann and J. Lenells. “On the mean-field antiferromagnetic gap for the half-filled 2D Hubbard model at zero temperature”. In: *Letters in Mathematical Physics* 116.2 (2026), p. 50. DOI: 10.1007/s11005-026-02085-5.

[123] A. H. MacDonald, S. M. Girvin, and D. Yoshioka. “t/U expansion for the Hubbard model”. In: *Physical Review B* 37.16 (1988), pp. 9753–9756. DOI: 10.1103/PhysRevB.37.9753.

[124] Dumitru Calugaru et al. “Spectroscopy of Twisted Bilayer Graphene Correlated Insulators”. In: *Phys. Rev. Lett.* 129.11 (11 Sept. 2022), p. 117602. DOI: 10.1103/PhysRevLett.129.117602.

[125] Jung Pyo Hong, Tomohiro Soejima, and Michael P. Zaletel. “Detecting Symmetry Breaking in Magic Angle Graphene Using Scanning Tunneling Microscopy”. In: *Phys. Rev. Lett.* 129.14 (14 Sept. 2022), p. 147001. DOI: 10.1103/PhysRevLett.129.147001.

[126] Yves H. Kwan et al. *Electron-phonon coupling and competing Kekul\’e orders in twisted bilayer graphene*. arXiv:2303.13602 [cond-mat]. Mar. 2023. DOI: 10.48550/arXiv.2303.13602.

[127] Ziyan Zhu et al. “Twisted Trilayer Graphene: A Precisely Tunable Platform for Correlated Electrons”. In: *Physical Review Letters* 125.11 (Sept. 2020), p. 116404. DOI: 10.1103/PhysRevLett.125.116404.

[128] Simon Turkel et al. “Orderly disorder in magic-angle twisted trilayer graphene”. In: *Science* 376.6589 (Apr. 2022), pp. 193–199. DOI: 10.1126/science.abk1895. eprint: https://www.science.org/doi/pdf/10.1126/science.abk1895.

[129] Cheng Shen et al. “Dirac spectroscopy of strongly correlated phases in twisted trilayer graphene”. In: *Nature Materials* 22.3 (Dec. 2022), pp. 316–321. ISSN: 1476-4660. DOI: 10.1038/s41563-022-01428-6.

[130] Shubhayu Chatterjee, Nick Bultinck, and Michael P. Zaletel. “Symmetry breaking and skyrmionic transport in twisted bilayer graphene”. In: *Physical Review B* 101.16 (16 Apr. 2020), p. 165141. DOI: 10.1103/physrevb.101.165141.

[131] D. M. Basko and I. L. Aleiner. “Interplay of Coulomb and electron-phonon interactions in graphene”. In: *Physical Review B* 77.4 (4 Jan. 2008), p. 041409. DOI: 10.1103/physrevb.77.041409.

[132] Fengcheng Wu, A. H. MacDonald, and Ivar Martin. “Theory of Phonon-Mediated Superconductivity in Twisted Bilayer Graphene”. In: *Phys. Rev. Lett.* 121.25 (25 Dec. 2018), p. 257001. DOI: 10.1103/PhysRevLett.121.257001.

[133] M. Angeli, E. Tosatti, and M. Fabrizio. “Valley Jahn-Teller Effect in Twisted Bilayer Graphene”. In: *Physical Review X* 9.4 (4 Oct. 2019), p. 041010. DOI: 10.1103/physrevx.9.041010.

[134] Andrea Blason and Michele Fabrizio. “Local Kekul\’e Distortion Turns Twisted Bilayer Graphene into Topological Mott Insulators and Superconductors”. In: *Phys. Rev. B* 106.23 (23 Dec. 2022), p. 235112. DOI: 10.1103/PhysRevB.106.235112.

[135] B. M. Hunt et al. “Direct Measurement of Discrete Valley and Orbital Quantum Numbers in Bilayer Graphene”. In: *Nature Communications* 8.1 (Oct. 2017), p. 948. ISSN: 2041-1723. DOI: 10.1038/s41467-017-00824-w.

[136] Jason Alicea and Matthew P. A. Fisher. "Graphene Integer Quantum Hall Effect in the Ferromagnetic and Paramagnetic Regimes". In: *Physical Review B* 74.7 (Aug. 2006), p. 075422. DOI: 10.1103/PhysRevB.74.075422.

[137] Ziwei Wang et al. *Putting a New Spin on the Incommensurate Kekulé Spiral: From Spin-Valley Locking and Collective Modes to Fermiology and Implications for Superconductivity*. Sept. 2025. DOI: 10.48550/arXiv.2509.12320. arXiv: 2509.12320 [cond-mat].

[138] Erin Morissette et al. "Dirac revivals drive a resonance response in twisted bilayer graphene". In: *Nature Physics* 19.8 (Aug. 2023), pp. 1156–1162. ISSN: 1745-2481. DOI: 10.1038/s41567-023-02060-0.

[139] Yves H. Kwan et al. "Textured exciton insulators". In: *Phys. Rev. B* 112.3 (3 July 2025), p. 035129. DOI: 10.1103/4k6g-hy6y.

[140] Yves H. Kwan, S. A. Parameswaran, and S. L. Sondhi. "Twisted bilayer graphene in a parallel magnetic field". In: *Physical Review B* 101.20 (May 2020), p. 205116. DOI: 10.1103/physrevb.101.205116.

[141] Ethan Lake and T. Senthil. "Reentrant superconductivity through a quantum Lifshitz transition in twisted trilayer graphene". In: *Physical Review B* 104.17 (Nov. 2021), p. 174505. DOI: 10.1103/physrevb.104.174505.

[142] Wei Qin and Allan H. MacDonald. "In-Plane Critical Magnetic Fields in Magic-Angle Twisted Trilayer Graphene". In: *Physical Review Letters* 127.9 (Aug. 2021), p. 097001. DOI: 10.1103/PhysRevLett.127.097001.

[143] Lihuan Sun et al. "Determining Spin-Orbit Coupling in Graphene by Quasiparticle Interference Imaging". In: *Nature Communications* 14.1 (June 2023), p. 3771. ISSN: 2041-1723. DOI: 10.1038/s41467-023-39453-x.

[144] Jiachen Yu et al. "Spin skyrmion gaps as signatures of strong-coupling insulators in magic-angle twisted bilayer graphene". In: *Nature Communications* 14.1 (Oct. 2023), p. 6679. ISSN: 2041-1723. DOI: 10.1038/s41467-023-42275-6.

[145] Zhenyuan Zhang et al. *Heavy Fermions, Mass Renormalization and Local Moments in Magic-Angle Twisted Bilayer Graphene via Planar Tunneling Spectroscopy*. Mar. 2025. DOI: 10.48550/arXiv.2503.17875. arXiv: 2503.17875 [cond-mat].

[146] Haruki Watanabe. "Counting Rules of Nambu–Goldstone Modes". In: *Annual Review of Condensed Matter Physics* 11.1 (Mar. 2020), pp. 169–187. ISSN: 1947-5454, 1947-5462. DOI: 10.1146/annurev-conmatphys-031119-050644.

[147] Eslam Khalaf et al. *Soft modes in magic angle twisted bilayer graphene*. Oct. 2020. DOI: 10.48550/ARXIV.2009.14827. arXiv: 2009.14827 [cond-mat].

[148] Tian Xie et al. "Long-Lived Isospin Excitations in Magic-Angle Twisted Bilayer Graphene". In: *Nature* (Aug. 2024), pp. 1–6. ISSN: 1476-4687. DOI: 10.1038/s41586-024-07880-5.

[149] Yuan Cao et al. "Pauli-limit violation and re-entrant superconductivity in moiré graphene". In: *Nature* 595.7868 (July 2021), pp. 526–531. ISSN: 1476-4687. DOI: 10.1038/s41586-021-03685-y.

[150] Miuko Tanaka et al. "Superfluid Stiffness of Magic-Angle Twisted Bilayer Graphene". In: *Nature* 638.8049 (Feb. 2025), pp. 99–105. ISSN: 1476-4687. DOI: 10.1038/s41586-024-08494-7.

[151] Ethan Lake, Adarsh S. Patri, and T. Senthil. "Pairing symmetry of twisted bilayer graphene: A phenomenological synthesis". In: *Phys. Rev. B* 106.10 (10 Sept. 2022), p. 104506. DOI: 10.1103/PhysRevB.106.104506.

[152] Le Liu et al. “Isospin Competitions and Valley Polarized Correlated Insulators in Twisted Double Bilayer Graphene”. In: *Nature Communications* 13.1 (June 2022), p. 3292. ISSN: 2041-1723. DOI: 10.1038/s41467-022-30998-x.

[153] Xiaobo Lu et al. “Superconductors, orbital magnets and correlated states in magic-angle bilayer graphene”. In: *Nature* 574.7780 (Oct. 2019), pp. 653–657. ISSN: 1476-4687. DOI: 10.1038/s41586-019-1695-0.

[154] Petr Stepanov et al. “Untying the insulating and superconducting orders in magic-angle graphene”. In: *Nature* 583.7816 (July 2020), pp. 375–378. ISSN: 1476-4687. DOI: 10.1038/s41586-020-2459-6.

[155] Yuan Cao et al. “Nematicity and competing orders in superconducting magic-angle graphene”. In: *Science* 372.6539 (Apr. 2021), pp. 264–271. ISSN: 1095-9203. DOI: 10.1126/science.abc2836.

[156] Zekang Zhou et al. “Gate-tunable double-dome superconductivity in twisted trilayer graphene”. In: *Nature Physics* (2025). DOI: 10.1038/s41567-025-03040-2.

[157] Youngjoon Choi et al. “Electronic correlations in twisted bilayer graphene near the magic angle”. In: *Nature Physics* 15.11 (2019), pp. 1174–1180.

[158] Jeong Min Park et al. “Tunable strongly coupled superconductivity in magic-angle twisted trilayer graphene”. In: *Nature* 590.7845 (Feb. 2021), pp. 249–255. ISSN: 1476-4687. DOI: 10.1038/s41586-021-03192-0.

[159] Zeyu Hao et al. “Electric Field–Tunable Superconductivity in Alternating-Twist Magic-Angle Trilayer Graphene”. In: *Science* 371.6534 (Mar. 2021), pp. 1133–1138. DOI: 10.1126/science.abg0399. eprint: https://www.science.org/doi/pdf/10.1126/science.abg0399.

[160] Elliott Lieb, Theodore Schultz, and Daniel Mattis. “Two soluble models of an antiferromagnetic chain”. In: *Annals of Physics* 16.3 (1961), pp. 407–466. ISSN: 0003-4916. DOI: https://doi.org/10.1016/0003-4916(61)90115-4.

[161] Masaki Oshikawa. “Commensurability, Excitation Gap, and Topology in Quantum Many-Particle Systems on a Periodic Lattice”. In: *Physical Review Letters* 84.7 (7 Feb. 2000), pp. 1535–1538. DOI: 10.1103/physrevlett.84.1535.

[162] M. B. Hastings. “Lieb-Schultz-Mattis in higher dimensions”. In: *Phys. Rev. B* 69 (10 Mar. 2004), p. 104431. DOI: 10.1103/PhysRevB.69.104431.

[163] Nick Bultinck, Shubhayu Chatterjee, and Michael P. Zaletel. “Mechanism for Anomalous Hall Ferromagnetism in Twisted Bilayer Graphene”. In: *Physical Review Letters* 124.16 (16 Apr. 2020), p. 166601. DOI: 10.1103/physrevlett.124.166601.

[164] Ya-Hui Zhang et al. “Nearly Flat Chern Bands in Moir\’e Superlattices”. In: *Physical Review B* 99.7 (7 Feb. 2019), p. 075127. DOI: 10.1103/physrevb.99.075127.

[165] Jong Yeon Lee et al. “Theory of correlated insulating behaviour and spin-triplet superconductivity in twisted double bilayer graphene”. In: *Nature Communications* 10.1 (2019), p. 5333. DOI: 10.1038/s41467-019-12981-1.

[166] Aleksandra Nelson et al. “Multicellularity of Delicate Topological Insulators”. In: *Phys. Rev. Lett.* 126 (21 May 2021), p. 216404. DOI: 10.1103/PhysRevLett.126.216404.

[167] Aleksandra Nelson et al. “Delicate topology protected by rotation symmetry: Crystalline Hopf insulators and beyond”. In: *Phys. Rev. B* 106 (7 Aug. 2022), p. 075124. DOI: 10.1103/PhysRevB.106.075124.

[168] Hua Chen and Kun Yang. "Interaction-driven quantum phase transitions in fractional topological insulators". In: *Phys. Rev. B* 85 (19 May 2012), p. 195113. DOI: 10.1103/PhysRevB.85.195113.

[169] Sutirtha Mukherjee and Kwon Park. "Spin separation in the half-filled fractional topological insulator". In: *Phys. Rev. B* 99 (11 Mar. 2019), p. 115131. DOI: 10.1103/PhysRevB.99.115131.

[170] Shunsuke Furukawa and Masahito Ueda. "Global phase diagram of two-component Bose gases in antiparallel magnetic fields". In: *Phys. Rev. A* 90 (3 Sept. 2014), p. 033602. DOI: 10.1103/PhysRevA.90.033602.

[171] Ya-Hui Zhang. *Composite Fermion Insulator in Opposite-Fields Quantum Hall Bilayers*. 2018. arXiv: 1810.03600 [cond-mat.str-el].

[172] Yves H. Kwan et al. "Exciton Band Topology in Spontaneous Quantum Anomalous Hall Insulators: Applications to Twisted Bilayer Graphene". In: *Phys. Rev. Lett.* 126 (13 Mar. 2021), p. 137601. DOI: 10.1103/PhysRevLett.126.137601.

[173] Yves H. Kwan et al. "Excitonic fractional quantum Hall hierarchy in moiré heterostructures". In: *Phys. Rev. B* 105 (23 June 2022), p. 235121. DOI: 10.1103/PhysRevB.105.235121.

[174] P. Myles Eugenio and Ceren B. Dağ. "DMRG study of strongly interacting $\mathbb{Z}_2$ flatbands: a toy model inspired by twisted bilayer graphene". In: *SciPost Phys. Core* 3 (2020), p. 015. DOI: 10.21468/SciPostPhysCore.3.2.015.

[175] Nikolaos Stefanidis and Inti Sodemann. "Excitonic Laughlin states in ideal topological insulator flat bands and their possible presence in moiré superlattice materials". In: *Physical Review B* 102.3 (3 July 2020), p. 035158. DOI: 10.1103/physrevb.102.035158.

[176] Shubhayu Chatterjee, Matteo Ippoliti, and Michael P. Zaletel. "Skyrmion superconductivity: DMRG evidence for a topological route to superconductivity". In: *Physical Review B* 106.3 (July 2022). DOI: 10.1103/physrevb.106.035421.

[177] Zhengyan Darius Shi et al. *Excitonic quantum criticality: from bilayer graphene to narrow Chern bands*. 2024. arXiv: 2402.12436 [cond-mat.str-el].

[178] Ke Yang. "Phase transition in bilayer quantum Hall system with opposite magnetic field". In: *Chinese Physics B* 32.9 (Sept. 2023), p. 097303. DOI: 10.1088/1674-1056/ace61d.

[179] K. Moon et al. "Spontaneous interlayer coherence in double-layer quantum Hall systems: Charged vortices and Kosterlitz-Thouless phase transitions". In: *Physical Review B* 51.8 (8 Feb. 1995), pp. 5138–5170. DOI: 10.1103/physrevb.51.5138.

[180] J.P. Eisenstein. "Exciton Condensation in Bilayer Quantum Hall Systems". In: *Annual Review of Condensed Matter Physics* 5.Volume 5, 2014 (2014), pp. 159–181. ISSN: 1947-5462. DOI: https://doi.org/10.1146/annurev-conmatphys-031113-133832.

[181] G. William Burg et al. "Correlated Insulating States in Twisted Double Bilayer Graphene". In: *Physical Review Letters* 123.19 (Nov. 2019), p. 197702. DOI: 10.1103/PhysRevLett.123.197702.

[182] Yuan Cao et al. "Tunable correlated states and spin-polarized phases in twisted bilayer–bilayer graphene". In: *Nature* 583.7815 (May 2020), pp. 215–220. ISSN: 1476-4687. DOI: 10.1038/s41586-020-2260-6.

[183] Renjun Du et al. “Ferroelectricity in Twisted Double Bilayer Graphene”. In: *2D Materials* 11.2 (Apr. 2024), p. 025015. ISSN: 2053-1583. DOI: 10.1088/2053-1583/ad2107. arXiv: 2404.18059 [cond-mat].

[184] Minhao He et al. “Symmetry Breaking in Twisted Double Bilayer Graphene”. In: *Nature Physics* 17.1 (Jan. 2021), pp. 26–30. ISSN: 1745-2481. DOI: 10.1038/s41567-020-1030-6.

[185] Xiaomeng Liu et al. “Tunable spin-polarized correlated states in twisted double bilayer graphene”. In: *Nature* 583.7815 (July 2020), pp. 221–225. ISSN: 1476-4687. DOI: 10.1038/s41586-020-2458-7.

[186] Peter Rickhaus et al. “Correlated Electron-Hole State in Twisted Double-Bilayer Graphene”. In: *Science* 373.6560 (Sept. 2021), pp. 1257–1260. DOI: 10.1126/science.abc3534.

[187] Carmen Rubio-Verdú et al. “Moiré Nematic Phase in Twisted Double Bilayer Graphene”. In: *Nature Physics* 18.2 (Feb. 2022), pp. 196–202. ISSN: 1745-2481. DOI: 10.1038/s41567-021-01438-2.

[188] Cheng Shen et al. “Correlated states in twisted double bilayer graphene”. In: *Nature Physics* 16.5 (Mar. 2020), pp. 520–525. ISSN: 1745-2481. DOI: 10.1038/s41567-020-0825-9.

[189] Canxun Zhang et al. “Visualizing Delocalized Correlated Electronic States in Twisted Double Bilayer Graphene”. In: *Nature Communications* 12.1 (May 2021), p. 2516. ISSN: 2041-1723. DOI: 10.1038/s41467-021-22711-1.

[190] Yujian Zhu et al. “Tunable Multi-Bands in Twisted Double Bilayer Graphene”. In: *2D Materials* 9.3 (May 2022), p. 034001. ISSN: 2053-1583. DOI: 10.1088/2053-1583/ac69bb.

[191] Minhao He et al. “Symmetry-Broken Chern Insulators in Twisted Double Bilayer Graphene”. In: *Nano Letters* 23.23 (Dec. 2023), pp. 11066–11072. ISSN: 1530-6984. DOI: 10.1021/acs.nanolett.3c03414.

[192] Mikito Koshino. “Band Structure and Topological Properties of Twisted Double Bilayer Graphene”. In: *Physical Review B* 99.23 (June 2019), p. 235406. DOI: 10.1103/PhysRevB.99.235406.

[193] Jianpeng Liu et al. “Quantum Valley Hall Effect, Orbital Magnetism, and Anomalous Hall Effect in Twisted Multilayer Graphene Systems”. In: *Phys. Rev. X* 9.3 (3 Aug. 2019), p. 031021. DOI: 10.1103/PhysRevX.9.031021.

[194] Narasimha Raju Chebrolu, Bheema Lingam Chittari, and Jeil Jung. “Flat Bands in Twisted Double Bilayer Graphene”. In: *Physical Review B* 99.23 (June 2019), p. 235417. DOI: 10.1103/PhysRevB.99.235417.

[195] Fatemeh Haddadi et al. “Moiré Flat Bands in Twisted Double Bilayer Graphene”. In: *Nano Letters* 20.4 (Apr. 2020), pp. 2410–2415. ISSN: 1530-6984. DOI: 10.1021/acs.nanolett.9b05117.

[196] Jeil Jung and Allan H. MacDonald. “Accurate Tight-Binding Models for the $\ensuremath{\pi}$ Bands of Bilayer Graphene”. In: *Physical Review B* 89.3 (Jan. 2014), p. 035405. DOI: 10.1103/PhysRevB.89.035405.

[197] Shaowen Chen et al. “Electrically Tunable Correlated and Topological States in Twisted Monolayer–Bilayer Graphene”. In: *Nature Physics* 17.3 (Mar. 2021), pp. 374–380. ISSN: 1745-2481. DOI: 10.1038/s41567-020-01062-6.

[198] Minhao He et al. "Competing Correlated States and Abundant Orbital Magnetism in Twisted Monolayer-Bilayer Graphene". In: *Nature Communications* 12.1 (Aug. 2021), p. 4727. ISSN: 2041-1723. DOI: 10.1038/s41467-021-25044-1.

[199] Si-yu Li et al. "Imaging Topological and Correlated Insulating States in Twisted Monolayer-Bilayer Graphene". In: *Nature Communications* 13.1 (July 2022), p. 4225. ISSN: 2041-1723. DOI: 10.1038/s41467-022-31851-x.

[200] H. Polshyn et al. "Electrical switching of magnetic order in an orbital Chern insulator". In: *Nature* 588.7836 (Nov. 2020), pp. 66–70. ISSN: 1476-4687. DOI: 10.1038/s41586-020-2963-8.

[201] H. Polshyn et al. "Topological charge density waves at half-integer filling of a moiré superlattice". In: *Nature Physics* 18.1 (Dec. 2021), pp. 42–47. ISSN: 1745-2481. DOI: 10.1038/s41567-021-01418-6.

[202] Shuigang Xu et al. "Tunable van Hove Singularities and Correlated States in Twisted Monolayer–Bilayer Graphene". In: *Nature Physics* 17.5 (May 2021), pp. 619–626. ISSN: 1745-2481. DOI: 10.1038/s41567-021-01172-9.

[203] Canxun Zhang et al. "Local Spectroscopy of a Gate-Switchable Moiré Quantum Anomalous Hall Insulator". In: *Nature Communications* 14.1 (June 2023), p. 3595. ISSN: 2041-1723. DOI: 10.1038/s41467-023-39110-3.

[204] Patrick J. Ledwith, Ashvin Vishwanath, and Eslam Khalaf. "Family of Ideal Chern Flatbands with Arbitrary Chern Number in Chiral Twisted Graphene Multilayers". In: *Phys. Rev. Lett.* 128.17 (17 Apr. 2022), p. 176404. DOI: 10.1103/PhysRevLett.128.176404.

[205] Ruiheng Su et al. *Generalized Anomalous Hall Crystals in Twisted Bilayer-Trilayer Graphene*. June 2024. DOI: 10.48550/arXiv.2406.17766. arXiv: 2406.17766 [cond-mat].

[206] Yves H. Kwan et al. *Textured Exciton Insulators*. June 2024. arXiv: 2406.15343 [cond-mat].

[207] Chen Fang, Matthew J. Gilbert, and B. Andrei Bernevig. "Bulk Topological Invariants in Noninteracting Point Group Symmetric Insulators". In: *Physical Review B* 86.11 (Sept. 2012), p. 115112. DOI: 10.1103/PhysRevB.86.115112.

[208] Yves H. Kwan et al. in preparation. 2024.

[209] S. M. Girvin, A. H. MacDonald, and P. M. Platzman. "Collective-Excitation Gap in the Fractional Quantum Hall Effect". In: *Physical Review Letters* 54.6 (Feb. 1985), pp. 581–583. DOI: 10.1103/PhysRevLett.54.581.

[210] S. M. Girvin, A. H. MacDonald, and P. M. Platzman. "Magneto-Roton Theory of Collective Excitations in the Fractional Quantum Hall Effect". In: *Physical Review B* 33.4 (Feb. 1986), pp. 2481–2494. DOI: 10.1103/PhysRevB.33.2481.

[211] S. A. Parameswaran, R. Roy, and S. L. Sondhi. "Fractional Chern Insulators and the W_∞ Algebra". In: *Physical Review B* 85.24 (June 2012), p. 241308. DOI: 10.1103/PhysRevB.85.241308.

[212] Rahul Roy. "Band Geometry of Fractional Topological Insulators". In: *Physical Review B* 90.16 (Oct. 2014), p. 165139. DOI: 10.1103/PhysRevB.90.165139.

[213] Daniel Varjas et al. "Topological Lattice Models with Constant Berry Curvature". In: *SciPost Physics* 12.4 (Apr. 2022), p. 118. ISSN: 2542-4653. DOI: 10.21468/SciPostPhys.12.4.118.

[214] M. O. Goerbig. "From Fractional Chern Insulators to a Fractional Quantum Spin Hall Effect". In: *The European Physical Journal B* 85.1 (Jan. 2012), p. 15. ISSN: 1434-6036. DOI: 10.1140/epjb/e2011-20857-6.

[215] Yang-Le Wu, B. Andrei Bernevig, and N. Regnault. "Zoology of Fractional Chern Insulators". In: *Physical Review B* 85.7 (Feb. 2012), p. 075116. DOI: 10.1103/PhysRevB.85.075116.

[216] Ganpathy Murthy and R. Shankar. "Hamiltonian theory of fractionally filled Chern bands". In: *Phys. Rev. B* 86 (19 Nov. 2012), p. 195146. DOI: 10.1103/PhysRevB.86.195146.

[217] E. Dobardžić, M. V. Milovanović, and N. Regnault. "Geometrical Description of Fractional Chern Insulators Based on Static Structure Factor Calculations". In: *Physical Review B* 88.11 (Sept. 2013), p. 115117. DOI: 10.1103/PhysRevB.88.115117.

[218] Martin Claassen et al. "Position-Momentum Duality and Fractional Quantum Hall Effect in Chern Insulators". In: *Physical Review Letters* 114.23 (June 2015), p. 236802. DOI: 10.1103/PhysRevLett.114.236802.

[219] T. S. Jackson, Gunnar Möller, and Rahul Roy. "Geometric Stability of Topological Lattice Phases". In: *Nature Communications* 6.1 (Nov. 2015), p. 8629. ISSN: 2041-1723. DOI: 10.1038/ncomms9629.

[220] David Bauer, T. S. Jackson, and Rahul Roy. "Quantum geometry and stability of the fractional quantum Hall effect in the Hofstadter model". In: *Phys. Rev. B* 93 (23 June 2016), p. 235133. DOI: 10.1103/PhysRevB.93.235133.

[221] Ching Hua Lee, Martin Claassen, and Ronny Thomale. "Band Structure Engineering of Ideal Fractional Chern Insulators". In: *Physical Review B* 96.16 (Oct. 2017), p. 165150. DOI: 10.1103/PhysRevB.96.165150.

[222] Tomoki Ozawa and Bruno Mera. "Relations between Topology and the Quantum Metric for Chern Insulators". In: *Physical Review B* 104.4 (July 2021), p. 045103. DOI: 10.1103/PhysRevB.104.045103.

[223] Bruno Mera and Tomoki Ozawa. "Kähler Geometry and Chern Insulators: Relations between Topology and the Quantum Metric". In: *Physical Review B* 104.4 (July 2021), p. 045104. DOI: 10.1103/PhysRevB.104.045104.

[224] Bruno Mera and Tomoki Ozawa. "Engineering Geometrically Flat Chern Bands with Fubini-Study Kähler Structure". In: *Physical Review B* 104.11 (Sept. 2021), p. 115160. DOI: 10.1103/PhysRevB.104.115160.

[225] Patrick J. Ledwith, Ashvin Vishwanath, and Daniel E. Parker. "Vortexability: A Unifying Criterion for Ideal Fractional Chern Insulators". In: (Oct. 2022). DOI: 10.48550/arXiv.2209.15023.

[226] Bruno Mera and Tomoki Ozawa. "Uniqueness of Landau Levels and Their Analogs with Higher Chern Numbers". In: *Physical Review Research* 6.3 (Sept. 2024), p. 033238. DOI: 10.1103/PhysRevResearch.6.033238.

[227] Yonglong Xie et al. "Fractional Chern insulators in magic-angle twisted bilayer graphene". In: *Nature* 600.7889 (Dec. 2021), pp. 439–443. ISSN: 1476-4687. DOI: 10.1038/s41586-021-04002-3.

[228] Steven H. Simon and Mark S. Rudner. "Contrasting Lattice Geometry Dependent versus Independent Quantities: Ramifications for Berry Curvature, Energy Gaps, and Dynamics". In: *Physical Review B* 102.16 (Oct. 2020), p. 165148. DOI: 10.1103/PhysRevB.102.165148.

[229] Steven H. Simon, Fenner Harper, and N. Read. "Fractional Chern insulators in bands with zero Berry curvature". In: *Phys. Rev. B* 92 (19 Nov. 2015), p. 195104. DOI: 10.1103/PhysRevB.92.195104.

[230] Jie Wang et al. "Exact Landau Level Description of Geometry and Interaction in a Flatband". In: *Physical Review Letters* 127.24 (Dec. 2021), p. 246403. DOI: 10.1103/PhysRevLett.127.246403.

[231] Patrick J. Ledwith et al. "Fractional Chern insulator states in twisted bilayer graphene: An analytical approach". In: *Physical Review Research* 2.2 (May 2020), p. 023237. DOI: 10.1103/physrevresearch.2.023237.

[232] Jie Wang and Zhao Liu. "Hierarchy of Ideal Flatbands in Chiral Twisted Multilayer Graphene Models". In: *Physical Review Letters* 128.17 (Apr. 2022), p. 176403. DOI: 10.1103/PhysRevLett.128.176403.

[233] Trithep Devakul et al. "Magic-angle helical trilayer graphene". In: *Science Advances* 9.36 (Sept. 2023), eadi6063. DOI: 10.1126/sciadv.adi6063. eprint: https://www.science.org/doi/pdf/10.1126/sciadv.adi6063.

[234] Junkai Dong et al. "Many-Body Ground States from Decomposition of Ideal Higher Chern Bands: Applications to Chirally Twisted Graphene Multilayers". In: *Physical Review Research* 5.2 (June 2023), p. 023166. DOI: 10.1103/PhysRevResearch.5.023166.

[235] Qiang Gao et al. "Untwisting Moiré Physics: Almost Ideal Bands and Fractional Chern Insulators in Periodically Strained Monolayer Graphene". In: *Physical Review Letters* 131.9 (Aug. 2023), p. 096401. DOI: 10.1103/PhysRevLett.131.096401.

[236] Jie Wang, Semyon Klevtsov, and Zhao Liu. "Origin of Model Fractional Chern Insulators in All Topological Ideal Flatbands: Explicit Color-Entangled Wave Function and Exact Density Algebra". In: *Physical Review Research* 5.2 (June 2023), p. 023167. DOI: 10.1103/PhysRevResearch.5.023167.

[237] Marek Kuczma. *An Introduction to the Theory of Functional Equations and Inequalities, 2ed.* Birkhauser Verlag, 2009. DOI: 10.1007/978-3-7643-8749-5.

[238] H. Kestelman. "On the functional equation $f(x+y) = f(x)+f(y)$". In: *Fundamenta Mathematicae* 34.1 (1947), pp. 144–147. DOI: 10.4064/fm-34-1-144-147.